

The logo for the Nanoscale Science, Engineering & Technology (NSET) program, featuring the acronym "NNIN" in a stylized, bold, blue font. Below the acronym is a series of horizontal lines of varying lengths, suggesting a molecular structure or a nanoscale pattern. The entire logo is set against a white diamond shape, which is itself on a dark blue background.

**NNIN**

Nanoscale Science,  
Engineering & Technology

**2005**  
**nnin reu**  
**research**  
**accomplishments**



**The 2005 National Nanotechnology Infrastructure Network  
Research Experience for Undergraduates Program  
Research Accomplishments**

**Table of Contents**

<i>National Nanotechnology Infrastructure Network .....</i>	<i>vi</i>
<i>2005 NNIN REU Introduction .....</i>	<i>vii</i>
<i>The 2005 NNIN REU Interns, by site</i>	
Cornell NanoScale Science & Technology Facility, Cornell University .....	viii
Microelectronics Research Center, Georgia Institute of Technology .....	viii
Center for Nanoscale Systems, Harvard University .....	ix
Howard Nanoscale Science & Technology Facility, Howard University .....	ix
Center for Nanotechnology Education & Utilization, The Pennsylvania State University .....	x
Stanford Nanofabrication Facility, Stanford University .....	x
Nanotech at UCSB, University of California Santa Barbara .....	xi
Michigan Nanofabrication Facility, The University of Michigan, Ann Arbor .....	xi
Nano Fabrication Center, University of Minnesota .....	xii
NanoScience @ UNM, University of New Mexico .....	xii
Microelectronics Research Center, University of Texas at Austin .....	xiii
Center for Nanotechnology, University of Washington .....	xiii

**The 2005 NNIN REU Research Accomplishments**

<i>Air Pressure Sensing by Monitoring Lateral Charge Carrier Transport in Pt Tetra(Carboxylphenyl) Porphyrins</i> Jock Bovington, Physics, and Electrical Engr/Specialization in Computer Engr, Seattle University .....	2
<i>Fabrication &amp; Characterization of Nanostructured Conducting Polymer Films on the Surfaces of Microfabricated Neural Prosthetic Biosensors</i> Amber Brannan, Applied Biology, Rose-Hulman Institute of Technology .....	4
<i>Self-Assembly of Nanofabricated Colloids</i> Blair Brettman, Chemical Engineering, University of Texas at Austin .....	6
<i>Fabrication of Nanomechanical Oscillators for Chemical and Biological Sensing</i> Caitlin Burger, Physics/Mathematics, Shippensburg University .....	8
<i>Polymer-Filled Optical Through-Wafer Interconnects for Heterogeneous 3-D Microsystem Integration</i> Ashley Carson, Biosystems Engineering, Clemson University .....	10
<i>Pressure Sensor Membrane Design &amp; Fabrication using Photo Electro-Chemical Etching on Thin Film &amp; Bulk SiC</i> Richard A. Castillo, Advanced Materials Engineering Research Institute (AMERI), Mechanical & Materials Engineering Dept., Florida International University .....	12

<b><i>Characterization of Nanofiltration Membranes</i></b>	
Michael Donnell Chestnut II, Computer & Electrical Engineering, North Carolina State University .....	14
<b><i>Fabrication &amp; Characterization of Nanoscale Electrochemical InN Sensors</i></b>	
Clara Ji-Hyun Cho, General Engineering, Franklin W. Olin College of Engineering.....	16
<b><i>A Microfluidic System for the Assembly and Culture of Tumor Spheroids</i></b>	
Eric Chu, Biomedical Engineering, Johns Hopkins University .....	18
<b><i>Microfluidic Devices for Biological Applications</i></b>	
Frank Cleary, Physics, Cornell University .....	20
<b><i>Development of Ti Doped Iron Oxide by Sol-Gel Synthesis Routes for Photocatalytic H<sub>2</sub> Production</i></b>	
Samantha C. Cruz, Materials Science and Engineering, Northwestern University.....	22
<b><i>Porous Nanostructured Titania</i></b>	
Michael Cullinan, Engineering, Swarthmore College .....	24
<b><i>Suspended Langmuir-Blodgett Film for Surround Gate Transistors</i></b>	
Minh Phuc Nguyen Dao, Electrical Engineering, Santa Clara University .....	26
<b><i>The Development of a New Method to Monitor the Activity of Neuronal Networks Using Microelectronic Chips</i></b>	
Aileen Dinin, Chemical and Biomedical Engineering, Carnegie Mellon University.....	28
<b><i>Polymer Process Optimization for Electrical and Optical I/O Interconnect Pillar Fabrication</i></b>	
Laura Doyle, Biomedical Engineering, Johns Hopkins University.....	30
<b><i>Material Characterization for Optimizing Passivation of Type-II InAs/GaSb Superlattice Infrared Photodetectors</i></b>	
Nicole Escudé, Physical Science - Chemistry, Biola University.....	32
<b><i>Properties and Performance of Molecular Glass Photoresists</i></b>	
Nkemdilim Ezeife, Chemistry, Temple University .....	34
<b><i>Model Micro-Channels for the Study of Aerobic, Nano-Porous Biocatalytic Latex Coatings</i></b>	
Johangel M. Figueroa, Industrial Biotechnology, University of Puerto Rico, Mayagüez.....	36
<b><i>Electrical, Optical, and Thermofluidic Wafer-Level Chip I/O Interconnects Enabled by Nano/Microimprint Lithography</i></b>	
Wand Gan, Biochemistry, University of Florida .....	38
<b><i>Hydrogen Passivation of Photodiodes</i></b>	
Niusha E. Gutierrez, Electrical Engineering, Florida Atlantic University .....	40
<b><i>Experimental Study of Nanoparticle Penetration Through Various Filter Media</i></b>	
Matthew Harrington, Electronics Engineering Technology, Oregon Institute of Technology .....	42
<b><i>Spin Polarized Transports Through a Polymer Using Half Metallic Manganites as Spin Injectors</i></b>	
Paul Harris, Applied Physics, California State University San Bernardino .....	44
<b><i>Laser Direct Write Grayscale Photolithography</i></b>	
James Thorpe Helton, Chemical Engineering, Arizona State University .....	46
<b><i>Nanomechanical Structures for Digital Logic</i></b>	
Joseph Heremans, Computer Engineering, The University of Michigan .....	48
<b><i>Porous Carbons for Environmental Cleanup</i></b>	
Nathan Honsowetz, Aerospace Engineering, University of Southern California.....	50
<b><i>FIB and TEM Analysis of Nanoscale Thin Films</i></b>	
Derek Hsen Dai Hsu, Materials Science and Engineering, Northwestern University.....	52
<b><i>Intercalation and Exfoliation of Herringbone Graphite Nanofibers</i></b>	
Sabil Huda, Chemical Engineering (Nanoscience Concentration), North Carolina State University.....	54

<b><i>New Techniques for Generating Core/Shell Nanoparticles</i></b>	
Jacob Hughey, Biomedical Engineering and Mathematics, Vanderbilt University .....	56
<b><i>Catalytically Induced Microfluidics: Induced Fluid Flow as a Function of Anode Surface Area</i></b>	
Jodi M. Iwata, Materials Engineering, San Jose State University .....	58
<b><i>E-Beam Lithography to Improve the Performance of Organic Optoelectronics</i></b>	
Jamie Jackson, Electrical Engineering, Morehouse College .....	60
<b><i>Thermal Stability of Ge-on-Si Thin Films</i></b>	
Miktosha James, Electrical Engineering, Prairie View A&M University .....	62
<b><i>Limits of Adaptive Liquid Lens</i></b>	
Joy Johnson, Electrical & Computer Engineering, North Carolina State University .....	64
<b><i>Characterization of Nanoimprinting HSQ Material</i></b>	
Thaddeus Koehn, Electrical Engineering and Physics, University of Rhode Island .....	66
<b><i>Fabrication of Gold/Chrome Microparticles to be Used in Drug Delivery Applications</i></b>	
Arthur K. Kuehl, Materials Sciences & Engineering, University of Arizona .....	68
<b><i>Colloidal Dimers for Reduced Symmetry Photonic Crystals</i></b>	
Amy Lee, General Engineering, Franklin W. Olin College of Engineering .....	70
<b><i>Structural &amp; Physical Characterization of Supramolecular Diblock Copolymers</i></b>	
Cheng-Yuk Lee, Chemical Engineering, University of Massachusetts Amherst .....	72
<b><i>The Relationship of Line Edge Roughness and Contrast by Deep UV Immersion Interferometric Lithography</i></b>	
David Light, Molecular, Cellular and Developmental Biology, Yale University .....	74
<b><i>Development of a Non-Contact DNA Spotting Method for Biosensors</i></b>	
Wade Luhman, Mechanical Engineer, Minnesota State University Mankato .....	76
<b><i>Bi-Layer Lithography Using Nanoimprinting</i></b>	
Aaron McDaniel, Applied Physics, Linfield College .....	78
<b><i>Silicon Morphology Evolution under Focused Ion Beam Irradiation</i></b>	
Matthew R. McGrath, Department of Physics, Vanderbilt University .....	80
<b><i>Ferroelectric Nonvolatile Memory Materials: Fundamentals of Reliable Ferroelectric Switching</i></b>	
David McIntosh, Electrical Engineering, Oregon State University .....	82
<b><i>Characterization of Beam Aberrations due to Magnetic Field Tilt in DIVA for Massively Parallel Electron Beam Lithography</i></b>	
Steve Meisburger, Physics, Carleton College .....	84
<b><i>In Situ Fabrication of Oxide Apertures in Vertical-Cavity Surface-Emitting Lasers</i></b>	
Andrew Melton, Electrical Engineering, University of Portland .....	86
<b><i>Focused Ion Beam Fabrication of Pt Electrodes with an Interelectrode Spacing Less Than 10 nm</i></b>	
Joshua Montague, Physics, Colby College .....	88
<b><i>Fabrication of Two-Dimensional Arrays of Inorganic-Binding Polypeptides for the Template-Directed Self-Assembly of Nanoparticles</i></b>	
Victoria Mooney, Chemistry, Viterbo University .....	90
<b><i>Compositional Analysis of W and Ti Bilayer Electrodes at the Metal-Dielectric Interface and Its Effects on Work Function</i></b>	
Que Anh Nguyen, Engineering (Materials Science & Applied Chemistry), Franklin W. Olin College of Engineering .....	92
<b><i>Electronic &amp; Thermoelectric Properties of Semiconductor Nanostructures</i></b>	
Luke Niewiadomski, Electrical Engineering, Michigan State University .....	94

<b><i>DNA Pyrosequencing Using Microfluidic Chips</i></b>	
William Noderer, Chemical Engr, and Integrated Business & Engineering, Lehigh University .....	96
<b><i>Growth of Cubic Silicon Carbide on Silicon Nano-Mesas</i></b>	
Brian Noel, Electrical Engr and Biomedical Engr, Virginia Commonwealth University .....	98
<b><i>Preparation of Silver Nanoparticle Formulations for Biocidal Applications</i></b>	
Virginia Noxon, Biology, Emory & Henry College .....	100
<b><i>Electrical and Structural Characterization of GaN for Optoelectronic Applications</i></b>	
Christopher Olson, Materials Science & Engineering, University of Florida.....	102
<b><i>Social and Ethical Dimensions of Nanofabrication</i></b>	
Priscilla Paul, General Engr, Concentration in Biomedical Engr, The Cooper Union for The Advancement of Science & Art..	104
<b><i>The Effects of SiO<sub>2</sub> Shell Coatings on High Temperature Annealing Behavior of FePt Nanocrystals</i></b>	
Jose Pelaez, Chemical Engineering, Columbia University .....	106
<b><i>Hexabenzocoronene as a 1-D Organic Semiconductor in FETs</i></b>	
Calvin Peng, Materials Science and Engineering, University of Pennsylvania .....	108
<b><i>Growth and Characterization of Vertically Aligned High-Density Gallium Nitride Nanowires</i></b>	
Edgar A. Peralta, Applied & Engineering Physics, Cornell University.....	110
<b><i>Molecular Packing of Charged Conjugated Polymer Studied by Atomic Force Microscopy</i></b>	
Alexandra Polosukhina, Physics, University of San Francisco.....	112
<b><i>Engineering Protein Scaffolds for Interactions with Nanoparticles</i></b>	
Laralynne Przybyla, Biochemistry and Molecular Biology, Purdue University .....	114
<b><i>Modeling of Anisotropic Surface Energies for Quantum Dot Formation and Morphological Evolution</i></b>	
Marc PunKay, Mathematics, Pomona College .....	116
<b><i>Electromechanical Characterization of One-Dimensional Solids</i></b>	
Nakul Reddy, Electrical Engineering, Georgia Institute of Technology .....	118
<b><i>Adhesion in Nanoimprint Lithography &amp; Embossing Related Thin-Films</i></b>	
Emily Rice, Physics and Economics, University of Florida.....	120
<b><i>Universal File Translator for First Principles Codes</i></b>	
Nathan Ridling, Physics, North Georgia College and State University .....	122
<b><i>Characterization of Thick Photoresist</i></b>	
Idaliz Rodríguez Dátil, Chemical Engineering, University of Puerto Rico, Mayagüez Campus.....	124
<b><i>Integrated UHF Magnetic Transducers</i></b>	
Sarah Ruch, Mechanical Engineering, University of Texas at Austin.....	126
<b><i>Nanoscale Gold Deformation and Characterization</i></b>	
Yaniv Scherson, Mechanical Engineering and Materials Science, UC Berkeley.....	128
<b><i>Microfabrication of a Parallel-Array DNA Pyrosequencing Chip</i></b>	
Neel Shah, Engineering, Harvey Mudd College .....	130
<b><i>Electrical Characterization of Semipolar Gallium Nitride Thin Films</i></b>	
Yu-ping Shao, Electrical Engineering, Colorado State University.....	132
<b><i>Gallium Nitride Nanowire Growth, and FET Device and Biosensor Fabrication</i></b>	
Kaylee Sill McElroy, Physics, Brigham Young University .....	134
<b><i>Surface Preparation for 3C-SiC Growth on 3C- and 6H-SiC by In Situ Etching in HCl</i></b>	
Janessa Smith, Mechanical Engineering, University of Delaware.....	136

<b><i>Nanometer-Thick Dielectric Films Deposited by Electron Cyclotron Resonance PECVD System</i></b>	
Matthew J. Smith, Material Science and Engineering, Johns Hopkins University .....	138
<b><i>Nanoscale Surface Acoustic Wave Sensors for Early Cancer Detection</i></b>	
Wafa Soofi, Bioengineering, Rice University .....	140
<b><i>Nanoscale Magnetic Characterization of FIB Patterned Bits on Perpendicular Magnetic Recording Media</i></b>	
Joshua Symonds, Physics and Applied Mathematics, University of Rochester .....	142
<b><i>Nanofiber Catalyst Production Using Anaerobic Bacteria</i></b>	
Rachel Thompson, Chemistry, Rockford College .....	144
<b><i>Whispering-Gallery-Mode Microdisk Optical Biosensor: Fabrication and Characterization</i></b>	
Abbie Tippie, Electrical Engineering, Colorado State University .....	146
<b><i>Synaptic Ultrastructural Reconstruction Using Serial Electron Microscopy</i></b>	
Winnie J. Tsang, Biomedical Engineering, Johns Hopkins University .....	148
<b><i>Patterning Proteins on Glass and Silicon Substrates</i></b>	
Brandon Walker, Department of Chemistry, Grambling State University .....	150
<b><i>Nanoscale Topography Affects on the Biocompatibility of Kidney Cells on Sculptured Thin Films</i></b>	
David Welch, Biomedical Engineering, Tulane University .....	152
<b><i>Fabrication and Electrical Analysis of Metal Bilayer Electrodes for Nanodevices</i></b>	
Heidi Wheelwright, Physics, Utah Valley State College .....	154
<b><i>Production and Analysis of Conjugate Polymer/ZnO Solar Cells</i></b>	
Michael White, Chemistry Major, Saint Michael's College .....	156
<b><i>Characterization of Semipolar, and N-Face Group III Nitrides</i></b>	
Jason Winders, Electrical Engineering, Penn State University .....	158
<b><i>Gray-Scale Electron-Beam Lithography</i></b>	
Yin Ian Yang, Electrical Engineering, University of Virginia .....	160
<b><i>Partially Self-Assembled Planar Photonic Structures</i></b>	
Shelley Zieren, Chemical Engineering, University of Texas-Austin .....	162
<b><i>Index</i></b> .....	<b>164</b>



Find the 2005 NNIN REU Research Accomplishments on the web, in PDF, at: <http://www.nnin.org>



**The National Nanotechnology Infrastructure Network  
is made up of the following thirteen sites, and is supported by  
The National Science Foundation, the NNIN sites,  
our corporate sponsors and research users.**

**Cornell NanoScale Science & Technology Facility**

**Cornell University**  
250 Duffield Hall • Ithaca, NY 14853  
607-255-2329 • <http://www.cnf.cornell.edu>

**Microelectronics Research Center**

**Georgia Institute of Technology**  
791 Atlantic Dr NW • Atlanta, GA 30332  
404-894-5266 • <http://www.mirc.gatech.edu/>

**Center for Nanoscale Systems**

**Harvard University**  
17 Oxford St., Cruft 314 • Cambridge, MA 02138  
617-384-7411  
<http://www.cns.fas.harvard.edu>

**Howard Nanoscale Science & Engineering Facility**

**Howard University**  
2300 6th St NW • Washington, DC 20059  
202-806-6618  
<http://www.msrfce.howard.edu/>

**Triangle National Lithography Center  
North Carolina State University**

(affiliate)  
218A EGRC - Engineering Grad Res Ctr, Box 7911  
Raleigh, NC 27695-7920  
919-515-5153 • <http://www.tnlc.ncsu.edu/>

**Center for Nanotechnology Education & Utilization**

**The Pennsylvania State University**  
101 Innovation Blvd, Ste 114 • University Park, PA 16802  
814-865-5285  
<http://www.cneu.psu.edu>

**Stanford Nanofabrication Facility**

**Stanford University**  
CIS 103 Via Ortega St, 420 Via Palou Mall  
Stanford, CA 94305-4085  
650-723-9508 • <http://snf.stanford.edu/>

**Nanotech at UCSB**

**University of California Santa Barbara**  
Electrical & Computer Engineering, 5153 Engineering I  
Santa Barbara, CA 93106-9560  
805-893-3244 • <http://www.nanotech.ucsb.edu/>

**Michigan Nanofabrication Facility**

**The University of Michigan, Ann Arbor**  
1301 Beal Ave • Ann Arbor, MI 48109-2122  
734-763-6650 • <http://www.eecs.umich.edu/ssel/>

**Nano Fabrication Center**

**University of Minnesota**  
200 Union St. SE, Rm 4-174 • Minneapolis, MN 55455  
612-625-6608 • <http://www.nfc.umn.edu/>

**NanoScience @ UNM**

**University of New Mexico**  
1313 Goddard SE, MSC04 2710  
Albuquerque, NM 87106  
505-272-7800 • <http://www.chtm.unm.edu/>

**Microelectronics Research Center**

**The University of Texas at Austin**  
J.J. Pickle Research Center, 10100 Burnet Rd, Bldg. 160,  
Mailcode R9900 • Austin, TX 78758  
512-471-6730  
<http://www.mrc.utexas.edu/>

**Center for Nanotechnology**

**University of Washington**  
Box 351721  
Seattle, WA 98195-1721  
206-616-9760  
<http://www.nano.washington.edu/index.asp>

**REU Program Corporate Sponsors:**

Advanced Micro Devices  
Agilent Technologies  
Analog Devices  
Applied Materials  
Canon  
Ebara Corporation  
Hewlett-Packard Company  
Hitachi, Ltd  
IBM Corporation  
Infineon  
Intel Corporation  
Intel Foundation  
LG Electronics, Inc.  
National Semiconductor Corporation  
Panasonic  
Philips  
Renesas Technology Corporation  
Robert Bosch Corp.  
Texas Instruments, Incorporated  
Toshiba  
TSMC (Taiwan Semiconductor Manufacturing Company)

**[www.nnin.org](http://www.nnin.org)**

## The 2005 NNIN REU Research Accomplishments

### Introduction



*The 2005 NNIN REU Interns at the network-wide convocation held at Stanford University, August 10-12, 2005*

***This is the second report of the Research Experience for Undergraduates (REU) Program of National Nanotechnology Infrastructure Network (NNIN).***

Providing a focused experimental research experience in nanotechnology and its foundational subjects in a 10 week period is a challenging task; this report demonstrates that enthusiastic participating students coupled to the sustained support from staff, faculty, and graduate students leads to significant accomplishments. The students participating in this effort have just started on the path of technical education and are getting their first experience with advanced hands-on research as part of our REU program. The NNIN national partnership, through our complementary strengths, inter-disciplinary effort, multi-site education, and use of each other's resources, provides exciting projects and the means to achieve them in a reasonable time. Each student in the NNIN REU completes an independent research project selected for completion in 10 weeks with strong technical support and faculty supervision, undergoes strong hands-on training and education (also available through our web-site [www.nnin.org](http://www.nnin.org) in the multimedia section),

participates in a convocation at individual sites and at a common site to present their research efforts, and works to time-tested program expectations.

81 interns from 66 different institutions across the United States and representing 37 fields of study participated in the program this year. All came to us with the common goal of gaining significant experience in hands-on, advanced research. As this book shows, even within the short ten weeks of the program, NNIN REU interns can make demonstrably important progress. The focus on advanced research and knowledge, the strong mentoring and support, the strong exposure to a professional research environment, the strong expectations built into the research and presentations at

convocations, the exposure to a wider variety of research conducted by peers and other users in diverse disciplines of science and engineering within the unifying facilities, and the strong scientific and social interactions across the network, have been critical to the program's success. Equally critical is the continuing dedication and effort from our staff, faculty, and graduate students. This year's participants also saw increased cross-site interactions through video-conferences and presentations, and hands-on experimentation. This year the network-wide convocation happened at Stanford University.

I wish the participants the best wishes for future technical careers; NNIN hopes to see them build on this summer's experience, and my thanks to the staff, the graduate student mentors, and the faculty for their participation and involvement. Particular thanks are due to Melanie-Claire Mallison at Cornell, Michael Deal at Stanford, and Nancy Healy at Georgia Institute of Technology for making their contributions in organizing and the logistics of the program and the convocation.

***Sandip Tiwari, Director, NNIN***





**2005 NNIN REU Program at  
Cornell NanoScale Science &  
Technology Facility, Cornell University**

*Front row, from left to right:*

Mr. Joseph Heremans.....pages 48-49  
 Mr. Nkemdilim Ezeife .....pages 34-35  
 Ms. Blair Brettmann.....pages 6-7  
 Mr. Brian Noel .....pages 98-99  
 Mr. Nathan Ridling .....pages 122-123  
 Ms. Kaylee Sill McElroy .....pages 134-135  
 Ms. Joy Johnson.....pages 64-65

*Back row, left to right:*

Ms. Melanie-Claire Mallison ..... *site coordinator*  
 Mr. James Helton .....pages 46-47  
 Ms. Caitlin Burger.....pages 8-9  
 Ms. Clara Ji Hyun Cho.....pages 16-17  
 Ms. Priscilla Paul .....pages 104-105  
 Ms. Amy Lee.....pages 70-71  
 Ms. Sarah Ruch .....pages 126-127  
 Ms. Shelley Zieren .....pages 162-163  
 Mr. Joshua Montague .....pages 88-89  
 Mr. Brandon Walker.....pages 150-151  
 Mr. Jamie Jackson.....pages 60-61  
 Dr. Lynn Rathbun..... *NNIN REU program coordinator*



**2005 NNIN REU Program at  
Microelectronics Research Center,  
Georgia Institute of Technology**

*Front row, from left to right:*

Ms. Wafa Soofi.....pages 140-141  
 Ms. Wand Gan.....pages 38-39  
 Ms. Laura Doyle .....pages 30-31

*Back row, left to right:*

Mr. Hiren Thacker..... *site mentor*  
 Mr. Jacob Hughey .....pages 56-57  
 Ms. Ashley Carson .....pages 10-11  
 Dr. Nancy Healy..... *NNIN Education Coordinator*  
 Mr. Muhannad Bakir ..... *site mentor*  
 Ms. Jennifer Tatham..... *site coordinator*  
 Mr. Yin Ian Yang .....pages 160-161  
 Ms. Susie Eustis ..... *site mentor*



**2005 NNIN REU Program at  
Center for Nanoscale Systems,  
Harvard University**

*From left to right:*

Mr. Matthew Smith .....pages 138-139  
Ms. Winnie Tsang .....pages 148-149  
Ms. Abbie Tippie.....pages 146-147  
Dr. Kathryn Hollar ..... *site coordinator*

*Not pictured:*

Mr. Matthew McGrath .....pages 80-81



**2005 NNIN REU Program at  
Howard Nanoscale Science &  
Technology Facility, Howard University**

*From left to right:*

Mr. Michael Chestnut.....pages 14-15  
Ms. Virginia Noxon.....pages 100-101  
Ms. Janessa Smith.....pages 136-137  
Mr. Edgar Peralta ..... pages 110-111  
Mr. Richard Castillo.....pages 12-13  
Ms. Idaliz Rodríguez Dátil.....pages 124-125  
Mr. James Griffin ..... *site coordinator*



**2005 NNIN REU Program at  
Center for Nanotechnology Education &  
Utilization, The Pennsylvania State University**

*From left to right:*

Mr. Nathaniel Honsowetz .....pages 50-51  
 Mr. David Welch .....pages 152-153  
 Mr. Sabil Huda .....pages 54-55  
 Ms. Jodi Iwata .....pages 58-59  
 Ms. Rachel Thompson .....pages 144-145  
 Mr. Paul Harris.....pages 44-45  
 Ms. Aileen Dinin .....pages 28-29  
 Mr. Nakul Reddy .....pages 118-119  
 Mr. Robert Ehrmann ..... *PSU staff*



**2005 NNIN REU Program at  
Stanford Nanofabrication Facility,  
Stanford University**

*Front row, left to right:*

Mr. Andrew Melton.....pages 86-87  
 Dr. Michael Deal ..... *SNF REU director*  
 Ms. Maureen Baran.....*SNF REU administrator*  
 Mr. Stephen Meisburger.....pages 84-85  
 Mr. Neel Shah .....pages 130-131

*Back row, left to right:*

Mr. William Noderer .....pages 96-97  
 Mr. Hsen Dai Hsu .....pages 52-53  
 Mr. Minh Phuc Dao.....pages 26-27  
 Ms. Emily Rice .....pages 120-121  
 Ms. Que Anh Nguyen .....pages 92-93  
 Ms. Heidi Wheelwright.....pages 154-155  
 Mr. Wade Luhman.....pages 76-77  
 Mr. Joshua Symonds .....pages 142-143  
 Mr. David McIntosh.....pages 82-83



**2005 NNIN REU Program at  
Nanotech at UCSB,  
University of California Santa Barbara**

*Front row, left to right:*

Mr. Christopher Olson .....pages 102-103  
Mr. Cheng-Yuk Lee.....pages 72-73  
Mr. Aaron McDaniel .....pages 78-79  
Mr. Yaniv Scherson .....pages 128-129  
Mr. Calvin Peng .....pages 108-109

*Back row, left to right:*

Mr. Michael Cullinan .....pages 24-25  
Mr. Yu-ping Shao .....pages 132-133  
Ms. Samantha Cruz .....pages 22-23  
Ms. Angela Berenstein ..... *site coordinator*  
Ms. Alexandra Polosukhina ..... pages 112-113  
Mr. Jason Winders.....pages 158-159  
Mr. Frank Cleary .....pages 20-21



**2005 NNIN REU Program at  
Michigan Nanofabrication Facility,  
The University of Michigan, Ann Arbor**

*From left to right:*

Mr. Luke Niewiadowski .....pages 94-95  
Ms. Amber Brannan .....pages 4-5  
Ms. Sandrine Martin ..... *site coordinator*  
Mr. Eric Chu.....pages 18-19  
Mr. Thaddeus Koehn.....pages 66-67  
Mr. Marc PunKay.....pages 116-117





**2005 NNIN REU Program at  
Nano Fabrication Center,  
University of Minnesota**

*From left to right:*

Mr. Arthur Kuehl.....pages 68-69  
Mr. Matthew Harrington .....pages 42-43  
Mr. Johangel Figueroa-Montiel .....pages 36-37



**2005 NNIN REU Program at  
NanoScience @ UNM,  
University of New Mexico**

*From left to right:*

Mr. David Light .....pages 74-75  
Ms. Nicole Escudé .....pages 32-33





**2005 NNIN REU Program at  
Microelectronics Research Center,  
University of Texas at Austin**

*From left to right:*

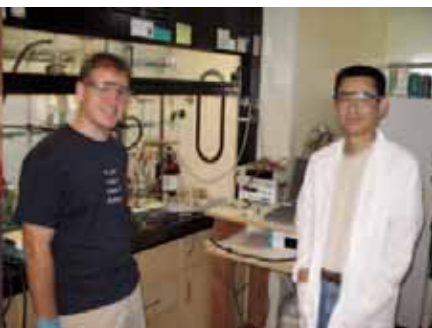
Ms. Miktosha James.....pages 62-63  
Ms. Niussha Gutierrez.....pages 40-41  
Mr. Jose Pelaez.....pages 106-107  
Ms. Amy Pinkston.....site coordinator



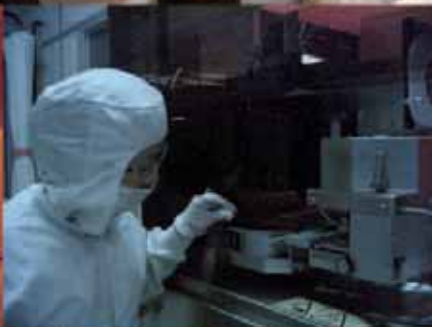
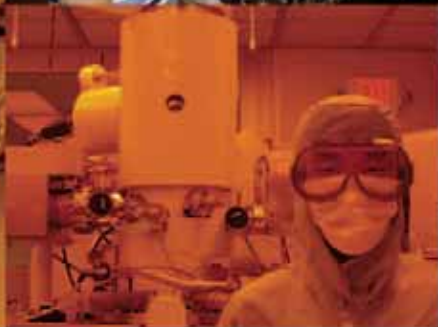
**2005 NNIN REU Program at  
Center for Nanotechnology,  
University of Washington**

*From left to right:*

Mr. Ethan Allen.....site coordinator  
Mr. Jock Bovington.....pages 2-3  
Ms. Laralynne Przybyla.....pages 114-115  
Mr. Michael White.....pages 156-157  
Ms. Victoria Mooney.....pages 90-91



# **2005 NNIN REU RESEARCH ACCOMPLISHMENTS**



# Air Pressure Sensing by Monitoring Lateral Charge Carrier Transport in Pt Tetra(Carboxylphenyl) Porphyrins

**Jock Bovington, Physics, and Electrical Engr/Specialization in Computer Engr, Seattle University**  
**NNIN REU Site: NanoTech User Facility, University of Washington**

*NNIN REU Principal Investigator: Dr. Babak Parviz, Electrical Engineering, University of Washington*

*NNIN REU Mentor: Dr. Jianchun Dong, Electrical Engineering, University of Washington*

*Contact: bovingtonj@seattleu.edu, babak@ee.washington.edu*

## Abstract:

In this project, we constructed a pressure sensor based on a lateral charge carrier transport channel made of Pt-5,10,15,20-tetra(carboxylphenyl)porphyrin-(Pt-TCPP) thin film deposited on a SiO<sub>2</sub>/Si chip. We directly converted pressure change into changed current flowing across this organic thin film.

To fabricate the device, we fabricated two interdigitated electrodes separated by a 5  $\mu$ m gap using photolithography followed by thermal evaporation of Cr/Au metal layers and consequent liftoff process. We formed the film on the SiO<sub>2</sub> surface between the electrodes by drop-casting 1% Pt-TCPP aqueous solution for 1 hour. Measurements were made on the device in a hermetic chamber with varied air pressure.

Compared to other conventional air pressure sensors, this new sensor can be easily made and directly converts the pressure change into electrical signal. More importantly, this device can be integrated with current CMOS circuits by a one-step dropcasting post-process. Furthermore, we can engineer the sensing molecule to improve its stability and sensitivity by exploiting the versatility of organic synthesis. By simply replacing the conjugated metal ion in the porphyrin ring, we can also alter the sensitivity spectrum of this device to sense other gases.

## Introduction:

It has been well known that the phosphorescence lifetime of Pt-porphyrin molecules can be a sensitive function of oxygen concentration and hence these molecules have been used as an active sensing component in the pressure sensitive paint which has found application in pressure sensing in wind tunnels [1]. However, monitoring the light emission of these molecules for pressure sensing needs complicated optical instruments and is difficult to be directly integrated with following signal processing circuits. Since the concentration of the excited Pt-porphyrin molecule is strongly affected by the oxygen concentration, the conduction through films made of this molecule may be also affected by the oxygen concentration. In this paper, we found that the

conduction through a thin film made of Pt-TCPP is indeed a strong function of the air pressure. Because this device measures the conduction through an organic thin film, it has the potential to be scaled down to nanometer range. Furthermore, both the performance and sensitivity spectra of this device can be easily altered through chemical modification, and this device can be easily interfaced with CMOS integrated circuits by only one additional process.

## Experimental Procedure:

The platform for this device was made with a series of standard microfabrication steps. First we took an Si wafer and thermally oxidized it to create a 100 nm thick SiO<sub>2</sub> insulation layer. Then we used photolithography to expose AZ1512 photoresist according to a design pattern for a pair of interdigitated electrodes. Then we evaporated a 5 nm thick Cr adhesion layer followed by a 50 nm thick gold layer. Using a liftoff process in an acetone bath assisted by sonication, we fabricated the microelectrode pair which is shown in Figure 1.

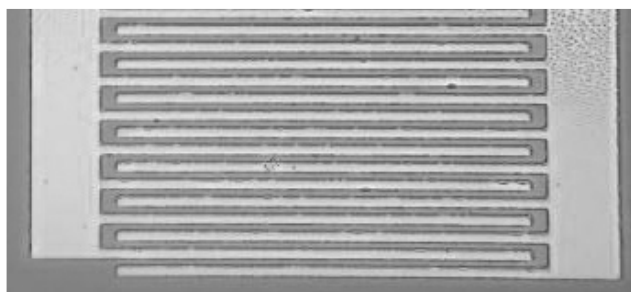


Figure 1: Interdigitated Cr/Au contacts.

Then we made 1% and 2% Pt-TCPP aqueous solutions. To increase the solubility of the molecule, we added NH<sub>4</sub>OH to a 0.5% final concentration. We tried two methods, spincoating or dropcasting to form the thin Pt-TCPP thin film. In dropcasting, we put Pt-TCPP solution on the chip patterned with the microelectrode and covered the chip with a PDMS stamp. We waited for 9 hrs to allow the water to be



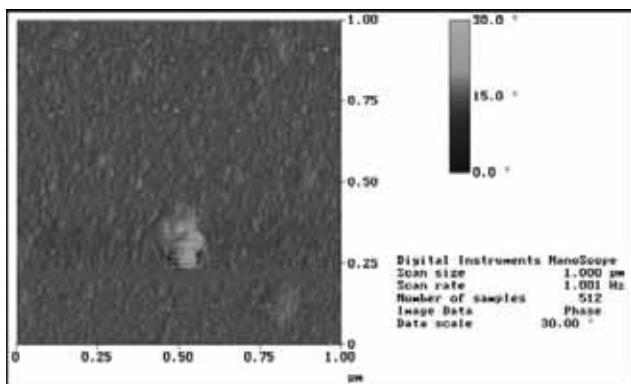


Figure 2: Crystallization of dropcast film.

completely evaporated and to allow crystals to form. In spincoating, a drop of the Pt-TCPP solution was placed on a chip and spun at 2,000 rpm for 180 seconds.

The morphologies of the thin films formed by these two methods were examined using both an optical microscope and AFM. Figure 2 shows an AFM of the crystals of the surface of the dropcast film.

To make the chip electrically connected, we used a wirebonder to ballbond the contacting pad of the microelectrodes to the pad in a standard 16 pin dual inline package. Testing of the finally fabricated chip was performed in a custom-made hermetically sealed chamber. By carefully controlling two valves leading to a house vacuum and the atmosphere respectively, we could alter the air pressure inside the chamber. We then measured the current through the fabricated devices under different pressure and plotted the current-pressure curve which is shown in Figure 3.

### Results and Conclusions:

Measurements of the Pt-TCPP show a linear dependence of current through the Pt-TCPP thin film on the air pressure. In this experiment, the device is biased at 5V constantly.

However, when we changed the partial oxygen pressure inside the chamber, we found little change in the electrical conduction through the thin film. This observation implies that though the excited Pt-porphyrin molecules respond to the oxygen concentration, conduction through the Pt-TCPP thin film is not affected by the oxygen concentration. It is likely the changed conduction through this film according to the varied air pressure is caused by water.

### Future Work:

The future work remaining on this project will be to decouple the observed affects due to oxygen from the affects due to water and other molecules in the air. For this reason some thought has been put into hydrophobic porphyrins such as fluorinated porphyrins.

With modifications in the molecule we will hopefully be able to isolate oxygen as the only substantial contributor to the variations in current through the film.

Once the proper molecule can be engineered, then scalability issues may be addressed. We can test how the lateral charge carrier transport is affected by a nano scale gap between contacts. Theoretically, a binary sensor could be developed to determine whether oxygen has bound to a given molecule or not.

### Acknowledgments:

NNIN REU Program, University of Washington Center for Nanotechnology, Nanoscale User Facility Staff/Administration.

### References:

- [1] Oxygen pressure measurement using singlet oxygen emission, Khalil et. al. University of Washington, Review of Scientific Instruments; May2005, Vol. 76 Issue 5, pN.PAG, 8p.

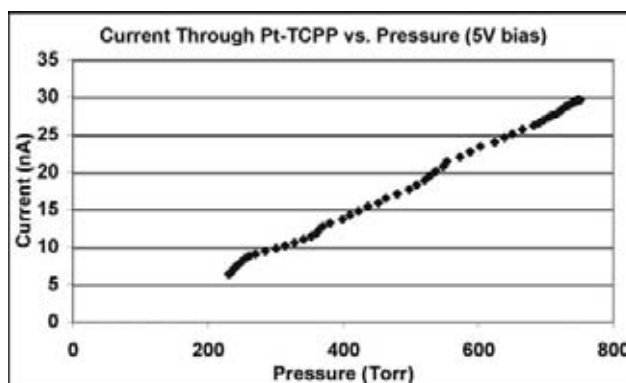


Figure 3: Variations in current through a dropcast Pt-TCPP film as a function of air pressure in a standard mixture of gases.

# Fabrication & Characterization of Nanostructured Conducting Polymer Films on the Surfaces of Microfabricated Neural Prosthetic Biosensors

**Amber Brannan, Applied Biology, Rose-Hulman Institute of Technology**  
**NNIN REU Site: Michigan Nanofabrication Facility, The University of Michigan**

*NNIN REU Principal Investigator: Dr. David Martin, Materials Science & Engineering, University of Michigan*  
*NNIN REU Mentor: Sarah Richardson-Burns, Ph.D., Materials Science & Engineering, University of Michigan*  
*Contact: milty@umich.edu, brannaag@rose-hulman.edu*

## Abstract:

Microfabricated neural prosthetics for implantation into the central nervous system (CNS) must accommodate for the differences in mechanical properties at the electrode/tissue interface. Biocompatibility and low electrical impedance are necessary for proper function. Previously the conducting polymer poly(3,4-ethylenedioxythiophene) (PEDOT) was electrochemically deposited on neural microelectrodes in the presence of crosslinked hydrogels to produce soft, low impedance materials with the potential to improve device performance after implantation. In this study, we evaluate the role of hydrogel concentration and crosslinking on the structure and properties of PEDOT networks deposited in the alginate and poly(vinyl alcohol) (PVA) hydrogels. The optimal electrochemical deposition conditions for lowest impedance, greatest charge capacity and largest surface area are presented.

## Introduction:

Our lab has been investigating the role of electrochemically deposited conducting polymers on the long-term performance of microfabricated neural prosthetics [1]. We have also shown that the conducting polymers can be deposited in the presence of hydrogels [2]. In this study, we worked with the conducting polymer PEDOT. In its oxidized state, PEDOT exists as a polycation with delocalized positive charge along its conjugated backbone which are neutralized

by counter ions during electrochemical polymerization [3]. Poly(styrene sulfonate) (PSS) was used as the source of counter ions.

## Experimental

### ABP Electrode Arrays:

Eight well electrode arrays were purchased from Applied Biophysics. The gold electrodes are delineated with an insulating film and mounted polycarbonate. Each well contained 1 Au electrode with a surface area of  $49087 \mu\text{m}^2$ .

### Material Preparation & Electrochemical Polymerization:

A solution of 0.25 g PSS (Aldrich) in 100 mL 1X phosphate buffered saline (PBS) (Cellgro) was used to prepare 0%, 0.5%, 1.0%, 2.5%, and 5.0% (w/v) alginate solutions, each containing 20  $\mu\text{l}$  EDOT (Bayer) monomer solution and having a final volume of 20 mL. Crosslinked alginate was prepared by adding a 2% calcium sulfate/DI (Sigma) solution. 0%, 1%, 10%, and 15% (w/v) PVA/DI solutions were prepared, each containing 0.025 g PSS, 10  $\mu\text{l}$  EDOT solution, and having a final volume of 10 mL. Crosslinked PVA was prepared by adding 2% sodium tetraborate decahydrate/DI (Sigma) solution. The hydrogel solutions were placed in separate electrode wells and covered with PBS to complete the circuit.

PEDOT was grown galvanostatically on the electrodes using an Autolab potentiostat/galvanostat PGStat12 (EcoChimie, Netherlands) as the electrical supply. The

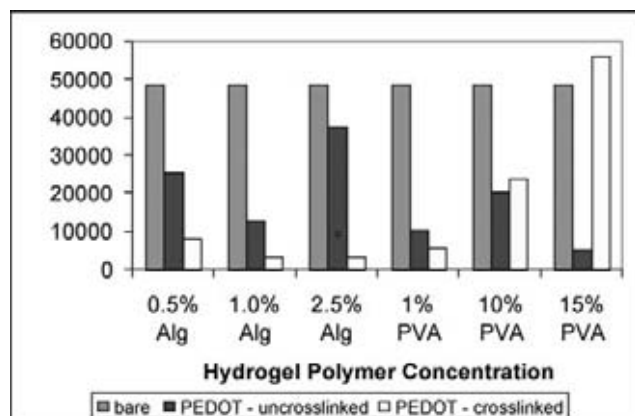


Figure 1. Effect of hydrogel crosslinking on impedance after PEDOT polymerization at 6 mC.

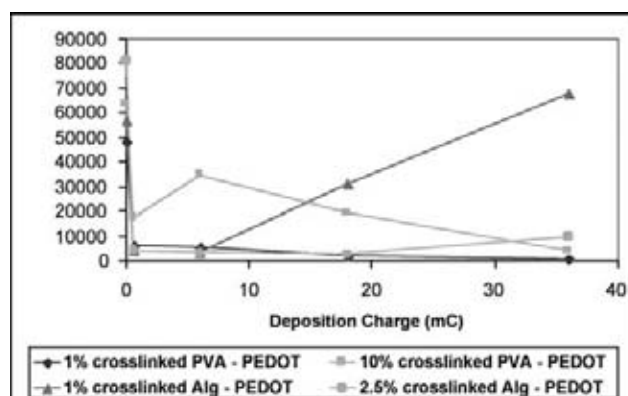


Figure 2. Relation between deposition charge and impedance.



electrode arrays were designed with a counter electrode and each individual well served as a working electrode. A saturated calomel electrode (SCE) was used as the reference electrode. The polymerizations were carried out at room temp. using a current density of 2.04 mA/cm<sup>2</sup>.

### Electrical and Morphological Characterization:

The Autolab was also used for EIS and CV analysis of the electrodes. A Leica DMIRB inverted microscope was used to view the PEDOT networks. Images were captured with an Olympus CCD digital camera.

## Results and Discussion

### Electrical Properties of PEDOT Networks in Hydrogels:

Taking EIS measurements both before and after electrochemical deposition gives qualitative and quantitative information about the effects of PEDOT on the electrical properties of the system, as well as the morphology of the electrode-medium interface. Figure 1 shows the impedance at 1 kHz of the PEDOT coated electrode sites in the presence of different hydrogel conditions with a bare electrode as a control.

PEDOT grown in the presence of 1% and 2.5% crosslinked alginate hydrogels resulted in impedance values of 3357 Ohm and 3334 Ohm, respectively. In the case of the PVA, the 1% crosslinked PVA showed the lowest impedance at 5623 Ohm.

The optimal deposition charge was found by depositing PEDOT for 1, 10, 30 and 60 minutes under a 10  $\mu$ A current in the presence of 1% and 2.5% crosslinked alginate as well as 1% and 10% crosslinked PVA hydrogels. The results are shown as a function of deposition charge (current in (A) \* polymerization time in (s)). Figure 2 shows that PEDOT in 1% crosslinked PVA hydrogel at 18 and 36 mC resulted in the lowest impedances of 1148 and 2061 Ohm, respectively. This was followed by PEDOT in 2.5% crosslinked alginate at 18 and 6 mC, resulting in impedance values of 2748 and 3334 Ohm, respectively.

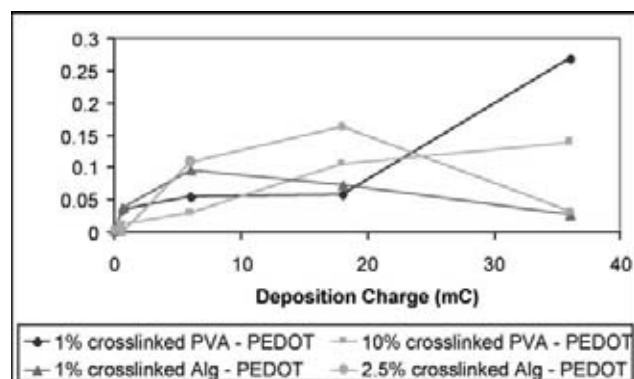


Figure 3. Relationship between charge capacity and deposition charge.

Using cyclic voltammetry under galvanostatic conditions, each coated electrode was swept through a potential of -1.0 to 1.0 V vs. SCE at a scan rate of 100 mV/s. During each cycle, the PEDOT undergoes a reversible redox reaction that is accompanied by the movement of ions into or out of the film. This results in an increased charge capacity shown in CV results. Figure 3 shows that PEDOT in 1% crosslinked PVA at 36 mC results in a charge capacity of 268.8  $\mu$ C. The next largest charge capacity (162.9  $\mu$ C) is seen in the case of PEDOT in 2.5% crosslinked alginate at 18 mC.

### Area Quantification:

Figure 4 shows PEDOT in 1% crosslinked PVA at 36 mC resulted in the largest surface area of  $2 \times 10^7 \mu\text{m}^2$ . PEDOT in 2.5% crosslinked alginate at 18 and 6 mC also produced relatively large surface areas ( $1.71 \times 10^7 \mu\text{m}^2$  and  $1.44 \times 10^7 \mu\text{m}^2$ , respectively); these conditions also correspond to lower impedances and higher charge capacities.

### Conclusions:

The conducting polymer PEDOT was electro-chemically deposited through crosslinked alginate and PVA hydrogels. EIS and CV results show that a 60 minute deposition in crosslinked 1% PVA gave the lowest impedance and the greatest charge capacity at the CNS-relevant frequency of 1 kHz. Surface area quantification confirms that the lowest impedance and highest charge capacity corresponds to the largest PEDOT network.

### Acknowledgements:

Special thanks to Dr. Sarah Richardson-Burns. Thanks to Jeffrey Hendricks, Mohammad Abidian, the University of Michigan, the NNIN REU, and the NSF.

### References:

- [1] Cui XY, Martin DC. Sens Actuators B-Chem 2003;89:92-102.
- [2] Kim DH, Abidian M, Martin DC. J Biomed Mater Res 2004;71:577-85.
- [3] Freemantel M. Chem. Eng. News 2000;78:39-45.

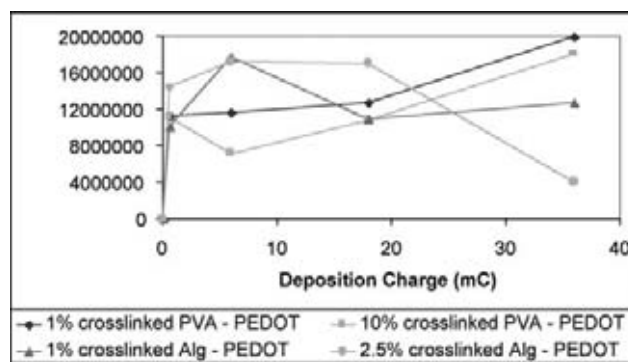


Figure 4. Relationship between relative surface area of the PEDOT network and deposition charge.

## Self-Assembly of Nanofabricated Colloids

**Blair Brettmann, Chemical Engineering, University of Texas at Austin**  
**NNIN REU Site: Cornell NanoScale Science & Technology Facility, Cornell University**

*NNIN REU Principal Investigator: Abraham Stroock, Chemical Engineering, Cornell University*  
*NNIN REU Mentors: Stephane Badaire & Joseph Woody, Chemical Engineering, Cornell University*  
*Contact: bbrettmann@mail.utexas.edu, ads10@cornell.edu*

### Abstract:

Colloidal dispersions are made of solid particles with sizing between 10 nm and 1  $\mu\text{m}$  in solution. These particles can self-assemble into crystals with lattice spacing on the order of the wavelength of visible light, and thus are useful in the field of optics. Currently, most scientists are working with spherical colloid particles, but we believe that cylindrical particles will also form intriguing crystals.

We use photolithography to define cylindrical objects on the order of 1  $\mu\text{m}$  out of silicon dioxide, and then release them from the substrate, forming a colloidal dispersion. Within the dispersion, the cylindrical particles will interact by shape-specific depletion interactions, forming structures that will be studied, and hopefully used in photonics applications.

In this study, we fabricated cylindrical colloid particles from silicon dioxide. We chose silicon dioxide for its well-known properties. We first used photolithography techniques to create cylinders of positive photoresist, which we used as a mask to plasma etch through a layer of silicon dioxide on a sacrificial substrate. In order to study the cylinders as freely dispersed colloidal particles, we released them from the substrate using phosphoric acid. We will study these particles in capillaries under various conditions to determine the structures formed.

### Introduction:

As the field of optics advances, engineers look for new crystals that will help them better control light. Self-assembled colloidal crystals are likely to be of use, and scientists are currently working with spherical particles to create these crystals. Spherical particles assemble into useful crystals, but particles of other shapes may also assemble into valuable structures.

Spherical particles are also widely available to laboratories who wish to use them, but other shapes are not available, and it is necessary to fabricate them. In this project, we fabricated cylindrical colloidal particles from silicon dioxide. We chose silicon dioxide because it is a well-studied substance and thus structures assembled from the particles could be easily compared to structures assembled from the spherical shape. We

chose to use photolithography to create the particles in order to control the size and shape, and to end with a monodisperse dispersion.

### Experimental Procedure:

The following process used photolithography and etching techniques to create silicon dioxide cylinders in the colloidal size range. We started with silicon wafers coated with 250 nm silicon nitride and 1  $\mu\text{m}$  silicon dioxide.

We first fabricated photoresist cylinders to be used as a mask in the etching process. We tried three different photoresists; SPR955-CM-2.1 and SPR220-3.0, positive photoresists, and SU8, a negative photoresist. Of these, only SPR220-3.0 held up well during etching. Before spinning the resist, we spun a 150 nm layer of XHRiC-16 antireflective coating and baked at 175°C for 60 sec. We then spun a 2.0  $\mu\text{m}$  layer of SPR220-3.0 positive photoresist, and baked at 110°C for 120 sec.

We exposed using the GCA Autostep and a mask with 1  $\mu\text{m}$  circles that were 2  $\mu\text{m}$  from center to center, and did a post exposure bake at 115°C for 90 sec. We developed in 300 MIF for 60 sec. The photoresist cylinders can be seen in Figure 1.

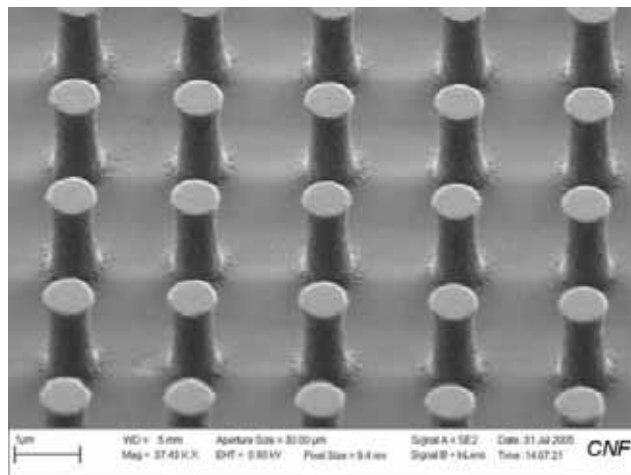


Figure 1: Photoresist cylinders, about 600 nm diameter.

Following the fabrication of the photoresist cylinders, we etched the silicon dioxide using the Oxford 80 plasma etcher. We first hardbaked the resist for 2-3 hours at 90°C. We then did a 60 sec oxygen plasma clean to straighten out the walls of the resist cylinders. The final etching process used a 50% CHF<sub>3</sub> and 2% O<sub>2</sub> gas combination for one hour to etch through the silicon dioxide. The etching process is anisotropic, and the etched cylinders can be seen in Figure 2.

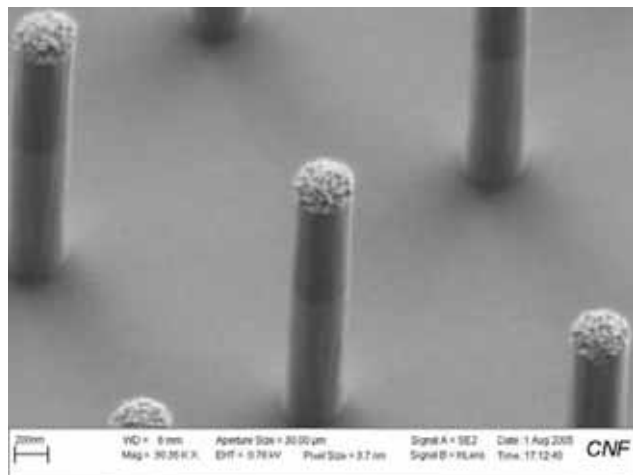


Figure 2: Etched cylinders with resist layer on top, about 300 nm diameter.

### Results:

The process developed to fabricate the SPR220-3.0 photoresist cylinders produced cylinders approximately 600 nm in diameter with smooth sidewalls. The cylinders should have been 1 µm in diameter, but because such a large area was exposed, they were smaller. The cylinders also had a small foot of resist on the bottom and a small lip on the top, making the sidewalls not completely straight. This was fixed using an oxygen plasma etch before the final etch.

The silicon dioxide cylinders created through the photolithography and etching process had smooth side-walls, but were only about 300 nm in diameter. This is probably due to the oxygen plasma etch used to straighten the resist cylinders, which may have etched too far into the resist sides, but 300 nm is still in the colloidal size range, so is useful for further studies.

### Future Work:

Before the cylindrical particles can be self-assembled, they must be removed from the silicon substrate. Initially we wanted to use silicon nitride as a sacrificial layer and etch it using hot phosphoric acid, releasing the cylinders, but this process may be too harsh for the cylinders to survive. So we will try an aluminum or chrome sacrificial layer and use a gentler etching process to release the cylinders.

Once the cylinders have been released, we would like to use the colloidal dispersion to perform self-assembly experiments to create crystals. We will use surfactants and their depletion interactions to self-assemble crystals that may take the shape seen in Figure 3. In studying the self-assembly, we will create a phase diagram of structures formed using the cylindrical colloidal particles.

### Acknowledgements:

I would like to thank the National Science Foundation, the Cornell NanoScale Science and Technology Facility, Cornell University, and NNIN for making this project possible. I would also like to thank Professor Abraham Stroock, Stephane Badaire, and Joseph Woody at Cornell and all of the CNF staff for their help and support.

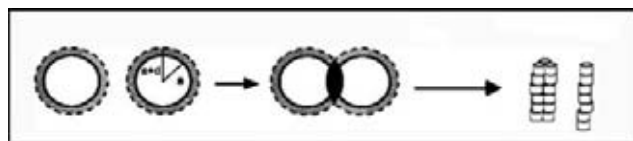


Figure 3: Possible assembly of cylindrical particles.

# Fabrication of Nanomechanical Oscillators for Chemical and Biological Sensing

**Caitlin Burger, Physics/Mathematics, Shippensburg University**  
**NNIN REU Site: Cornell NanoScale Science & Technology Facility, Cornell University**

*NNIN REU Principal Investigator & Mentor: Rob Illic, Cornell NanoScale Facility, Cornell University*  
*Contact: cb4412@ship.edu, rob@cnf.cornell.edu*

## Abstract:

Cantilevers are commonly used as transduction mechanisms for sensing purposes. For the main focus of this project, the nanoelectro-mechanical (NEMS) oscillators will be used to detect chemical and biological species. In this work, devices composed of silicon nitride suspended above silicon are fabricated and tested. The cantilevers are fabricated using both optical lithography and electron-beam lithography methods. The widths of the devices range in size from 150 nm to 1  $\mu\text{m}$  and the lengths range in size from 6  $\mu\text{m}$  to 12  $\mu\text{m}$ . Gold dots are used to achieve adhesion via thiolate self-assembly.

The objective of this research is to detect a difference in resonance frequency before and after the addition of the attached mass; the change in resonance frequency will give information about the adhered mass. The basic model can be related to the equations involved in Hook's law regarding a rectangular leaf spring.

## Introduction:

MEMS or NEMS sensors operate by detecting changes in the mechanical characteristics of a micromechanical transducer. These changes are caused by physical, chemical, or biological stimuli. One form of detection involves measuring an oscillator's change in resonance frequency. Cantilevers are highly

sensitive devices that are attached at one end, and thus are enabled to oscillate freely. As opposed to other sensors, cantilevers are also more reliable, smaller, and have higher accuracy. Both cantilevers and bridges of various widths and thicknesses can be fabricated in order to test for their unique resonance characteristics.

The resonance frequency of the cantilever is dependent upon its mass and spring constant. The higher its spring constant is, the higher its resonant frequency will be. Also, shorter cantilevers can detect smaller amounts of bound materials. Less stiff cantilevers are also more susceptible to thermal noise, giving inaccurate frequencies. Binding of various biological materials may be studied by measuring the changes in resonant frequency of the harmonic oscillators.

Interferometry has become a popular method for MEMS readout because of its ability for high-bandwidth high-resolution mapping of oscillations by small cantilevers.

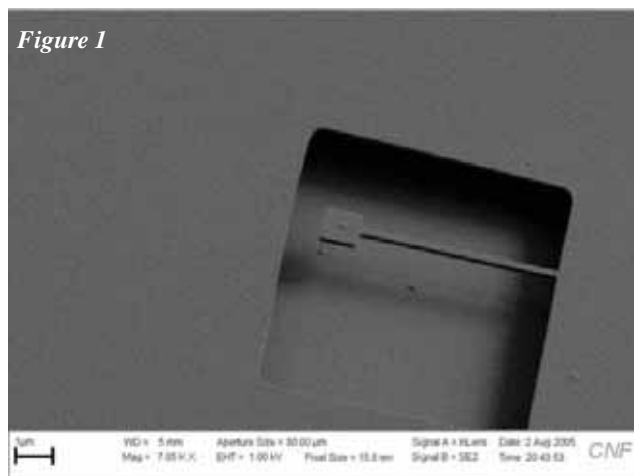
## Fabrication Process:

This was a multi-layer process, beginning with nitride and thermal oxide on silicon wafers. The nitride was measured to be about 200 nm using ellipsometry. Photolithography was used to make the devices. Larger areas of the device were exposed using optical lithography and the small cantilever devices and gold adhesion surfaces were exposed using e-beam lithography. An etch mask was constructed with 25 nm of chrome. The exposed nitride was removed using  $\text{CF}_4$  plasma. The fluorinated chrome was then removed using oxygen plasma, and the remaining chrome was removed using a chrome etch wet chemistry. Gold was used for the binding sites, with chrome as an adhesion layer. The oxide was then removed using HF. Figure 1 shows a released cantilever.

## Experimental Procedure:

Interferometry was used to measure the frequency of oscillation of the cantilevers. The cantilevers were encapsulated in a vacuum to achieve a high quality

Figure 1





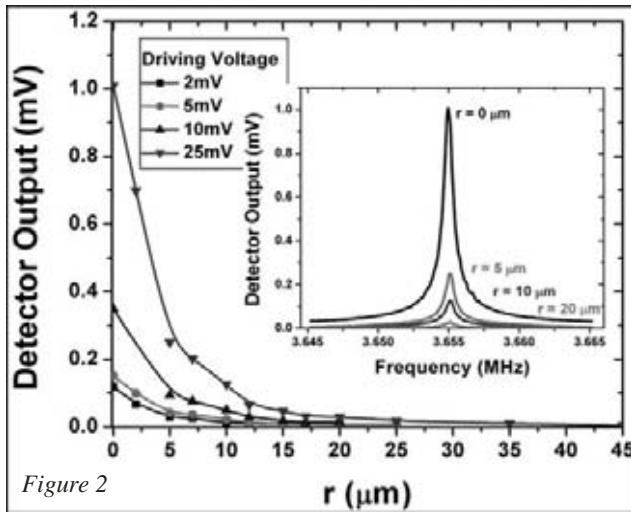


Figure 2

factor. A modulated blue laser thermally excites the cantilever at its base and a red laser is used to detect the motion in conjunction with a single cell photo-detector. Shown in Figure 2, as the excitation laser is placed further from the base, the amplitude of vibration diminishes with the resonant frequency remaining constant. This implies the driving signals were constrained within the linear regime. The quality factor, a factor related to damping and which is inversely proportional to the change in angular frequency ( $\Delta\omega$ ), is increased by encapsulating the cantilever samples in a vacuum chamber. *Baculovirus*, an insect virus, is uniformly attached to the oscillators.

### Results and Conclusions:

A definite frequency shift was observed in all of the cantilevers, see Figure 3. The black graph to the right represents the frequency before a material was attached; the grey graph to the left represents the frequency after the material was attached. This is an indication that the virus adhered to all of the cantilevers, as planned. Due to time constraints, the mass was not calculated. We also found that several of the longer, thinner cantilevers had problems with sticking to the silicon substrate after being released. This was due to their lack of stiffness.

Different frequency peaks were also found by analysis of the photo detector. Theoretically, we found the approximate values for the 1<sup>st</sup>, 2<sup>nd</sup>, and 3<sup>rd</sup> harmonics. Other peaks were also detected. Although they gave weak signals, they are believed to be in-plane peaks. The first of these peaks was located at 19.45 MHz. Some torsional motion may also have been detected. Theoretically the frequency is directly proportional to the thickness of the cantilever, and the frequency of the in-plane motion (the primed frequency) is directly proportional to the width of the

cantilever. Using the experimental values for the width and thickness, see Figure 4, we see that the theoretical value is relatively close to the experimental value.

### Future Work:

The future of this project could include the optimization of the in-plane motion of the cantilevers and analyzing the fundamental limits of sensing biomolecules by way of mass-based detection. Ultimately, we hope to encapsulate these oscillators in fluidic networks where functionalization takes place *in-situ*.

### Acknowledgments:

I would like to thank the CNF staff, especially Rob Ilic for all of his help and guidance. Also, thanks to the NSF and the NNIN for their financial support.

### References:

- [1] N. Lavrik, M. Sepaniak, and P. Datskos. Review of Scientific Instruments, 75,7(Jul 2004).
- [2] B.R.Ilic, Y.Yang, and H. Craighead. App. Physics Letters, 85, 13(27 Sept 2004).

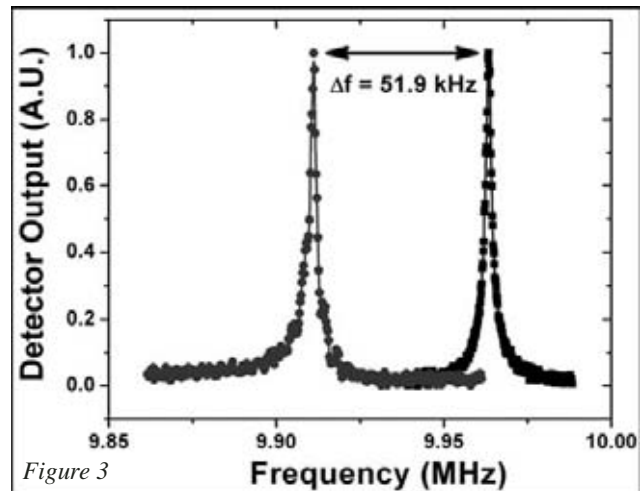


Figure 3

$$f_i = \beta_i^2 \frac{1}{2\pi} \left( \frac{E}{12\rho} \right)^{\frac{1}{2}} \frac{t}{l^2}$$

$$f_i \propto t; f_i' \propto t'; w = t'$$

$$\frac{f_i'}{f_i} = \frac{w}{t} = \frac{1\mu m}{0.220\mu m} \approx 5$$

$$f_i' \approx 5f_i = 5(3.84MHz) \approx 19.2MHz$$

$$f_{1measured} = 3.84MHz$$

$$f_{1measured}' = 19.45MHz$$

Figure 4



# Pressure Sensor Membrane Design & Fabrication using Photo Electro-Chemical Etching on Thin Film & Bulk SiC

**Richard A. Castillo, Advanced Materials Engineering Research Institute (AMERI),  
Mechanical & Materials Engineering Dept., Florida International University  
NNIN REU Site: Howard Nanoscale Science & Engineering Facility, Howard University**

*NNIN REU Principal Investigator: Dr. Gary L. Harris, PE, PhD, Electrical Engineering, Howard University*

*NNIN REU Mentor: James Griffin, Sr. Research Associate, HNF, Howard University*

*Contact: rcast001@fiu.edu, gharris@msrce.howard.edu, griffin@msrce.howard.edu*

## Abstract:

Photo-electro-chemical etching (PEC) is a method that can be used for bulk micromachining in which a material is electrochemically etched using UV radiation and an electrolyte etching solution such as hydrofluoric acid (HF) or potassium hydroxide (KOH). This will be the targeted method for the machining process of silicon carbide (SiC) in order to create a defined structure to be used for pressure sensing. PEC has been chosen since the process generates highly anisotropic, selective and very smooth etch morphologies, perfect for pressure sensor diaphragm design.

This project will be limited to: (1) characterizing the etching rates of such processes including the introduction of different etching solutions/electrolytes, and (2) studying the interaction and behavior of defect densities and micro pipe presence during SiC etching. The quality of the PEC process is very dependent on the amount/densities of such defects within the SiC material. The proposed sensor has been chosen to be part of a pressure sensing device that could be implanted within the human body.

Because SiC has a wide bandgap, is chemically inert, and possesses a very high Young's modulus, it is an ideal material that can withstand the temperature, reactivity and stresses within several regions of the human body.

## Introduction:

In the field of biotechnology, pressure sensors have gained notoriety because of their ability to perform in very remote, sensitive and very harsh environments.

Measuring *in-situ* blood pressure on vascular tissue brings all of these challenges to the design board, and the use of specific materials is crucial for efficient sensor functionality. With this in mind, a proposed blood pressure sensor membrane will be fabricated of silicon carbide (SiC). Silicon carbide, a compound material mainly composed of silicon and carbon, is a synthetically made material and has over 200 polytypes. This material has mechanical properties similar to diamond, has a wide-bandgap which allows

for high temperature operation, and is very chemically resistant.

Given these and many other physical and chemical properties of SiC, we used the 3C-SiC polytype for our membrane design. This polytype has the highest carrier mobility ( $\sim 600\text{-}1000 \text{ cm}^2 \cdot \text{V}^{-1} \cdot \text{s}^{-1}$ ), which is perfect for our chosen method of fabrication using photo-electro-chemical (PEC) etching. This method of micromachining is a relatively easy way of machining silicon carbide.

## Experiment:

Within our project, both bulk and surface micromachining were attempted using the PEC method. Using the principle of EHP (electron-hole-pair) generation, we used a UV source to excite the surface of the SiC. Excess holes or electrons are created in the sample by the UV light. By applying a bias through the solution, the SiC will etch through an oxidation reduction process. For this project hydrofluoric acid (HF) was chosen as our main electrolyte solution. The HF electrolyte concentration was varied with high concentration levels providing fast etch rates and good surface morphology. Figure 1 shows the diagram of the setup used in this project to perform the PEC etching.

Even though previous experiments have been per-

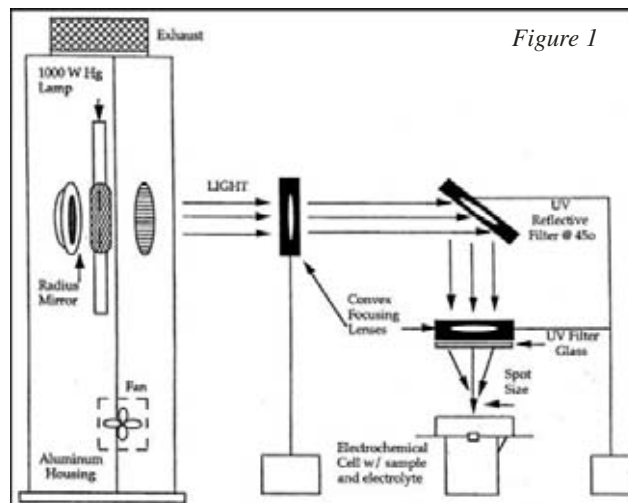
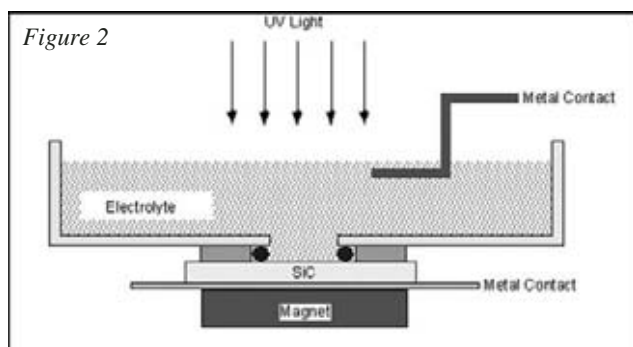


Figure 1



formed with more powerful lamps, we used an existing 200W USHIO mercury vapor lamp we had on hand.

The UV light is focused and reflected with high reflectivity mirrors and lenses onto a spot on a custom built electrolytic cell where the sample is mounted and the electrolyte solution is making contact with it. Figure 2 shows a similar schematic of the custom built cell. Instead of using a spring-loaded screw, in our experiment we used a magnet to attach the sample sandwiched between a metal washer and o-ring to prevent electrolyte loss. The diagram illustrates how the wafer is being exposed to the solution on the top side while being held against the cell with a magnet. The back side of the substrate has an ohmic contact metallization which was evaporated by electron-beam evaporation. The purpose of the ohmic contact was to improve electrical contact between the wafer and the back electrode. Photolithography was employed to create the patterned membrane on the top surface. We also used wax as a mask for etching.

## Results and Conclusions:

Photolithography provided limited success because it was attacked by the electrolyte. We had much better success with the wax because it was

very resistant to HF and other etchant attacks during PEC. The HF was an excellent electrolyte for this experiment. We obtained etch rates as high as 1  $\mu\text{m}/\text{min}$  for SiC and even higher rates were obtained for silicon. This PEC process is an ideal method for SiC MEMS sensor applications. Etching rates were first established for silicon for various concentrations of HF solutions. The etching process was then performed on bulk SiC and then on epitaxial SiC ( $\sim 5 \mu\text{m}$  thick) on a Si substrate.

Figure 3 shows one of the etchs done on a thin film of 3C-SiC. It can be seen how the 3C-SiC thin film started to delaminate from the Si substrate. This is the initial step in the fabrication of the thin film membrane for our sensor application. A complete SiC blood pressure sensor mask set was developed and will be fabricated.

To conclude, we have seen that by using this method we have acquired high etching rates, good stop-etch selectivity according to the doping of materials, and the ability to electro-polish the substrates for further processing. It was also found that we do not need high concentrations of etching solutions. This by itself has a lot of implications regarding the decrease in costs from safety to manufacturing and machinery costs.

All of these findings have shown that further optimization of this process is very attainable, not only for sensorial applications but for other MEMS related devices.

## Acknowledgements:

I would like to thank Prof. Gary Harris, Ph.D., Mr. James Griffin, the NNIN and the NSF for their contributions in making this opportunity a rewarding experience in my career as a mechanical engineering student and a professional.

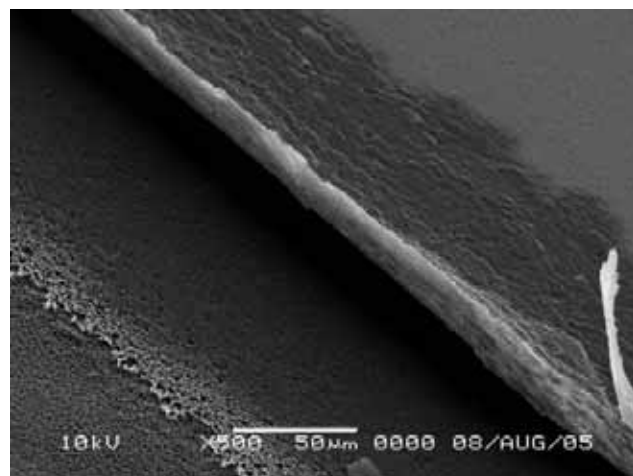


Figure 3: Figure on right is close up of boxed area on left.

## Characterization of Nanofiltration Membranes

**Michael Donnell Chestnut II, Computer & Electrical Engineering, North Carolina State University**  
**NNIN REU Site: Howard Nanoscale Science & Engineering Facility, Howard University**

*NNIN REU Principal Investigator: Dr. Kimberly Jones, Department of Civil Engineering, Howard University*

*NNIN REU Mentor: Dr. Jermei Matthews, Department of Civil Engineering, Howard University*

*Contact: mdchestn@ncsu.edu, kjones@scs.howard.edu*

### Abstract:

The goal of this research was to characterize the surface properties of nanofiltration membranes. The processes that are used to characterize these membranes are standard but the membranes are synthesized in the laboratory and the applications for these membranes are novel. Several properties will be investigated in detail. These include membrane charge, the surface roughness, and the membrane pore size. The membrane flux and rejection levels are also examined, but are not reported in this paper.

The particular focus of this paper is surface charge and roughness of the membrane as well as possible pore imaging and identification. The equipment employed to study the charge of the membrane included an Electro Kinetic Analyzer, used to measure zeta potential (proportional to surface charge) and an Atomic Force Microscope (AFM) with a liquid cell, used to image the morphology of the membrane. This paper also provides background information on the applications and systems which use these membranes. There is good agreement between theoretical and experimental results for such things as the zeta potential.

### Introduction:

Howard University, the Nanobiotechnology Center at Cornell University, and the Wadsworth Center in Albany, NY, were assigned the task of speeding up the

process of separating DNA from hemoglobin coming from blood extracted from newborn babies. This DNA is to be analyzed for any birth defects so that they can be altered before any serious illnesses develop. Much of the performance of the separation process is related to the specific properties of the membranes that will be characterized.

There are several different classifications for membranes. The more commonly used membranes are for microfiltration, ultrafiltration, nanofiltration, and reverse osmosis. Microfiltration has the largest size pores and reverse osmosis contains the smallest size pores. As the pores decrease so does the range of solutes able to pass through the membranes [1]. Pressure is typically used to drive the transport through the membranes and it increases as the pores become smaller. Membranes used in this process are either inorganic or polymeric.

Nanofiltration is a process in which membranes with nano-size pores are used to separate solutes or salts based on size and/or charge [2]. This mechanism underscores the importance of the zeta potential, which is directly proportional in sign and magnitude to the surface charge density [3], and the surface morphology, which can give the surface properties and porosity, and is most accurately observed by AFM imaging (Figure 1). The surface charge is responsible for the rejection of ions of similar charge and the surface roughness

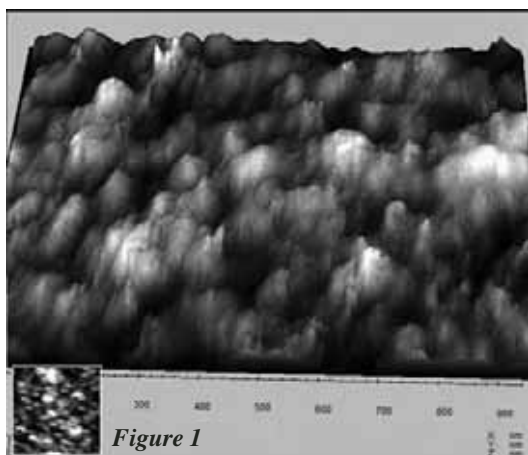


Figure 1

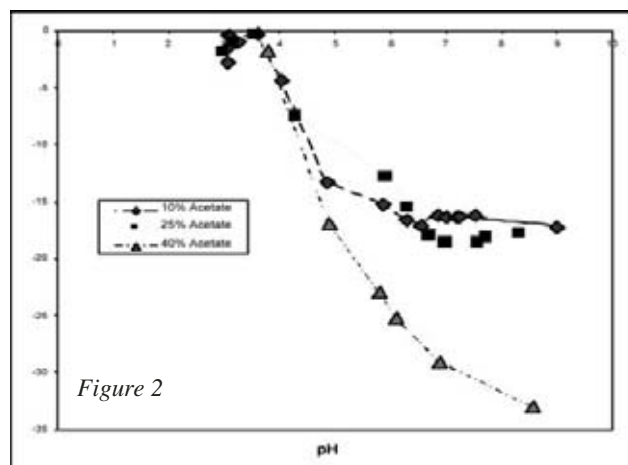


Figure 2

has been shown to improve solute flux while also increasing the rate of membrane fouling (Hirose, 1997).

The main use for the membranes is the removal of bacteria, viruses, salts, and other organic and inorganic material from water. This process is found at wastewater plants. The processed water can not only be used for city purposes but also beverage products such as soft drinks and coffee. Other applications can be found within the medical field where membranes are attached to silicon wafers as a means of separating biomolecules [4].

### Procedures:

Samples were imaged by AFM in a PicoPlus fluid cell (Molecular Imaging, Inc.) under Magnetic AC (MAC) mode in 1 mM KCl electrolyte solution. The cantilever was the MAClever Type IV (Molecular Imaging, Inc.) made of silicon nitride with a resonance frequency of 15 kHz and a force constant of 0.02 N/m.

The zeta potential was measured by streaming potential with the EKA Analyzer (Brookhaven Labs) over a pH range of 3-9 using 1 mM KCl electrolyte and HCl and KOH as pH adjusters.

Figure 1 is an AFM of the 10% acetate concentration membrane.

### Results:

**EKA: Effect of pH and Acetate Concentration on Zeta Potential/Charge Density;** In Figure 2, the y axis represents the change in zeta potential which is the uncontrolled variable and the x axis represents the pH, the controlled variable. The zeta potential (and hence the surface charge) was negative throughout the entire pH range, and as the percentage of the acetate concentration within the membrane increased so did the zeta potential which should hold true in theory (Elimelech, 1999). This was observed for the 40% acetate membrane. But there seems to be no significant difference in zeta potential between the 10% acetate and 25% acetate membranes.

**AFM: A Study of the Surface Topography;** The data on the surface roughness, shown in Figures 3 and 4, did not support the assumption that roughness has a positive dependence on the acetate concentration. The roughness therefore depends more on other parameters such as how the membranes were made during the spin process, along with reactants in the process which were all held constant. The peak to valley ratio does however seem to depend on the concentration of acetate in the membrane—the greater the concentration the less the height difference from the peaks to the valley. This relationship is assumed to be based on the reactants being more aggregated with the increase of acetate.

### Conclusions:

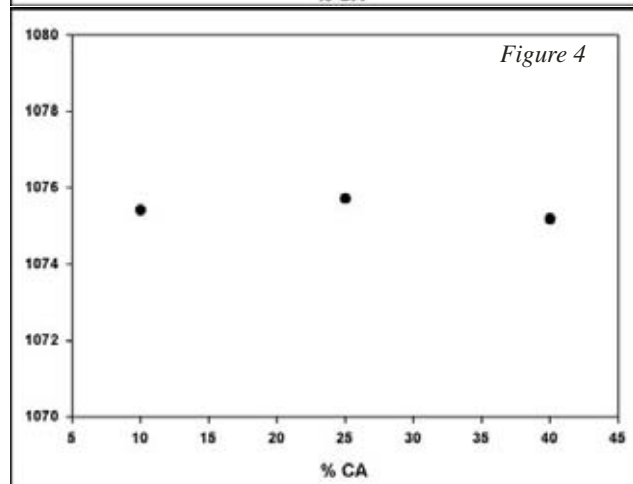
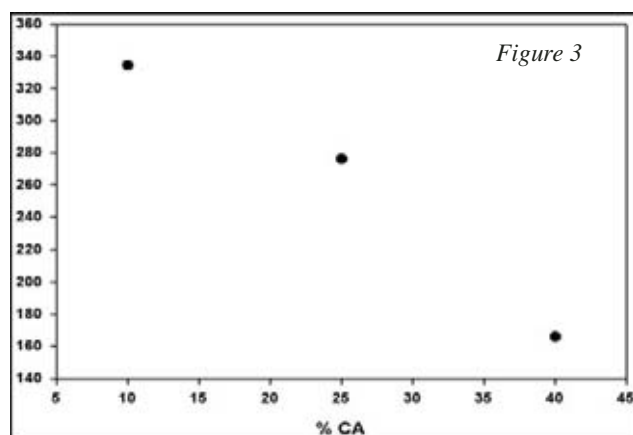
In conclusion the general assumption and theory of the acetate playing a major role in the surface roughness and on the zeta potential held true only for a small portion of the experiment. The roughness of the membrane did not appear to vary much with a change in acetate concentration. The zeta potential had a larger negative charge for the 40% acetate membrane than 10% or 25% as expected but it is hard to differentiate any effect on the zeta potential as a result of acetate concentration between the 25% and 10% membranes.

### Acknowledgements:

The author wishes to thank Dr. Kimberly Jones, Dr. Jerney Matthews, HNF, NNIN and NSF.

### References:

- [1] Membrane Technology and Applications; 2 ed.; Baker, R. W., Ed.; John Wiley & Sons, Ltd.: Chichester, 2004.
- [2] Nanofiltration: Principles and Applications; A.I. Schafer, A. G. F., T.D. Waite, Ed.; Elsevier, Ltd.: Oxford, 2005.
- [3] Elimelech, M.; Xiaohua Zhu; Childress, A. E.; Seungkwan Hong. Journal of Membrane Science 1997, 127, 101.
- [4] Russo, A. P.; Retterer, S. T.; Spence, A. J.; Issacson, M. S.; Lepak, L. A.; Spencer, M. G.; D.L. Martin; MacColl, R.; Turner, J. N. Separation Science and Technology 2004, 39, 2515.





# Fabrication & Characterization of Nanoscale Electrochemical InN Sensors

**Clara Ji-Hyun Cho, General Engineering, Franklin W. Olin College of Engineering**  
**NNIN REU Site: Cornell NanoScale Science & Technology Facility, Cornell University**

*NNIN REU Principal Investigator: William J. Schaff, Electrical & Computer Engineering, Cornell University*

*NNIN REU Mentor: Ho-Young Cha, Electrical & Computer Engineering, Cornell University*

*Contact: clara.cho@students.olin.edu, schaff@iiv.tn.cornell.edu*

## Abstract:

Indium Nitride (InN) has some advantages over other semiconductor materials in sensor applications because of high surface electron concentrations. In this project, we have patterned nanometer-size holes on InN to increase the surface area and electrochemical sensitivity. A patterning process involving an anodized aluminum oxide (AAO) etch mask and an ECR etch recipe was developed. Holes 100 nm in diameter and 100 nm in depth were achieved with this process. Preliminary experimental results indicate selective sensitivity with different gas exposures.

## Introduction:

Recent advancements in the growth of singly crystalline InN has allowed more accurate identification of fundamental properties of InN, such as the narrow band gap (0.6-0.7 eV) and the surface electron charge accumulation. These properties suggest the potential applications of InN and InGaIn in fields such as photovoltaic systems and optical fiber communications [1]. The charge accumulation on the surface of InN also makes it sensitive to environment, which brings up the possibility of using InN as an electrochemical sensor.

Although there has been a study done on wet chemical sensitivity of planar surface InN, no gas sensitivity study has been done on InN [2]. The goal of this research project is to fabricate electrochemical InN sensors with nanometer hole patterns in the channel area for gas sensing applications. An array of conventional and non-conventional lithographic methods was incorporated to fabricate InN sensor devices.

## Procedures:

All samples in this study were grown by a conventional molecular beam epitaxy technique. Sensors were fabricated using a variety of methods. All hole patterns were first etched onto an SiO<sub>2</sub> layer and later transferred to InN and InGaIn samples via the ECR etching process.

**Electron-Beam Lithography:** Hole patterns varying

in size from 50 nm to 1.5  $\mu$ m were written onto a 200 nm PMMA photoresist layer of the sample using Leica VB6-HR with a beam dose of 100  $\mu$ C/cm<sup>2</sup>. After developing the patterns, a CHF<sub>3</sub>/Ar RIE process was used to etch the SiO<sub>2</sub> layer.

**UV-Nanoimprint Lithography:** A quartz master with nanometer-sized pillars was first fabricated via electron-beam lithography using negative photoresist and varying beam doses. Quartz etching was done using a CHF<sub>3</sub>/Ar RIE process. Using molecular vapor deposition, a monolayer of fluorooctyltrichlorosilane (FOTS) was then deposited on the surface to serve as a release layer.

Approximately 600 nm of UV-curable resist PAK-01 was spun onto the sample prior to the imprinting process. The master was then pressed against the sample, and the entire apparatus was exposed with a UV light source for 30 seconds using CNF's EVG620-NIL contact aligner. The CHF<sub>3</sub>/Ar RIE process was used to transfer the patterns onto SiO<sub>2</sub> layer.

**AAO Etch Mask Process:** 200 nm of Al was deposited onto the sample with an insulating layer of SiO<sub>2</sub> between the InN and Al layers. The Al layer was then anodized in an electrolyte solution of 0.3 M oxalic acid with a constant voltage of 40 V and copper as the cathode. The sample was subsequently immersed in a solution of 5% H<sub>2</sub>PO<sub>4</sub> for 30 minutes. CH<sub>4</sub>/O<sub>2</sub> and CHF<sub>3</sub>/Ar RIE processes were used for the pattern transfer.

The patterns generated by optical lithography, electron-beam lithography, and the AAO etch mask were then transferred from the SiO<sub>2</sub> layer onto InN thin films using an ECR etch process. 12.5 sccm CH<sub>4</sub>, 3 sccm Cl<sub>2</sub>, and 4 sccm Ar gases were used with an etching rate of ~ 80 nm/min. A mesa etch was performed to create channel areas, followed by 30 nm Ti and 400 nm Au metallization layers for ohmic contacts.

## Results and Conclusions:

The minimum hole feature we were able to fabricate using electron-beam lithography was 100 nm in diameter with 200 nm spacing. Although the holes were



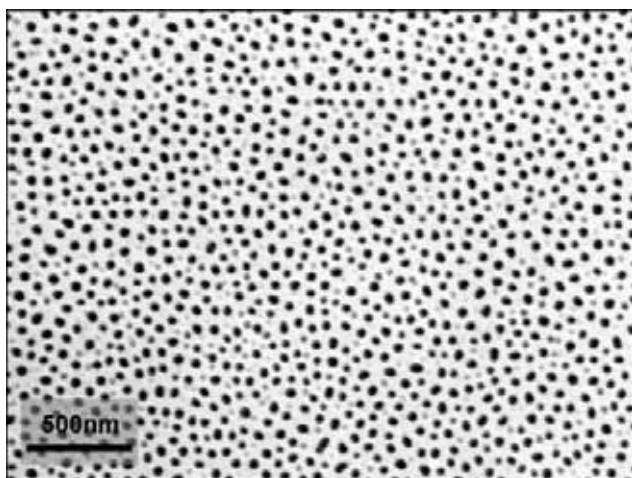


Figure 1: SEM micrograph of porous alumina layer.

small, there was only a marginal increase in the surface area due to the large spacing. Using UV-nanoimprint lithography, densely packed holes 350 nm in diameter were fabricated. The hole size was actually limited by the smallest pillar size we were able to fabricate on the quartz master, which was around 300 nm in diameter and 200 nm in height.

Figures 1 and 2 respectively show the as-fabricated porous alumina layer and the surface of InN after the pattern transfer. Holes on AAO etch mask range from 30-50 nm in diameter, and the final holes on InN are 80-100 nm in diameter and 100 nm in depth. The increase of the final hole size is due to the  $\text{H}_2\text{PO}_4$  soak and  $\text{CH}_4/\text{O}_2$  RIE step in the process. These steps are needed, however, in order to guarantee that we etch through the thin layer of alumina underneath the porous alumina structure. Overall, using the AAO etch mask process, we were able to increase the surface area of InN by 76%.

Figure 3 shows photoluminescence spectra of InN sensors fabricated via electron-beam lithography. The results indicate the dependence on the size of fabricated holes. The increase in electron density with increasing hole size is because larger holes allow greater exposure to plasma during the etching process. Exposure to

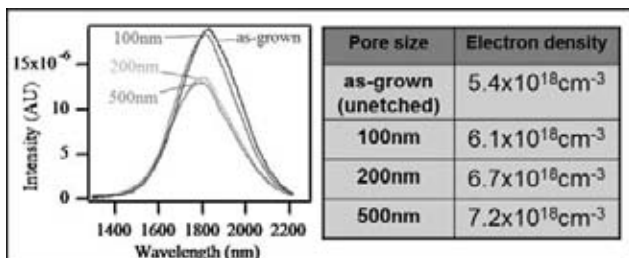


Figure 3: Photoluminescence spectra of InN sensors fabricated via electron-beam lithography.

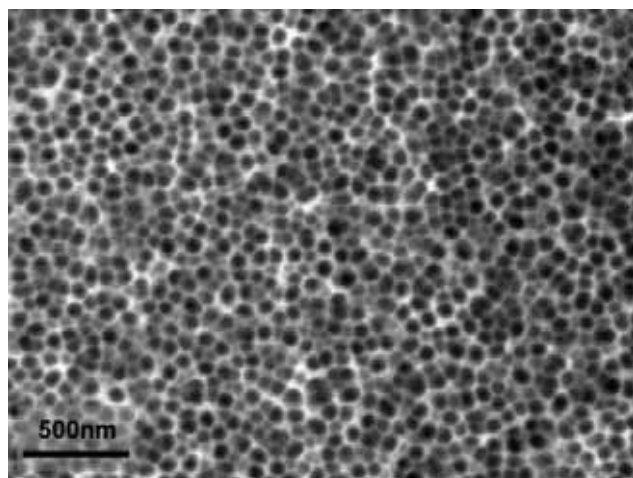


Figure 2: SEM of InN surface after the pattern transfer.

plasma might have induced some surface defects which in turn increased the electron density.

The change in resistance as a function of time for InGa $\text{N}:\text{Mg}$  upon various gas exposures is shown in Figure 4. Some selective responses with  $\text{CO}_2$  and  $\text{H}_2$  are shown, which are exciting results because gas detection selectivity in electrochemical sensors is a tough problem to solve. More data needs to be collected to verify the repeatability of these results.

#### Acknowledgements:

The author would like to thank Dr. William Schaff, Dr. Ho-Young Cha, Xing Qun Jiang, Rey Javier, Troy Richards, CNF, NBTC, NNIN, and NSF for all their support.

#### References:

- [1] H. Lu, W. J. Schaff, L. Eastman, "Surface charge accumulation of InN films grown by molecular-beam epitaxy", American Institute of Physics, Vol. 82, No. 11, pp 1736-1738, March 2003.
- [2] H. Lu, W. J. Schaff, L. Eastman, "Surface chemical modification of InN for sensor applications", American Institute of Physics, Vol. 96, No. 6, pp 3577-3579, September 2004.

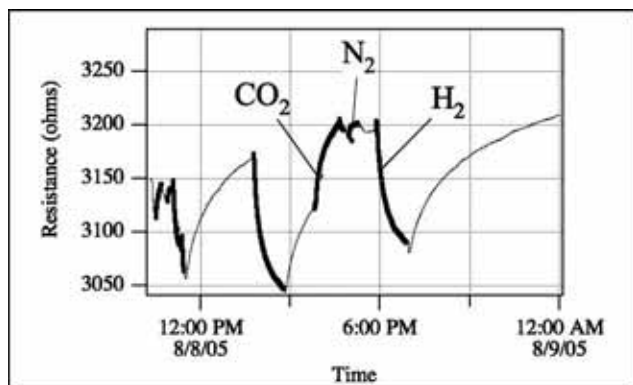


Figure 4: Preliminary gas exposure data on InGa $\text{N}:\text{Mg}$  sensor.

# A Microfluidic System for the Assembly and Culture of Tumor Spheroids

**Eric Chu, Biomedical Engineering, Johns Hopkins University**  
**NNIN REU Site: Michigan Nanofabrication Facility, The University of Michigan**

*NNIN REU Principal Investigator: Michel Martin Maharbiz, Electrical Engineering, University of Michigan*

*NNIN REU Mentors: Mikhail Pinelis & Tushar Bansal, Electrical Engineering, University of Michigan*

*Contact: ebchu@jhu.edu, maharbiz@eecs.umich.edu*

## Abstract:

Multicellular tumor spheroids are 3-dimensional cell clusters that play an important role in the study of cancer. Tumor spheroids can serve as a model for *in vivo* tumor tissue because they have similar geometry and behavior to certain tumor types. Multicellular tumor spheroids have been used as an *in vitro* model for studying tumor cell response to therapy. Spheroidal cell studies have progressed to the investigation of differentiation, apoptosis, invasion, and other basic biological mechanisms.

The purpose of this work was to fabricate a micro-fluidic device in which multicellular tumor spheroids can be grown to a specific size and then cultured within the device for period up to one week. Initially myoblast spheroids were assembled, myoblast cells were passed through fabricated microchannels, and then trapped by perforated, semicircular wells within these channels. Arrays of wells embedded in the microchannels were fabricated with diameters ranging from 200-800  $\mu\text{m}$ .

## Introduction:

*In vitro* studies of multicellular tumor spheroids have advanced the understanding of the role of cellular microenvironments in tumor biology [1]. Studies have shown that compared to conventional monolayer cultures, tumor spheroids more closely resemble *in vivo* cells with regards to geometry and cellular environment [2]. For example, in cell-to-cell interactions and cell-to-extracellular matrix multicellular spheroids are a better model than monolayer cultures [2]. Tumor spheroids can also be used to investigate therapies for tumor cells, like drug resistance [2]. Studies have progressed to basic biological mechanisms like apoptosis, differentiation, and invasion. In particular, interest has been placed on the role of the metabolic three-dimensional microenvironment; for example, oxygen, glucose, and lactate distribution, in the development of cell quiescence and necrotic cell death [2].

Current methods for growing and culturing multicellular tumor spheroids are challenging. They are

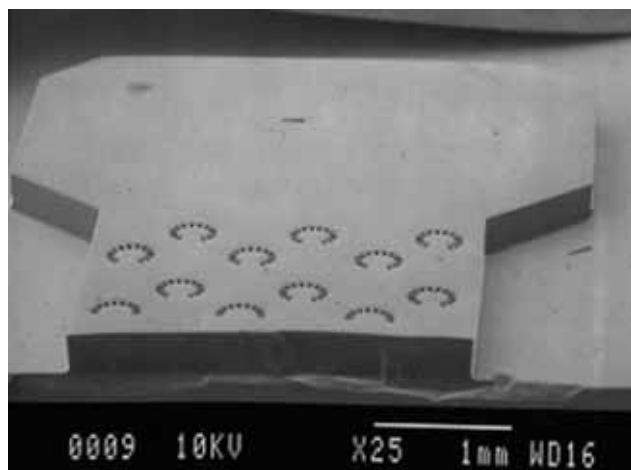


Figure 1: Scanning electron micrograph of SU-8 mold.

cultured in part by rotating them in suspension creating unequal spheroid diameters [1].

## Experimental Procedure and Materials:

SU-8 was chosen for the mold material because it allows fabrication of structures with thicknesses greater than 100  $\mu\text{m}$ , Figure 1. PDMS was used because of biocompatibility, ease of use, and low cost of fabrication. The microfluidic device mold was made from SU-8 2050 photoresist (MicroChem, Newton, MA). The SU-8 had to be characterized for a two coat process. From Figure 3, we can see that two coats at 1600 rpm provide our specified thickness of 200  $\mu\text{m}$ . Photoresist thicknesses were measured at different location on each mold using a Dektak 6M Surface Profiler.

Subsequently, the SU-8 was exposed with the non-contact ACS200 stepper and developed. The release agent 230 Fluid (Dow-Corning) was then spun on the cured mold to facilitate the removal of PDMS from the mold. The PDMS chip was fabricated using a 10:1 ratio of base to curing agent of Sylgard 184 (Dow-Corning) [3]. After PDMS was poured on the mold, it was degassed for 1 hour and baked for 24 hours at 90°C to cure. The PDMS was bonded to a glass slide by

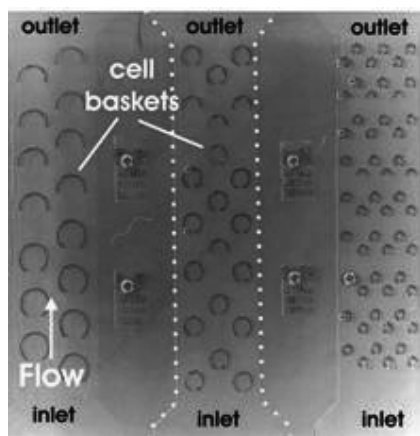


Figure 2:  
Optical micrograph  
of device.

exposing both the glass and the PDMS faces to oxygen plasma and then pressing them into each other lightly. To improve the PDMS-glass bond, the assembled device was baked for 30 minutes at 115°C.

Once the device was fully assembled, myoblast  $C_2C1_2$  cells were flown through the channels in three different flow rate regimes of 20, 50, and 75 mL/hr. Each trial was run for 15 minutes using an automated syringe pump.

### Results and Discussion:

The final device had 3 channels with well diameters of 200, 500 and 800  $\mu\text{m}$  and a height of 200  $\mu\text{m}$ . (See Figure 2.) Each channel was approximately 2 mm wide with 3 mm wide inlet and outlet ports. Cells were trapped in perforated, semicircular wells with pores ranging in size from 15 to 30  $\mu\text{m}$ . The aspect ratio for the “pillars” comprising the wells was approximately 10 with a width of 20  $\mu\text{m}$  and a height of 200  $\mu\text{m}$ . 230 fluid was utilized in our process as a mold release agent between the PDMS and SU-8 to prevent rupturing of PDMS while demolding. PDMS was then baked for 24 hours at 90°C after the initial hotplate bake of 1 minute at 110°C [3]. The longer bake time ensured maximum cross-linking and Young’s modulus which prevented

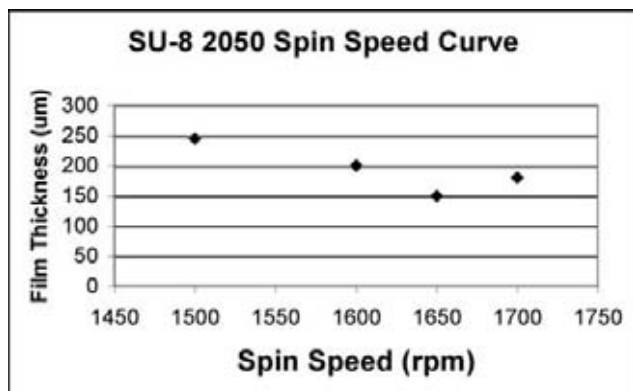


Figure 3: SU-8 spin speed curve.

the “pillars” from collapsing.

Our initial cell experiments involved myoblast  $C_2C1_2$  cells. Cells accumulated in wells for only the 20 mL/hr flow rate after approximately 10 minutes, Figure 4. At the faster flow rates, cells did not accumulate because the high rate forced the cells through the gaps in the wells. However, the slowest rate of 20 mL/hr provided enough time to allow for cells to form clusters.

### Future Work:

The next iteration of the device will be fabricated with geometries that will accommodate more efficient assemble of the three dimensional cell constructs. This includes varying gap widths in between “pillars” of the wells. Also, testing on the myoblast/ $C_2C1_2$  cells will be finalized. Finally, tumor cell experiments will be conducted.

### Acknowledgments:

This study was funded by the NSF through the NNIN REU program at the University of Michigan Solid State Electronics Laboratory in Ann Arbor. I would like to thank Professor Michel Maharbiz, Mike Pinelis, Tushar Bansal, and the rest of the Maharbiz Group for their support with my research. Also, I would like to thank Sandrine Martin and the SSEL staff.

### References:

- [1] Walenta S, Doetsch J, Mueller-Klieser W and Kunz-Schughart LA: Metabolic imaging in multicellular spheroids of oncogene-transfected fibroblasts. *J Histochem Cytochem* 48: 509-522, 2000.
- [2] W. Mueller-Klieser: Tumor biology & experimental therapeutics. *Crit Rev Oncol Hematol*. 36:123-139, 2000.
- [3] Gray, D.S., J. Tien, and C.S. Chen. 2003. Repositioning of cells by mechanotaxis on surfaces with micropatterned Young’s modulus. *J Biomed Mater Res*. 66A:605-14, 2003.

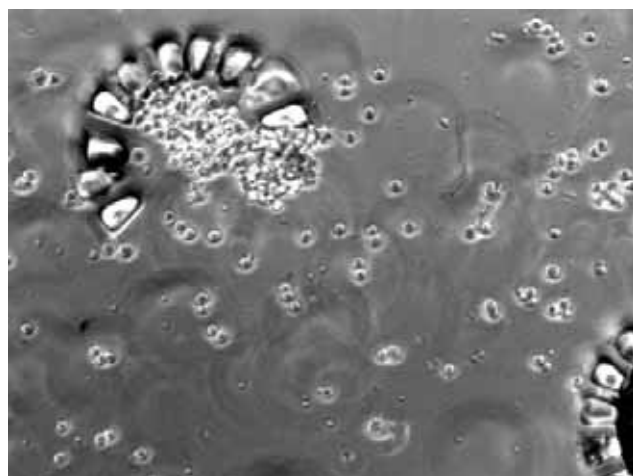


Figure 4: Myoblast cell accumulation.



# Microfluidic Devices for Biological Applications

**Frank Cleary, Physics, Cornell University**

**NNIN REU Site: Nanotech, University of California at Santa Barbara**

*NNIN REU Principal Investigator: Andrew Cleland, Physics, University of California, Santa Barbara*

*NNIN REU Mentor: David Wood, Physics, University of California, Santa Barbara*

*Contact: fbc4@cornell.edu, anc@physics.ucsb.edu*

## Abstract:

In recent years much interest has been generated in devices in which fluid is moved through micrometer scale channels. These so-called microfluidic devices show great promise in their application to biology and medicine. One possible application is a cheap, disposable cell sorting device that requires only small sample sizes. Such a device would be very useful in immunology and cancer research as current cell sorting technology has none of these desirable properties.

One key problem in creating a microfluidic cell sorter is that the fluid flow must be switched between two or more collection points. By fabricating a microfluidic device in which fluid flow is switched by the application of an electric field, an important element of a microfluidic cell sorter is completed. We have investigated the fabrication and use of such a device made out of polydimethylsiloxane (PDMS), a silicon elastomer. We present our fabrication process as well as data on device performance. We also present data from simulations of a bead in a microfluidic channel as it moves over a coplanar waveguide, a promising scheme for the detection of cells.

## Introduction:

The need to separate specific cell types from a diverse population is essential to modern cancer and immunology research. Current technology relies on Fluorescence Activated Cell Sorting (FACS). A FACS machine differentiates cells by shining a laser on them and detecting fluorescence. The cell is then encased in a droplet of water charged according to the type of cell. The droplet is deflected by an electric field into the proper container.

Although FACS provides fast, efficient sorting of cells, it has several major drawbacks. FACS machines are expensive, hard to clean and require relatively large sample sizes. A microfluidic cell sorter could be made to be cheap and disposable, requiring only very small sample volumes. The microfluidic devices we have fabricated show potential for use in a microfluidic cell sorting system.

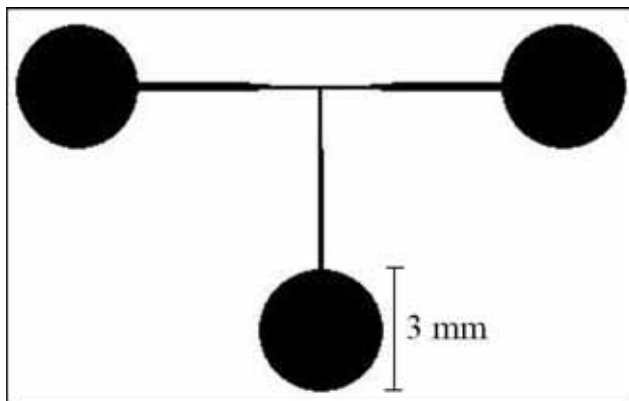


Figure 1: A schematic of a microfluidic device.

Our microfluidic devices (Figure 1) were designed to use electroosmosis as a means of switching fluid flow from one collection point to another. Electroosmosis is a phenomenon that arises because of the buildup of charged ions along the walls of the device. Applying an electric field causes these ions to move, dragging the rest of the fluid with them.

Besides switching fluid flow, another key problem in the creation of a microfluidic cell sorter is that of detection. Current laser detection systems are large and expensive. In exploration of new detection schemes we have simulated the motion of a Teflon™ bead as it passes over coplanar electrodes. As the bead moves over the electrodes its presence changes the resistance and capacitance between them. This demonstrates the potential for an electronic detection method that would be far cheaper than current optical techniques.

## Methods:

PDMS microfluidic devices were fabricated as described in [1]. Roughly, 50  $\mu\text{m}$  thick SU-8 photoresist was patterned on a 3" silicon wafer. PDMS prepolymer was mixed with curing agent then poured over the wafer and baked. The cured PDMS was then peeled off and individual devices cut from it. The devices were bonded to glass microscope slides. Predrilled holes in the slide were used to connect the device to external fluid lines.



We attempted to create electroosmotic flow by placing platinum electrodes in two different collection wells and applying a high voltage ( $\sim 150$  V) between them. Flow was visualized using  $10\text{ }\mu\text{m}$  diameter polystyrene beads.

Simulations were run using Ansoft's HFSS software. A model with a  $25 \times 25\text{ }\mu\text{m}$  channel of seawater running over coplanar electrodes was constructed (see Figure 2). Electrical impedance data as a function of bead position was extracted from the simulations.

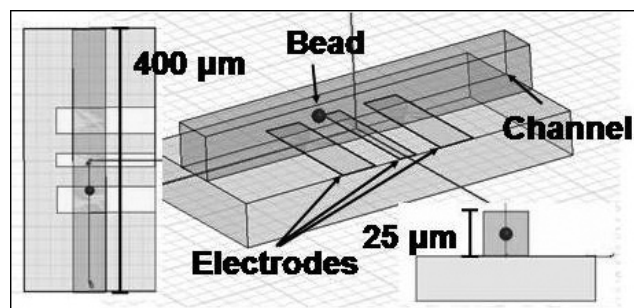


Figure 2: Three views of the model used to simulate the motion of a bead over a coplanar waveguide.

### Results and Discussion:

Working microfluidic devices were fabricated and  $10\text{ }\mu\text{m}$  diameter polystyrene beads were observed moving through the channels. Electroosmotic flow was not observed although electric current was flowing between the electrodes. A possible explanation of this is that the minimum channel dimensions of  $50 \times 30\text{ }\mu\text{m}$  were too large for electroosmotic flow to occur. Smaller channels would possibly improve electroosmotic flow.

A typical plot of impedance vs. bead position is shown in Figure 4. In this case, the bead was made of Teflon<sup>TM</sup>, an insulating material. A conducting bead will cause the real and imaginary parts of the impedance to change in opposite directions.

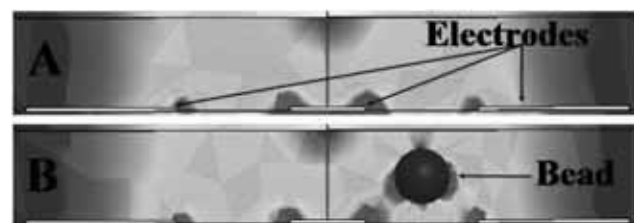


Figure 3: Electric field magnitude (side view of channel). Note change when bead is present (in B).

Simulations of a bead as it moves over coplanar electrodes show promising results for the electronic detection of cells. With a working detection model different objects can be simulated giving researchers data on what geometries and materials will provide the greatest signal.

### Conclusion:

We have constructed a microfluidic device that is capable of supporting fluid flow. The method used is fast and inexpensive since the mold used to make the device can be reused, eliminating the need for further photolithography.

By simulating the passage of a bead over coplanar electrodes, we demonstrate the theoretical basis for a promising detection scheme. In the future, researchers will be able to use this simulation model to experiment with different geometries and materials without going through a long and difficult fabrication and testing process.

### Acknowledgements:

Omar Saadat contributed greatly to the microfluidic device fabrication process in the course of his work alongside the authors. Chris McKenney, Michael Stanton and Loren Swenson aided in various parts of the project. We also thank Martin Vandenbroek and Mike Wrocklage for their technical assistance. Funding was provided by the National Science Foundation and the NNIN.

### References:

- [1] Micro-fluidics Lab Process Summary (M.I.T., unpublished) Available: [http://hackman.mit.edu/6152J/SP\\_2004/lab\\_manuals/sp\\_2004\\_fluidics\\_manual.pdf](http://hackman.mit.edu/6152J/SP_2004/lab_manuals/sp_2004_fluidics_manual.pdf)

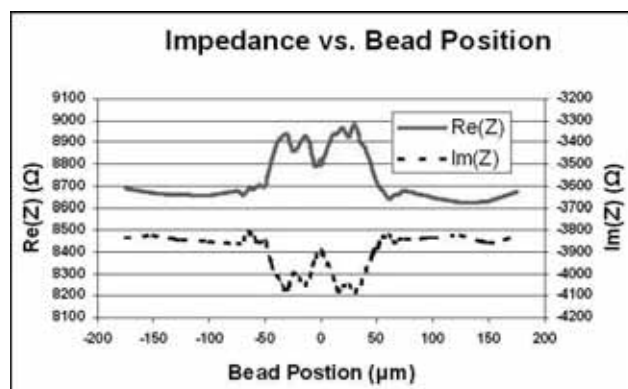


Figure 4: Real and imaginary parts of the electrical impedance of the system as the bead moves through the channel.

# Development of Ti Doped Iron Oxide by Sol-Gel Synthesis Routes for Photocatalytic H<sub>2</sub> Production

**Samantha C. Cruz, Materials Science and Engineering, Northwestern University**  
**NNIN REU Site: Nanotech, University of California at Santa Barbara**

*NNIN REU Principal Investigator: Eric W. McFarland, Department of Chemical Engineering, UCSB*  
*NNIN REU Mentor: Alan Kleiman-Shwarsstein, Chemical Engineering, University of California, Santa Barbara*  
*Contact: s-cruz@northwestern.edu, mcfar@engineering.ucsb.edu*

## Abstract:

The push for a hydrogen economy has created a need for more efficient methods of production of the fuel. Although limited by the efficiency of the materials used as catalysts, photoelectrolysis is attractive as a sustainable, non-polluting method of hydrogen production. This work focuses on the synthesis of  $\alpha$ -Fe<sub>2</sub>O<sub>3</sub> (hematite) using the sol-gel process for its production. Titanium doped hematite showed two orders of magnitude improvement in photocurrent production over undoped samples. XRD was used to confirm that the hematite phase was preserved after doping.

## Introduction:

The potential environmental crisis due to the increasing greenhouse gas emissions by fossil fuel burning has led to the quest for a sufficient renewable source of a clean burning fuel. Recent developments and advances in the field of hydrogen as a fuel has renewed interest in what has been called a “holy grail” in photoelectrochemical research—splitting water with visible light, both abundant, low cost resources—which was first demonstrated by Fujishima and Honda in the early 1970’s [1]. Figure 1 illustrates the method by which hydrogen is photoelectrochemically produced from water. Incident photons impinging on the semiconductor electrode create electron-hole pairs that can perform redox chemistry to create hydrogen and oxygen. Hydrogen is an attractive fuel source because combustion with oxygen releases only water as a byproduct.

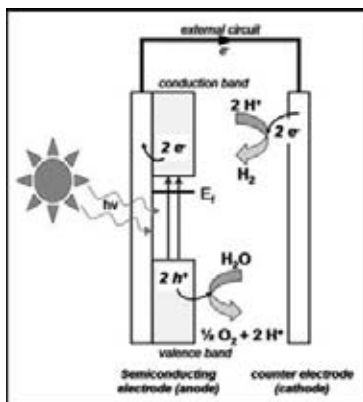


Figure 1:  
Schematic of an n-type semiconducting photoelectrochemical cell.

Since the materials used for this process are in an aqueous environment, they must be resistant to photo-corrosion, as well as have electronic properties suitable for the photo-catalytic reaction, namely a bandgap well positioned for absorbance of the solar spectrum (bandgap 1.8-2.23 eV). Oxides generally have the robustness necessary for the task, but few have the valance and conduction bands matching the redox level of water. Hematite has a bandgap in the range of 2.0-2.2 eV which has the ability to absorb about 40% of the solar spectrum, but does not match the redox levels necessary to photo-electrochemically split water.

$\alpha$ -Fe<sub>2</sub>O<sub>3</sub> can be created through the thermal oxidation of iron, and the sol-gel process allows for an industrially scalable process in which an iron oxide precursor is deposited on substrates from solution and trapped in a gel matrix. This process also allows for some controlled doping of the oxide.

## Procedure:

Various compositions of Fe sol-gels were made using Fe(NO<sub>3</sub>)<sub>3</sub>•9H<sub>2</sub>O as the iron precursor and a process similar to those previously published by Gash et al [2]. The solution was allowed to cure and then fluorine doped tin oxide (FTO) slides were dip coated in the solution using an automated micrometer. The rate at which the samples were dip coated varied from 100-500  $\mu$ m/s with a 5s stand in the solution. The samples were then allowed to air dry, and finally calcined at 450-600°C for 6 hrs. Further sol-gels were synthesized with the addition of metal salts as dopants (Ti, Ni, Co, Cu and Mg).

Electrochemical and physical characterizations of the films were performed on all the samples. Transient photocurrent measurements were taken under light illumination and at dark to record the amount of current produced while illuminating. IV curves were also performed under chopped illumination to obtain the flat band potential of the samples. A schematic demonstrating the photocurrent measurements configuration is shown in Figure 2.

Physical characterizations of the films were done through microscopy and spectroscopy. Confirmation of

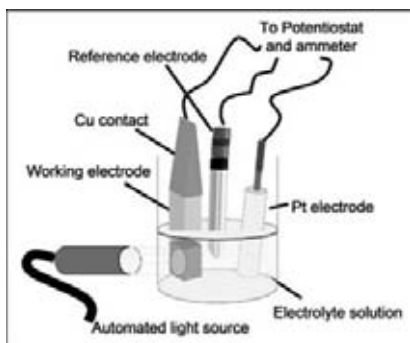


Figure 2: Photo-electrochemical measurement set-up.

the presence of hematite was made through powder x-ray diffraction and further analysis was made through UV-VIS absorbance spectroscopy to approximate bandgaps for each film. Film morphology was observed through optical profilometry and scanning electron microscopy.

### Results:

XRD spectra resulted in peaks matching those of polycrystalline  $\alpha\text{-Fe}_2\text{O}_3$  references for the experimental films, Figure 3. There was no observable difference in the spectra of the Ti doped samples, indicating no evidence of new phases. Absorbance spectroscopy showed that for a sample set of undoped and doped films, the average bandgap is  $2.1 \pm 0.3$  eV, which is consistent with the bandgap of hematite. Surface analysis of the hematite showed that films had thicknesses ranging from 50-600 nm depending on the length of cure time of the sol-gel. Further, the thicker ( $> 400$  nm) samples had a more cracked surface as opposed to the very thin ( $\sim 100$  nm) samples which had fewer visible cracks.

Zero-bias photocurrent measurements of undoped hematite records less than  $1 \mu\text{A}$ , where Ti doped films show lab record photocurrent for hematite at zero-bias

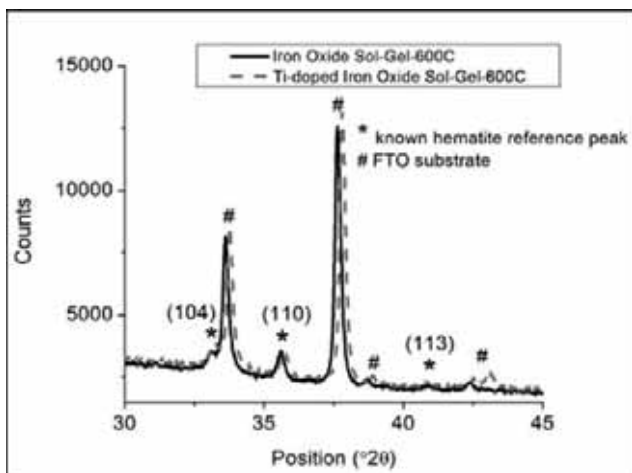


Figure 3: XRD spectra of undoped and doped hematite.

with two orders of magnitude increase. Figure 4 displays the photocurrent measured with and without UV filtration of the incident light for both Ti-doped and undoped hematite films. External-bias photocurrent studies show significant increase of photocurrent at positive bias with respect to an Ag/AgCl reference. For an undoped sample the flatband potential was around 0.26 V where Ti doped samples had larger flatband potentials with 0.45 V at 5% Ti loading in the solution, but decreasing as doping increased.

### Conclusions:

$\alpha\text{-Fe}_2\text{O}_3$  films can be synthesized using the sol-gel process for the photocatalytic production of hydrogen. Doping of hematite with Ti can be performed during the solution stage of the sol-gel dip-coating process. Ti doped samples do not show titania-hematite phase separation as indicated through XRD as well as the presence of induced photocurrent using only the VIS spectrum, since titania only absorbs UV light. Further, increased Ti doping increases photocurrent, as well as decreases the amount of external bias needed for photoelectrolysis of water.

### Acknowledgments:

Special thanks to Mike Northen and Asanga Ranasinghe for surface imaging. Partial funding and facilities support was provided by the NSF-MRSEC funded Materials Research Laboratory (Award #DMR00-80034), DOE (Hydrogen Program Award # GO15040), NSF and NNIN.

### References:

- [1] Fujishima A, Honda K. Nature 1972; 238:37-38.
- [2] Gash AE et al. Chem Mater 2001; 13:999-107.

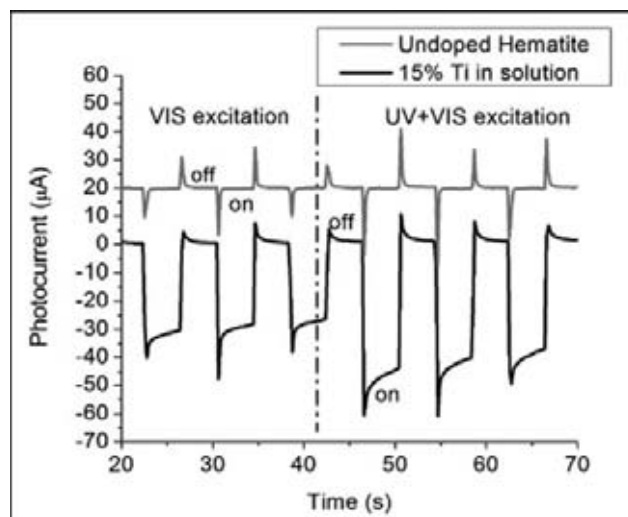


Figure 4: Zero-bias transient photocurrent of hematite with chopped light source.

# Porous Nanostructured Titania

Michael Cullinan, Engineering, Swarthmore College  
NNIN REU Site: Nanotech, University of California at Santa Barbara

NNIN REU Principal Investigator: Noel C. MacDonald, Mechanical and Environmental Engineering, UCSB

NNIN REU Mentor: Marcus S. Ward, Materials, UCSB

Contact: mcullin1@swarthmore.edu, nmacd@engineering.ucsb.edu

## Abstract:

The excellent electrical and mechanical properties of porous nanostructured titania (NST) make it an ideal material for many different applications including dye sensitized solar cells (DSSC). While DSSCs are cheaper to manufacture than silicon-based cells, they are also less efficient. The efficiency of the DSSCs depends on how well the sensitizing dye coats the cell and how well the electron recombination source infiltrates into the porous NST [1]. Consequently, the structure of the NST has a great effect on the efficiency of the cell.

Different processing parameters were studied to determine their effects on pore size and surface area. Overall, it was found that increasing the deposition rate and the thickness of the original titanium film increased the pore size of the NST. Also, it was found that increasing the concentration of the hydrogen peroxide used to oxidize the titanium, increased the pore size of the NST. In general, it was also found that as pore size increased, surface area decreased.

## Introduction:

Traditional NST production techniques, such as sol-gel processing, screen-printing, and reactive sputtering, all result in the formation of cracks throughout the NST. These processes also do not allow for *in situ* control over the pore size of the NST. However, we have developed a simple technique that is compatible with current micro-electronic manufacturing practices and produces crack-free NST with a sponge-like structure. It is proposed that control over the porous nature of this NST will allow for better dye sensitization and yield more efficient solar cells.

## Procedure:

The process we have developed for producing crack-free, porous NST is relatively simple. First a layer of titanium is evaporated onto a layer of silicon dioxide that is grown either thermally or by plasma enhanced chemical vapor deposition (PECVD) (see Figure 1) [2]. Following the titanium evaporation layer, a sacrificial mask layer of  $\text{SiO}_2$  is deposited by PECVD. Then  $20\text{ }\mu\text{m}$

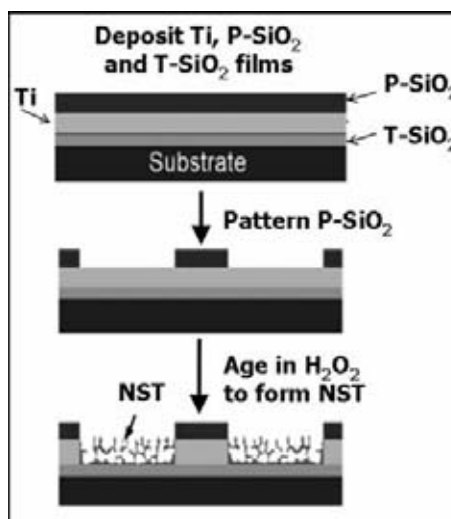


Figure 1:  
Schematic of  
NST production  
process.

pads are etched into an  $\text{SiO}_2$  mask. The size of these pads effectively stops cracks from forming in the NST.

The exposed titanium is then oxidized using a hydrogen peroxide solution in order to produce titania. The titania is then annealed at  $300^\circ\text{C}$  for 10 hours which produces crystalline porous NST. The average pore sizes of the NST samples can then be found using gas absorption techniques. The effect of the parameters on surface area is also determined from the data.

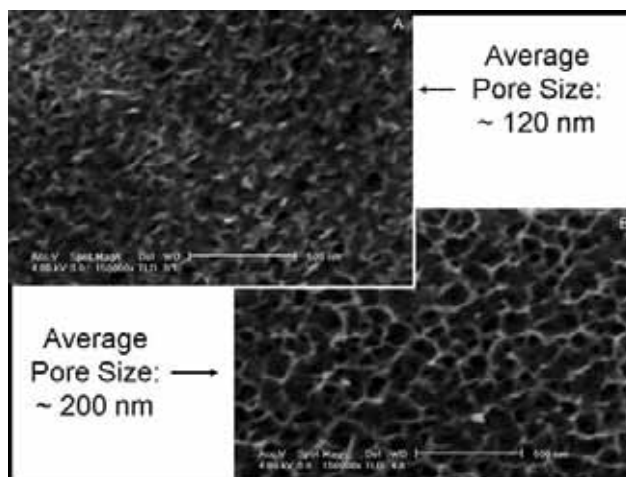


Figure 2:  $500\text{ nm}$  thick Ti deposited at A)  $2.5\text{ }\text{\AA}/\text{s}$ . B)  $4.5\text{ }\text{\AA}/\text{s}$ .



## Results and Conclusions:

Overall, the effects of three different process parameters were tested. The first parameter tested was the deposition rate of the titanium layer, which was varied between 0.5 and 4.5 Å/s. It was found that increasing the deposition rate increased the pore size. This can be seen in Figure 2 where the NST deposited at 4.5 Å/s has an average pore size of 200 nm while the NST deposited at 2.5 Å/s has an average pore size of 120 nm. It is proposed that this result is mainly due to fact that titanium films deposited at higher rates have larger average grain sizes.

The second parameter tested was the concentration of the hydrogen peroxide solution used to oxidize the titanium. The concentrations were varied from 5% to 20% and it was found that increasing the hydrogen peroxide concentration increased the average pore size. This can be seen in Figure 3 where the deposition rate is held constant and the concentration is allowed to vary.

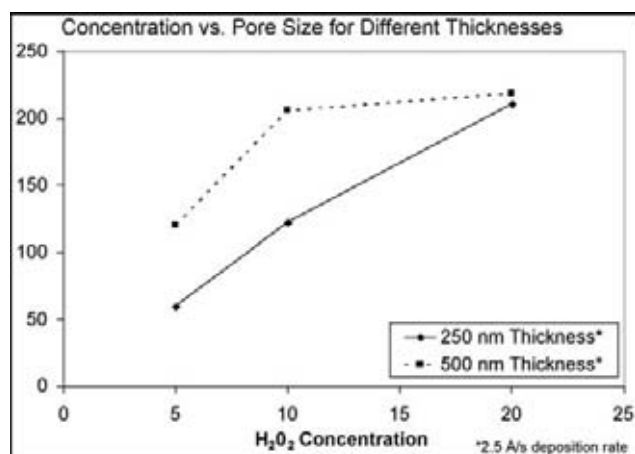


Figure 3: Variations in pore size by  $H_2O_2$  concentration and Ti thickness.

Overall, this result is related to fact that higher hydrogen peroxide concentrations significantly reduce the oxidation time of the titanium because the diffusion of oxygen through the top gel layer formed during the nucleation stage is much faster. Faster diffusion could be one mechanism that produces the larger pores.

Finally, the effect of the thickness of the titanium layer was tested. Overall, it was found that as the thickness increased, the pore size increased as well. This can be seen in Figure 3, where 500 nm thick films generally have larger pores than 250 nm thick films. However, it appears that this result diminishes as the  $H_2O_2$  concentration rises and becomes the dominant factor in pore size determination.

The effects of these three parameters on the surface area of the NST were also tested. Overall, it was found that as the deposition rate increased, the surface area decreased. Also, as the hydrogen peroxide concentration increased, the surface area of the NST decreased. Overall, these results show a clear negative correlation between pore size and surface area. This negative correlation can also be seen when the thickness of the Ti layer is increased. That is, doubling the thickness does not double the surface area because pore size increases reduce the surface area.

## Future Work:

In order to implement these new results into actual DSSCs, much more testing must be done. Since the one major component on the effectiveness of such solar cells is dependent on how well the electron recombination source infiltrates into the NST, increasing the pore size is proposed to produce better cells. However, the effectiveness of the cells is also dependent on how much surface area is covered by the electron recombination source. This means that increasing the pore size too much could actually reduce the effectiveness of the cells because the surface area is decreased. Therefore, in the future, tests must be done in order to determine the best combination of pore size and surface area.

## References:

- [1] Gratzel, Michael. "Photoelectrochemical Cells." *Nature*. 414, 338-344 (2001).
- [2] Zuruzi, A. S., Ward, M. S., MacDonald, N. C., "Fabrication and characterization of patterned micrometer scale interpenetrating Au-TiO<sub>2</sub> network nanocomposites", *Nanotechnology*, 16, 1-6 (2005).

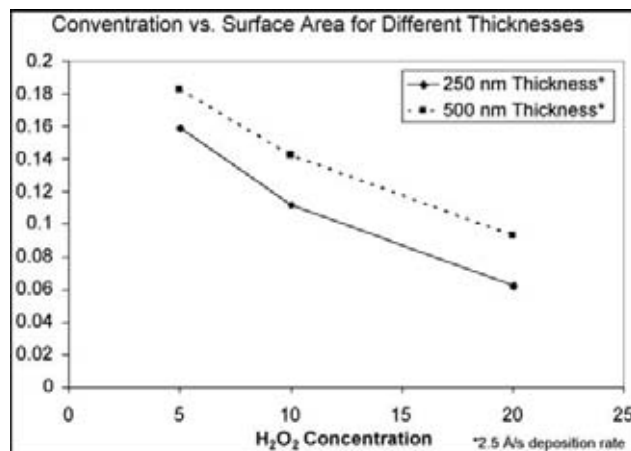


Figure 4: Variations in surface area by  $H_2O_2$  concentration and Ti thickness.

# Suspended Langmuir-Blodgett Film for Surround Gate Transistors

**Minh Phuc Nguyen Dao, Electrical Engineering, Santa Clara University**  
**NNIN REU Site: Stanford Nanofabrication Facility, Stanford University**

*NNIN REU Principal Investigator: Hongjie Dai, Chemistry, Stanford University*

*NNIN REU Mentor: Qian Wang, Chemistry, Stanford University*

*Contact: mpdao@scu.edu, hdai@stanford.edu*

## Abstract:

Transistors with surround gates can carry more current and allow for higher gate efficiency. In suspending a thin Langmuir-Blodgett (LB) film of germanium nanowires across a trench between the source and drain, we can implement a surround gate design by coating the suspended film with high- $\kappa$  material and sputtering the metal for the gate. In this experiment, we developed the processes, fabricated the transistors, took SEM images and characterized the devices with DC measurements.

## Introduction:

A nanowires LB film transistor with only a top gate has a limited channel as the electric field is not uniformly applied to the wire. Accordingly, the performance of the device suffers, since not much current can be conducted through the device. However, with a surround gate design, the applied electric field on the wire is uniform and a full channel can be created, resulting in more current and higher gate efficiency.

In order to realize this design, we developed a process flow that would allow for a high- $\kappa$  dielectric ( $\text{HfO}_2$ ) coated germanium nanowire film to be suspended over a trench. Then, metal could be sputtered underneath and over the suspended wire, effectively acting as a surround gate for the transistor (Figure 1). For the experiment to be valid, it is critical that film stay

suspended throughout the process and the wires form good contact with the source and drain metal.

## Experiment 1: Non-Suspended Germanium Nanowire Film Transistor

Since the non-suspended film transistors are to be used as reference, we did not fabricate any trenches on the substrate. Following the film transfer, our process was as follows: (a) define the device area with lithography, (b) etch away the excess wires, (c) pattern the source and drain, (d) deposit metal (titanium) for source and drain and liftoff, (e) anneal at  $400^\circ\text{C}$ , (f) coat the chip with high- $\kappa$  material, (g) define the gate area, and (h) sputter the gate metal (platinum).

According to the DC measurements, prior to high- $\kappa$  coating, the device exhibited p-type characteristics; however, after we coated the wire and sputtered the gate metal, the transistor behaved like an n-type device (Figure 2). We believe that this unexpected change may have been due to the patterning process and the Ti electrodes. Also, the current was much lower than we expected, only in the hundreds of nA range. The low conductance may have been due to the poor quality of the film and transfer process.

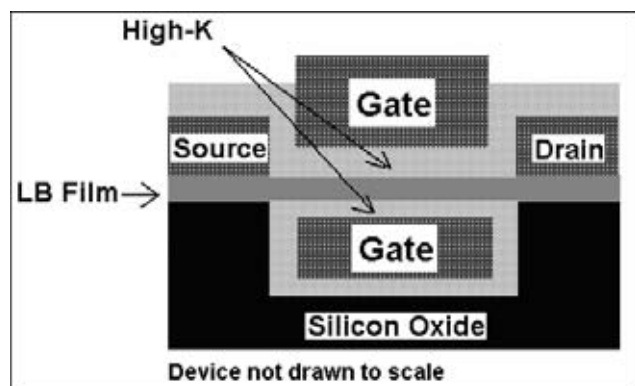


Figure 1: Surround gate design for nanowire film transistor (cross sectional view).

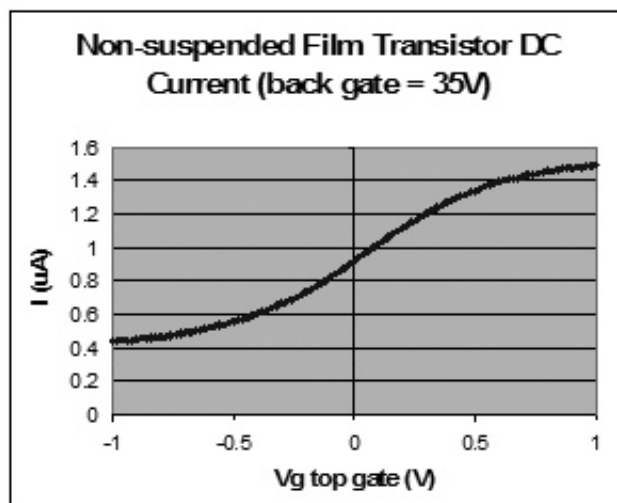


Figure 2: DC current of device with non-suspended film and back gate at 35V.

## Experiment 2: Suspended Germanium Nanowire Film Transistor

This experiment used essentially the same process flow as the devices with non-suspending film. However, before the film transfer, trenches with 200 nm depth and 400 nm width are fabricated via e-beam lithography. Therefore, after the film was transferred and excess wires were etched away, the remaining nanowires should be suspended over the trench. Since suspension was a critical requirement for our design, we used SEM images to verify that enough wires had survived through the processes. Furthermore, we took DC measurements of the current between the source and drain to confirm that the wires formed good contact with the metal electrodes.

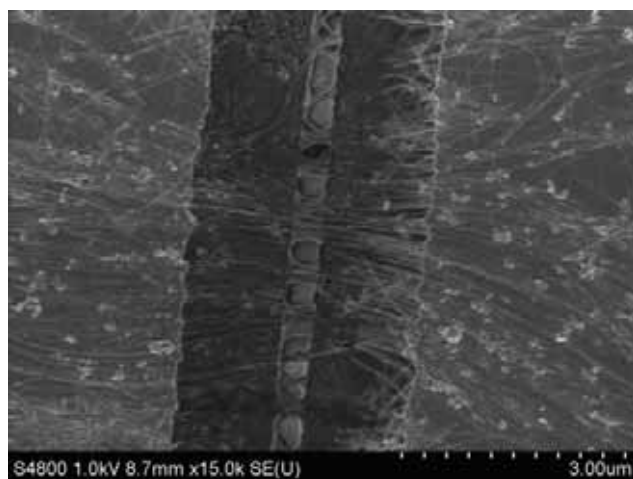


Figure 3: Nanowire film suspended over a trench.

The SEM image shows that most of the nanowires remained suspended over the trenches (Figure 3). However, in some sections, the nanowires were broken, leaving gaps in the trench. Most likely, in these areas, the nanowires were not perpendicularly stretched across the trench; as a result, there were longer suspending sections that were more susceptible to breaking during the fabrication process. Furthermore, the transferred nanowire film was not entirely uniform, resulting in many parts of the chip having no nanowires. Unfortunately, the quality and alignment of the film was a critical factor that we could not control in our experiment. As such, some film breakage occurred, leading to low current conduction.

We have not yet coated the suspended device with high- $\kappa$  because our first experiment with the non-suspending transistor showed a change from p-type to n-type behavior. Also, we still have current only in the hundreds of nA (Figure 4), not high enough to make a useful device. As such, we need to refine our process before we continue on to the high- $\kappa$  coating step.

## Conclusion and Future Works:

Our experiment in fabricating surround-gate transistors using suspended nanowire film generated interesting results that warrant further investigations.

We have confirmed through SEM images that many nanowires remained suspended over the trench after the processes. However, there are still problems with film breakage, low current, and the change in behavior from p-type to n-type following the high- $\kappa$  coating and gate metal sputtering. With a different process and higher quality film, we will be able to complete the fabrication of our suspended film transistor and hopefully obtain higher device performance.

## Acknowledgments:

I would like to thank Hongjie Dai, Qian Wang, and the Dai Group for their help in my project. Also, I would like to acknowledge Stanford University and the NSF for hosting and funding the REU research programs. Lastly, I especially appreciate Michael Deal, Jane Edwards, Maureen Baran, Marni Goldman, and the staff at the SNF for all their help during my stay at Stanford University.

## References:

- [1] Wang, DW; Wang, Q; Javey, A; Tu, R; Dai, HJ; Kim, H; McIntyre, PC; Krishnamohan, T; Saraswat, KC, "Germanium nanowire field-effect transistors with SiO<sub>2</sub> and high-kappa HfO<sub>2</sub> gate dielectrics", Appl. Phys. Lett.; SEP 22 2003; v.83, no.12, p.2432-2434.
- [2] Jien Cao, Qian Wang, Dunwei Wang, Hongjie Dai, "Suspended Carbon Nanotube Quantum Wires with Two Gates", 2005, Small, 1, 138.
- [3] Dunwei Wang, Yinglan Chang, Hongjie Dai, "Surface Chemistry and Electrical Properties of Germanium nanowires", J. Am. Chem. Soc., 126, 11602, (2004).

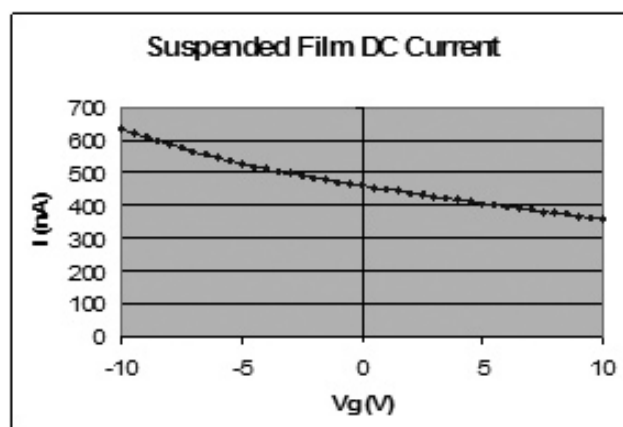


Figure 4: DC current of device with suspended film.

# The Development of a New Method to Monitor the Activity of Neuronal Networks Using Microelectronic Chips

**Aileen Dinin, Chemical and Biomedical Engineering, Carnegie Mellon University**  
**NNIN REU Site: The Penn State Nanofabrication Facility, The Pennsylvania State University**

*NNIN REU Principal Investigators: Jian Xu, Osama O. Awadelkarim,  
Engineering Science and Mechanics, The Pennsylvania State University  
Contact: adinin@andrew.cmu.edu, jianxu@psu.edu, ooaesm@engr.psu.edu*

## Abstract:

It has already been proven that microelectronic chips can monitor neuronal networks in a planar configuration, that is, with only one surface of the cell contacting the electrodes. The focus of this paper is the fabrication and testing of a device that would allow for three-dimensional contact between the neuronal cells and the electrodes, yielding a stronger signal from the cells.

First, as a feasibility test, wells were etched in silicon and glass substrates and cell growth was tested. Once cell growth was deemed sufficient, process details were determined from a rough outline and then the chips were produced.

After several trials, a chip was constructed with gold electrodes and contact plates and a single large well for the cells, which could contain both cells and medium. Wells were constructed using benzocyclobutene, a spin-on dielectric, and were approximately 5  $\mu\text{m}$  deep. The action potentials of the neuronal cells will be monitored with the fabricated chips of microelectrode arrays.

## Introduction:

Researchers at the Max Planck Institute for Biochemistry have created microelectronic devices that provide an interface between electrodes and small cultured neuronal networks. These devices have also

been used to interface with cultured brain slices. Using transistors on the devices, researchers were able to record the action potentials of multiple cells simultaneously on the small networks, and record changes in potential across the brain slices.

The disadvantage of these chips is that they have a planar interface with the cell surface. This planar interface only puts one surface of the cell membrane in contact with the electrodes.

The goal of our project is to create a microelectronic chip that allows for a three-dimensional interface with the cell. The cell would be contained in a well, as in Figure 1, that would maximize contact between the chip surface and the cell membrane. We expect that this design would increase the electrical signal measured by up to two or three times.

Applications of this research are studies of neuronal network functioning. Eventually, we hope that these devices may be used to study disorders that involve abnormal neuronal network functioning, such as Alzheimer's or epilepsy.

## Experimental Procedure:

The initial stage of the project was to test the adhesion of neuronal cells on silicon and glass substrates. Square wells of a depth of 1  $\mu\text{m}$  were etched into the substrates and AtT-20 neuroendocrine cells were cultured on the surface. These cells were examined under an optical microscope and counted.

The next step was to fabricate microelectronic devices capable of registering the action potentials from the cells. Using a rough process outline and a set of masks already created (Figure 2), fabrication techniques were refined. The first step of the process was electrode formation with a liftoff technique, using 500  $\text{\AA}$  of Ti and 3000  $\text{\AA}$  of Au. After the electrodes were deposited, a plasma-enhanced chemical vapor deposition process was used to deposit 1  $\mu\text{m}$  of  $\text{SiO}_2$ , in order to protect the wires connecting the electrodes to the contact pads. The  $\text{SiO}_2$  was then patterned and dry etched with a reactive ion etching process to reveal the electrodes while retaining the insulation on the wires.

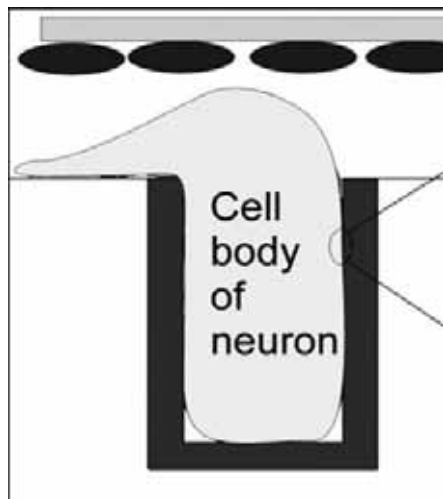


*Figure 1: The ideal cell-device interface.*



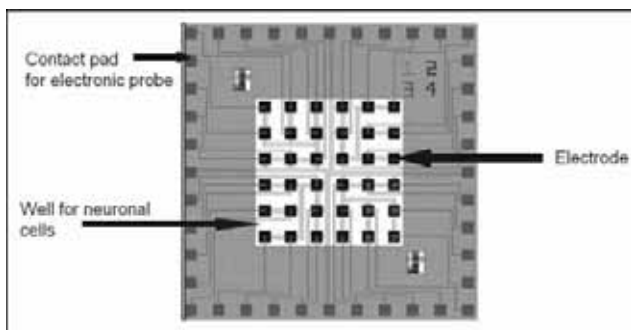


Figure 2: A diagram of the microelectronic device.

After the  $\text{SiO}_2$  etch, wells were formed using benzocyclobutene (BCB or Cyclotene), a spin-on, photosensitive polymer. The initial design called for a square well over each electrode, resulting in a six-by-six array of wells  $300\ \mu\text{m}$  on a side. However, it was determined that these wells would be suboptimal for testing, as it would be difficult to keep the surface of the chip dry while retaining enough medium to keep the cells alive. Therefore, the masks were redesigned to create a square well 4 millimeters on a side, which allowed neurons and medium to be in contact with all of the electrodes. The BCB was used to create wells  $5\ \mu\text{m}$  deep. Cells were then cultured on the surface of the chip and examined under a microscope.

### Results and Conclusions:

As this project was just started this summer, data was not obtainable in such a short time frame. However, the process was refined significantly, and specific parameters were obtained for all aspects of the process. It was demonstrated that the chips could be fabricated and that neuronal cells could be grown on them (Figure 3). Testing of the devices should begin shortly.

### Future Work:

Fabrication and testing of the chips must continue in order to gain reproducible results from the current design. In addition, chips must be designed that allow for better contact between the electrode and the cell, in order to get closer to our ideal concept of a three-dimensional electrical contact. Once the optimum design has been achieved, comparisons must be made with planar-contact type chips to confirm that the three-dimensional-contact chips strengthen the signal.

### Acknowledgments:

I'd like to thank Dr. Jian Xu and Dr. Osama Awadelkarim for giving me this great project, and the NSF and NNIN for making the opportunity possible. Also, many thanks to the PSU Nanofabrication Facility, especially John McIntosh and Guy Lavallee, without whom none of this would have happened.

### References:

- [1] Fromherz, Peter. "Semiconductor chips with ion channels, nerve cells and brain"; *Physica E*, p. 24-34, 2003.

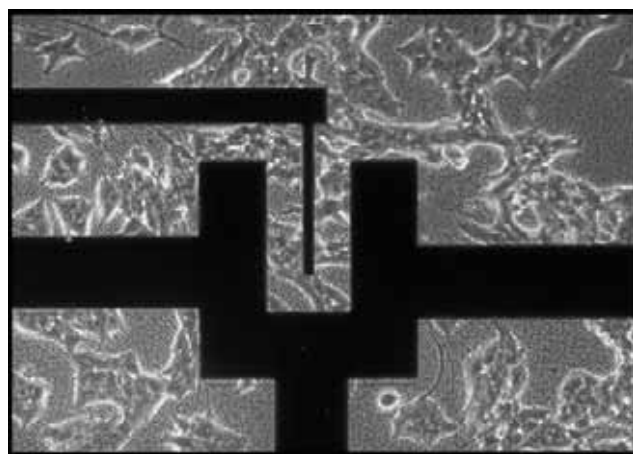


Figure 3: A picture of an electrode from the device, with neuronal cells cultured on the surface (40x).

# Polymer Process Optimization for Electrical and Optical I/O Interconnect Pillar Fabrication

**Laura Doyle, Biomedical Engineering, Johns Hopkins University**  
**NNIN REU Site: Microelectronics Research Center, Georgia Institute of Technology**

*NNIN REU Principal Investigator: Dr. Paul Kohl, Chemical Engineering, Georgia Tech*

*NNIN REU Mentor: Ate He, Chemical Engineering, Georgia Tech*

*Contact: Laura.Doyle@jhu.edu, Paul.Kohl@che.gatech.edu*

## Abstract:

Polynorbornene polymers have long been considered desirable materials for electrical and optical interconnects due to their low dielectric constants, high indices of refraction, low elastic moduli, and photodefinability.

In recent developments, polymer pillars have been coupled with metallic conductors to transmit electrical and optical signals. These more complicated structures require precisely constructed features. For optical interconnects, the sidewalls of the pillars should be smooth to reduce scattering and subsequent optical losses. For electrical applications, interior cavities should be cleanly developed down to the underlying surface to ensure reliable electrical contacts. Choosing an appropriate polymer formula is essential to obtain these results. Each formula yields different results in fabrication, so preliminary tests are necessary to determine the optimal material for each application.

Three different formulas of the polynorbornene polymer Avatrel were tested under different exposure doses, post exposure bake temperatures, and durations. The formula that developed best overall with respect to structural perpendicularity, smoothness, depth of interior development, and top surface flatness was then further tested in fabrication applications. Through these fabrication processes, it was shown that the chosen formula can be used to create smooth 130  $\mu\text{m}$  tall polymer pillars for optical uses and copper-core polymer pillars for solid electrical interconnection between a chip and a board.

## Introduction:

Norbornene-based polymers make good electrical and optical input-output interconnects due to their innate structural properties. This type of polymer has a low dielectric constant to limit crosstalk, high index of refraction for optical signal conduction [1], low elastic modulus to compensate for thermal expansion coefficient mismatch between board and die [2], and the material is photodefinable for ease of fabrication.

An effective electrical-optical interconnect should have a cleanly developed interior to allow for solid electrical connection and smooth exterior surfaces to

reduce optical losses. Such development characteristics vary among different polymer formulas. For best results, polymer formulas should undergo preliminary testing to determine which formula is best for which application. Here high aspect ratio polymer pillar-like structures are used to provide a physical optical path or waveguide between the chip and the board, while metal-core polymer pillar-like structures are used to provide electrical interconnection.

## Materials and Methods:

The experiment described here tested the structural development of three polymer formulas. Polymer pillar processing began with a 36  $\mu\text{m}$  film of polymer spun onto the wafer. The samples then underwent a 10 minute soft bake on a 100°C hotplate. Wafers were cleaved into standardized rectangles for better mask contact. Subsequent UV exposure doses were 150 or 350mJ/cm<sup>2</sup>. The post exposure bake condition was also subject to variable temperature (95°C or 105°C) and duration (10 or 20 minutes). Finally, development occurred in a beaker of limonene floating in an ultrasonic developer for a duration of 90 seconds for all samples, followed by a 30 second immersion bath in isopropyl alcohol. A reduced factorial experimental design governed the conditions of each trial.

In order to obtain photographs of the samples on a scanning electron microscope (SEM), the samples had to be diced into one by two centimeter rectangles, mounted perpendicularly, and coated with gold. It was desirable that cleavage planes bisect structures with interior cavities for the purpose of demonstrating the depth and clarity of development.

To determine whether pillar-type waveguides are possible with that material, 130  $\mu\text{m}$  pillars were fabricated and evaluated using SEM imaging. To achieve a 130  $\mu\text{m}$  film, a 50  $\mu\text{m}$  layer was spun and soft baked for 8 minutes before another layer was spun at the same speed. The wafer was then soft baked for 45 minutes.

Copper-filled coaxial pillars were also fabricated. A silicon wafer was layered with first copper, then

silicon dioxide. Using photoresist, the silicon dioxide was etched away to leave exposed circles of copper. Polymer was spun onto the wafer and patterned to form hollow-core pillars centered above the copper circles. A copper core was then grown from these circles using electroplating (electrodeposition). The pillars were bonded by hand to a copper-plated wafer using solder.

### Results:

The criteria used to evaluate the development of each formula were side smoothness, perpendicularity, top flatness, and interior clarity. Evaluation was based on a standardized rubric describing the characteristics associated with each numerical score in each category. Most OEM-41 samples showed good depth of development and perpendicularity, but sidewalls had extensive vertical ridging. OEM-61 samples had smooth sides, but interior cavities were often occupied by “buttress” filaments spanning the gap between walls. A few samples also exhibited structural warping not attributed to development or cleavage artifacts. All precipitated OEM-61 samples exhibited poor perpendicularity and interior clarity.

The surface-normal waveguide pillars had excellent perpendicularity. Some bending at the edge of the sample was attributed to wafer cleavage. Sidewalls showed smooth exterior surfaces, but top flatness seemed to be reduced with increased height, possibly due to unevenness in the thick film.

The copper-core polymer pillars were successfully bonded, from visual inspection, to a copper surface using solder.

### Conclusion:

Polynorbornenes like Avatrel are becoming an important material in microsystems packaging owing to their physical properties. Due to variances in formula development characteristics, preliminary experiments were conducted on three formulas of Avatrel to choose the best for different packaging applications. The OEM-41 formula demonstrated characteristics best suited for electrical applications while the OEM-61 is best suited for optical uses. Fabrication processes were

then developed for optical waveguide pillars and the bonding between die and substrate using copper-filled coaxial pillars.

### Acknowledgements:

Thanks to Dr. Kohl, Ate He, Dr. Bakir, Ed Elce and Dr. Meindl for their knowledge and guidance in this research.

### References:

- [1] Y. Bai, et al, “Photosensitive polynorbornene based dielectric. I. Structure-property relationships,” *Journal of Applied Polymer Science*, vol 91, pp. 3023-3030, 2004.
- [2] M. Bakir, et al, “Sea of Polymer Pillars: Compliant Wafer-Level Electrical-Optical Chip I/O Interconnections,” *IEEE Photonics Technology Letters*, vol. 15, pp. 1567-1569, Nov. 2003.



Figure 1: OEM-41 result.



Figure 2: OEM-61 result.

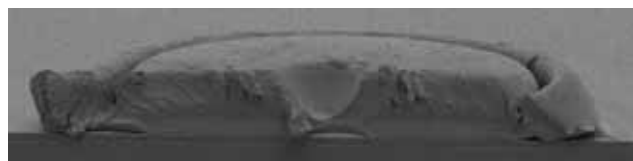


Figure 3: OEM-61 precipitated result.

# Material Characterization for Optimizing Passivation of Type-II InAs/GaSb Superlattice Infrared Photodetectors

**Nicole Escudé, Physical Science - Chemistry, Biola University**  
**NNIN REU Site: Nanoscience @ UNM, University of New Mexico**

*NNIN REU Principal Investigator: Sanjay Krishna, Electrical Engineering, University of New Mexico*

*NNIN REU Mentor: Elena Plis, Electrical Engineering, University of New Mexico*

*Contact: Nicole.c.escude@biola.edu, skrishna@chtm.unm.edu*

## Abstract:

High-temperature superlattice (SL) infrared (IR) photo-detectors have applications in thermal imaging. However, surface states on the superlattice trap charge carriers and greatly decrease detector performance. Passivating the photodetectors by sulfidization has been shown to reduce surface states, thus improving device performance. Towards optimizing a passivation method for III-V SLs, material characterization was performed on one unpassivated detector. Its performance was determined based on the analysis of basic detector figures of merit extracted from spectral response, dark-current, and total current measurements. Combining this data with further data could be used to: (1) compare the efficacy of aqueous and non-aqueous sulfur-based passivation solutions, and (2) find the most effective recipe and application time for a chosen solution on type-II, III-V SL photodetectors.

## Introduction:

When layers of p- and n-type material are grown below and above the SL region of a strained-layer superlattice (SLS), a photovoltaic diode that responds to IR radiation is produced [1]. Research on SLSs of two alternating III-V semiconductor binaries for use in IR detectors and lasers continues.

Uncooled IR detectors have many potential applications in thermal imaging, including optical remote sensing, night-

vision, fire control, etc. Type-II broken band gap III-V SLS IR photodetectors have several advantages over competing IR detectors, including an easily tailored bandgap, better spatial uniformity, and high operation temperatures [2].

Research in SLS IR detector fabrication must address the problem of surface states (localized electronic states within the forbidden energy region between the semiconductor valence and conduction bands [3]). Surface states trap charge carriers, increasing detector dark-current and decreasing photocurrent. Performing surface passivation can improve detector performance, and sulfidization facilitates both chemical and electronic passivation by protecting the surface from oxidizing and decreasing surface state density.

Outlined here is an experimental/analytical procedure by which the effectiveness of aqueous and non-aqueous sulfur-based passivation solutions can be compared, and an optimized passivation scheme for type-II InAs/GaSb SL photodetectors reached.

## Experimentation:

The sample chip, L5-68-diced, held two InAs/GaSb-based, individually diced unpassivated SL photodetectors. The photodetector structure is shown in Figure 1, with n-contact Ti/Au 500Å/3000Å, p-contact Ti/Pt/Au 500Å/500Å/3000Å, and aperture diameter 200 µm.

The sample was loaded into the cryostat sample chamber of a Janis closed cycle refrigerator system. Checking the connections on the device contacts using a Semiconductor Parameter Analyzer (set up to plot current flowing through the device over a range of applied biases) revealed that only

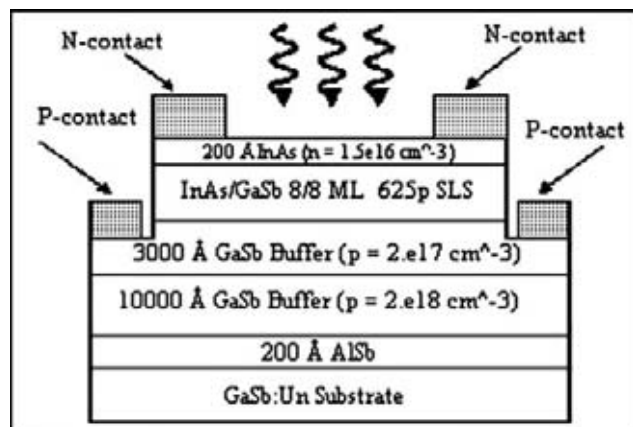


Figure 1: L5-68-Diced sample detector composition.

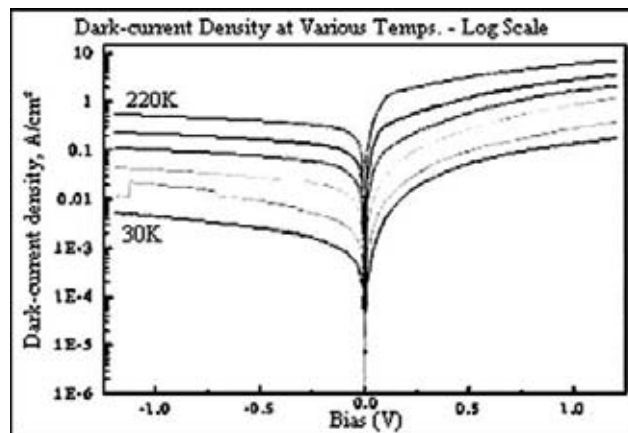


Figure 2: Dark-current density.



one of the detectors was functioning. Thus, the inoperative detector was disregarded for all remaining measurements.

For spectral response measurements, the sample chamber was sealed and cooled to 90.000 Kelvin (K). Measurements (with the background spectrum subtracted) were taken using Thermo Electron Corporation's OMNIC software. Sample temperature was increased gradually from 90K until a nontrivial detector response was no longer observable. At each temperature, measurements were taken for  $\pm 0.6000\text{V}$  applied bias.

The software was then set up to measure current through the detector. Total current was measured with the blackbody light source incident to the detector, and dark-current with all light blocked from the detector. Temperature was varied from 30 to 300K, and at each temperature voltage bias was varied in 0.01V increments from 1.2V to  $-1.2\text{V}$ .

### Results:

Detector spectral response was best at lower temperatures, since that is where thermal carrier generation was minimal and measured current intensity was high. Still, a nontrivial response was detected for up to 280K.

Dark-current density (measured dark-current divided by the device's active optical area) is displayed in Figure 2. At 90K and  $-1.0\text{V}$  of bias, dark-current density for this device was found to be approximately  $10^{-2}\text{ A/cm}^2$ , indicating high (but typical) leakage current.

Subtracting dark-current data from measured total current yields photocurrent values. However, at lower temperatures these values were unreasonable, and it was concluded that the total current measurements were erroneous. Plans were made to re-measure total current, but all further use of the cryostat system was prevented, as compressor maintenance was required. Detector figures of merit that depend on photocurrent (background limited infrared photon temperature and specific detectivity) are therefore unreliable, and thus not presented.

Detector responsivity, shown in Figure 3, is the current output produced in response to one watt of input optical radiation from the blackbody source [4].

The dynamic impedance-area product ( $R_o A$ ) at zero bias is shown in Figure 4 for temperatures from 30-240K. At 50K, a poor data point was obtained and corrected for.

### Conclusions:

These procedures and characterizations outline a good starting point for further experimentation and investigation into the benefits of passivation, and discovering which passivation methods are most effective. Accordingly, the intended next step in this experiment was to passivate the sample, recalculate all figures of merit, and compare the results of the passivated detector with results obtained prior to passivation. Multiple detectors, passivated and unpassivated, could then be tested and compared in a similar fashion. Also, various types of passivation could be evaluated. Here, the intended focus was on liquid sulfidization, contrasting aqueous and non-aqueous passivating solutions. After discovering which of these two

sulfidization methods most improved type-II InAs/GaSb photodetector performance, solution concentration and application time could be fine-tuned.

Moreover, information obtained from such experiments might be applied to other SLS structures. For InAs/(GaIn)Sb photodetectors, will the same passivation scheme work? If not, what changes must be made, and why? These and other related questions could be explored.

### Acknowledgements:

Thanks to NNIN, the University of New Mexico and the Center For High Technology Materials for facilitating this investigation, and Dr. Sanjay Krishna and Elena Plis for all their help.

### References:

- [1] C.R. Nave, HyperPhysics (2005), <http://hyperphysics.phy-astr.gsu.edu/hbase/hframe.html>.
- [2] A. Rogalski, P. Martyniuk, Infrared Phys. & Technol. (2005). [Online]
- [3] J.P. McKelvey, Solid State and Semiconductor Physics, Harper and Row (1966) 485-6.
- [4] E.L. Dereniak, G. D. Boreman, Infrared Detectors and Systems, Wiley Series in Pure and Applied Optics (1996).

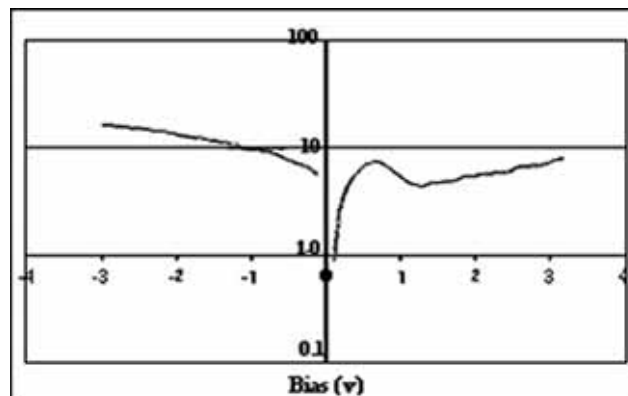
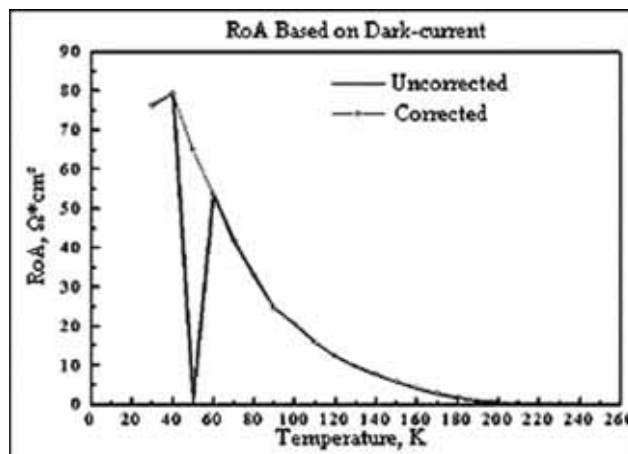


Figure 3, above: Responsivity.

Figure 4, below:  $R_o A$ -product, zero bias.



# Properties and Performance of Molecular Glass Photoresists

**Nkemdilim Ezeife, Chemistry, Temple University**

**NNIN REU Site: Cornell NanoScale Science & Technology Facility, Cornell University**

*NNIN REU Principal Investigator: Prof. Christopher Ober, Materials Science & Engineering, Cornell University*

*NNIN REU Mentor: Nelson Felix & Anuja De Silva, Chemical Engineering, Cornell University*

*Contact: tua09042@temple.edu, cober@ccmr.cornell.edu*

## Abstract:

Molecular glasses are small molecules that have the ability to form amorphous films. They are promising candidates as low line-edge roughness resists because of their small size compared to conventional polymeric photoresists. This is especially important as the critical dimensions of photoresist features become even smaller.

The objectives of this project are to find the right processing conditions and to evaluate their plasma etch resistance. Optimal exposure and development times were also found for these molecular glass resists. Profilometer measurements of resist film thickness were used in order to establish etch rates as well as post-development film thicknesses. 10x i-line stepper patterning was also performed to produce patterns for observation using SEM.

## Introduction:

As smaller feature sizes are required for progress in the semiconductor industry and nanotechnology in general, new processes need to be developed in order to support these changes. The types of photoresist used are an integral part of the changes that occur with reduction of feature size.

Molecular glasses have many desirable properties. Their relatively small molecular size (1-2 nm), low crystallization tendency and exceptional uniformity give these glasses the ability to be incorporated into new photoresists for smaller features.

Molecular glasses are present in two varieties: positive tone and negative tone. Negative tone molecular glass resists require the use of a crosslinker molecule (Powderlink®) in order to create a polymer-like matrix upon exposure. (See Figure 1.)

Positive-tone molecular glasses work by having their tetrabutoxycarbonyl (tBOC) groups cleaved off when photoacid generator (PAG) replaces them with hydroxyl groups which can be dissolved in tetramethyl ammonium hydride (TMAH).

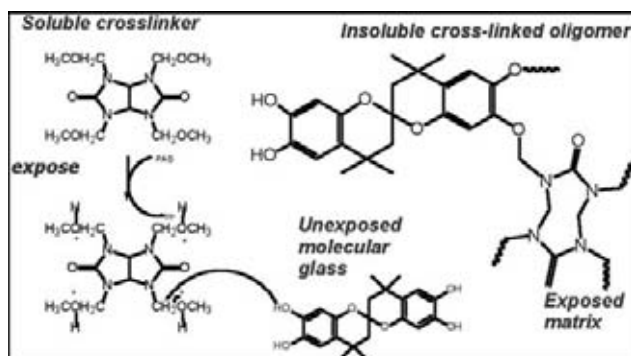


Figure 1: Schematic of a negative-tone molecular glass photoresist being exposed.

## Experimental Procedure:

To prepare molecular glasses for dosage experiments, 10 percent (by mass) molecular glass and crosslinker (if necessary) were dissolved in propylene glycol methyl ether acetate (PGMEA) solvent. 5 mg photoacid generator (PAG) was then used per 100 mg of molecular glass. The resist was spun at 2000 rpm for 30 seconds. Positive-tone molecular glasses were spun onto HMDS primed silicon wafers whereas the negative-tone glasses were spun onto bare silicon. Exposure times of 0, 5, 20, 50 and 90 seconds were used on the 1.2 mW/cm<sup>2</sup> 253 nm UV lamp with other times added as deemed necessary. Post-spin bake and post-exposure bake times and temperatures were held constant throughout the experiments.

Each molecular glass was subjected to an optimal development concentration test that involved varying concentrations and dilutions of 0.26N TMAH in H<sub>2</sub>O. Film thickness measurements were subsequently taken by profilometer in order to establish contrast curves for the various molecular glass resists.

CHF<sub>3</sub>/O<sub>2</sub> etching of the molecular glasses was done using polyhydroxystyrene, a polymer, as a standard. This was accomplished in 30s increments

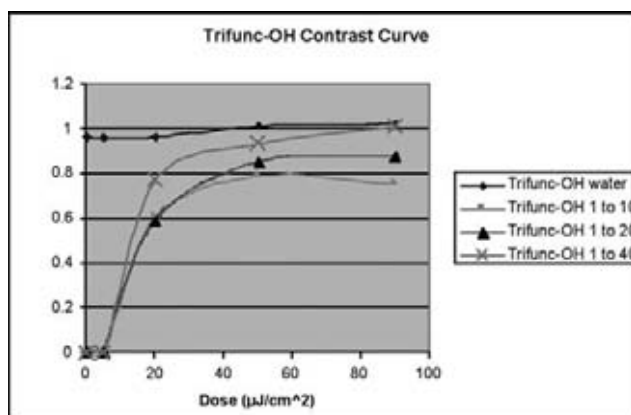


Figure 2: Negative-tone molecular glass contrast curve with various development concentrations.

with intermittent film thickness measurements until suitable etch rates could be determined for each of the molecular glasses after several minutes of etching.

### Results and Conclusions:

The contrast curve of the particular molecular glass in Figure 2 demonstrates that a dilute solution of TMAH coupled with a UV light dose around  $90\mu\text{J}/\text{cm}^2$  provides optimal exposure and development conditions for this particular resist. Contrast curves were also developed for the other molecular glasses that had undergone experimentation.

The plasma etch rates in Figure 3 obtained for the molecular glasses were in the range of 20 to 30 nm per minute, which is a higher rate than desired. One particularly promising molecular glass demonstrated a lower etch rate around 10 nm/min.

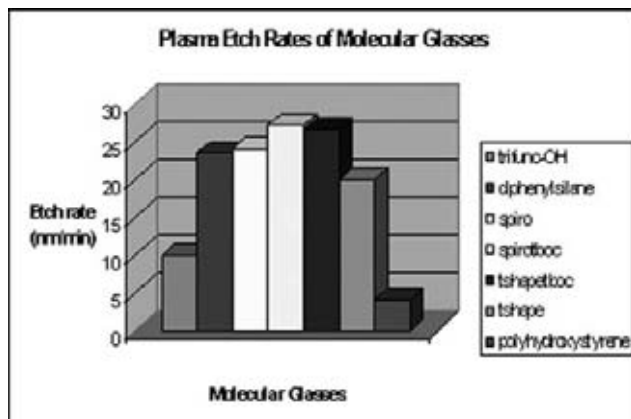


Figure 3:  $\text{CHF}_3/\text{O}_2$  etch rates of molecular glasses against a polyhydroxystyrene standard.

SEM imaging of another resist (shown in Figure 4) was done after patterning on a 10x i-line (365 nm UV) stepper. This particular molecular glass resist has well-defined features and may very well be a viable alternative to polymeric resists. Further testing will need to be done on this resist in order to confirm this.

### Future Work:

There is plenty of future work that can be done to further the characterization of these molecular glasses. Atomic force microscopy for line edge roughness, ellipsometer tests for refractive index and measurements for the dielectric constant of these films still need to be done to confirm the viability of these films in industrial applications. Additional patterning and etch work can be done as well as performing experimental runs on other molecular glasses.

### Acknowledgments:

I would like to thank the following people and organizations for making my research experience a possibility: Prof. Christopher Ober, Nelson Felix, Anuja De Silva, Ms. Melanie-Claire Mallison, Dr. Lynn Rathbun, CNF staff and NSF. Special thanks to the Intel Foundation for funding this project. I enjoyed my research time at the CNF during the summer.



Figure 4: SEM of resolution lines taken with 10x i-line stepper.

## Model Micro-Channels for the Study of Aerobic, Nano-Porous Biocatalytic Latex Coatings

**Johangel M. Figueroa, Industrial Biotechnology, University of Puerto Rico, Mayagüez**  
**NNIN REU Site: Minnesota Nanotechnology Cluster, University of Minnesota**

*NNIN REU Principal Investigator: Dr. Michael C. Flickinger, Biochemistry, Molecular Biology, and Biophysics, Biotechnology Institute, University of Minnesota, Twin Cities*  
*NNIN REU Mentor: Dr. M. Fidaleo, Department of Food Science and Technology, University of Tuscia, Italy*  
*Contact: johangel@hotmail.com, mflick@cbs.umn.edu*

### Abstract:

Embedding bacteria in a nano-porous, self-assembled polymer coating would create highly reactive biocatalysts useful in micro-channel reactors. Our model system is an  $\sim 65\ \mu\text{m}$  thick nano-porous acrylate/vinyl acetate latex coating containing the bacterium *Gluconobacter oxydans*. *G. oxydans* is a rod shaped obligate aerobe, which can carry out many oxidations, such as D-sorbitol to L-sorbose, using membrane bound dehydrogenases. This oxidation is non-growth associated, oxygen dependant and can be measured using HPLC.

Bioconversion of D-sorbitol to L-sorbose was initially studied using  $2.5\ \text{cm}^2$  latex coatings in a non-growth media. A high reaction rate per surface area of coating was observed. Model micro-reactor channels ( $\sim 500\ \mu\text{m}$  to  $1000\ \mu\text{m}$  deep) where designed. Microscopic images of a nano-porous coating in  $\sim 450\ \mu\text{m}$  wide channels where obtained.

A macro-channel, 10 mm wide, in which coated strips of *G. oxydans* can be tested was developed in order to measure the reaction rates accurately with HPLC. The reaction rates obtained in this larger channel, with a three-phase bubbly slug flow, will help us predict biocatalytic activity of *G. oxydans* in  $< 500\ \mu\text{m}$  micro-channels, and aid us in the engineering of nano-porous biocatalytic coatings for micro-channel bioreactors.

### Introduction:

The use of living, catalytically active microorganisms as industrial biocatalyst highly depends on the use of a suitable matrix for immobilization. An appropriate immobilization matrix must enhance catalytic activity, stability and protect from deactivation and degradation of the cells. The use of multilayer coatings and printing technology provides a suitable matrix for embedding of bacteria in a thin, adhesive and nano-porous latex biocatalytic coating. The nano-porous structure is generated by latex polymer particle coalescence and can contain 50% (v/v) of non-growing metabolically active microorganisms. It has recently been demonstrated that the aerobic bacteria *G. oxydans* can be entrapped in this thin nano-porous latex coating and carry out the bioconversion of D-sorbitol to L-sorbose

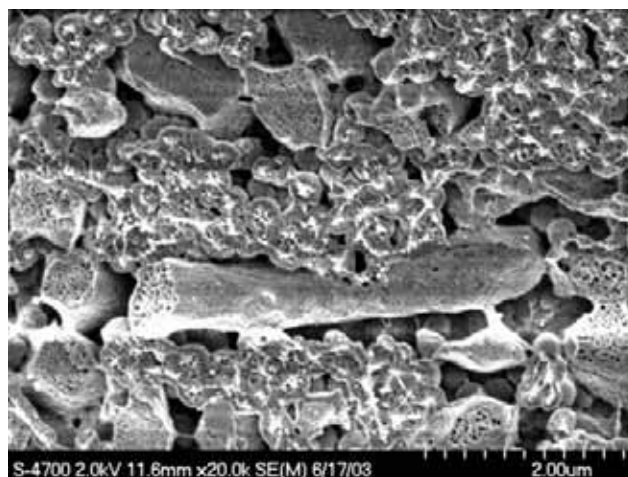


Figure 1: Freeze fracture CRYO-FESEM of nano-porous structure and *G. Oxydans* fractured cells.

with high efficiency [1]. Freeze fracture CRYO-FESEM images of the previously mentioned coating have been obtained (Figure 1) [1].

The main objective of this project was to create model micro-channels for the study of *G. oxydans* biocatalytic latex coating. Biocatalytic micro-channel reactors can serve as a model for process intensification in the biotechnological industry. Process intensification is a very popular concept, which refers to the miniaturization and integration of many systems into one. This concept brought us computer micro-chips and, in the biotechnological industry, allows for processes to run at higher temperatures, with shorter residence time, with faster kinetics and with smaller reaction volumes, all these providing for a more efficient and cost-effective process.

### Experimental Procedure:

We initially wanted to test the bioconversion capability of *G. oxydans* inside the latex coating. To do so we grew a fresh culture of *G. oxydans* cells in Petri dishes for  $\sim 72$  hours until isolated colonies could be detected. We later transferred one colony of these cells to SYE growth medium and incubated it at  $30^\circ\text{C}$  and 90 rpm until an  $\text{OD}_{600} \sim 1.5$  was obtained. These cells



where later centrifuged and 2.5 cm<sup>2</sup> coated strips were created using the method developed by Lyngberg et. al [2]. These strips were placed in 60 mm x 15 mm Petri dishes containing the sorbitol rich SPP medium and incubated at 30°C for around 150 hours. Samples were taken every 24 hours to measure the accumulation of sorbose using an analytical HPLC machine.

After the viability of the cells inside the biocatalytic latex coating was determined, we proceeded to create a ~ 450 μm wide micro-channel by stacking a series of ~125 μm polyester sheets and separating them (in order to create the channel) with a previously measured metal spacer. These channels were coated and imaged through phase microscopy (Figure 2).

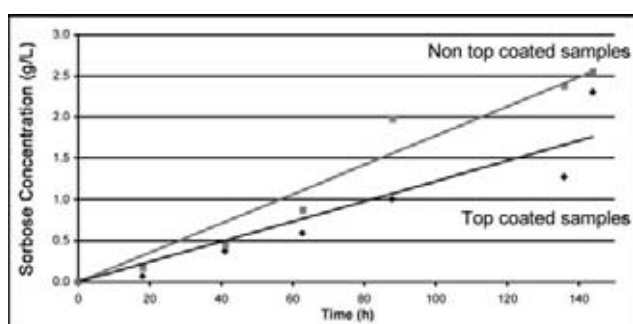


Figure 2: Phase microscopy of uncoated micro-channel.

In order to model the behavior of the ~ 450 μm micro-channels, a macro-channel (10 mm wide) where coated strips of *G. oxydans* can be placed was created. Inside these novel macro-channel 7.5 cm<sup>2</sup> coated strips were placed, and a three phase flow was achieved by the assembly of two peristaltic pumps (air and media) connected simultaneously to the channel inlet. SPP at ~ 27°C was continuously flowed through the channel and the outlet liquid was collected in a flask kept at 4°C. This product was also measured for accumulation of sorbose with and analytical HPLC.

### Results and Conclusions:

Top-coated and non-top-coated latex strips were prepared for the bioconversion studies in Petri plates. As observed in Figure 3, bioconversion or accumulation of sorbose increased linearly with time, therefore showing that our strip can remain catalytically active for more than 150 hours. These encouraging results led to the creation of micro-channels for bioconversion studies. Microscopic images of these channels showed a nano-porous latex coating inside the novel channel. No measurable bioconversion was obtained with these

channels. In the macro-channel, created to model the micro-channel, accumulation of sorbose was recorded with time. Despite this, more experiments need to be carried out with these macro-channels before results can be presented.

These results serve as an example to the great suitability of using nano-porous coating techniques as an immobilization matrix. Novel micro- and macro-channels where these coating technology for aerobic bacteria can be effectively tested where efficiently developed and may serve in the near future as great examples and models for process intensification purposes.

### Acknowledgements:

Thank You: To Dr. M.C. Flickinger for providing me with such an invaluable opportunity; To all the hard workers in Dr. Flickinger's laboratory, especially Dr. Marcello Fidaleo for his knowledge and support; To all the great REU interns at the University of Minnesota; To the NNIN coordinators at Cornell and the University of Minnesota.

### References:

- [1] Fidaleo, M. et. al Determination of the rate of oxidation of D-sorbitol to L-sorbose by thin bi-layer latex coatings of *Gluconobacter Oxydans* in microbioreactors.
- [2] Lyngberg, O.K. et al. *Biotechnol. Bioeng.* 62: 44-55 (1999).

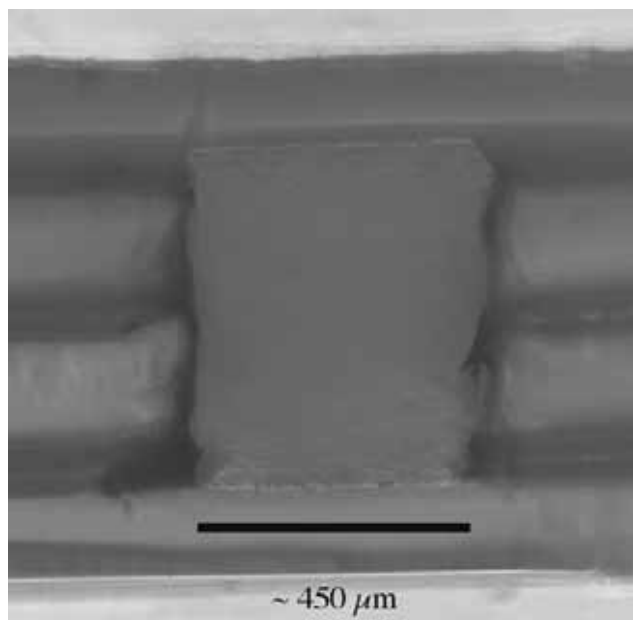


Figure 3 : Accumulation of sorbose with time for 2.5 cm<sup>2</sup> top coated and non-top coated strips in Petri dishes bioreactors.

# Electrical, Optical, and Thermofluidic Wafer-Level Chip I/O Interconnects Enabled by Nano/Microimprint Lithography

Wand Gan, Biochemistry, University of Florida

NNIN REU Site: Microelectronics Research Center, Georgia Institute of Technology

NNIN REU Principal Investigator: Kevin Martin, Electrical & Computer Engr, Georgia Institute of Technology

NNIN REU Mentor: Muhannad Bakir, Electrical & Computer Engineering, Georgia Institute of Technology

Contact: wygan@ufl.edu, kevin.martin@mirc.gatech.edu

## Abstract:

The increasing demands of silicon microprocessor technology on current delivery ( $>400\text{A}$ ), chip input/output (I/O) bandwidth ( $>50\text{ Tb/s}$ ), and heat removal ( $200\text{W/cm}^2$ ), have affected a need for the development of compatible electrical, optical and thermofluidic chip I/O interconnections (or multimodal I/O).

The goal of this project is to develop low cost wafer-level batch fabrication techniques for multimodal I/O interconnections using nano/microimprint lithography technology. The fabrication of these structures involves spin coating and soft baking a thick, photodefinable polymer film, subsequently transforming the surface topology of the film using nano/microimprinting, and finally UV irradiation through a patterned mask, followed by hard baking and spray developing. General fabrication techniques for nano/microimprinting have been developed, both in template fabrication, with features as deep as  $25\mu\text{m}$ , and in demolding, for which various anti-adhesion layers have been tested. We have successfully produced the following unique interconnect structures: (1) surface-normal optical waveguides terminating in mirrored tips to be used as dual-mode pins, transmitting electrical and optical signals simultaneously, (2) board level, funnel-shaped sockets to hold and align dual-mode polymer pins, and (3) thermofluidic back-side heat sinks compatible with dual-mode pins. The development of these processes has also introduced the possibility of using nano/microimprint lithography in further applications.

## Introduction:

As silicon microprocessor technology continues to advance according to Moore's Law, the performance of these high performance chips become limited by interconnects performing communication functions. There are three system level limiting interconnect technologies to chip performance: (1) current deliver ( $>400\text{A}$ ), heat removal ( $>100\text{W/cm}^2$ ), and chip input/output (I/O) bandwidth ( $>50\text{Tb/s}$ ). These factors have incited a need for the development of electrical, optical, and thermofluidic chip I/O interconnects to enable each of the above listed challenges, respectively.

The goal of the project is to develop wafer-level batch fabricated electrical and optical chip I/O interconnections and methods of attaching these to the board. The strategy

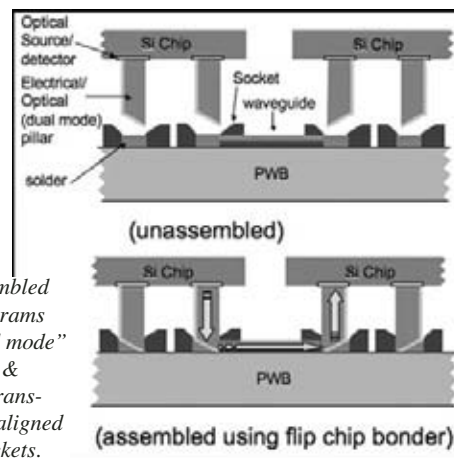


Figure 1: Unassembled & assembled diagrams for slant tip "dual mode" pillars for optical & electrical signal transmission held and aligned by board level sockets.

for achieving this was the fabrication of an array of slant tip pillars which will function as both electrical and optical means of signal transmission between chips, described as a Sea of Polymer Pillars (SoPP) in previous research [1]. These pillars will be held in place on the printed wiring board by board-level funnel shaped sockets. A schematic of this can be seen in Figure 1. Imprinting would be ideal for this process as it would allow the batch fabrication of these interconnect structures, allowing for patterning submicron features using easy processing [2] as a low cost, high throughput alternative to lithography [3].

## Fabrication:

### A. Template Fabrication:

The first set of fabrication processes created templates to be used during imprinting. This was done by spinning positive resist on a  $\text{SiO}_2$  coated silicon wafer, soft baking at  $100^\circ\text{C}$  for 2 minutes, then patterning using a mask. The wafer was then developed, and the  $\text{SiO}_2$  was etched using BOE, and the silicon was subsequently etched using TMAH. The sample to be imprinted was prepared by spinning a layer of Avatrel 2000P polymer onto a  $\text{SiO}_2$  or  $\text{SiN}$  coated substrate, at varying thicknesses depending on the desired height of the structure, then soft baked at  $100^\circ\text{C}$ , then at  $125^\circ\text{C}$ . Following the fabrication, the template is coated with a layer of trifluoropropyldimethylchlorosilane (TFS), a low surface tension coating for anti-adhesion purposes.

### B. Imprinting Process and Interconnect Fabrication:

A nanoimprint tool manufactured by Obducat was used to compress, and subsequently demold, the template from the

polymer coated substrate. Upon separation, the surface of the polymer is imprinted with the inverse template pattern.

Pillars were fabricated by imprinting a 100  $\mu\text{m}$  thick polymer with a channel template, UV exposing the imprinted polymer through a mask, and finally developing and curing to create an array of pillars with patterned tips. The pillars were then metal coated. To fabricate the sockets with which to hold these pillars, a 12  $\mu\text{m}$  layer of polymer was imprinted with a template consisting of an array of 5  $\mu\text{m}$  tall cylindrical structures. The sample was then aligned and UV exposed through a mask, and developed and cured.

During the course of this project, it was discovered that fluidic channels would be fabricated using similar methods, and could be integrated directly on the backside of the chip. To make these channels, a thick polymer layer was spun and imprinted using a channel template. The imprinted sample was then metal coated, then soldered to a blank silicon wafer to create polymer based microfluidic channels.

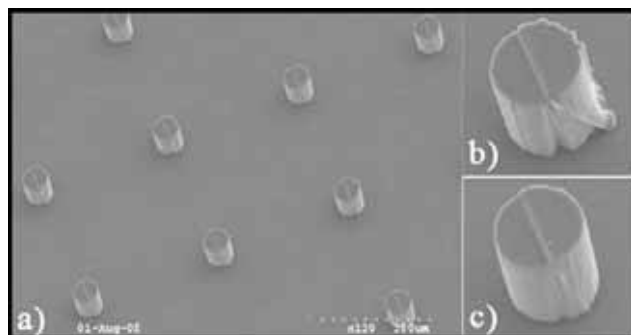


Figure 2: a) Array of slant tip pillars; b) Pillar with un-even UV exposure; c) Pillar UV exposed evenly by immersing in water.

### Results and Conclusions:

Arrays of 80  $\mu\text{m}$  tall pillars were fabricated successfully, as seen in Figure 2a. One problem encountered during fabrication was the uneven UV exposure due to the imprinted slant, which provided a surface for refraction of light, and resulted in exposure of polymer beyond the area of the pillar. Because the imprinted slant was at an angle of  $54.7^\circ$ , according to Snell's Law,  $n_1 \sin \theta_1 = n_2 \sin \theta_2$ , incoming UV light would be refracted at an angle of  $33.0^\circ$  from the normal. The result was pillars with extra polymer "tails" (Figure 2b). This issue was successfully resolved by immersing the imprinted polymer surface in water during UV exposure, to provide a surface with a uniform index of refraction (Figure 2c).

Optical transmission measurements were then made on a metallized pillar array constructed on a glass substrate by illuminating the backside of the substrate and recording images using a CCD camera. As seen in Figure 3, the optical transmission in the area of the slant was very low, indicating the ability to use these pillars for optical purposes.

Sockets were fabricated (Figure 4), with a funnel-like shape created by imprinting. These sockets will greatly simplify pillar-to-board mechanical alignment, and are designed to self correct for any misalignment, solving what

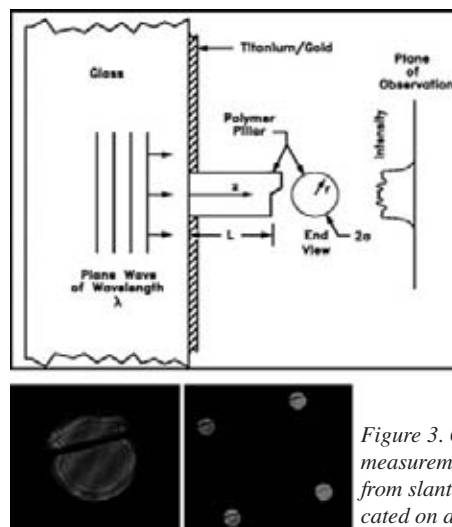


Figure 3. Optical transmission measurement setup & results from slant tip pillars fabricated on a glass substrate.

the ITRS 2005 calls a key issue in assembly. Preliminary results were achieved for the polymer based microfluidic channels. The development of these processes has had a broad impact by introducing the possibility of using nano/microimprint lithography in a number of applications. For example, the unique fabrication process described above was used to fabricate waveguides terminated with mirrors in another REU project [4].

In summary, this is the first demonstration of wafer-level batch fabrication of electrical, optical and thermofluidic I/O interconnects. The fabrication of the three structures listed above will help to address issues of power delivery, heat removal, as well as high chip input/output bandwidth. Future work should include characterization and measurements of these structures.

### Acknowledgements:

I would like to thank Muhannad S. Bakir, James Meindl, Kevin Martin, Oluwafemi Ogunsola, and Jennifer Tatham for all their contributions and guidance. I would also like to acknowledge the MiRC cleanroom staff, as well as the Georgia Institute of Technology.

### References:

- [1] M. Bakir et al., IEEE Trans. Electron Dev., vol. 51, no. 7, pp. 1069-1077, 2004.
- [2] Chou, S. Y. et al. 1997. J. Vac. Sci. Technol. B 15 2897.
- [3] Guo, L. J. 2004. J. Phys. D: Appl. Phys. 37 R123-R141.
- [4] Carson, A., 2005 NNIN REU Research Accomplish., pgs 10-11.

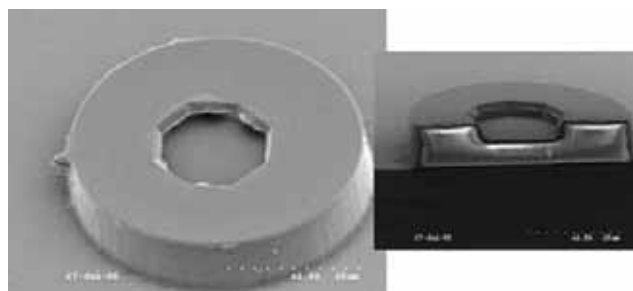


Figure 4. Funnel shaped socket structure and cross section (inset) with inner slope formed by imprinting.

## Hydrogen Passivation of Photodiodes

**Niusha E. Gutierrez, Electrical Engineering, Florida Atlantic University**  
**NNIN REU Site: Microelectronics Research Center, University of Texas at Austin**

*NNIN REU Principal Investigator: Archie L. Holmes, Jr., Electrical Engineering, University of Texas, Austin*

*NNIN REU Mentor: Jeff Hurst, Electrical Engineering, University of Texas, Austin*

*Contact: gastatiempo@yahoo.com, holmes@ece.utexas.edu*

### Abstract:

The objective of this project was to investigate the effects that hydrogen passivation has on the dark current of p-i-n InGaAs/InP photodiodes. The p-i-n InGaAs/InP photodiodes were grown using Molecular Beam Epitaxy (MBE); their I-V characteristics at room temperature were obtained using a micromanipulator and a HP 4156B Semiconductor Parameter Analyzer.

Our results show that the dark current can be reduced by an average factor of 1.2 under optimized conditions.

### Introduction:

Photodiodes are two terminal devices designed to respond to photon absorption. One of the important aspects of these devices is their bandgap, which determines the wavelength of the absorbed photon. The smaller the band-gap is, the longer wavelength it is able to detect.

In the MBE group at The University of Texas at Austin, photodiodes are being pursued for use in mid-infrared (MWIR) detection and single photon counting. An important shared aspect of devices for these applications is that they both need a low dark current.

When a bias is applied to a photodetector, a current is generated, the current can be dark current (output current under no radiant power/background) or photocurrent (output current under radiant power). The photocurrent is directly related to the number of photons absorbed. Thus a low dark current is needed to detect a small number of incoming photons. Because of properties in the semiconductor, traps are created in the semiconductor. The more traps there are, the higher the dark current is, regardless of the band-gap.

The main focus of the project, involved hydrogen passivation of the samples; that is, exposing the photodiode to atomic hydrogen (created via a H<sub>2</sub> plasma) to passivate the electron traps, or defects. This process would ultimately make the dark current be as small as possible.

Various methods for surface passivation of III-V semi-conductor devices exist, including hydrogen

plasma treatment and deposition of dielectric films such as silicon nitride, silicon dioxide, and polyamide. Although the effects of hydrogen passivation have been studied in other III-V compound devices [1], this has not been done with InGaAs/InP photodiodes.

### Procedure:

The samples were fabricated into mesas by standard photolithography, chemical wet etching (1 phosphoric acid : 1 Hydrogen Peroxide : 10 water) , evaporation and lift-off processes. The top (p) contacts were made with Cr-Au, and the bottom (n) contacts were made with Au-Ge-Ni-Au to obtain circular devices ranging from 40  $\mu\text{m}$  to 160  $\mu\text{m}$  in diameter.

### Hydrogen Passivation:

To create the atomic hydrogen, the samples were exposed to a hydrogen plasma created in a Reactive Ion Etcher (RIE). In the Phase I experiments, all samples were exposed to the plasma for ten minutes while other parameters (power, hydrogen flow rate, and pressure) were varied. The values tried are shown in Table 1. Afterwards, when the best values were obtained, the only variable left to experiment with was time. This was varied in the Phase II experiments.

### Results and Conclusions:

The first few samples were lost because after

RECIPES TRIED			
Recipe Try	Pressure (mTorr)	Flowrate (sccm)	Power (W)
III	200	100	90
IV	200	100	25
V	200	10	25
VI	200	100	25
VII	500	100	25
VIII	44	100	25
IX	44	100	100
X	44	5	100

Table  
1



getting the I-V characteristics, when it came time to give them H plasma treatment, the samples came out covered with a kind of oxide which made retaking accurate measurements impossible. We realized that this unknown coating was a residue of an InGa eutectic smeared on the back of the samples; this somehow reacted with the hydrogen plasma and created said coat on top of the device.

The process was repeated on devices without InGa eutectic. The best recipe found for the hydrogen plasma was:

- A power of 100W.
- A hydrogen flow rate of 5 sccm,
- A chamber pressure of 44 mTorr.

A maximum power of 100W was applied because we feared stronger power would ionize too much the particles and burn the device, since after the process was done, in one of the runs with more contamination, it looked as if a small explosion had occurred inside the chamber around the device.

The average factor of increase in dark current for all Phase I samples is shown in Figure 1. This is defined as the average difference between the dark current values of the devices before and after the processes, taken from an average of five devices per sample. The effects of time on recipes VIII and X are shown in Figure 2 and Figure 3, respectively.

After longer exposure to recipe X, a coating of contaminants formed on top of the device. The solution to this problem was to give a longer oxygen clean to the chamber before running the process. Even though the last treatment did decrease the dark current, and as an added bonus it increased the photocurrent by an average factor of 1.2, a light coat of contaminant still formed on top of the device.

### Summary and Future Work:

Different hydrogen plasma formulas were tried to find out if a treatment would passivate the defects, reducing the dark current of InGaAs photodiodes; satisfactory results were obtained for two different recipes at the times listed.

Further research is needed to explain the reaction of the InGaAs samples to the different hydrogen plasma treatments, as well as the InGa eutectic reaction the hydrogen. In addition, more work is needed to investigate other cleaning techniques for the chamber and devices before the process, and the different effects this variations might have since the experiments suggest that cleanliness is key.

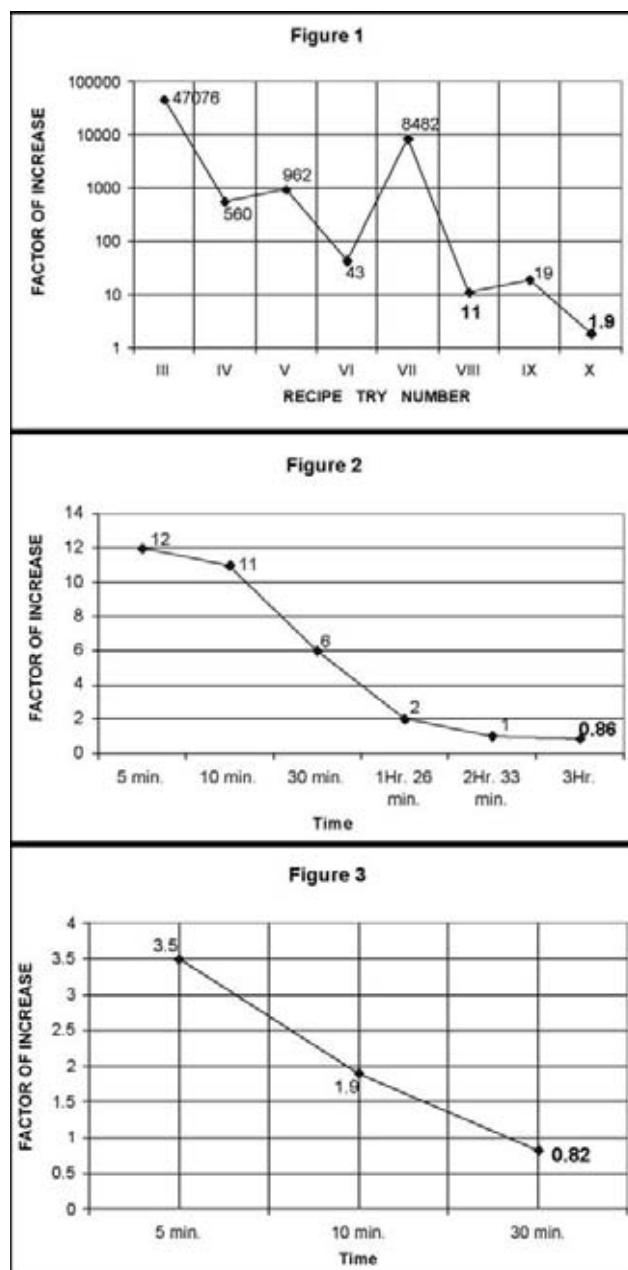
### Acknowledgments:

I would like to thank the following for their support

and guidance: Dr. Archie Holmes, the MBE group, Ms. Amy Pinkston, Ms. Melanie-Claire Mallison, the MER staff, and thanks to all the people and institutions that made this opportunity possible for me.

### References:

- [1] M. Bissiri, G. Baldassarri Ho ger von Ho gersthal, A. Polimeni, V. Gaspari, F. Ranalli, and M. Capizzi, Phys. Rev. B 65, 235210 (2002).
- [2] D. G. Yu, C.-H. Chen, A. L. Holmes Jr., S. P. DenBaars and E. L. Hu, JVST B. 15(6), Nov/Dec 1997.
- [3] M. Schwartzman, V. Sidorov D. Ritter and Y. Paz, JVST B. 21(1), Jan/Feb 2003.
- [4] Design, Fabrication and Characterization of Quantum Dot Infrared Photodetectors, Zhengmao Ye, Ph.D, The University of Texas at Austin, 2003, Doctoral Dissertation.



# Experimental Study of Nanoparticle Penetration Through Various Filter Media

**Matthew Harrington, Electronics Engineering Technology, Oregon Institute of Technology**  
**NNIN REU Site: Minnesota Nanotechnology Cluster, University of Minnesota**

*NNIN REU Principal Investigator: Dr. David Y. H. Pui, Mechanical Engineering, University of Minnesota*

*NNIN REU Mentor: Dr. Seong Chan Kim, Mechanical Engineering, University of Minnesota*

*Contact: simplychilln@msn.com, dyhpui@umn.edu, schankim@me.umn.edu*

## Abstract:

The purpose of this study is to investigate the penetration of nanoparticles (3 to 20 nm) through an assortment of filter media. The testing system, composed of a furnace, DMA, and filter holder, produces a monodisperse of neutrally charged, agglomerated silver nanoparticles to impact the filters. An Ultrafine CPC is used to physically count the particles upstream and downstream of the filters. Penetration/filtration efficiency is plotted as a function of particle size and combined with tests conducted by 3M for accuracy.

## Introduction:

Our society is technologically advancing at a dramatic rate. As modern technology grows smaller and faster, the issue of nanotechnology in the workplace has in fact become a reality and will one day become commonplace. Recent studies have shown that the health risks corresponding with the inhalation of nanoparticles are significant. As the exposure to nanoparticles increases, it becomes important to protect people and the environment from any harm that these particles may inflict. Therefore, it seems reasonable that the employment of a filtration mechanism would alleviate this dilemma.

Recent investigations of nanoparticle penetration have been conducted and concluded with some rather curious results. It would seem that in the nanoparticle domain, filtration efficiency should continually increase with decreasing particle size. One study shows otherwise [1], claiming that the effects of thermal rebound may be the cause. However, due to the delicacy of the testing system, we believe that something else may have contributed to this effect.

## Experimental Procedure:

The production and testing of nanoparticles through a filter medium is as follows. First, airflow is passed through a furnace containing silver. Nanoparticles of many different sizes are created here, and the flow of air exiting the furnace now contains a polydisperse

aerosol of nanoparticles. Next, the polydisperse is given a Boltzman charge distribution. Finally, the polydisperse is sent into a Nano Differential Mobility Analyzer (Nano DMA) where only one specific size of particles is extracted. The Nano DMA uses a sheath flow, a slit, and an electric field to select a known particle size, and outputs these identical particles as a monodisperse aerosol. By simply changing the electric field inside the DMA, we can change and know the size of particles that make up the monodisperse. Finally, the monodisperse is neutralized and sent to the filter holder to attempt to penetrate the filter medium.

An Ultrafine Condensation Particle Counter (UCPC) counts the particles before and after the filter for a set amount of time. These counts are recorded as the particle size is swept. The filters are changed after each test set to provide for a broad analysis. Penetration is defined by the number of particles counted downstream divided by the number counted upstream. Filtration efficiency is simply one minus penetration.

We find that penetration is a function of a particle's face velocity, size, and charge, as well as the filter's composition. In order to compare penetration percentages of particles of different sizes, we need to assure that all other variables are held constant. The selected size and charge of the particles will be maintained by the system, while the compositions of the filter media are homogenous. The face velocity will be maintained by ensuring a constant flow rate through the filter via a thermal mass flowmeter.

Since we want to simulate the face velocity encountered with a typical respirator, a 5.3 cm/s value is obtained by setting the flow rate according to the following equation:  $Q = U_0 A$ , where  $Q$  = flow rate,  $U_0$  = desired face velocity, and  $A$  = cross sectional area of exposed filter.

Still, prior to the testing procedures described above, investigations of the furnace must be made. Particle concentrations must remain constant during the counts. A simple test (Figure 1) shows that a minimum of 1200 seconds (20 minutes) must be allowed for the

furnace to warm up to a sufficient consistency. It is also important to provide large concentrations of particles to the filter. Figure 2 describes the size distribution of the polydisperse created by the furnace. Note that particle concentration is a function of both particle size and furnace temperature. Thus, the furnace is adjusted to provide the maximum number of particles without exceeding the range of the UCPC.

### Results and Conclusions:

The results from the standard and specialized filter media test each provided similar trend lines. Filtration efficiency was found to continually increase with decreasing particle size (Figure 3), and the error bars shown in the penetration plot (Figure 4) indicate a high degree of accuracy. We also observe that these plots show no effect of the thermal rebound proposed by Balazy et al [1]. We believe that these effects may be due to low particle counts and leakage in the system.

We can see that the majority of these filters probably do not provide enough protection from a highly saturated volume of air. However, the few on top do seem promising. By the time nanotechnology becomes common in the workplace, filters will prove to provide sufficient protection to employees.

### Future Work:

The results provided by this study will be used to develop a mathematical model of penetration through the standard filters. These results will be also be analyzed by the filter manufacturers in the attempt to create a better filter medium. New studies will be conducted to observe the penetration results when the particle's shape and charge are varied.

### Acknowledgements:

The author wishes to thank Dr. Pui and Dr. Kim, the University of Minnesota REU staff, NNIN and NSF.

### References:

- [1] Balazy, A., A. Podgorsky and L. Gradon, 2004. EAC Proceeding Vol. II, S967-S968.
- [2] Hinds, W.C., 1999. Aerosol Technology: Properties, Behavior, & Measurement of Airborne Particles. John Wiley & Sons, NY.

Figure 1: Particle stability due to the furnace.

Figure 2: Particle distributions produced by the furnace.

Figure 3: Filter efficiency vs. particle size for specialized filters.

Figure 4: penetration vs. particle size for standard filters.

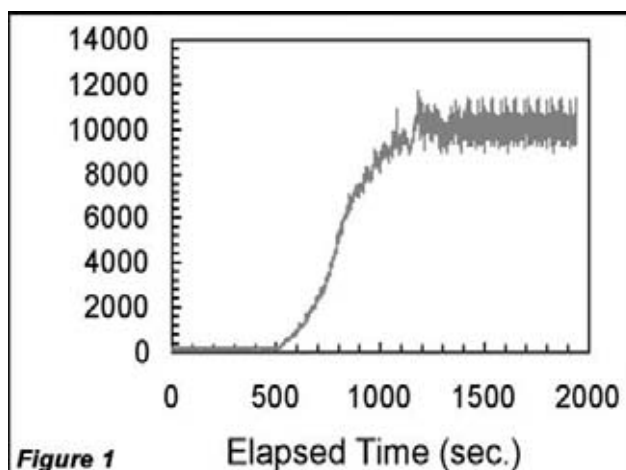


Figure 1

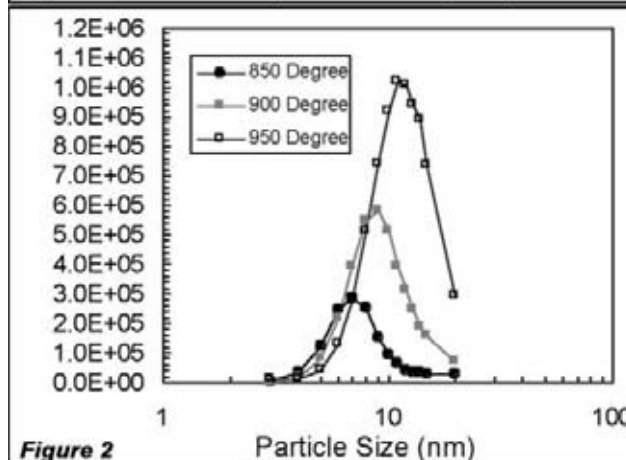


Figure 2

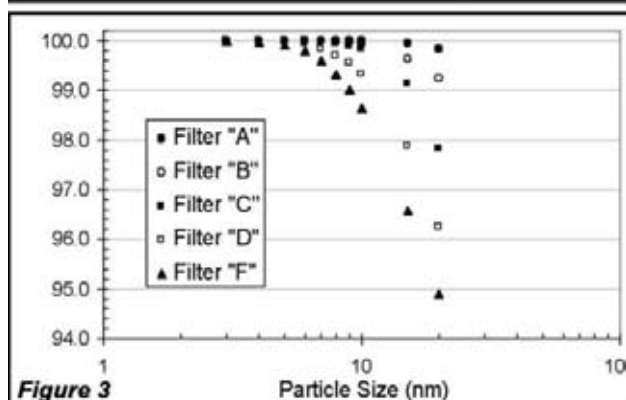


Figure 3

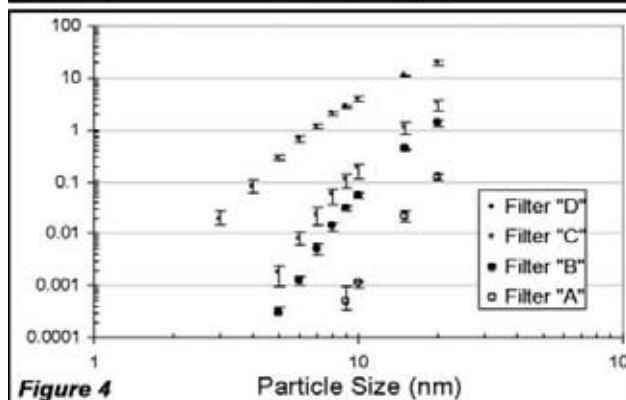


Figure 4

# Spin Polarized Transports Through a Polymer Using Half Metallic Manganites as Spin Injectors

**Paul Harris, Applied Physics, California State University San Bernardino**  
**NNIN REU Site: The Penn State Nanofabrication Facility, The Pennsylvania State University**

*NNIN REU Principal Investigator: Dr. Qi Li, Physics, The Pennsylvania State University*

*NNIN REU Mentor: Venimadhav Adyam, Physics, The Pennsylvania State University*

*Contact: harris@csusb.edu, qil1@psu.edu*

## Abstract:

The research focus is on spin polarized transport through thin polymer spacers using manganite electrodes in lithographically patterned nanostructures. The giant magnetoresistance (GMR) effect can be observed in magnetic thin films, which are composed of ferromagnetic layers and nonmagnetic (spacer) material. The ferromagnetic material being used in our research is  $\text{La}_{0.7}\text{Sr}_{0.3}\text{MnO}_3$  (LSMO), which is nearly half metallic with very high spin polarization at Fermi Surface. When the ferromagnetic layers are parallel, they have a low resistance as opposed to when they are antiparallel. With an applied magnetic field, the direction of the magnetization can be altered.

## Introduction:

Most if not all electronics are still based on a system that is driven by the charge of the electron rather than its spin characteristics. This quantum property known as the spin has lead to an emerging field of electronics called spintronics. The orientation of the spin of the electrical carriers allows spintronics to read, write and store information [1].

Spintronics plays an important role in Magnetic Random Access Memory (MRAM), which is an avenue for the future of electronic devices. MRAM is believed to be a fast, nonvolatile memory device and is suppose to have a high density of dynamic RAM (DRAM). Some of the flaws seen in DRAM is that it loses data when the power is turned off, which will be remedied with the incorporation of MRAM into technologies. MRAM is an application to this project.

The current research is mainly focused on developing new materials for the next generation of spin-polarized (SP) carriers and on the exploration of new materials able to transport a coherent spin to distances up to  $10^2$ - $10^3$  nm [2]. The aims of this project were to have a SP transport through a polymer using a half metallic manganite as a spin injector and to observe a magnetoresistance (MR) effect at room temperature.

## Experimental Procedures:

The half metallic materials we used in this project was LSMO grown on  $\text{SrTiO}_3$  substrates using pulse laser deposition. Our devices were fabricated by using a standard photolithography process and then focus ion beam patterning.

We first spun Micro-Chem LOR 5A lift-off resist over the substrate at 4000 rpm for 45.0 seconds. The substrate was then baked at  $180^\circ\text{C}$  for 10 minutes. Afterwards, we spun SPR 3012 photoresist at 4000 rpm for 45.0 seconds, which was followed by a soft bake at  $110^\circ\text{C}$  at 60 seconds. We then used a Karl Suss MA-6 contact aligner to expose the photoresist through a chrome mask for 3.2 seconds, followed by a post exposure bake (PEB) at  $110^\circ\text{C}$  at 30 seconds. The substrate was then developed in Shipley's CD-26 developer for 60 seconds.

Next, we used a Lesker Evaporator to deposit 20 nm of Ag and 300 nm of Au. A second photolithography process followed the deposition, where the Au was now patterned. We were able to complete the lift-off process by putting the device in acetone, which aided in the removal of the leftover resist. Then we did a reactive ion etch (RIE) of the Au over the LSMO film using an applied materials cluster tool with a high-density decoupled plasma source (DPS).

The next step in the device process was the use of a focus ion beam (FIB) to mill away segments of the film varying in width. Our smallest cut was at  $\sim 500$  nm.

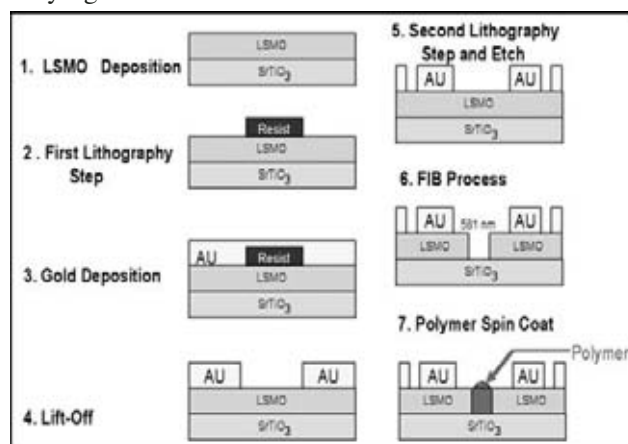


Figure 1: Device fabrication.



After the segments of the film had been milled away, we then spin coated a poly-3 hexyl-thiophene polymer over our device.

## Results and Conclusions:

After its completion, we measured the difference in voltage by applying a current across the device and later, the same device coated with the polymer. Both of the measurements were taken at room temperature. We found out what the IV curve for the device alone was linear with, without and after removing the magnetic field (Figure 2).

When we computed the results of the IV curve for the device coated with polymer, we found that there was a slight curvature to the graph with and after the magnetic field was removed (Figure 3). By drawing the best fit line over Figure 3, the average resistance calculated for the device with polymer was  $1.08 \times 10^5 \Omega$ . From the data shown in Figure 4, we were able to deduct that the magnetic field has an effect on the resistance of the material, which means that we had

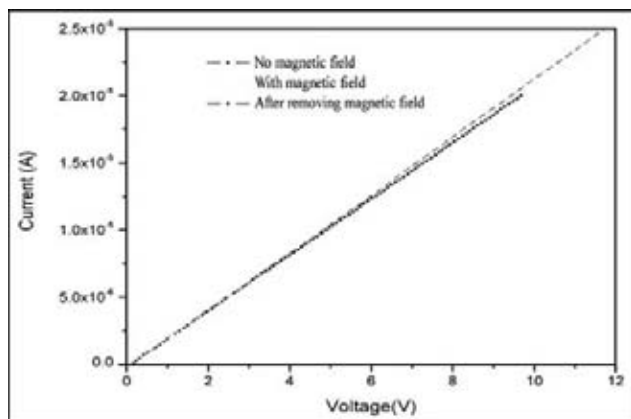
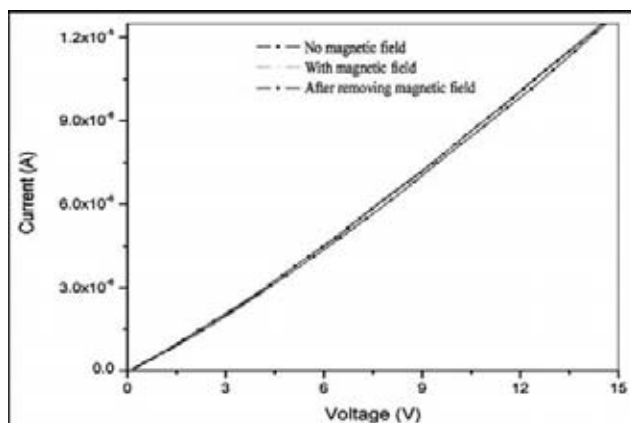


Figure 2, above: The data was linear for the IV curve of the device.

Figure 3, below: The IV curve for the device with polymer had a slight curvature.



observed an MR effect and also a spin dependent effect. We were able to calculate a small MR in between the curves to be. Although we were able to receive results for the device, we felt that these results could have been better if we would have had more time to make and test more samples and try different conditions.

## Future Work:

We would like to conduct more MR measurements with varying the temperature and vary the dimensions of the cut on the LSMO film. We would also like to try is to use alternative spacer materials in between the ferromagnetic layers.

## Acknowledgements:

I would like to thank Dr. Qi Li for all your help, my mentor Venimadhav Adyam for your guidance and patience. I would like to thank the NNIN-REU for providing me with the opportunity and the experience of working in an exciting field. I would also like to thank the NSF and MRSEC for the funding of this project. Finally, extending my thanks to Chang Hyon Ha for providing me with information regarding the GMR effect.

## References:

- [1] G.A. Prinz, Science 282 (1998) 1660.
- [2] V. Dedu, M. Murgia, F.C. Matocota, C.Taliani, S. Barbanera, et al., Solid State Communications 122 (2002) 181.

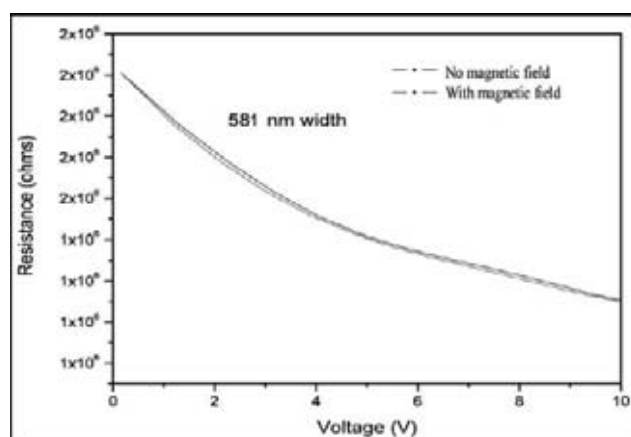


Figure 4: The MR measurement for the device.

## Laser Direct Write Grayscale Photolithography

**James Thorpe Helton, Chemical Engineering, Arizona State University**  
**NNIN REU Site: Cornell NanoScale Science & Technology Facility, Cornell University**

*NNIN REU Principal Investigator & Mentor: Dr. Michael Guillorn, CNF, Cornell University*  
*Contact: aikiribati@yahoo.com, guillorn@cnf.cornell.edu*

### Abstract:

Laser direct write photolithography is typically used to make two dimensional patterns on photoresist coated substrates. The intensity of the beam is chosen such that the resist is completely exposed during pattern writing while the beam is in the “on” state. Three dimensional (3D) pattern writing can be achieved by modulating the intensity of the beam to partially expose the resist [1]. This type of exposure is commonly referred to as “grayscale” photolithography and is capable of creating microscale features with multilevel topography.

This project investigated two applications of this fabrication technology: microlenses for micro-optics and filtering structures for microfluidics.

### Introduction:

Grayscale photolithography is frequently performed using projection photolithography. This process requires the use of a specially designed photomask. These masks employ variable optical transmission materials and/or complex patterning techniques to modulate the intensity of the exposed pattern. In contrast to binary or 2D patterning where photoresist is either completely exposed or unexposed, this process produces a 3D surface profile. Unfortunately, production of these photomasks is both costly and time consuming.

Laser direct write grayscale photolithography (LDWGP) differs from reduction techniques in that the mask is eliminated. The intensity of the laser is directly modulated as it is scanned across the substrate, producing the same affect [1]. By using this maskless approach, grayscale patterns can be designed and exposed rapidly allowing for increased flexibility. This project focused on the development of LDWGP processes and their use in two application areas: micro-optics and microfluidics. LDWGP combined with reactive ion etching (RIE) was successfully used to create arrays of microlenses in quartz and microfluidic filtering devices in Si.

### Procedure:

**Microlens Structures:** In this work, a Heidelberg Instruments DWL 66 laser pattern generator was used to perform LDWGP exposures. This system uses an acousto-optic crystal to modulate the intensity of the beam to 31 different intensity or “gray” levels where level 31 has the most intensity and level 1 is barely exposed. The resulting 3D structures in the resist can be transferred into the target substrates using RIE.

90  $\mu\text{m}$  diameter microlens structures were designed using a selection of 24 of the available 31 gray levels to obtain optimal curvature. A 100 mm diameter quartz wafer was used as the substrate. Vapor priming in hexamethyldisilazane (HMDS) was performed to improve the adhesion of photoresist to the wafer. Following this process, the wafer was coated with approximately 3.8  $\mu\text{m}$  of Shipley 1045 resist and baked in a 90°C oven for 30 minutes.

The wafer was then exposed using the DWL 66. Exposed wafers were developed in a Hamatech HMP 900 using 300 MIF for 2 minutes using a double puddle process. Developed wafers were placed on a 185°C hotplate for 3.5 minutes to reflow the photoresist and smooth out the transition between the gray levels. Pattern transfer was performed with the Oxford 100 deep reactive ion etcher using an ICP  $\text{CHF}_3/\text{O}_2$  plasma. Selectivity of quartz to resist was  $\sim 1:1.4$  resulting in a final lens height of 2.7  $\mu\text{m}$  at the apex (Figure 1).

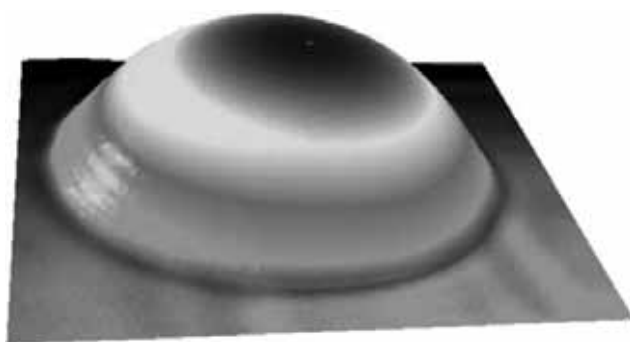


Figure 1: Optical profilometer image of a completed lens. The height is 2.7  $\mu\text{m}$  tall at the apex and the base is 90  $\mu\text{m}$  in diameter.

**Microfluidic Filtering Devices:** The microfluidic filtering devices were designed to filter particles smaller than  $1\ \mu\text{m}$  from larger particles. This was accomplished by creating a ramp separating a  $2.5\ \mu\text{m}$  deep region from a  $0.7\ \mu\text{m}$  deep region of a fluidic channel [2].

Fabrication of these devices was performed on Si substrates using the same exposure and development process as the microlens structures but without the vapor priming step. Pattern transfer was performed with the Oxford 100 deep reactive ion etcher using an ICP  $\text{CF}_4$  plasma. Images of a completed structure are shown in Figure 2. A film of polydimethylsiloxane (PDMS) was used to cover the channel. Holes were cut into the PDMS to allow transport of fluid into and out of the channel.

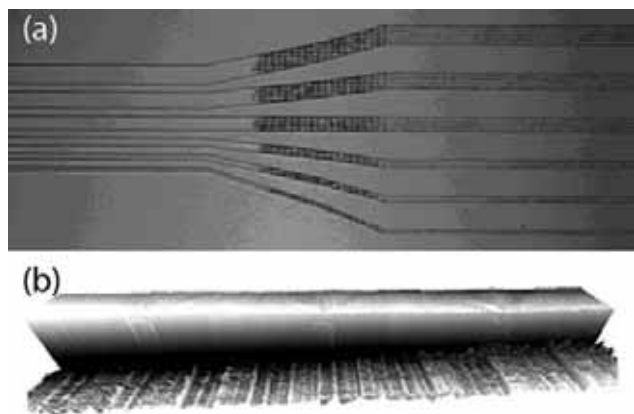


Figure 2: Microfluidic filtering device showing the gradual transition from the deep end (left) to the shallow end (right). (a) Optical microscope image of the channels. (b) Optical profilometer image of the channel transition region. The deepest part of the channel is  $2.5\ \mu\text{m}$ , the shallowest  $0.7\ \mu\text{m}$ .

### Results:

To test the microlenses, a pinhole aperture was inserted into the illumination path of an Olympus BX60 optical microscope. An image of the aperture was obtained by placing the focal plane of the microlens into the focal plane of the objective lens of the microscope. This was accomplished by moving the stage towards the objective lens. A series of images showing this process is presented in Figure 3, demonstrating the operation of a single lens.

Verification of the microfluidic filtering device was not completed during this project. However, a simple experiment involving  $1\ \mu\text{m}$  and  $0.5\ \mu\text{m}$  diameter latex beads could be used to demonstrate its functionality. The larger beads should remain trapped in the deeper region of the channel while the  $0.5\ \mu\text{m}$  diameter beads should flow through the channel unrestricted.

### Conclusion:

LDWGP is a useful tool for the fabrication of microstructures with multilevel topography. This work demonstrated the application of LDWGP to micro-optics and microfluidic systems. By using this maskless approach to grayscale photolithography, it is possible to reduce the cost and complexity traditionally associated with mask-based grayscale techniques.

### Acknowledgements:

I would like to thank NNIN and the National Science Foundation for the funding provided to make this Research Experience for Undergraduates possible. I would also like to thank the Cornell NanoScale Facility staff. Lastly, I would like to thank my principal investigator and mentor, Michael Guillorn, for his guidance and support throughout the summer.

### References:

- [1] University of Arizona Optical Sciences Center, July 28, 2003. "High Speed Maskless Grayscale Lithography," 1 Aug. 2005 [www.optics.arizona.edu/microoptics/MGL\\_Rev\\_D.pdf](http://www.optics.arizona.edu/microoptics/MGL_Rev_D.pdf).
- [2] Microfluidic Tutorial, 7 Sep. 2001. "Basic Microfluidic Concepts," 1 Aug. 2005, <http://faculty.washington.edu/yagerp/microfluidictutorial/basicconcepts/basicconcepts.htm>.

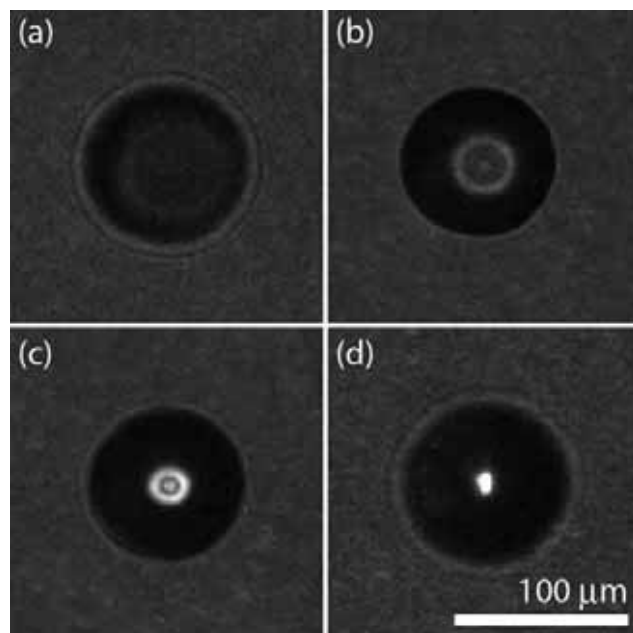


Figure 3: Optical microscope images of a single microlens illuminated with a pinhole aperture. The stage height is changed in (a) - (d) to find the focal plane of the lens.

# Nanomechanical Structures for Digital Logic

**Joseph Heremans, Computer Engineering, The University of Michigan**  
**NNIN REU Site: Cornell NanoScale Science & Technology Facility, Cornell University**

*NNIN REU Principal Investigator: Amit Lal, Electrical and Computer Engineering, Cornell University*

*NNIN REU Mentors: Shankar Radhakrishnan & Norimasa Yoshimizu,*

*Electrical and Computer Engineering, Cornell University*

*Contact: jhereman@umich.edu, lal@ece.cornell.edu*

## Abstract:

As electromechanical systems decrease in size, researchers have become interested in scalability effects. We address these issues with regards to nanoscale electromechanical systems (NEMS) cantilevers and present potential new applications. The primary issues we explored were the following: pull-down voltage, switching speed, static power loss due to Brownian Motion, and fabrication constraints. We then explored potential applications for such NEMS such as static power reduction in transistors, ultra-low power logic gates, and zero stand-by power Static Random Access Memory (SRAM) devices.

## Introduction:

It is always useful to decrease the stand-by power of transistors. In Figure 1, as physical gate lengths continue to decrease, the dynamic power is predicted to remain relatively constant. However, the sub-threshold leakage power, (stand-by power) has become larger by comparison, and therefore more problematic. Therefore our main goal for NEMS is to decrease and eliminate this leakage stand-by power. Indeed, small cantilevers could be used to shunt the source and the drain, and when open, interrupt the flow of current.

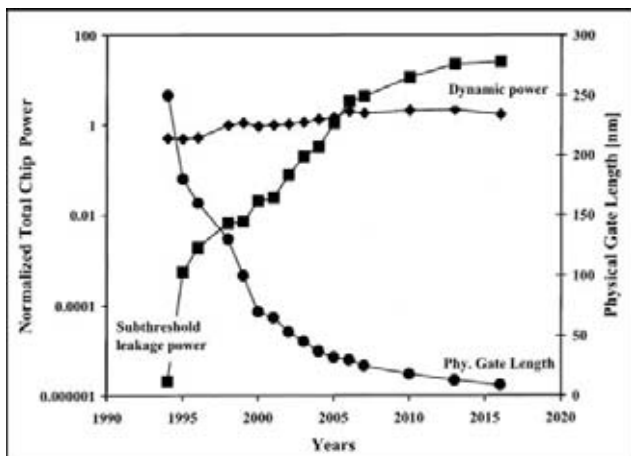


Figure 1: Stand-by and dynamic power comparison.

## Procedure

### Primary Considerations:

The primary issues with small cantilever designs are their physical size, pull-down voltage, switching speed, and Brownian motion noise. The physical size limit is dictated by our fabrication process, and modeling shows that the pull-down voltage can be held constant by appropriately scaling the relevant variables. The spring constant is the primary factor controlling both the switching speed and Brownian motion noise, and is inversely proportional to the pull-down voltage. The modeling leads us to design an acceptable compromise.

### Theoretical Findings:

Modeling the primary considerations, we are able to develop scaling constraints which can isolate and accentuate desired characteristics of the nano-scale cantilevers, or mask undesirable characteristics. Defined in terms of the minimum photolithographic feature size of any given device,  $\lambda$ , these equations can be tailored to suit its application.

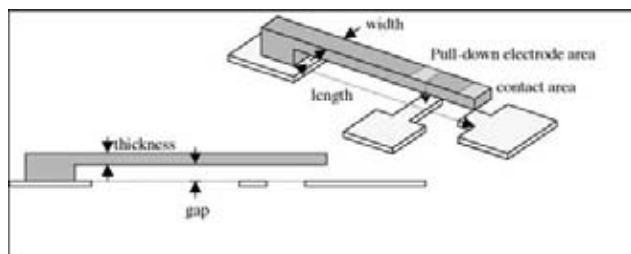


Figure 2: Physical parameters governing cantilever performance.

The physical parameters which govern the properties of the cantilever are: length, width, thickness, gap, Pull-down electrode area and Young's modulus of the material (see Figure 2 for more details).

Certain ideas to consider, however, are that electromechanical devices will always be slower than electronic devices of the same size, resulting in a lower switching speed for the given transistor. Also, the pull-down voltage must remain reasonably similar



<p>Pull-down Voltage: <math>V_{pd} = \sqrt{\frac{8kg^3}{27A_{cap}\epsilon_0}}</math></p> <p>Switching Speed: <math>\omega = \sqrt{\frac{k}{m}}</math></p> <p>Static Power Loss: <math>P_{rms} = V_{std}^2 \frac{A_{cap} \cdot \epsilon_0}{g^2} \cdot \dot{x}_{rms}</math></p>	<p>l: length w: width t: thickness g: gap k: spring constant <math>A_{cap}</math>: pull-down electrode area <math>\epsilon_0</math>: permittivity of free space <math>V_{std}</math>: power supply voltage</p>
---	--

Figure 3: Cantilever equations.

to the saturation threshold voltage of comparable conventional transistors, or else no benefit will result. The defining equations can be found in Figure 3.

### Fabrication Design:

Our proposed designs were two-fold. We first wanted to make a conventional complementary metal oxide transistor (CMOS), on top of which we would place two cantilevers. The intention was that when either the PMOS or NMOS transistor was turned on by the latching of the cantilever, the opposite transistor would be unlatched and thus eliminate power leakage. Our second proposed idea was simply to eliminate the CMOS transistor altogether and create a transistor out of simple cantilevers. This design would allow for a much simpler fabrication process, and would also create little stand-by power leakage.

## Results and Conclusions

### Theoretical Results:

For our fabrication test cases, we designed the pull-down voltages to be similar to the saturation threshold voltages according to the International Technology Roadmap for Semiconductors (ITRS). We then fitted the remaining parameters to optimize the switching speed as this was a detrimental factor we wanted to minimize. Afterwards we compared our stand-by power loss compared to the current ITRS predictions and found an almost complete order of magnitude improvement. Another advantage of these new designs is that as devices become smaller and smaller, the static power losses decrease instead of typically increase as it does in the current design.

### Experimental Results:

Our experimental results were far from successful. We were trying to make nano-scale cantilevers and ran into two major fabrication constraints: curl-up and stiction. We determined that the curl-up was caused by stressed placed on the cantilevers while releasing the cantilevers from the sacrificial layer underneath.

In Figure 4, clear examples of both curl-up (the 3 left most cantilevers) and stiction (the 2 right most cantilevers) are seen. We have ideas in how to correct such fabrication constraints but haven't had time to fabricate these improvements yet.

### Future Work:

Our future work consists of resolving fabrication complications (mainly curl-up and stiction) as well as characterizing several metals to determine optimal parameters for given applications. In order to resolve the issue of curl-up, we propose to design cantilevers with a higher spring constant. To resolve the problem of stiction, we propose to use a dimpled array of small indentations rather than a solid wall for the contact pad. This will reduce the surface area to edge ratio of the contact pad and eliminate stiction. Following the guidelines set forth in our experiments, this should not be terribly difficult to complete.

### Acknowledgements:

I would like to acknowledge the following people: Shankar Radhakrishnan, Norimasa Yoshimizu, Professor Amit Lal, the SonicMEMS group at Cornell University, the Cornell NanoScale Science and Technology Facility Staff, the NNIN, and the NSF.

### References:

- [1] Ultimate limits to inertial mass sensing based upon nanoelectromechanical systems, KL Ekinci, YT Yang, ML Roukes - Journal of Applied Physics, 2004.
- [2] Influence of automatic level control on micromechanical resonator oscillator phase noise, Seungbae Lee, Nguyen, C.T.- C. Proceedings of the 2003 IEEE International Frequency Control Symposium and PDA Exhibition., 2003, p 341-9.
- [3] MEMs relay based digital logic systems, Ezekiel J. J. Kruglick, Kristofer S. J. Pister - Transducers 1999, Sendai, Japan.
- [4] Noise: How important is it in the applications of MEMS and MOEMS? A Selvarajan - Proceedings of SPIE, 2003.

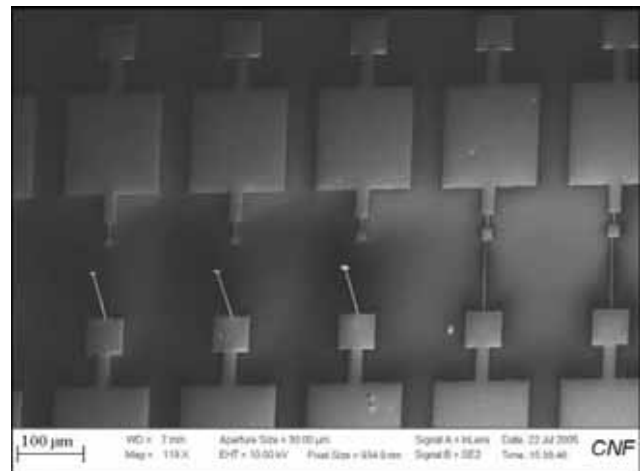


Figure 4: Curl-up and stiction.

## Porous Carbons for Environmental Cleanup

**Nathan Honsowetz, Aerospace Engineering, University of Southern California  
(Formerly of Physical Science, Biola University)**

**NNIN REU Site: The Penn State Nanofabrication Facility, The Pennsylvania State University**

*NNIN REU Principal Investigator: Dr. Fred Cannon, Environmental Engr, The Pennsylvania State University*

*NNIN REU Mentor: Adam Redding, Environmental Engineering, The Pennsylvania State University*

*Contact: nathanhonsowetz@hotmail.com, fcannon@engr.psu.edu*

### Abstract:

Porous carbons are used primarily for purification purposes through adsorption of contaminants on the surface of the activated carbon. The specific functional groups on the activated carbon are important to know since different functional groups adsorb different chemicals. Because different functional groups have different pKa values, a titration of an activated carbon indicates which functional groups are attached to the carbon. Also, a titration of two activated carbons with varying ionic strengths indicates the pH of zero charge for that activated carbon. This project's focus is to determine the appropriate equilibrium time for various activated carbons in titrations used for these purposes.

### Introduction:

Activated carbons are aromatic carbons used in a variety of both liquid and gas purification applications. The name "activated carbon" originates from any of a variety of processes whereby the carbons are activated and become excellent adsorbing materials. Thus, these carbons are excellent purifiers for such reasons as their high volume, high surface area, high surface reactivity, and favorable pore size.

The specific functional groups on these activated carbons largely determine the ability of the activated carbons to adsorb various chemicals. Titrations of these activated carbons are important since through these titrations one can determine the functional groups on the activated carbon. Consequently, the task of determining a standard protocol, specifically proper equilibrium times, for titrations of specific activated carbons is crucial in accurately carrying out these titrations.

This project's primary purpose was to establish this standard protocol along with aiding in the characterization of these carbons when appropriate.

### Experimental Procedure:

Various activated carbons were ground to the appropriate mesh size (200 x 400 holes per square inch) and kept in a desiccator until use. Each activated carbon was titrated twice to allow solutions of different ionic strengths to be tested; the two solutions used were 0.01 and 0.1 molar sodium chloride solutions. The protocol used included acid addition, pH electrode calibration, and base addition prior to the addition of the activated carbon. Nitrogen gas was continually bubbled through the solutions both prior to and during the duration of the titrations to expel carbon dioxide from the solutions. The pH was raised immediately prior to the titrations, and the titrations were allowed to run to completion. The chosen equilibrium time between acid additions was 30 minutes with 0.05 milliliter increments of 0.1 molar hydrogen chloride solution until 5.0 milliliters of acid were added.

### Results and Conclusions:

Proper equilibrium times were not determined in this project, although work has been done to that end. Titrations of four activated carbons were completed (Symbio, Super Darco, Hydro Darco, and a coconut

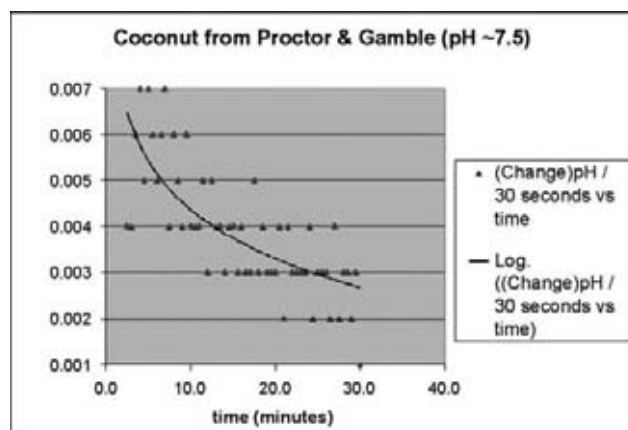


Figure 1: The change in pH over the 30 minute equilibrium time for a coconut carbon from Proctor & Gamble.

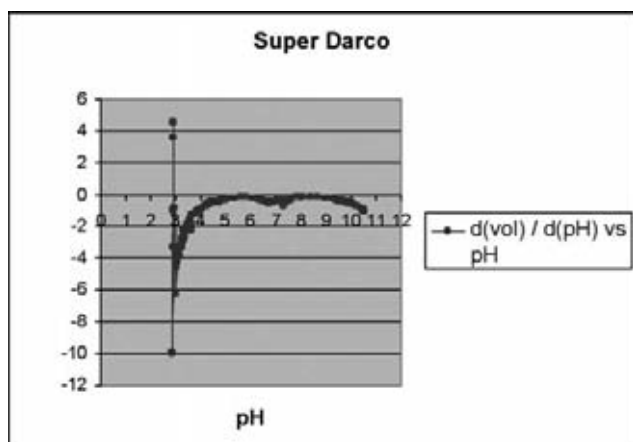


Figure 2: This graph demonstrates how specific functional groups are determined.

carbon from Proctor & Gamble) with 30 minute equilibrium times for each.

Graphs demonstrating the change in pH over the 30 minute equilibrium time give an approximation of the activated carbon's required equilibrium time (see Figure 1 for example). These graphs were ascertained for three activated carbons (Symbio, Hydro Darco, and a coconut carbon from Proctor & Gamble). Also, these graphs give an indication of the approximate pore size of the activated carbon since equilibrium times are related to pore size. Clearly, larger pore sizes require shorter equilibrium times.

The primary purpose for titrations can be seen in Figure 2; determining the functional groups on the activated carbon. From peaks on this graph, one can postulate that Super Darco contains a lactone group ( $pK_a \sim 7$ ) and a carboxyl group ( $pK_a \sim 3$ ). However, because this is purely raw, unduplicated data, more work must be done to confirm this. The general concavity of the graph is due to the influence of water; only the distinct peaks on the graph are of interest here.

In addition, the point of zero charge (pzc) of three activated carbons (Symbio, Super Darco, and Hydro Darco) was determined through the graphs of the solutions of different ionic strengths (see Figure 3 for example). The pzc occurs when these two curves

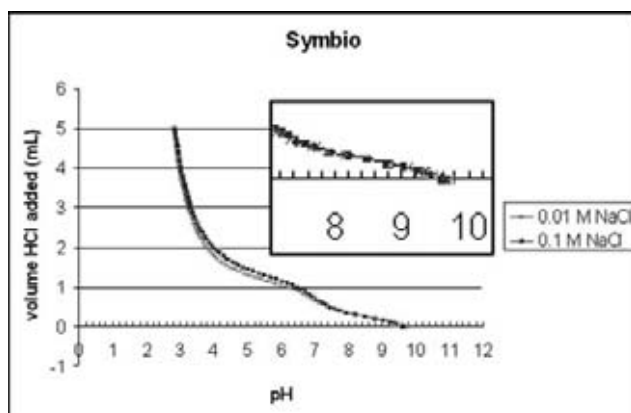


Figure 3: The pzc for Symbio is  $\sim 8.5$ .

intersect, indicating the point where there is zero charge on the activated carbon and the natural pH of the carbon when in water.

Furthermore, slurry pH values were obtained for all four activated carbons, attempted to confirm the values of the pzc obtained. However, the validity of these values is highly questioned since they did not agree well with the pzc values.

### Future Work:

Because of the complexity of the exact required equilibrium times for these activated carbons, these values were not obtained for any activated carbon. Also, the exact value for how small the change in pH over time must be was not determined. Thus, more work both in the duplication and evaluation of all data obtained is required in order to obtain this necessary equilibrium time and corresponding standard protocol. Titrations with longer equilibrium times (up to one hour) and the corresponding data would be very helpful in determining these proper equilibrium times.

### Acknowledgements:

The author wishes to thank Dr. Fred Cannon, Adam Redding, the NNIN and the NSF.

## FIB and TEM Analysis of Nanoscale Thin Films

**Derek Hsen Dai Hsu, Materials Science and Engineering, Northwestern University**  
**NNIN REU Site: Stanford Nanofabrication Facility, Stanford University**

*NNIN REU Principal Investigator: Robert Sinclair, Materials Science and Engineering, Stanford University*

*NNIN REU Mentor: Richard Chin, Materials Science and Engineering, Stanford University*

*Contact: h-hsu3@northwestern.edu, bobsinc@stanford.edu*

### Abstract:

Wire-drawn pearlitic steel has a refined lamellar microstructure of alternating ferrite ( $\alpha$ -Fe) and cementite ( $\text{Fe}_3\text{C}$ ) phases. Consequently, modeling the system by multilayer deposition and observing changes in periodicity and composition may reveal different applications. Using sputter deposition, thin film samples of alternating iron and carbon layers (with 0.1-5 nm periodicity) have been made to duplicate the microstructure.

In this study, we will use the dual-beam Focused Ion Beam (FIB)/Scanning Electron Microscope (SEM) to prepare cross-section Transmission Electron Microscope (TEM) samples. These will be characterized thoroughly, with the eventual goal of examining them *in situ* to view the behavior of the system during the annealing process. This will illuminate how small changes in Fe/C thin film compositions can result in immense differences in structure and hence, the properties.

### Introduction:

Historically important in industry, pearlitic steel drawn to wire form has demonstrated a very high tensile strength without sacrificing its ductility and durability. Therefore, we have decided to reproduce this structure in thin film form to explore its properties at the nanoscale.

Since it has a lamellar microstructure of alternating ferrite ( $\alpha$ -Fe) and cementite ( $\text{Fe}_3\text{C}$ ) phases, we have modeled this system by sputter deposition, creating thin films with repeated layers of iron and carbon [1]. Previous research has suggested that as the drawing strain increases, the microstructure becomes finer,



Figure 1: Bright field TEM of 0.2 mm pearlitic steel wire.

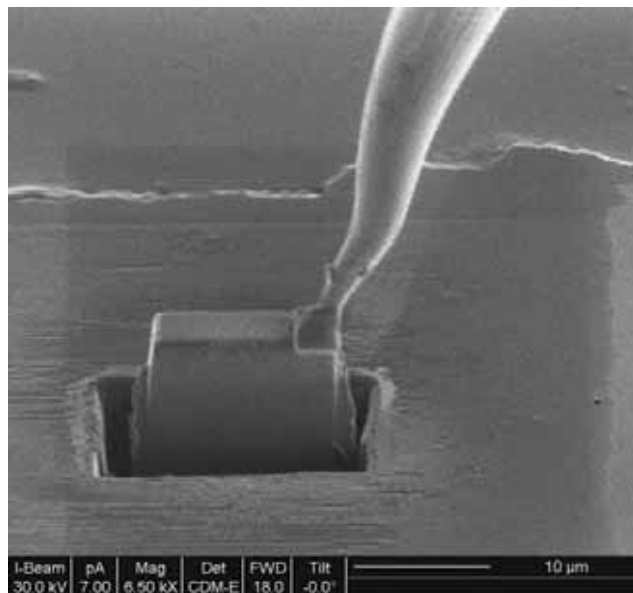


Figure 2: Transporting sample with Omniprobe.

thus improving its strength [2]. Also, the size, shape, and composition of the carbide layers have a great deal of influence on the mechanical properties of steel [3]. Consequently, one main goal of our research is to vary the thickness of the iron-carbon layers to mimic the effect of fine lamellar microstructure on steel properties.

Because we want to observe the interactions between the layers, the most important viewing angle is through the cross-section. Although prior conventional sample preparation techniques yielded some results, the success rate was very low. Furthermore, the differential etching rate of the constituent elements created samples where bright-field imaging was possible, but quality high-resolution imaging was not. Therefore, using the FIB/SEM to shape and polish samples to uniform electron transparency is expected to produce higher quality samples at a better rate of success.

Another important aspect of this research is to examine the structural changes of the iron-carbon thin films during annealing. *In situ* TEM is a prime technique to record the behavior of the system during this process.



Sputtered thin film samples of alternating iron and carbon layers with 0.1-5 nm periodicity were provided. For this experiment, we examined a sample with layer periodicities 19.75 Å Fe/2.6 Å C, sequentially deposited to 3 μm thickness, starting with Fe and ending with C, on Si substrates with native oxide. 30kV Ga<sup>+</sup> ions in the FIB were used for rough shaping of the TEM cross-sections; they were finished using 10kV ions. These samples were then characterized using various TEM imaging techniques. We also planned to use *in situ* TEM to view the structural changes and reactions of the iron-carbon thin films during the annealing process in the temperature range of 350-450°C.

Since we are interested in viewing the full thickness of the thin film, we used two methods to protect the area under examination from being etched during milling. The first approach was to deposit a rectangular 1  $\mu\text{m}$  thick layer of Pt over the area we wanted to preserve. However, possible implantation effects produced negative results that prompted us to make a second sample using a marker to lay down a coat of ink instead. We then milled out a rectangular wedge with approximate dimensions of 14 x 10 x 4  $\mu\text{m}$  using the FIB. The wedge was transported to a copper TEM half-grid using the FIB Omniprobe. Pt was deposited to weld the sample to the Omniprobe needle and, later, to the grid. Then, the needle was severed using the ion beam. Next, we thinned the wedge to below 0.1  $\mu\text{m}$  with the FIB for electron transparency in the TEM.

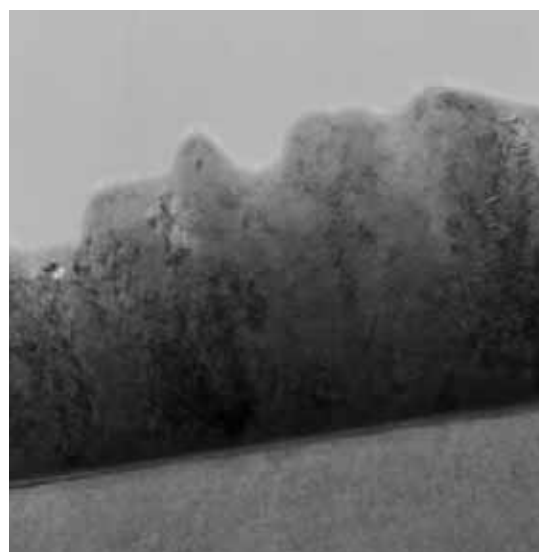
5 μm

that we could not differentiate the iron and carbon layers reliably, yet we could see the Si lattice image of the substrate. Examination of the first sample led us to believe that it was not yet electron transparent. However, after making another sample, we concluded that the iron and carbon layers may have reacted before being put into the TEM. Thus, these samples were not appropriate for use in the *in situ* phase of the research.

Because the sample seems to have reacted before conducting the *in situ* TEM, we were not able to view the reactions and behavior of the iron-carbon system during the heating process. We suspected that the sample prematurely reacted during the FIB process or there were possible problems stemming from the sputter deposition of this particular geometry.

I would like to acknowledge the NSF, NNIN, and CIS for funding this project. Also, I would like to thank Mike Deal and rest of the SNF staff, Prof. Robert Sinclair, and Richard Chin for their guidance and support throughout the research.

- [1] DA Porter & KE Easterling. Phase Transformations in Metals and Alloys, 327, 2001.
- [2] JD Embury & RM Fisher. Acta Metallurgica, Vol.14, 147, 1966.
- [3] VN Gridnev & VG Gavriljuk. Phys. Metals, Vol. 4, 532, 1982.



## 2005 NNIN REU Research Accomplishments

# Intercalation and Exfoliation of Herringbone Graphite Nanofibers

**Sabil Huda, Chemical Engineering (Nanoscience Concentration), North Carolina State University**  
**NNIN REU Site: The Penn State Nanofabrication Facility, The Pennsylvania State University**

*NNIN REU Principal Investigator: Dr. Angela Lueking, Earth & Mineral Science, The Pennsylvania State University*

*NNIN REU Mentors: Deepa Narayanan & Puja Jain, Earth and Mineral Sciences,*

*and Dr. Humberto Rodriguez Gutierrez, The Pennsylvania State University*

*Contact: shuda@ncsu.edu, adl11@psu.edu*

## Abstract:

We investigated how to control the expansion of the structure of graphite nanofibers (GNF). Lueking et. al. [1] have reported that this goal can be accomplished via intercalation followed by exfoliation. We studied the various factors that affect the exfoliation of GNF. We found that the conditions of both the intercalation and exfoliation influence the final structure of GNF.

Temperature controlled desorption (TPD) data was used to show that the exfoliated GNF (EGNF) structure is unstable and changes with time. High-Resolution Transmission Electron Microscopy (HRTEM) was used to monitor changes in structure after exfoliation. B.E.T. surface area measurements helped determine the degree of exfoliation or change in surface area.

## Introduction:

GNF are interesting because their properties can be manipulated using various intercalation compounds and exfoliation techniques. Lueking et. al. [1] have reported that by varying the exfoliation process, the GNF lattice spacing can be expanded from 5% to 20-fold and the surface area can be expanded up to 10-fold. We hope to characterize the exfoliation process thus making the surface area and pore-size tunable. This versatile process can be used to make GNF useful in a variety of industries textiles to Micro-Electro-Mechanical systems (MEMS) devices.

## Experimental Method

### Intercalation and Exfoliation:

Ultra-high purity Herringbone graphite nanofibers with high order (Figure 1) were obtained from Catalytic Materials LLC. This material was intercalated using a 1:1 mixture of concentrated sulfuric acid and nitric acid. Starting materials were mixed in a plastic beaker and stirred with a magnetic stirrer for 2 hours. The GNF were exfoliated using a flat-bed oven in ultra-high purity (UHP) nitrogen atmosphere flown in at 100 cc. Exfoliation was also done in a volatile matter furnace at room temperature and pressure (250°C and 1 atm).

## Characterization:

Temperature programmed desorption data was obtained using a Perkin Elmer Thermo Gravimetric Analyzer (TGA) 7 (c) in an UHP argon atmosphere. The sample was first degassed *in situ* at 1500°C for 4 hours. For analysis and degassing, the heating rate was 100°C/min and argon (UHP) gas was flown in at 100 cc.

Surface area data was obtained using nitrogen as the adsorbent at 77 K. The sample was first degassed at 1100°C (heating rate 100°C/minute) for 2 hours. The surface area was determined using the B.E.T. equation. All measurements and calculations were done using Micromeritics 2020(c).

High-resolution transmission electron microscope (HRTEM) images were obtained with a JEOL 2010F (200 kV). These pictures were taken by Dr. Humberto Rodriguez Gutierrez of Pennsylvania State University.

## Data

### Temperature Programmed Desorption:

The temperature programmed desorption data allowed us to study the rate of mass loss at different temperatures (Figure 1). The longer the sample was stored, the narrower the dips of the derivative became. The red graph was created from data collected

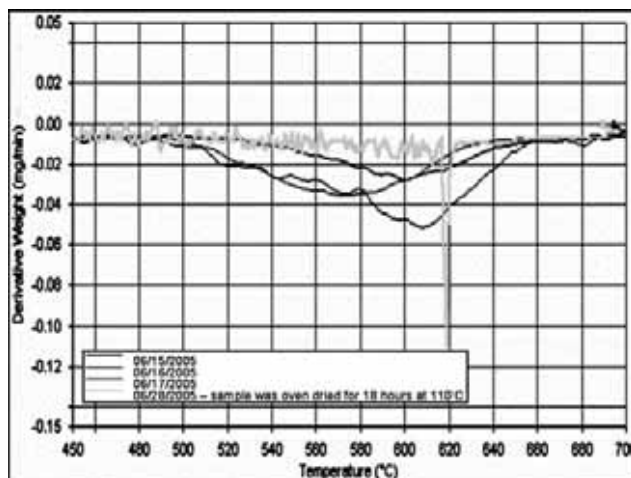


Figure 1: Phase change temperature of sample changes.

immediately after exfoliation. This graph has the broadest peak half-width area (500°C). The blue sample was characterized one day after exfoliation and had a peak half-width area of 37.50°C. The green sample was studied two days after exfoliation and has a peak half-width area of 350°C. The samples contain approximately 5 wt% of GNF and so, as the sample ages, more volatile intercalates leave the sample. This leads to a more stable compound. The sharpest dip is for the sample that was oven dried at 1100°C for 18 hours and was studied 13 days after exfoliation (cyan). We currently believe the heating led to better intercalation, such that the intercalant was driven inside the GNF to form a very stable compound. Future mass spectroscopy data will help investigate our hypothesis.

### Surface Area:

The surface area data indicates that changing the exfoliation temperature changes the surface area of the sample (Table 1).

Sample	B.E.T. Surface Area (m <sup>2</sup> /g)
Original GNF	75.7
GNF after heating at 225°C for 37 hours	102.3
GNF after heating at 700°C for 2 minutes	24.8
GNF after further heating at 1000°C for 6 hours	190.8
GNF after further heating at 1000°C for 36 hours	361.7

Table 1: Summary surface area varying with exfoliation treatment.

Exfoliation of GNF at higher temperatures causes the surface area to increase. The anomaly seems to be for the 700°C for 2 minutes treatment. This is probably because the sample contains intercalates and since the surface area is reported in m<sup>2</sup>/g, the number is artificially small. In the future we can verify this by studying the weight % of GNF.

### HR-TEM:

The HR-TEMs revealed that the lattice spacing of GNF becomes more distorted after exfoliation (Figure 2). Our HR-TEMs indicate the cross-section of the GNF to be circular (Figure 3c). Catalytic Materials LLC reported their material has a rectangular cross-section. This discrepancy could be due to a lack of information when the stacked-card model was proposed or because the samples are different.

### Conclusion:

From our studies, we can conclude that despite their high aspect ratio, GNF can be exfoliated using acid intercalates. The surface area was shown to be a function of exfoliation temperature and time of treatment. TPD data shows the intercalant desorbs from the GNF with time. The intercalated structure can be stabilized by heat treatment which causes intercalants to be more ordered [2]. HR-TEM shows that the structure of the GNF resembles stacked cones with a circular cross-section rather than the previously proposed stacked card model with a rectangular cross-section.

In the future, we wish to conduct XRD studies to research changes in lattice spacing and structure. Mass spectroscopy needs to be studied to understand the phase changes indicated by our TPD data. We want to test the applicability of GNF.

### Acknowledgements:

The author wishes to thank Dr. Lueking, Deepa, Puja, and Humberto for their assistance. Also, thanks to Penn State, NNIN and NSF for this REU program.

### References:

- [1] Lueking, A. D., J. Phys. Chem. B., 2005 109: 12710.
- [2] Inagaki, M., F. Kang and M. Toyoda, Exfoliation of Graphite via Intercalation compounds, L.R. Radovic, Editor. 2004, Marcel Dekker: New York. p. 1.
- [3] Dresselhaus, M.S. and G. Dresselhaus, Adv. Phys., 2002. 51: 1.
- [4] Rodriguez, et. al., Langmuir, Vol. 11, No. 10, 1995.

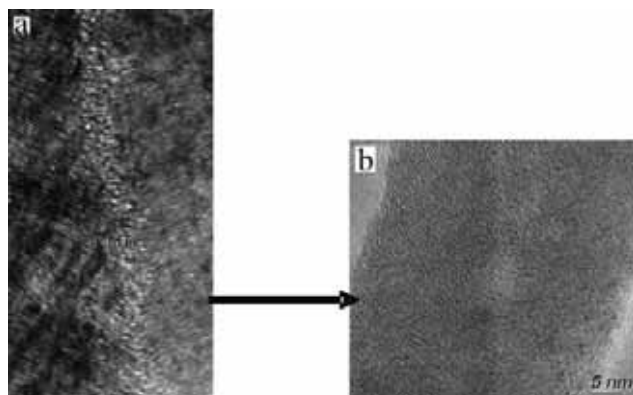
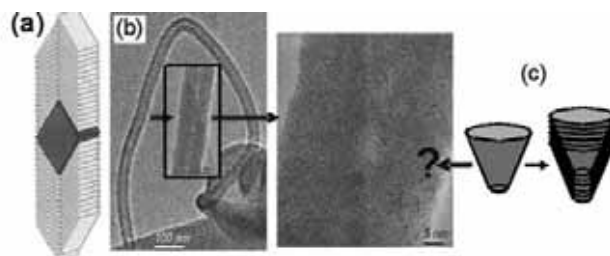


Figure 2, above: HR-TEM of (a) Original GNF4; (b) GNF at 700°C for 2 minutes. Figure 3, below: (a) Stacked card model4; (b) HRTEM of GNF after being treated at 700°C for 2 minutes; (c) stacked cone model.





## New Techniques for Generating Core/Shell Nanoparticles

**Jacob Hughey, Biomedical Engineering and Mathematics, Vanderbilt University**  
**NNIN REU Site: Microelectronics Research Center, Georgia Institute of Technology**

*NNIN REU Principal Investigator: Mostafa A. El-Sayed, Laser Dynamics Laboratory,  
School of Chemistry and Biochemistry, Georgia Institute of Technology*

*NNIN REU Mentor: Susie Eustis, Laser Dynamics Laboratory, School of Chemistry  
and Biochemistry, Georgia Institute of Technology*

*Contact: jake.hughey@vanderbilt.edu, mostafa.el-sayed@chemistry.gatech.edu*

### Abstract:

The outstanding potential of core/shell nanoparticles stems from the ability to obtain structures with combinations of properties that neither individual material possesses. Although spherical gold nanoparticles generally have a surface plasmon resonance at a wavelength of about 520 nm, a spherical silica core with a gold shell offers a very highly tunable plasmon wavelength depending on the thickness of the shell and the core diameter.

While silica core/gold shell nanoparticles have been fabricated previously by chemical reduction of gold ions, our work attempted to generate these structures by photochemical reduction and by nanosphere lithography. These techniques could provide finer control over the properties of the shell. In addition to using gold, the nanosphere lithography method was also attempted with silver. Optical spectroscopy and electron microscopy were used in the characterization of these nanoshells. Although both techniques are able to generate nanoparticles on the silica core, the current experimental conditions fail to provide a smooth shell.

### Introduction:

Although the inherent nature of core/shell nanoparticles makes them potentially very useful in

many areas, it is the biomedical applications that are getting the most attention. Our research focused on new ways of fabricating nanoparticles with a silica core and a shell of gold or silver, a concept pioneered by Halas et al [1]. The motivation for developing this structure lies with the surface plasmon resonance, which is the collective oscillation of free electrons in an applied electromagnetic field, resulting in intense absorption and scattering. Using a silica core, the plasmon becomes very sensitive to the shell thickness. Using silica/gold nanoshells with an 800 nm plasmon, Halas et al. found that NIR laser light (808 nm) focused on tumors with nanoshell accumulation results in localized heat delivery that selectively kills the tumors cells [2]. However, the considerable surface roughness of typical core/shell structures leaves room for improvement. This research attempted to apply the methods of photochemical reduction and nanosphere lithography to produce the nanoshells.

### Experimental:

The photochemical reduction is a combination of the procedures of Halas et al [1] and Eustis et al [3]. Small gold colloid (1-2 nm) was prepared as described by Duff et al [4]. Silica nanoparticles 110 nm in diameter were suspended in ethanol and functionalized with 3-aminopropyltriethoxysilane (APTES). The APTES-covered silica was purified and the pH was adjusted. The negatively charged gold seeds absorbed onto the positively charged amine groups on the silica surface. A solution was prepared of the gold-modified silica and  $\text{HAuCl}_4$  in ethylene glycol. Irradiation was performed with a mercury xenon lamp and a band filter selecting wavelengths from 230 nm to 400 nm. Absorbance spectra were measured with a Shimadzu UV-3103-PC spectrophotometer. Nanoshells were analyzed using a JEOL100 transmission electron microscope.

The nanosphere lithography method was performed as described by Van Duyne et al [5]. The unmodified silica nanoparticles mentioned previously were used. A PVD75 Filament Evaporator was used to deposit 5, 10, and 20 nm of gold and silver on the silica. Without

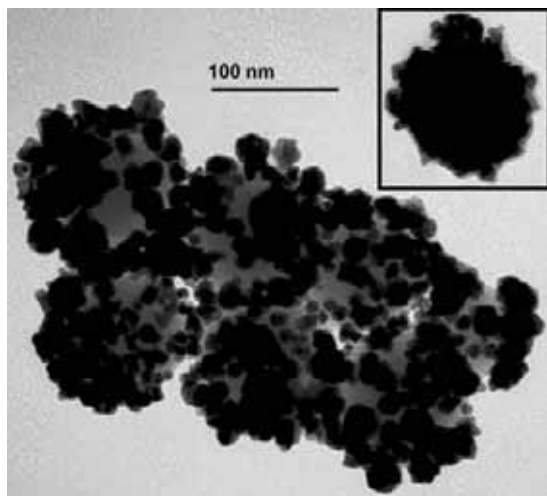


Figure 1: TEM images from photochemical reduction.



removing the silica layer, absorbance spectra were measured with a Beckman DU 650 Spectrophotometer. Samples were further analyzed using a LEO 1530 Scanning Electron Microscope.

## Results and Discussion:

Figure 1 shows a sample of the photochemical reduction after irradiation. The vast majority of silica nanoparticles appeared as seen here, characterized by incomplete coverage of the silica surface. Some silica particles were observed with complete gold coverage of the silica, shown in the inset. However, these particles had very rough shells, due to the growth of clusters of gold nanoparticles that encased the silica. The low yield of core/shell structures explains the absence of a plasmon peak near 800 nm, and the absorption peak at 540 nm can be attributed to spherical gold nanoparticles formed in solution and on the silica.

Though not yet ideal, this result demonstrates that the photochemical reduction is capable of reducing gold onto the surface of silica nanoparticles. In addition, without the gold seed, no gold is reduced onto the surface of the silica.

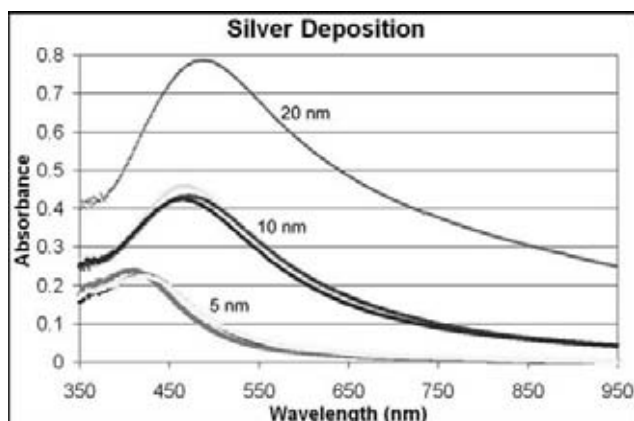


Figure 2: Absorbance spectra for varying deposition thicknesses.

With nanosphere lithography, as the deposition thickness was increased for both gold and silver, the plasmon peak red-shifted and the absorbance increased (silver is shown in Figure 2). Both of these facts are consistent with theoretical calculations for the growth of a shell [2]. As seen in Figure 3 from left to right, at 5 nm thickness, quasi-spherical silver nanoparticles pepper the surface of the silica and at 10 nm, almost completely cover the silica surface. However, the silver particles fail to coalesce to form a shell and at 20 nm thickness, the silica is buried under large, irregularly-shaped silver particles.

## Future Work:

To maximize the amount of gold reduced on the surface of the silica rather than in solution during the photochemical reduction, the initial concentration of  $\text{HAuCl}_4$  might be reduced or  $\text{HAuCl}_4$  might be added incrementally. The effects of changing lamp power, using a narrow band filter, or otherwise altering the speed of the reaction, should also be explored. The nanosphere lithography technique may require better monodispersity of the silica nanoparticles or modification of the silica surface. For both methods, it will be necessary to encourage the formation of a smooth shell instead of isolated gold particles.

## Acknowledgments:

A sincere thanks goes to my mentor Susie Eustis, graduate student Wenyu Huang, and my P.I., Dr. Mostafa El-Sayed. I also thank Jennifer Tatham, the Microelectronics Research Center, Laser Dynamics Lab, NNIN, and NSF.

## References:

- [1] Oldenburg, S.J.; Averitt, R.D.; Westcott, S.L.; Halas, N. J. Chem. Phys. Lett. 1998, 288, 243.
- [2] O'Neal, D.P.; Hirsch, L.R.; Halas, N.J.; Payne, J.D.; West, J.L. Cancer Lett. 2004, 209, 171.
- [3] Eustis, S; Hsu, HY; El-Sayed, M.A. J Phys. Chem. B 2005, 109, 4811-4815.
- [4] Duff, D.G.; Baiker, A.; Edwards, P.P. Langmuir 1993, 9, 2301.
- [5] Hulteen, J.C.; Van Duyne, R.P. J. Vac. Sci. Technol. A 1995, 13, 1553-1558.

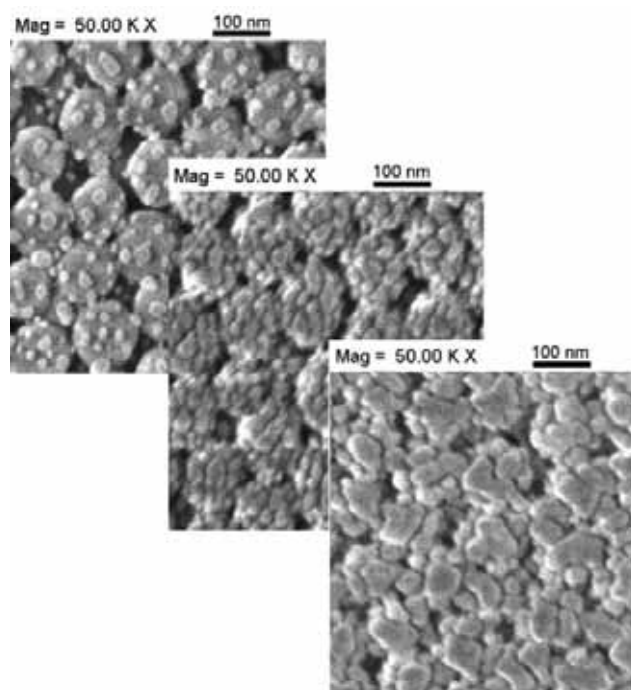


Figure 3: SEM images of silver deposition.

# E-Beam Lithography to Improve the Performance of Organic Optoelectronics

**Jamie Jackson, Electrical Engineering, Morehouse College**  
**NNIN REU Site: Cornell NanoScale Science and Technology Facility, Cornell University**

*NNIN REU Principal Investigator: Alan Bleier, CNF, Cornell University*  
*NNIN REU Mentor: Matthew Lloyd, Materials Science & Engineering, Cornell University*  
*Contact: scooby2k2@hotmail.com, bleier@cornell.edu*

## Abstract:

This project focused on improving the performance of a standard organic solar cell by using electron beam lithography. Roughening the bottom of an organic solar cell has been proven to increase its efficiency. Thus, we hope to achieve an increase in efficiency in a modified solar cell by making a device pattern on a silicon wafer with e-beam lithography, placing a PDMS layer to produce a stamp of this device pattern, and using the stamp in a hot press to emboss PEDOT on the underlayer of the cell. Efficiency of the un-embossed cells was verified using a computer interface, and embossing PEDOT is underway. Other methods, such as using the stamp as a cell substrate, were also considered in this project.

## Introduction:

In recent years, researchers have produced organic photovoltaics as a cost-efficient alternative to silicon-based solar cells. Solar cells with deposited layers of organic material work in the same manner as silicon-based cells, except that light produces excitons, which go into the interface when split into electrons and holes. Further motivation for this project came from the work of Roman, et al., with organic solar cells. They developed a cell using an elastic polymer stamp with a rigid pattern. The stamp was then embossed on the organic material to roughen the layer. Such a technique allowed for an increase in surface area as well as light trapping and interfacial absorption. They measured a significant increase in the performance of organic solar cells. Such results motivate us to proceed with our experiment, but with using e-beam lithography to develop a grating pattern for our stamp.

## Experimental Procedure:

In preparation of our embossing stamp, we used the L-Edit CAD program to design four rectangular gratings, each with its own dose, and each made up of lines at a certain thickness, repeated along a uniform spacing. This produced the grating pattern for our desired embossing stamp. A dose test was performed

using a 4-inch Si wafer to determine at least two doses that would produce desirable results. Each wafer went through a two-minute pre-bake at 170°C with a one-minute cool-off. XR-1541 resist (HSQ, Dow-Corning Corporation) was then spun on a 4-inch Si wafer at 1500 rpm for 60 seconds, followed by two more 2-minute pre-bakes at 170°C each, with another one-minute cool off.

Twenty squares with nanoscale grating patterns were exposed with a range of doses using a Leica VB6 E-Beam Lithography system. Another two-minute pre-bake was performed at 170°C with a cool-off before being developed in TMAH. Finally, the wafer was rinsed for three minutes in deionized water. We inspected each dose to determine which doses were sufficient for the grating pattern. Using atomic force microscopy, we determined that a dose of 645  $\mu\text{C}/\text{cm}^2$  proved adequate for the grating pattern in two cases of line thickness and uniform spacing—one with 128 nm period and the other with 192 nm period (the second case is featured in Figure 1).

The grating pattern was then exposed on a Si wafer using the aforementioned wafer preparation and the determined dose from the dose testing. PDMS was cast onto the patterned wafer and cured in the oven at 70°C

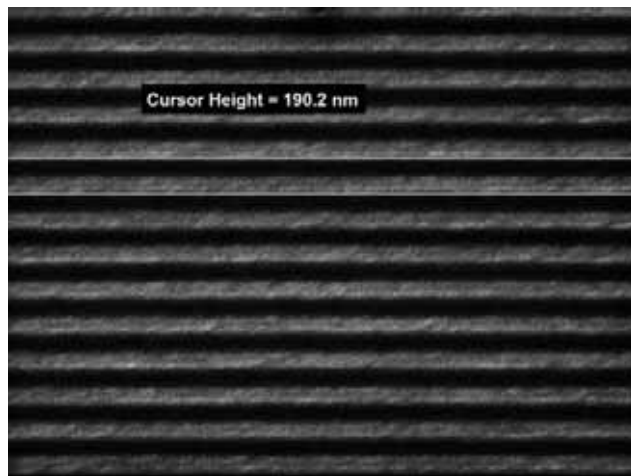


Figure 1: SEM image of grating with 192 nm period.

for 60 minutes. Alignment marks were exposed in the grating pattern, which allowed us to cut an even square around the grating pattern. In peeling the PDMS piece out of the Petri dish, we were able to make an imprint of the grating pattern on the bottom layer of the PDMS and thus produce our embossing stamp. We fabricated our solar cell by patterning indium tin oxide on a glass substrate. Approximately 250  $\mu\text{L}$  of PEDOT was then spun onto the substrate at 2000 rpm. The embossing stamp was then placed on top of the PEDOT layer and placed in a hot press, where heat and pressure were applied in order to roughen the layer. After which, layers of pentacene and C60 were deposited on the cell along with a patterned Al/Cs cathode layer. Finally, the cell's performance was tested and recorded using a computer interface.

### Results and Conclusion:

Complications to our experiment occurred when residue from the PEDOT layer was adhering to the embossing stamp, which we intended to reuse to produce more embossed cells. We therefore resorted to depositing an FOTS layer on the stamp to produce a hydrophobic layer in the hopes of preventing the adhering of PEDOT. Meanwhile, we tested a cell, which was made using an embossing stamp as a substrate. Using a standard solar cell as a control, we tested and analyzed the performance of the cell with the stamp.

In analyzing the photovoltaic response of both the control and the embossing stamp cell, we produced the

graph shown in Figure 2. The plot for the embossing stamp cell shows how the device has shorted, whereas the control cell had a photovoltaic response with an open circuit voltage of  $\sim 0.3\text{ V}$  and a current density of  $\sim 3\text{ mA/cm}^2$ .

From this experiment, we have developed a process for making imprint masters using e-beam lithography and succeeded in making an imprint-compatible control cell.

### Future Work:

Currently, we are using hydrophobic monolayers, such as FOTS, to imprint a grating pattern in organic thin film electrodes, such as PEDOT, to avoid the residue adhesion problem in the solar cell.

### Acknowledgements:

I would like to acknowledge Alex Mayer, Dan Bernards, and Dr. George Malliaras, of the Materials Science and Engineering Dept. at Cornell University, Dr. David Tanenbaum of Pomona College, the faculty and staff of the Cornell NanoScale Facility, and the NNIN for their support of this project. Special thanks to the Intel Foundation for funding this project.

### References:

- [1] "Trapping Light in Polymer Photodiodes with Soft Embossed Gratings," L.S. Roman, et al., *Advanced Materials*, 2000, 12 (3), 189-195.

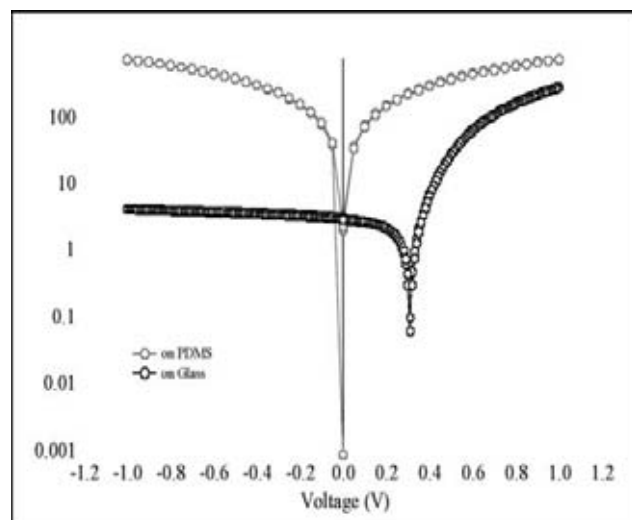


Figure 2: Semi-log plot of photovoltaic response.

## Thermal Stability of Ge-on-Si Thin Films

**Miktosha James, Electrical Engineering, Prairie View A&M University**  
**NNIN REU Site: Microelectronics Research Center, University of Texas at Austin**

*NNIN REU Principal Investigator: Sanjay Banerjee, Electrical Engineering, University of Texas at Austin*  
*NNIN REU Mentors: David Kelly & Isaac Wiedmann, Electrical Engineering, University of Texas at Austin*  
*Contact: mikjam54@yahoo.com, banerjee@ece.utexas.edu*

### Abstract:

The purpose of this project was to examine the effects of thermal annealing on film quality germanium (Ge) grown directly on silicon (Si), as measured by atomic force microscopy (AFM). The temperature stability of the Ge-on-Si films was observed for different annealing temperatures and times.

AFM scans the sample surface to image the surface topography. These images can then be used to determine the surface roughness of the films, which indirectly provides an indication of film quality. For this experiment, thermal annealing conditions were applied to a set of eight wafers, each with a different Ge-on-Si growth condition. Each wafer was labeled and subdivided into 10 pieces.

The first set of four wafers consisted of blanket Ge films grown over the entire Si wafer, with no additional layers. The second set had blanket Ge films, but with a thin high- $\kappa$  dielectric deposited on top. The 10 pieces of each wafer consisted of a control piece (with no thermal annealing), a piece used for film thickness measurement by AFM step height, 4 pieces that underwent rapid thermal annealing, and 4 pieces that were furnace annealed.

All eighty pieces (8 wafers times 10 pieces each) were measured using the AFM system.

### Introduction:

Metal-oxide-semiconductor (MOS) capacitors are two-terminal semiconductor devices where a dielectric insulator separates the metal from the semiconductor. The insulator is silicon dioxide ( $\text{SiO}_2$ ) because of its compatibility with conventional Si processes. The MOS capacitor is the foundation the metal-oxide-semiconductor field-effect transistor (MOSFET) device. The MOSFET structure comprises a gate layered on an insulator, layered on a semiconductor channel that separates the source and drain. When a voltage is applied to the gate, the MOSFET operates as a semiconductor switch that connects the source and drain terminals by creating a conducting channel region filled with charge carriers (electrons or holes). The gate of the MOSFET controls the number of charge carriers in the channel.

The charge carriers in the channel have a property called mobility ( $\mu$ ). The mobility of the charge carriers determines the current capacity of the MOSFET, which in turn determines the switching speed of a logic circuit that incorporates MOSFETs. The advantage of Ge is it produces higher  $\mu$  (for both electrons and holes) than Si. It's difficult to grow Ge on Si because of the 4% larger lattice constant of Ge compared to Si. However, very thin Ge films can still be grown on Si at low growth temperatures. The thermal stability of these thin Ge-on-Si films should be examined to determine their resilience to high-temperature processing.

Ge MOSFETs have drawn more attention in the research literature in recent years due to the advent of high- $\kappa$  dielectrics. High- $\kappa$  dielectrics have been shown to be compatible with Ge. In addition, high- $\kappa$  dielectrics are effectively thinner (but physically thicker) than  $\text{SiO}_2$  layers because of their higher dielectric constant, therefore reducing gate leakage.

Figure 1 shows leakage characteristics for a Ge-on-Si film with hafnium oxide ( $\text{HfO}_2$ ) dielectric and TaN metal, which are greatly affected by film quality. The purpose of this work is to improve leakage characteristics of Ge-on-Si MOS capacitors. Since the Ge film quality determines the electrical quality

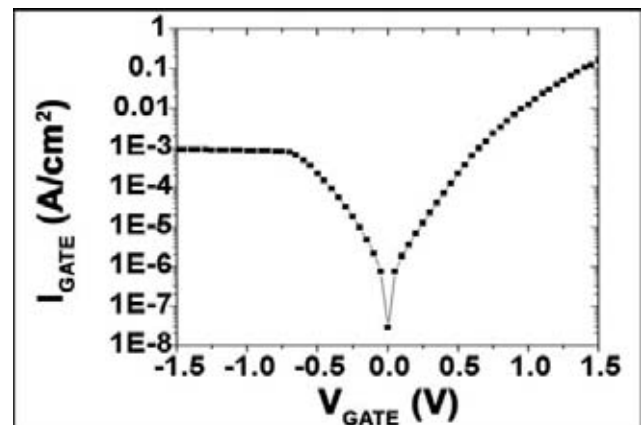


Figure 1: Gate leakage characteristics of Ge-on-Si MOS capacitor.



of the MOS capacitors, it is important to study how film quality maintains throughout the MOS fabrication process, so thermal stability studies have been performed for thin Ge-on-Si films.

### Experimental Procedures:

The Ge-on-Si films were already fabricated for use, using ultra-high-vacuum chemical vapor deposition (UHVCVD). The high- $\kappa$  deposition,  $\text{HfO}_2$ , was sputtered over the germanium at 60-70 Å thickness, deposited by reactive DC magnetron sputtering.

After the growth process was completed, the eight wafers were labeled with an alphabet and then split into 10 pieces where a number (ranging from 0-9) was applied. By doing so, we are able to then apply thermal annealing conditions properly in accordance to the number. The 10 pieces of each wafer consisted of a control piece (piece 8, with no thermal annealing), a piece (piece 9) used for film thickness measurement by AFM step height, 4 pieces (pieces 4-7) that underwent rapid thermal annealing (RTA), and 4 pieces (pieces 0-3) that were furnace annealed. Then time (in minutes), temperature (in  $^{\circ}\text{C}$ ), roughness (in nanometers, nm), and the film's thickness were recorded for each sample.

### Conclusion:

Figure 2 shows a comparison on blanket Ge films both furnace (left set of plots) and RTA (right set of plots) anneals. There was no significant difference in roughness between furnace and RTA annealed samples.

In Figure 3, we see that the Ge films with no high- $\kappa$  have higher roughness than those films with high- $\kappa$  whether furnace or RTA annealed under the assumption that the high- $\kappa$  improves the stability of Ge. At 600 $^{\circ}\text{C}$ ,

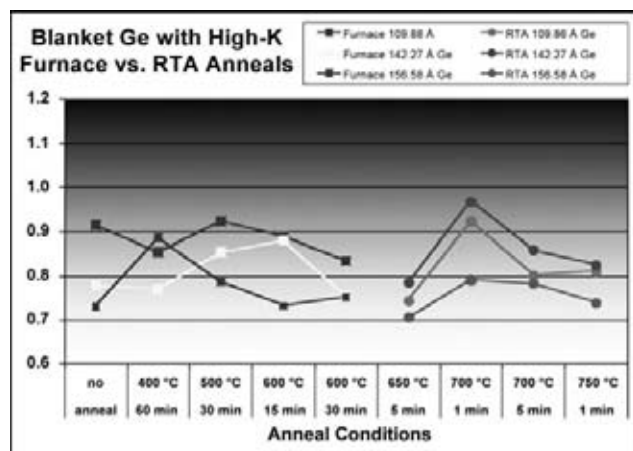


Figure 2. Comparison of surface roughness for furnace and RTA annealing.

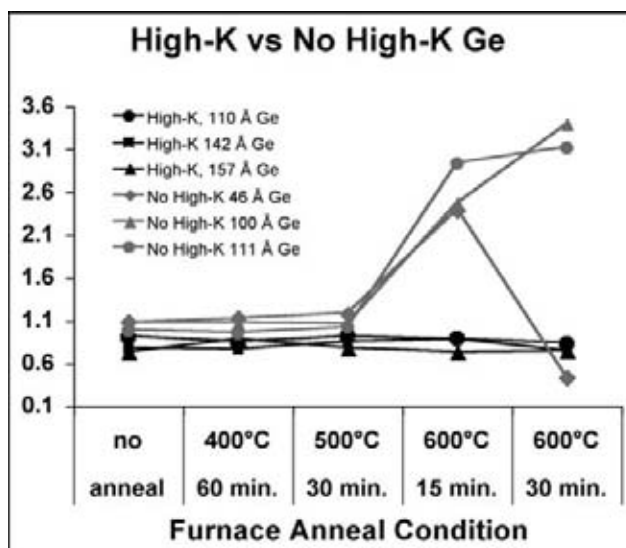


Figure 3. Comparison of surface roughness for high- $\kappa$  and non-high- $\kappa$  samples.

30 min, the plot dropped because all of the Ge desorbed off, leaving only bare silicon to be measured.

### Future Work:

Future revisions will focus on the study of area dependency, which would require developing patterned wafers. The patterned wafers will consist of a field oxide layer thermally grown on a Si wafer with windows, with different areas etched into the oxide and Ge selectively grown inside the patterned windows. The objective is to compare the blanket wafers to the patterned wafers to see which film has a higher quality when used for Ge MOSFETs. The completion of RTA anneals for blanket Ge films without a high- $\kappa$  are needed to be compared to RTA anneal with the additional layers.

### Acknowledgment:

Thanks to Ms. Melanie-Claire Mallison, Ms. Amy Pinkston, Dr. Sanjay Banerjee, NSF, Semiconductor Research Corp, Joe Donnelly, David Kelly, and Isaac Weidmann.

### References:

- [1] R. F. Pierret, "Field Effect Devices," Second Edition, Addison-Wesley, 1990.
- [2] B. G. Streetman and S. Banerjee, "Solid State Electronic Devices," Fifth Edition, Prentice Hall, 2000.

## Limits of Adaptive Liquid Lens

**Joy Johnson, Electrical & Computer Engineering, North Carolina State University**  
**NNIN REU Site: Cornell NanoScale Science and Technology Facility, Cornell University**

*NNIN REU Principal Investigator: Prof. Sandip Tiwari,  
Director of NNIN; Electrical & Computer Engineering, Cornell University*  
*NNIN REU Mentor: Jay S. Van Delden, Visiting Scientist, Electrical and Computer Engr, Cornell University*  
*Contact: jmjohns4@ncsu.edu, st222@cornell.edu*

### Abstract:

Practical limitations of a variable liquid lens using an electrowetting effect are investigated. Electrowetting, the change in contact angle at a solid-liquid interface as a result of an applied voltage, can be used to control the focal length of a liquid lens. SU8 chambers are prepared on a fused silica substrate with TiN electrodes, an Al mask layer, SiO<sub>2</sub> dielectric layer and FOTS hydrophobic monolayer. Excitation of the resulting chambers causes variations in the observed far-field diffraction patterns thus verifying electrically-induced changes in refractive power. Such changes to  $\mu\text{m}$ -sized lenses could be used for spatial light modulators, CCD cameras, and 3D displays in adaptive optics.

### Introduction:

In order to investigate the practical size limits of the electrowetting effect, we had to define a process in which we could create variable-size liquid chambers on the micron scale. Initially, experimental procedures were performed on microscope slides to determine which films to use, as well as their respective thicknesses, in order to successfully show the electrowetting effect. Applying the knowledge gained in this preliminary setup, we fabricated arrays of micro lenses on a quartz substrate and performed tests using both a microscopic and laser setup.

### Experimental Procedure:

For the preliminary setup, we characterized the materials and thicknesses for the electrodes (31 nm of titanium nitride, TiN), dielectric layer (500 nm of silicon dioxide, SiO<sub>2</sub>), and hydrophobic monolayer (Fluorooctyl Trichlorosilane, FOTS) on microscope slides. A droplet of salt water (0.5M) was placed on the microscope slide and a voltage applied to the electrodes to show proof of principle.

For the wafer embodiment, we used the following procedure: First, we patterned the quartz substrate using our first mask, processing SPR 220-7.0 resist approximately 10  $\mu\text{m}$  thick for etching. After the soft bake, the wafer was exposed to UV light using the

EV620 at 12 mW/cm<sup>2</sup>. Next, the quartz was dry etched approximately 3.6  $\mu\text{m}$  deep using a CHF<sub>3</sub>/O<sub>2</sub> recipe. To create the bottom electrode, a thin conductive layer of TiN was sputtered onto the quartz substrate at a thickness of approximately 30 nm. The aluminum mask was then evaporated on top of the TiN layer approximately 250 nm thick.

Next, a thick layer of SPR 1075 photoresist, approximately 11  $\mu\text{m}$ , was spun on as a "planarization agent." After the softbake, the resist was baked for 180 minutes in a 90°C oven in order to get the resist as hard as possible. In order to planarize the resist we used a Strasbaugh Chemical Mechanical Polisher (CMP), with an oxide recipe, in intervals of 5 seconds, in order to planarize the resist to be flush with the top of the wells, until the aluminum was visible. Following planarization, the substrate was flood exposed to allow any solvents to escape, avoiding reactions between the photoresist and the SU8. Then, to dehydrate the surface, the substrate was baked 90 minutes in a 90°C oven and oxygen plasma cleaned to optimize surface adhesion prior to further resist processing.

Next, the SU8 was processed and patterned with the second mask to form liquid chambers. The SU8, at a thickness of approximately 50  $\mu\text{m}$ , was exposed to UV light using a contact aligner (EV620). After the SU8 was developed, the planarizing agent, SPR 1075 photoresist, was cleared completely using an oxide etch.

Finally, for the top electrode, another thin, conductive layer of TiN was sputtered onto the substrate at a thickness of approximately 31 nm. SiO<sub>2</sub> was deposited as the dielectric layer using evaporation at a film thickness of approximately 500 nm. Lastly, we deposited a hydrophobic monolayer of FOTS. Our completed devices are shown in the SEM images in Figures 1 & 2.

### Results and Conclusions:

In order to observe and investigate the electrowetting effect in our SU8 wells, we used an optical setup in which a HeNe laser beam was reflected by two mirrors

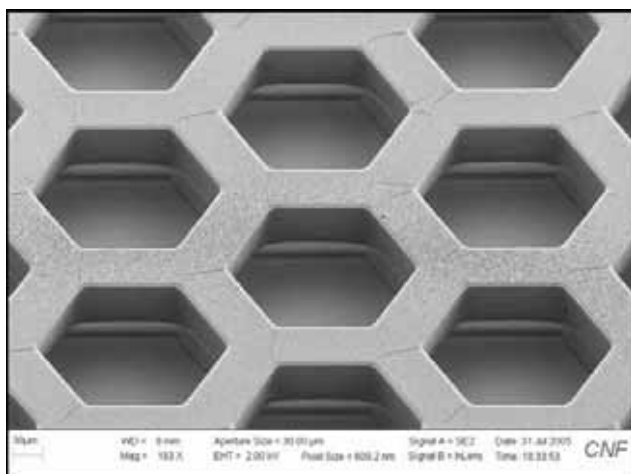


Figure 1: Hexagonal arrays apertures.

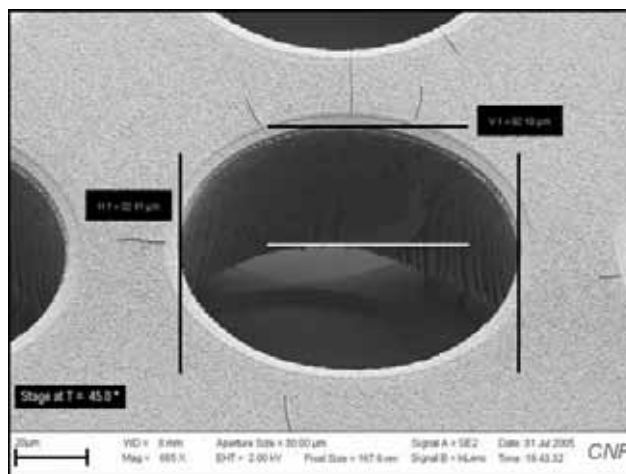


Figure 2: Circular array apertures.

and then through the apertures on our wafer. The apertures were filled with a polar liquid (salt water of 0.5M) and increasing voltages were applied to the top and bottom electrodes from 0 to 100 volts. Using the laser, we were able to observe the diffraction patterns created by the aperture before, during, and after voltage application; the diffraction pattern allowed us to observe electrically induced changes taking place on the microscale (Figures 3 & 4). The 200  $\mu\text{m}$  leg hexagonal aperture was the microlens in which we observed definitive effects taking place. We also performed a test using microscopy, observing changes in focal length with the application of a voltage. The results obtained using microscopy were less definitive than those yielded by the observation of diffraction patterns.

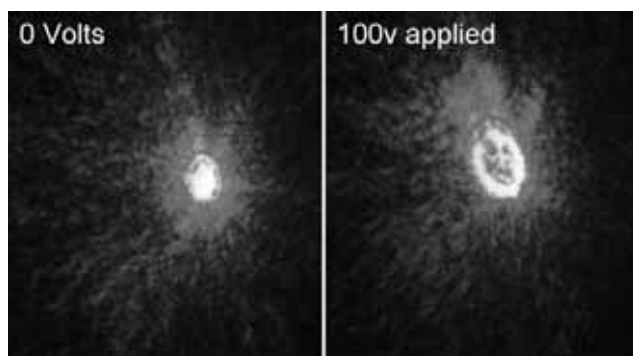


Figure 3, left: Diffraction pattern prior to voltage. Figure 4, right: Diffraction pattern after 100V applied.

### Future Work:

In order to optimize our device, we would like to make some changes to our mask design in order to create a more distinct separation between the top and bottom electrodes during processing to solve the problem of shorts in the wafer. In addition, we would also like to isolate the arrays such that each array can be probed and excited individually as opposed to the excitation of the entire wafer. In the future, we would like to perform software simulations to investigate wave propagation through the arrays of apertures due to the electrowetting effect.

### Acknowledgements:

I would like to thank my PI, Professor Sandip Tiwari, my mentor Jay Van Delden, and my co-researcher Rohit Gupta. I would also like to thank Dr. Michael Guillorn for his help with my SEM photos, as well as the rest of the CNF staff. Special thanks to the Intel Foundation for funding this project.

### References:

- [1] Lazar, Paul PhD. Dissertation Seminar, Max Plank Institute. Contact angle and wetting films. July 30, 2004. URL <http://www.mpikg-golm.mpg.de/gf/1> Accessed August 21, 2004.
- [2] M. Vallet, M. Vallade et B. Berge, "Limiting phenomena for the spreading of water on polymer films by electrowetting", Eur. Phys. J. B11 (1999) 583-591.
- [3] C. Quilliet, Bruno Berge, "Investigation of effective interface potentials by electrowetting" Eurphysics letter, 1 October 2002, PP 99-105.
- [4] Duke University; [www.ee.duke.edu/Research/microfluidics/](http://www.ee.duke.edu/Research/microfluidics/)

## Characterization of Nanoimprinting HSQ Material

**Thaddeus Koehn, Electrical Engineering and Physics, University of Rhode Island**  
**NNIN REU Site: Michigan Nanofabrication Facility, The University of Michigan**

*NNIN REU Principal Investigator: Lingjie (Jay) Guo, Electrical Engineering, University of Michigan*

*NNIN REU Mentor: Li-Jing (Larry) Cheng, Electrical Engineering, University of Michigan*

*Contact: tkoehn@mail.uri.edu, guo@eecs.umich.edu*

### Abstract:

Nanoimprinting is a technique for creating nanostructures based upon mechanical embossing. This process uses a mold with nanoscale surface relief structures to press into a polymer layer cast on a substrate. Under high pressures, the polymer will be shaped by the mold.

We will be looking at the rheological behavior, which determines how the polymer will deform under varying pressures and temperatures. We will look specifically at hydrogen silsesquioxane (HSQ) and find how it will behave in the imprinting process. Determining whether this polymer has a Newtonian (or viscosity independent of shear stress), or non-Newtonian flow will allow us to better understand the nanoimprinting process. Understanding how time and pressure affect the depth of an imprint will make it possible to precisely engineer devices using this method.

### Introduction:

Nanoimprinting makes use of a hard mold containing nanoscale features as a pattern. That pattern is then replicated by embossing it into a polymer material found on a substrate. The process takes place under controlled temperature and pressure conditions. This mechanical process of deforming the polymer material does not have the resolution limiting factors common in the more traditional lithography approaches.

One of the more critical parts of this process is the specific polymer material. This material must have properties of interest to the project at hand, whether electrical circuits or nanofluidic channels, and more critically, the material must be amenable to the deformation process required of nanoimprinting.

Hydrogen silsesquioxane (HSQ) is one such material that has properties which make it of strong interest in the nanoimprinting field. HSQ, in contrast to many other polymers, can be imprinted at room temperature. The material also possesses a low dielectric constant. This makes it an ideal material for providing insulation within an electrical circuit. Finally, it also is hydrophilic, which means that it has a strong affinity to

water, which makes it ideal for constructing nanofluidic channels. These properties make it important to study how HSQ behaves in the imprinting process and characterize it so as to make the material useful for mass production.

This characterization requires that we understand how HSQ will deform under stress—the science of rheology. Shear is a deformation in which both elasticity, which is reversible, and flow, which is irreversible, deformations take place. The shear rate ( $\dot{\gamma}$ ) is defined as the change in velocity of flow at which one layer of fluid passes over an adjacent layer. To simplify our model, we will treat the polymer as an ideal viscous fluid which will exhibit only deformation of flow and not those associated with that of elasticity. The stress ( $\sigma$ ) is the force per unit area. The viscosity ( $\eta$ ) of an ideal viscous body is defined as the stress divided by the shear rate,  $\eta = \sigma/\dot{\gamma}$ .

Fluids that exhibit a constant viscosity are known as Newtonian fluids. The plot of the stress vs. shear rate would reveal a straight line with the slope being the viscosity. An example of a Newtonian fluid would be air or water, their viscosity remains constant regardless of the force, and thus stress, exerted. There also exist non-Newtonian fluids whose viscosity is not constant.

### Theory:

Figure 1 shows how the polymer will deform under stress exerted downward. We see that the greatest

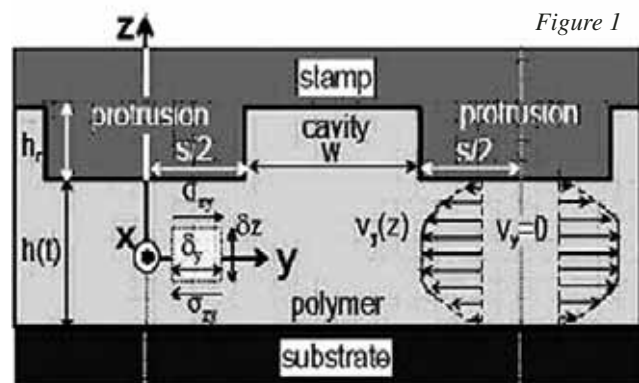


Figure 1



velocity change will take place underneath the protrusion. By modeling the polymer as an ideal fluid, we can derive equations for how the imprint depth will behave as a function of pressure and time. We find that the imprint depth will be proportional to the pressure to the  $-k/(k+1)$  power. Imprint depth is proportional to time to the  $-1/(k+1)$  power. Here  $k$  is a property of the material.

### Procedure:

We used a mold with a grating pattern consisting of a large set of parallel straight-line protrusions. From a cross section they can be considered a square wave with an amplitude or height of  $0.5\ \mu\text{m}$  and a period of 700 nm. The width  $s$  of the protrusion and valley would then be 350 nm. The polymer HSQ was first spun on to a silicon substrate at 1500 rpm for 10 seconds after which the mold was immediately applied. Pressure was applied 105s after the spinning was completed. The sample was then imprinted under a variety of time and pressure combinations, and the imprint depth of the sample was measured using SEM.

### Results:

We plotted the imprint depth vs. pressure for a time of 10 minutes and suggested a possible fit in the dotted line of Figure 2. The solid line represents what a Newtonian fluid would act like.

In Figure 3, imprint depth vs. time is plotted for a pressure of 850 PSI in the dotted line with the Newtonian as the solid line.

We also found that there was variation in the data depending on the day of the imprinting, so Figure 4 shows depth vs. time at 750 PSI.

### Conclusion:

According to both Newtonian and non-Newtonian theory, the imprint depth vs. pressure graph (Figure 2) should resemble a Newtonian curve if  $k$  is small. However, we see a difference in the imprint depth vs. time graph (Figure 3), as our data is concave upward while the Newtonian fluid is concave downward.

Figure 4 shows that the imprint depth decreases with time, an impossibility according to both ideal Newtonian and non-Newtonian flow models. Such a deviation forces the conclusion that there were other unaccounted for variables. Several possibilities exist to account for this behavior. One such possibility is a change in the humidity which could easily affect how the HSQ deforms. Also our theory ignored elasticity. If we consider a visco-elastic model, the data would be a better fit. That would require plotting the speed at which the stress is applied.

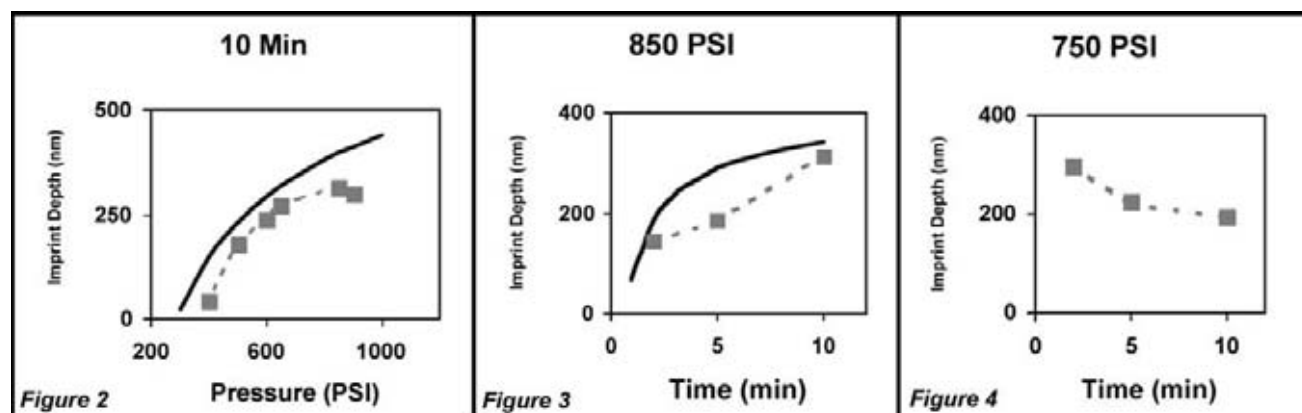
We can conclude from Figure 3 that HSQ behaves similar to an ideal non-Newtonian fluid, however other factors are involved which will require additional research.

### Acknowledgements:

Many thanks to L. Jay Guo, Larry Cheng, Philip Choi, and Song Ge.

### References:

- [1] Ge, Song; Thin Film Rheology in Nanoimprinting.
- [2] H. Schiff, L. Heyderman, Nanorheology: Squeeze Flow in Hot Embossing of Thin Films, Paul Scherrer Institut, Villigen PSI, Switzerland.
- [3] L. Jay Guo, Recent Progress in Nanoimprint Technology and its Applications, Journal of Physics D: Applied Physics, (2004).



## **Fabrication of Gold/Chrome Microparticles to be Used in Drug Delivery Applications**

**Arthur K. Kuehl, Materials Sciences & Engineering, University of Arizona**  
**NNIN REU Site: Minnesota Nanotechnology Cluster, University of Minnesota**

*NNIN REU Principal Investigator: Steven Campbell, Electrical Engineering, University of Minnesota*  
*Contact: akuehl53@yahoo.com, campbell@ece.umn.edu*

### **Abstract:**

The norm in drug delivery carriers is a polymeric shell that encapsulates drugs and escorts them to a targeted area. Metallic particles have the advantage of being smaller than polymeric carriers, and they are less likely to be removed from the body due to recognition as a foreign object. In this work, a process for making micron-sized metallic particles for use as drug delivery carriers was evaluated. These particles were gold and chromium coated silicon nitride made using known technologies such as photolithography and dry etching procedures. The scope of the project included analyzing the particles to find their stiffness, but this was not accomplished due to a lack of adhesion between the free particles and the sampling substrate.

### **Introduction:**

There are many challenges that must be overcome to construct a biopharmaceutical or biotechnological drug that is effective in the human body. Some of these challenges are: poor drug solubility, short half-life, poor bioavailability and drug targeting. Up to 90% of intravenously delivered drugs may be gathered up by macrophages within the first five minutes inside the body. Many other drugs simply cannot stand up to the environment of the blood and will break apart before reaching their targets [1].

The standard answer to this problem is to encapsulate and protect the drugs inside a carrier molecule. Many of these carrier molecules are polymeric micelles that are functionalized to limit recognition by the body's mononuclear phagocytic system (MPS), which is useful to increase half-life within the body, and also to place a targeting moiety on the particles [2].

A more novel answer to this problem would be to use a metallic microparticle as the drug carrier. These particles could have high affinity to biological molecules, and thus adhere very strongly, as well as slip through smaller channels. It is also advantageous to have the drug connected to the particle surface rather than inside a polymer matrix. Some metallic particles

(e.g. magnetite,  $\text{Fe}_3\text{O}_4$ ) also have the advantage of being able to be targeted through the use of magnetic fields [3].

The scope of this project included evaluating a procedure for fabricating microparticles and secondarily, characterizing the stiffness of the particles produced. Existing techniques used for photolithography, dry etching, wet etching, and metal deposition were employed.

The Atomic Force Microscope (AFM) was used to try to measure the stiffness of the fabricated particles. This device operated the cantilever in a mode in which the tip of the cantilever would come into contact with the surface of the sample. The stiffness of the material could be determined from force vs. displacement data gathered with the AFM.

### **Experimental Procedure:**

The beginning materials for this process were 4-inch Si wafers with phosphosilicate glass and low-stress nitride layers on the surface. The process used to fabricate these particles consisted of two separate photolithography procedures separated by metal deposition, and then a dry and a wet etch. The first photolithography left uncovered the shapes of the metallic layers on the nitride. The metal was deposited and the remaining photoresist was removed, thereby lifting off the unwanted metal. The second photolithography procedure left uncovered channels between the particles, which were dry-etched in order to eat the nitride out from between the particles. After this etch, an HF vapor etch was done to release the particles from the PSG layer beneath the nitride. The result of this final etch was an aqueous solution of gold/chrome microparticles on a nitride backing.

The particles fabricated were then spun onto wafers patterned with trenches in order to hold the particles for AFM sampling. The AFM was used to try and sample the stiffness of these particles.

## Results and Conclusions:

Metal-based particles in the micron-size range could provide an attractive alternative drug carrier for the biotechnology industry. In this work, a procedure utilizing well-known processes used in microchip production was developed to fabricate these particles. The procedure—including photolithography, and wet and dry etching—has proven to be effective in making particles on the micron scale with specific geometries. All four geometries—filled rectangles, filled circles, rectangular rings and circular rings—were successfully produced and harvested from the original wafer substrates.

## Future Work:

The main work remaining within the scope of this project is to image the particles produced, and determine their stiffness using the AFM. Using the probing tip of the AFM, force versus displacement data can be taken, and from this information, the stiffness of the particles can be calculated. This information about the stiffness of the particles is important in determining whether the nitride/metal microparticles could survive inside the body.

## Acknowledgements:

Thanks to Dr. Steve Campbell, Mark Fisher, and the NFC staff. Also, thanks to Greg Haugstad and the CharFac for their assistance. I also thank the NSF and the NNIN for providing funding. A very special thanks to the other REU students at UMN for making this a wholly wonderful summer experience.

## References:

- [1] Muller, R. H. and C. M. Keck. "Challenges and Solutions for the Delivery of Biotech Drugs - A Review of the Drug Nanocrystal Technology and Lipid Nanoparticles". *Journal of Biotechnology*. 113 (2004) 151-170.
- [2] Rosler, A., G. W. M. Vandermuelen, and H. Klok. "Advanced Drug Delivery Devices View Self-Assembly of Amphiphilic Block Copolymers". *Advanced Drug Delivery News*. 53 (2001) 95-108.
- [3] Chattopadhyay, P. and R. B. Gupta. "Supercritical CO<sub>2</sub> Based Production of Magnetically Responsive Micro- and Nanoparticles for Drug Targeting". *Ind. Eng. Chem. Res.* 41 (2002) 6049-6058.
- [4] Madou, Marc J. *Fundamentals of Microfabrication: The Science of Miniaturization*. CRC Press, LLC. Boca Raton, FL 2002.

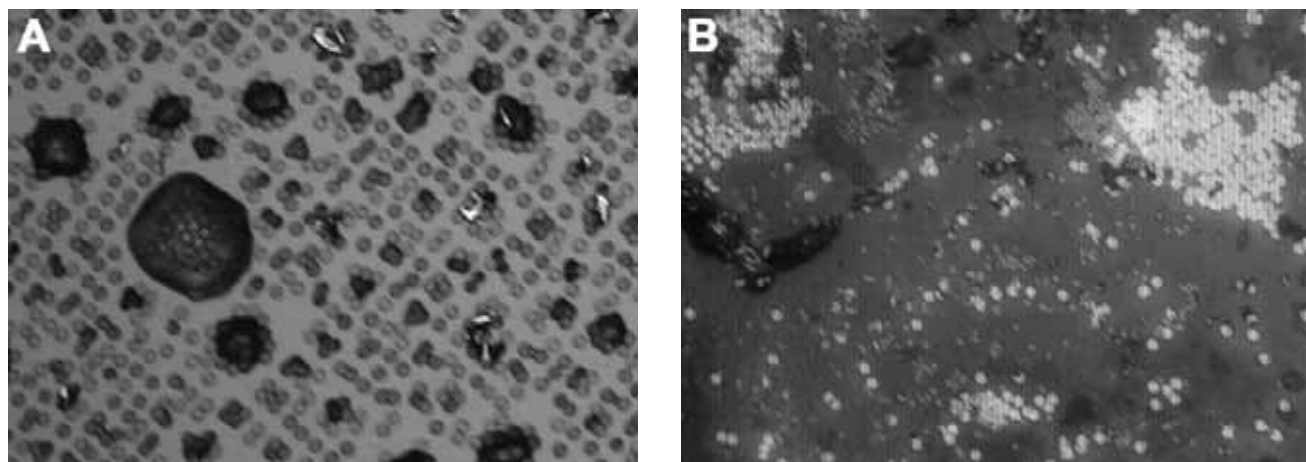


Figure 1: SEMs ~300  $\mu\text{m}$  across. A. Clumped particles previous to removal from substrate wafers. B. The wafer after the etching procedure was done to release the particles, showing how the particles continue to coagulate.

# Colloidal Dimers for Reduced Symmetry Photonic Crystals

Amy Lee, General Engineering, Franklin W. Olin College of Engineering  
NNIN REU Site: Cornell NanoScale Science and Technology Facility, Cornell University

NNIN REU Principal Investigator: Chekesha Liddell, Materials Science and Engineering, Cornell University

NNIN REU Mentor: Stephanie Lee, Materials Science and Engineering, Cornell University

Contact: amy.lee@students.olin.edu, cliddell@ccmr.cornell.edu

## Abstract:

The primary concentration of this project was to synthesize monodispersed, non-spherical, high refractive index colloids with a well-defined, asymmetric shape to be used as building blocks for photonic crystal structures with stable three-dimensional bandgaps. To achieve this aim, crosslinked polystyrene seed particles with varying levels of divinylbenzene (DVB) were synthesized. A seeded dispersion polymerization technique was utilized to swell the seed particles and create polystyrene dimers. Samples containing the asymmetric particles, along with other morphology types, were synthesized. Parallel to the dimer synthesis, we have successfully coated polystyrene seed particles with materials of high refractive index, such as zinc sulfide and titania. These core-shell particles were used to create hollow high refractive index shell structures by dissolving the polystyrene core with toluene. Polystyrene/DVB and coated particles were characterized via SEM.

## Introduction:

Photonic crystals are dielectric structures with a periodic variation in the refractive index which may permit the manipulation of light in the same manner as semiconductors do for electrons. This property can lead to applications in zero-threshold lasers, coherent LED emission and low-loss waveguiding for all optical circuits. Computational studies have shown that using non-spherical building blocks in constructing the face-centered cubic lattice can break the symmetry-induced degeneracy of the photonic band structure. An additional condition under which a photonic crystal will exhibit a complete bandgap is a minimum contrast in refractive index between the two dielectric materials. In order to satisfy this condition, particles may be coated with high refractive index materials and then turned into hollow particles through dissolution of the core.

## Experimental Section:

**Polystyrene Seed Particles Crosslinked with DVB:** Monodispersed particles of 400-500 nm dia. were obtained by combining the following reagents: 50 mL ethanol, 20 mL deionized water, 3 mL purified styrene, 73.3 mg sodium lauryl sulfate (SLS), and 66.7 mg potassium persulfate (KPS). Crosslinking densities from 0.5% to 3% were achieved by substituting DVB for the corresponding percentage of styrene. The mixture was then magnetically

stirred and polymerized at 70°C for 24 hours before being washed and resuspended in ethanol.

## Polystyrene Peanuts using Seeded Dispersion

**Polymerization:** Crosslinked polystyrene/DVB spheres were first resuspended into a 2 wt% EtOH/H<sub>2</sub>O solution. Then, 35 mL of EtOH/H<sub>2</sub>O solution, 5 mL P(S/DVB) solution, 0.4 mL styrene, 47.5 mg SLS, and 33.3 mg KPS were mixed in a 100 mL bottle. The solution was stirred for 24 hours to allow swelling of the crosslinked particles. Then, polymerization was initiated by raising the temperature to 70°C for an additional 24 hours. Refer to Figure 1.

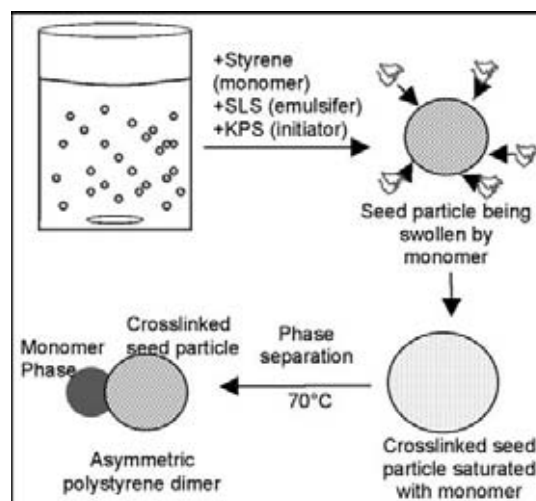


Figure 1: Synthesis schematic for polystyrene peanuts via seeded dispersion polymerization.

## Polystyrene Spheres Coated with Zinc Sulfide:

Coating of un-crosslinked polystyrene spheres was done using a chemical bath deposition technique. First, 0.2g poly(vinylpyrrolidone) (PVP), 0.5 mL polystyrene, and 50 mL deionized water were added to a 200 mL volumetric flask and sonicated. Next, 0.6060g zinc nitrate, 0.0430g manganese nitrate, and 1.4370g thioacetamide were dissolved into the flask. Deionized water was added to balance and the solution was transferred to a heated water bath at 85°C for either 1, 1.5, or 2 hours. The reaction was terminated by quenching the solution to below 10°C in an ice bath. To remove the polystyrene cores, an excess of toluene was added to the coated spheres overnight.

**Polystyrene Spheres Coated with Titania:** Coating of un-crosslinked polystyrene spheres was done through the hydrolysis of titanium tetraisopropoxide (TTIP) in a method



adapted from Imhof [1]. The following reagents were mixed in a 100 mL bottle: 27 mL ethanol, 289 mg PVP, 672.04  $\mu\text{L}$  5 mM NaCl solution, 10 mL polystyrene, and 302.4  $\mu\text{L}$  TTIP in 4 mL ethanol. Hydrolysis occurred rapidly after 1 minute of stirring and the suspension was allowed to stand for 15 minutes before washing and redispersing in ethanol.

## Results and Discussion:

**Polystyrene Seed Particles Crosslinked with DVB:** Particles with 0.5%, 1%, 1.5%, 2%, and 3% DVB were successfully synthesized. In order to verify monodispersity, the coefficient of variation (standard deviation/mean) was calculated and confirmed to be under 9%. An interesting result of a synthesis of P(S/3%DVB) done at 90°C was that peanut-shaped particles were formed. This is likely due to particle aggregations arising from collisions above the glass transition temperature. This sample contained a large percentage of dimers that may be separated, leading to possibilities of a one-step process of the formation of polystyrene peanuts.

**Polystyrene Peanuts using Seeded Dispersion Polymerization:** An early experiment using P(S/0.2%DVB) seed particles in 5:2 EtOH:H<sub>2</sub>O produced ellipsoidal-shaped particles, trimers, tetramers, and spherical particles speculated to be a new nucleation of seed particles (See Figure 2: P(S/2%DVB) seed particles in 5:2 EtOH:H<sub>2</sub>O). Literature has shown that smaller particles require a larger percentage crosslinking in order to exhibit phase separation, so the next experiment was done with P(S/2%DVB). Additionally, the solution was changed from a 5:2 EtOH:H<sub>2</sub>O to 2:5 EtOH:H<sub>2</sub>O in order to encourage swelling of the monomer in seed particles. The result of the modified experiment was a nearly uniform solution of agglomerated football-shaped particles. While these particles are not useful due to agglomeration, the uniform building block formed is encouraging. Another experiment was run using P(S/3%DVB) in a H<sub>2</sub>O solution. Again, some ellipsoids were synthesized in addition to swollen spheres and other morphologies.

**Polystyrene Spheres Coated with Zinc Sulfide:** Longer experimental times created a more uniform, thicker coating of ZnS on the polystyrene spheres. The coating thicknesses were measured to be 70.5 nm, 84 nm, and 99.5 nm for the 1, 1.5 and 2 hour experiments, respectively (See Figure 3: Hollow ZnS shells - 2 hour deposition). Verification for the coating material was conducted using energy dispersive spectroscopy.

**Polystyrene Spheres Coated with Titania:** The titania coating was fairly uniform with a thickness of 44 nm (See Figure 4: TiO<sub>2</sub> coated polystyrene.). Formation of secondary titania particles may be due to the use of anionic polystyrene spheres as compared to the cationic ones reported by Imhof. Thicker coatings may likely be achieved by increasing the TTIP concentration.

## Conclusions:

In the future, focus will be placed on creating uniform polystyrene dimers, which may require higher crosslinking densities. Additionally, a one-step peanut process by

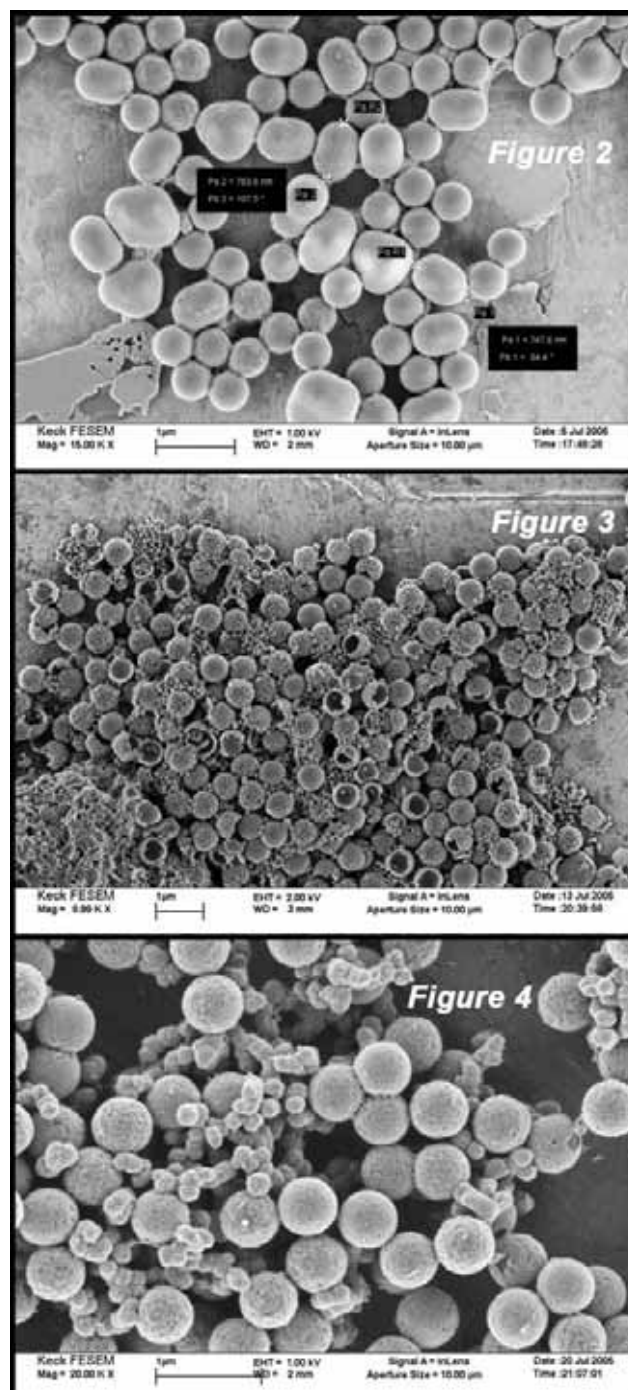
controlling emulsifier quantity and reaction temperature may be used. Coatings using tin sulfide and noble metals will be done. Once dimers are formed, we will try to assemble them using template-assisted self assembly and proceed to characterize the crystals.

## Acknowledgements:

I would like to thank Dr. Cheksha Liddell and Stephanie Lee for their incredible support and guidance.

## References:

- [1] Imhof, A. Langmuir 2001, 17, 3579-3585.



# Structural & Physical Characterization of Supramolecular Diblock Copolymers

**Cheng-Yuk Lee, Chemical Engineering, University of Massachusetts Amherst**  
**NNIN REU Site: Nanotech, University of California at Santa Barbara**

*NNIN REU Principal Investigator: Dr. Edward J. Kramer, Chemical Engr, University of California Santa Barbara*

*NNIN REU Mentor: Kathleen E. Schaefer, Materials Dept, University of California Santa Barbara*

*Contact: ChengL@student.umass.edu, dkramer@mrl.ucsb.edu, schaefer@mrl.ucsb.edu*

## Abstract:

Recent interest in diblock copolymers has grown because of their ability to form periodic structures on the size scale of 10-100 nm; hence, these materials can be used for advanced lithographic templating applications. However, supramolecular diblock copolymers, in which the bond between the two blocks can be reversibly broken at high temperature, have not yet been effectively characterized. In order to better understand their behavior, we are developing a model covalent diblock copolymer system. We were especially interested in measuring their order-disorder transition (ODT) temperatures ( $T_{ODT}$ ) by using small-angle X-ray scattering and rheology to determine the relationship between  $T_{ODT}$  and the degree of polymerization, providing a reference point for future studies of more complex systems.

## Introduction:

Block copolymers are very common in our daily life, for example in upholstery foam and adhesive tape [1]. Diblock copolymers consist of two thermodynamically incompatible homopolymers linked by a covalent bond. Due to thermodynamic incompatibility, they tend to phase separate from each other. The phase separation depends on three variables: temperature, chemical incompatibility, and chain length. At temperatures below the characteristic ODT, the two blocks microphase separate; however, above  $T_{ODT}$  they become miscible. The goal of this project is the measurement of  $T_{ODT}$  for symmetric diblock copolymers of different molecular weights of poly(benzyl methacrylate-block-tert butyl acrylate) (P(bnMA-b-tBA)).

## Materials and Procedure:

Living free radical polymerization by reversible addition-fragmentation (RAFT) was used to synthesize the symmetric diblock copolymers [2]. The synthesis of p(bnMA-b-tBA) involved two steps. First poly(benzyl methacrylate) was synthesized by dissolving benzyl methacrylate (3.3M), RAFT agent (0.066M), and 2,2'-Azobis(2-methylpropionitrile) (AIBN, 0.0132M) initiators in 10 mL of dioxane. The reaction mixture

was sealed in a glass ampule under vacuum and heated at 70°C for the desired reaction time, then cooled and precipitated into methanol to isolate the p(bnMA) macro-RAFT agent. The second block was added by mixing tert-butyl acrylate (4.5M) with p(bnMA) macro-RAFT agent (0.0155M) and AIBN (0.9M) into 10 mL of dioxane. The reaction mixture was again sealed under vacuum and heated at 70°C for their desired reaction time.

Polymers were characterized by nuclear magnetic resonance (NMR), gel permeation chromatography (GPC) and rheology. NMR was used to determine the conversion of the reaction and the estimated molar composition of the diblock copolymers. GPC was used to determine the average molecular weight ( $M_n$ ) of the polymer relative to polystyrene and the polydispersity index (PDI). Rheological measurements were performed to obtain the  $T_{ODT}$ .

## Results and Discussion:

In RAFT polymerizations, the molecular weight of the polymer can be controlled either by the reaction time or the molar ratio of monomer to RAFT agent in the reaction mixture. Polymerization kinetics were studied by keeping the reactant concentrations constant while running the reaction for different amounts of

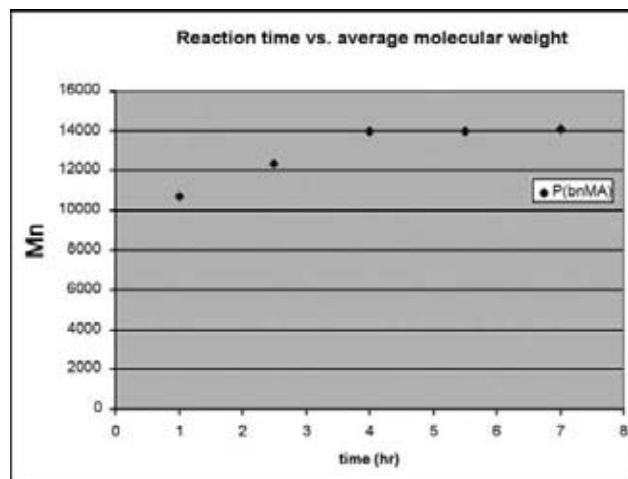


Figure 1: GPC data from poly(benzyl methacrylate) samples.

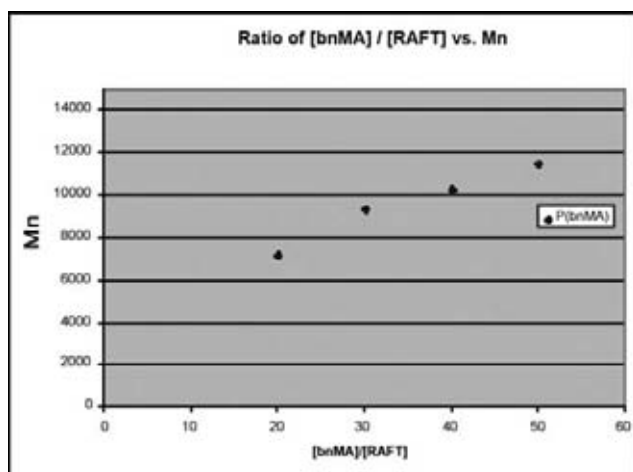


Figure 2: The relationship between  $M_n$  and concentration ratio of reactants.

time, ranging from 1 to 7 hours; Figure 1 is a plot of  $M_n$  as a function of reaction time, which indicated that the p(bnMA) reached a maximum molecular weight at a reaction time of 4 hours. Four different molecular weights were also synthesized by running reactions at ratios of 20, 30, 40, and 50 moles of monomer per mole of RAFT agent.

GPC data are plotted in Figure 2, which displays that the molecular weight is directly proportional to the molar ratio of monomer to RAFT agent.  $^1\text{H}$  NMR and GPC were run to determine the molecular weight as well as the diblock copolymer composition. In order for p(bnMA-b-tBA) to be symmetric (each block occupying the same volume), the number of monomers in the p(bnMA) block  $N_{\text{bnMA}}$  and p(tBA) block  $N_{\text{tBA}}$  must have the following relationship [3]:

$$N_{\text{tBA}} = 1.28N_{\text{bnMA}}$$

The estimated compositions were obtained by integrating the area of the corresponding peaks from  $^1\text{H}$  NMR data of p(bnMA-b-tBA), and are shown in Figure 3. It was observed that reaction time for the three lowest molecular weight p(bnMA) samples should be shorter than 0.5 hr.  $^{13}\text{C}$  NMR was also used to measure the composition of the highest molecular weight diblock copolymer, and the estimated p(tBA) block length was roughly 1.32 times that of p(bnMA), suggesting that the high molecular weight polymer was symmetric. This sample was then measured with the rheometer to determine  $T_{\text{ODT}}$ .

Due to instrumental limitations it was not possible to measure a clear transition, but it was certain that  $T_{\text{ODT}}$  was below  $80^\circ\text{C}$ .

## Conclusion & Future Work:

It was found that both reaction time and the concentration ratio of monomer to RAFT agent had major effects on the degree of polymerization. To compare the behavior of these diblocks against a related system in which the link between the two blocks can be broken at higher temperatures, it is necessary to study higher molecular weights with  $T_{\text{ODT}}$  around  $100^\circ\text{C}$  to  $150^\circ\text{C}$ . In the future, the covalent bonded diblock copolymers model system will be tested with small angle X-ray scattering (SAXS) and UV absorption. SAXS is an alternative method for determining the  $T_{\text{ODT}}$  as well as the morphology of the diblock copolymers, and UV absorption can be used to measure the absolute molecular weight of the diblock copolymers.

## Acknowledgement:

I need to thank National Science Foundation for funding my research, and I would like to give special thanks to my mentor Kathleen E. Schaefer and my principal investigator Dr. Edward J. Kramer for giving me the opportunity to work on this REU project. I also want to acknowledge the rest of Kramer's group, Dr. Craig Hawker and his group, Krystyna Brzezinska and Angela Berenstein.

## References:

- [1] F.S. Bates and G.H. Fredrickson, Block Copolymers-Designer Soft Materials, *Physics Today*, Feb 1999, 32-38.
- [2] S. Perrier, P. Takolpuckdee, and C.A. Mars, Reversible Addition-Fragmentation Chain Transfer Polymerization: End Group Modification for Functionalized Polymers and Chain Transfer Agent Recovery, *Macromolecules*, 2005, 38, 2033-2036.
- [3] This equation was obtained by Katie Schaefer, Materials Dept, University of California, Santa Barbara.

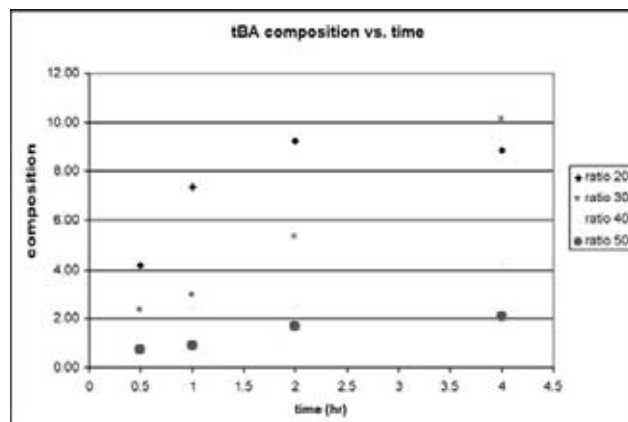


Figure 3: tBA block composition verse time.



# The Relationship of Line Edge Roughness and Contrast by Deep UV Immersion Interferometric Lithography

David Light, Molecular, Cellular and Developmental Biology, Yale University  
NNIN REU Site: Nanoscience @ UNM, University of New Mexico

NNIN REU Principal Investigator: Steve Brueck, Director, Center for High Technology Materials, UNM  
NNIN REU Mentor: Alex Raub, Center for High Technology Materials, University of New Mexico  
Contact: david.light@yale.edu, brueck@chtm.unm.edu

## Abstract:

In today's microchip industry, focus has been shifted to immersion lithography due to water's 44% higher refractive index than air for deep UV, which allows for lens NA values greater than 1. This new technology has been allowing for the printing of smaller and smaller structures on silicon wafers. However, the problem of the roughness of these features is gaining importance at such small sizes. This experiment attempts to ascertain the relationship between the severity of line edge roughness (LER) and the reduction of contrast.

To accomplish this task, 150 mm silicon wafers were coated with a dual layer of ARC and an 80 nm layer of IRC1500 positive photoresist. These wafers, behind a film of de-ionized water, were exposed to varying amounts of two-beam interferometric light and one beam light generated by a 193 nm Excimer Laser (this variance produces differing contrast), which produced a 71 nm half-pitch. The exposed areas were cleaved from the wafers, gold plated to  $\sim 40\text{\AA}$ , and viewed under a scanning electron microscope at 100 kX and 150 kX. The pictures taken from the SEM undergo a Fourier Transform which is analyzed to produce a value for the LER which can be plotted against the percent contrast used in the sample.

## Introduction:

In order to allow for the proliferation of faster, cheaper and smaller microchips, the immersing problem of LER (line edge roughness) must be fully understood. Since the primary and insurmountable problem causing LER is a loss of contrast, this paper investigates the direct mathematical relationship between contrast and LER.

## Procedure:

In order to create variable contrast, an interferometric setup was utilized (see Figure 1). This was achieved by splitting and recombining a 193 nm laser beam generated by an ArF Excimer Laser. The beam was split 50/50 with a fused silica beam splitter and then recombined through a window and a thin layer of water

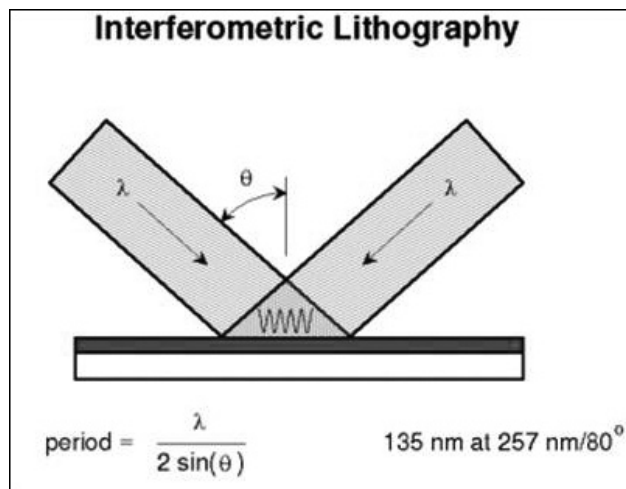


Figure 1: Diagram of interferometric lithography.

onto a silicon wafer coated with an 80 nm layer of IRC 1500 photoresist. Immersion was used to emulate immersion lithography conditions so that the effects of the interaction of water with the photoresist could be observed. Activating this set up with 120 laser pulses generated uniform lines approximately 65 nm thick and 65 nm apart with 100% contrast. To vary the contrast, a shutter was installed to block one of the split beams.

The one beam exposure had the effect of lowering the contrast of the two beam exposure by a factor of one fourth of the double beam pulses due to it having one fourth the intensity of an interferometric, two beam exposure. Since the power was kept constant in order to preserve a 1:1 ratio of line thickness to line spacing, the number of pulses was calculated according to [2-beam:  $(120-n)$  1-beam:  $(4n)$ ] and contrast calculated as  $[(\text{total 2-beam pulses})/120] \times 100$ .

Once exposures were generated with varying levels of contrast, the degree of roughness had to be quantitatively analyzed. To do this, exposures were first plated with approximately  $40\text{\AA}$  of gold and viewed under a scanning electron microscope at 100,000x and 150,000x (see Figure 2). At least eight pictures were taken of each exposure so that LER values could be averaged. In order to assign a quantitative value to



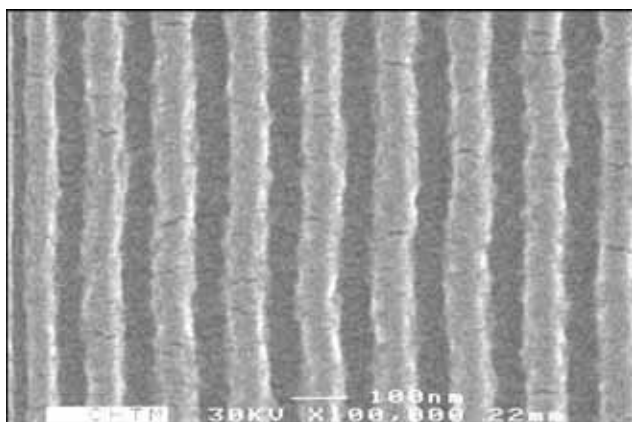


Figure 2: 100,000x SEM image of 70% contrast. Note horizontal gold cracks.

LER, Fourier Transforms were performed on the SEM pictures. Since the lines in the pictures were vertical, frequencies in the y-direction were averaged and full-width-half-maximum points were derived and recorded with respect to the number of pixels away from the center. This was necessary because the amplitude of the average frequencies in the y-direction was highly sensitive to the brightness of the images; a factor that could not be controlled.

### Results and Conclusions:

Data was compiled for both 150,000x and 100,000x in graphs plotting LER versus percent contrast. The resulting graphs showed a strong power and exponential relationship with the 150,000x data resulting in an  $R^2$  value of 0.8055 for a power regression and 0.7101 for exponential, and the 100,000x data displaying  $R^2$  values of 0.8787 and 0.8209 for the power and exponential regressions respectively. Combining the

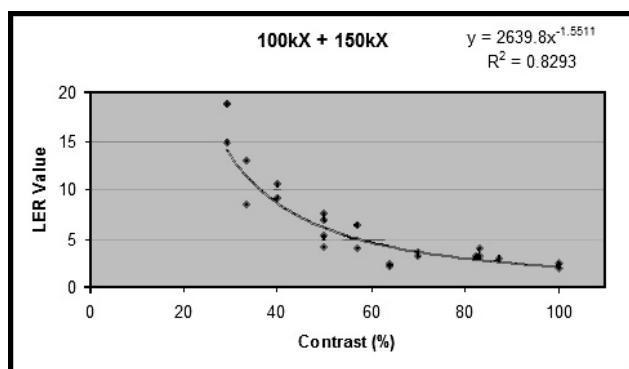


Figure 3: Power regression for 100,000x and 150,000x combined data.

data results in Figure 3. It was also observed, through side-view SEM images, that the “roughness” found on the lines was actually uniform across the breadth of the lines and their spaces instead of being confined to the edges (see Figure 4).

### Further Research:

Further research could be conducted on a few different related matters. First, and probably of greatest interest, would be to perform the same experiment in air and observe any differences. To possibly improve the accuracy of the data, one could repeat the same experiment but use more laser pulses at a lower energy so as to do a better job of averaging out the variations in the laser, use higher resolution images, and/or plate with chromium instead of gold to prevent gold cracks from creating artificial roughness or simply use a more powerful SEM that does not require metal plating.

### Acknowledgements:

For their integral role in this project, I would like to acknowledge and thank Alex Raub, Steve Brueck, Vanessa Porter, and the NNIN program.

### References:

- [1] Brueck, S. R. J. “Directions in Nanoscale Lithography and Pattern Transfer” PowerPoint (2005).

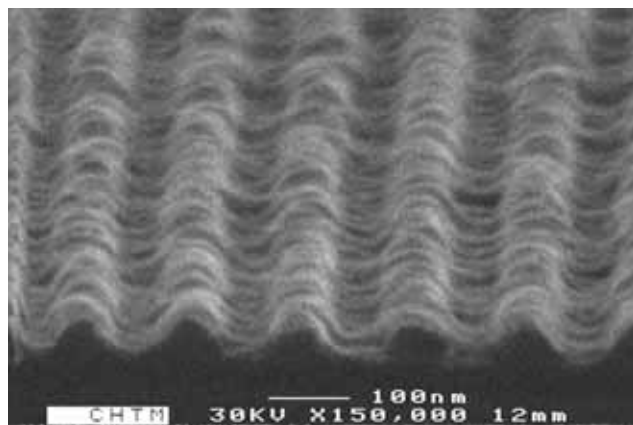


Figure 4: 150,000x side view of 50% contrast.

## Development of a Non-Contact DNA Spotting Method for Biosensors

**Wade Luhman, Mechanical Engineer, Minnesota State University Mankato**  
**NNIN REU Site: Stanford Nanofabrication Facility, Stanford University**

*NNIN REU Principal Investigator: Shan X. Wang, Material Science, Stanford University*

*NNIN REU Mentors: Nader Pourmand, Stanford Genome Technology Center,  
and Sebastian Osterfeld, Material Science, Stanford University*

*Contact: wade.luhman@mnsu.edu, sxwang@stanford.edu*

### Abstract:

Small, finely spaced magnetoresistive biosensors need to be individually functionalized with various DNA probes. Due to the small pitch of different functionalization spots, the functionalization chemistry is best applied to the biosensors with a precise robotic applicator. We currently have a robotic system that will perform DNA spotting with a hard needle. The present problem is that contact is needed to deposit the DNA onto the targeted sensor. The physical contact damages the sensor's surface which degrades its functionality.

By developing a non-contact approach, damage to the sensor will be avoided. Entirely contactless deposition of a DNA-containing fluid droplet is more difficult to achieve with a high degree of accuracy than hard-contact printing. Therefore we modified the current robotic system with new spotting pins and new software parameters that allow for DNA spotting with zero to minimal contact with the sensor surface.

Time restrictions made testing of the final system unfeasible. But once tested, the sensor can be examined using a scanning electron microscope and/

or tapping mode atomic force microscope to assess spot sizes, spotting uniformity, and the reduction of any damage to the sensor. If successful, the spotting technique can be carried over to a larger-scale production, allowing for cheaper and more standardized biochips.

### Introduction:

The biosensor system that is being developed will be used as a high-sensitivity DNA detection and identification system [1]. To ensure that the device functions correctly, it is important to individually functionalize each sensor with various DNA probes. Figure 1 shows an individual sensor. Currently, a microarray robotic system is being used to spot DNA onto the sensor. The microarray robot uses split pin spotting technology that requires physical contact to dispense fluid onto the intended substrate. Figure 2 shows a magnified view of the spotting process [2].

The goal of this project is to develop a method that will precisely spot DNA onto the surface of the sensor without the physical contact which damages the surface of the sensor.

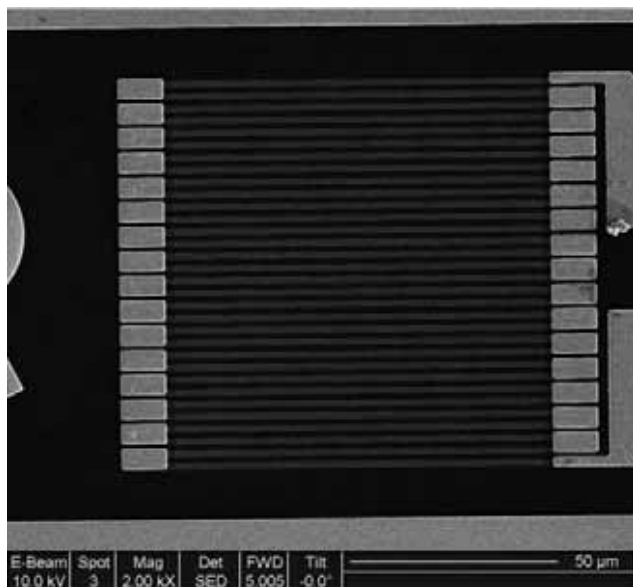


Figure 1: An individual sensor in the system. The sensor is  $90 \mu\text{m}^2$  and one of our spotting targets.

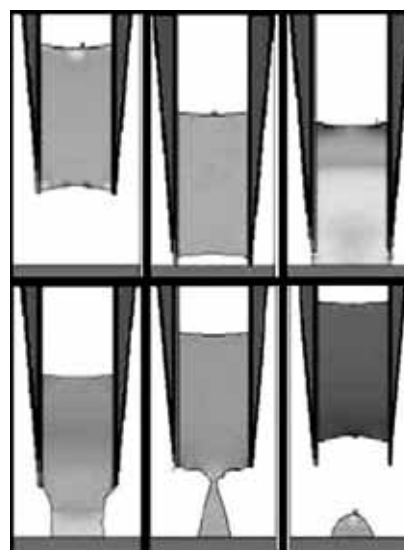


Figure 2: A magnified view of the tip for split pin spotting. Because the meniscus of the fluid is within the orifice opening, contact is needed to dispense the fluid.

### Investigation:

We started by investigating the spotting options that would be applicable for this project. We considered three main options in our decision-making. One option was the current microarray spotting system. The benefit of this machine is that it was already in-house, but the system would need to be modified to allow for non-contact spotting. A liquid handling system was another option. This machine provided a non-contact method for spotting but was limited by its spot size and spot spacing that was too large for our applications. A third alternative that we looked at was inkjet printing technology. This would provide a non-contact method for spotting, with parameters that would meet our specifications. By using this technology, we would need to incorporate it onto our current robotic system or a new machine would need to be brought into the lab, being complicated and expensive respectively.

We decided to modify the current microarray spotting system to allow for non-contact spotting. One reason that this decision was made is because a new pin design was found that would allow for the possibility of non-contact spotting which the conventional split pins did not have. Figure 3 shows the difference between the conventional tweezer and split pin designs, and the new micro spotting pins [3]. The micro spotting pins have a small amount of fluid outside of the capillary space making it possible for the fluid to be dispensed onto the substrate without physical contact between pin and sensor.

A camera system was also designed for the robotic system allowing us to see the tip of the pin and observe when it made contact with the sensor. The camera was also used to align the sensor for the spotting process.

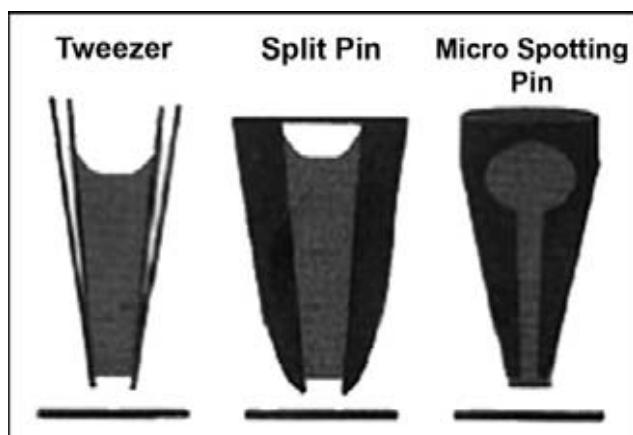


Figure 3: Different spotting pin designs. Notice the fluid outside of the orifice on the micro spotting pin and not the other designs.

We then worked on optimizing the robotic movement by using a software program that would allow us to change the robotic parameters and would show us the position error curve relative to the position of the pin. We found parameters that would minimize the movement error to 1-2.5  $\mu\text{m}$ , down from  $\sim 20 \mu\text{m}$  for the conventional spotting set up.

### Summary:

We decided to use the microarray robot for our spotting system. Several modifications were made to convert the current system, which used physical contact to spot fluid, into a system with the ability to spot fluid without damaging the sensor surface. A camera bracket, software program, new robotic parameters, and new micro spotting pins were implemented into the system to allow for a non-contact spotting method.

### Future Work:

It is important to verify that this procedure is spotting the sensors without damaging the surface. Sensors will be spotted with the microarray robot, the system modifications, and the micro spotting pins. The sensors will then be examined with a scanning electron microscope and/or atomic force microscope to determine if damage has occurred to the sensor surface.

### Acknowledgements:

I would like to thank Shan Wang, Nader Pourmand, and Sebastian Osterfeld for their help and assistance in this project. I would also like to thank Stanford University, the NNIN, and the NSF for the research opportunity.

### References:

- [1] S.X. Wang et al. "Towards a Magnetic Microarray for Sensitive Diagnostics," *Journal of Magnetism and Magnetic Materials* 293 (2005) pp731-736.
- [2] J. Zeng et al. "A Dynamic Spotting Method for Split-Pin Based Microarrays," *Technical Proceedings of Micro Total Analysis Systems* (2001).
- [3] <http://www.andrew.cmu.edu/user/jamess3/microarrays.pdf>.

# Bi-Layer Lithography Using Nanoimprinting

Aaron McDaniel, Applied Physics, Linfield College  
NNIN REU Site: Nanotech, University of California at Santa Barbara

NNIN REU Principal Investigator: Mark Rodwell, Electrical & Computer Engineering, UC Santa Barbara

NNIN REU Mentor: Brian Thibeault, Electrical & Computer Engineering, UC Santa Barbara

Contact: amcdani@linfield.edu, rodwell@ece.ucsb.edu

## Abstract:

Nanoimprinting is a way to replicate nanoscale features of 10 nm or less in size from one surface into another. To reproduce nanoscale features, traditional techniques such as electron-beam lithography can cost thousands of dollars per wafer and can be time consuming. With nanoimprinting, only a master, using traditional fabrication techniques, needs to be made and it can be stamped repeatedly into polymer-coated substrates. These patterns can then be transferred to the substrates by reactive ion etching techniques.

In this work, the bi-layer process of imprinting into a polymer and transferring the pattern into the substrate by chlorine-based reactive ion etching is developed and described.

## Introduction:

Nanoimprinting is a low cost, fast, and relatively easy method of replicating nano- and micro-scale features. With a single master, many negative molds of the stamp can be reproduced over large surfaces. This technique has many applications in industry and research, such as nano optical coating, greater memory capacity, nanofluidic channels and high-resolution OLED pixels. These applications require a deep pattern transfer into a substrate from the imprinted polymer. Chlorine-based reactive ion etching (RIE) is often used to etch nano-scale feature dimensions deeply into silicon and many compound semiconductor materials, such as GaAs and GaN. Since chlorine-based RIE

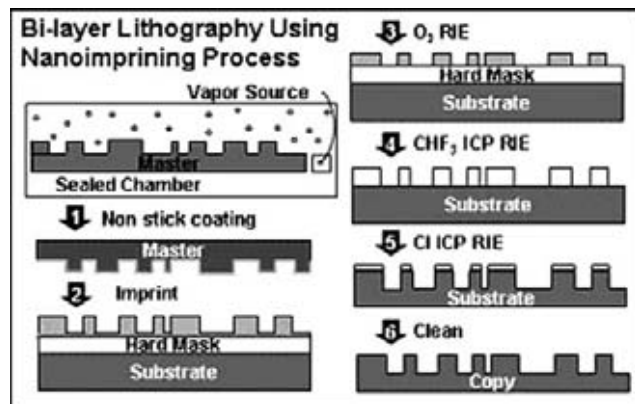
often attacks polymers at similar or higher rates than the substrates, an intermediate hard mask, such as  $\text{SiO}_2$ , is desired to provide a better etch mask for the substrate. Therefore, a bi-layer process was developed that would effectively transfer a shallow pattern deeply into a substrate.

This paper will look at and address the three main areas of the process: imprint polymers, pattern transfer to the hard mask, and silicon etch into the substrate.

## Experimental Procedure:

A master stamp was made by electron-beam lithography and dry etched into a Si substrate. In our case, only a small amount of the overall stamp area was patterned, featuring a repetitive square field of channels and holes ranging in size from 80-1000 nm in width, and 100 nm in depth. The master was chemically cleaned and  $\text{O}_2$  plasma was used to remove any particle matter left on the surface. After cleaning, perfluorotrichlorosilane, a self-assembled monolayer of fluorocarbon monomers, was vapor coated in a clean dry environment to give the master a non-stick surface (Figure 1, step 1).

The master was then used to imprint a prepared bi-layer sample, consisting of a polymer and a hard mask layer on top of a Si substrate. The hard mask material, an  $\text{SiO}_2$  that was deposited by Plasma Enhance Chemical Vapor Deposition (PECVD), was 200 nm thick. The imprint polymer, a thermal-plastic resist, NX-1010 by Nanonex Corp., was spin-coated to 200 nm in thickness and baked to drive out solvents. The sample was then imprinted by heating up the polymer and uniformly pressing the treated master into the mold for a set time. This caused the viscous polymer film to compress and deform as the polymer flowed into the master mold (Figure 1, step 2). After imprinting, the pattern was then transferred into the hard mask. Prior to the pattern transfer, the thin residual layer was removed by  $\text{O}_2$  RIE (Figure 1, step 3). It was removed to allow for a window in the polymer film for the fluorine-based etch to penetrate into the hard mask.





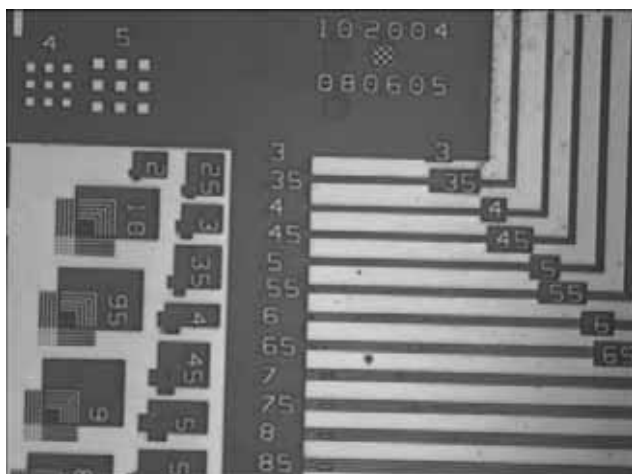


Figure 2: Optical image of full polymer flow.

Next, a  $\text{CHF}_3$  inductively coupled plasma (ICP) RIE transferred the pattern through the hard mask (Figure 1, step 4). Finally, a  $\text{Cl}_2$  ICP RIE etch was used to etch deeply into the substrate (Figure 1, step 5).  $\text{Cl}_2$  was used instead of  $\text{CHF}_3$  because of its isotropic etch properties. Any leftover  $\text{SiO}_2$  on the surface was then removed through a wet chemical process (Figure 1, step 6).

### Results and Conclusions:

Three polymers, ZEP-540A, NX-1010, and FOX-14, were tested to see which polymer had the best characteristics for imprinting. NX-1010 gave the best results because of its lower imprint conditions and smaller number of imprint defects. For NX-1010 on PECVD  $\text{SiO}_2$  and Si substrate, the minimum imprint parameters for the polymer flow into all regions of the mold were 300 psi at  $130^\circ\text{C}$  for 1 minute (Figure 2 shows a copy with complete polymer flow into the master mold). Etch rates for the NX-1010 resist layer, the  $\text{SiO}_2$  layer, and the Si substrate were determined to be 100 nm/min, 200 nm/min, and 200 nm/min for  $\text{O}_2$  RIE,  $\text{CHF}_3$  and  $\text{Cl}_2$  ICP RIE, respectively.

Using these parameters, three samples went through the complete process. Due to overetching of the NX-1010 resist in oxygen, we were left with  $\sim 50$  nm of polymer mask. Using this very thin 50 nm polymer mask and the bi-layer process, we were able to etch over 350 nm deep lines and over 400 nm deep holes into the silicon substrate, giving net etch ratios of  $\sim 7:1$  and  $8:1$  (Figure 3). This successfully demonstrated a good aspect ratio which allows for deep etches into the substrate.

Future work could include further enhancing the etch ratio, improving  $\text{Cl}_2$  etching to reduce trenching, edge wall slope, and determining the imprint parameters for different types of master patterns.

### Acknowledgments:

I would like to thank Brian Thibeault and Bill Mitchell for their mentoring and guiding me this summer. I would also like to extend my thanks to Angela Berenstein and the staff in the Computer and Electrical Engineering Department and the UCSB Nanofabrication Facility. Finally, my thanks to the NSF funding through the NNIN REU program at UCSB that has made this study possible.

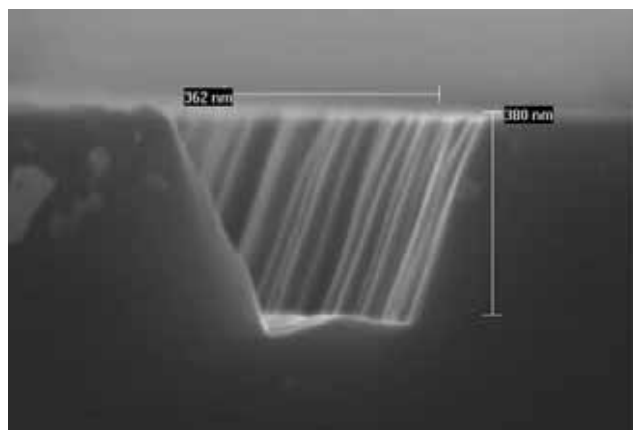


Figure 3: SEM of the ICP RIE  $\text{Cl}_2$  etch of a line.

# Silicon Morphology Evolution under Focused Ion Beam Irradiation

**Matthew R. McGrath, Department of Physics, Vanderbilt University**  
**NNIN REU Site: Center for Nanoscale Systems, Harvard University**

*NNIN REU Principal Investigator: Michael J. Aziz, Engineering and Applied Sciences, Harvard University*

*NNIN REU Mentor: H. Bola George, Division of Engineering and Applied Sciences, Harvard University*

*Contact: matthew.r.mcgrath@vanderbilt.edu, maziz@harvard.edu, hgeorge@fas.harvard.edu*

## Abstract:

As state-of-the-art lithography techniques approach fundamental limits, interest has increased in alternative nanofabrication methods, including the creation of self-organizing surface topographic morphologies by methods such as ion sputtering. Practical use of this technique requires a thorough quantitative understanding of the morphology evolution and various models have been advanced, but none satisfactorily describes the evolution of all features, especially that of steep slopes (40-90 degrees from horizontal). A recently developed nonlinear model makes novel predictions about the evolution that are partially confirmed by optical profilometry of sputtered surfaces.

## Introduction:

The production of novel nano-scale devices and the continuing miniaturization of conventional semiconductors will require new fabrication methods. While lithography in its various forms is rapid, convenient, and well understood, the technique faces several intrinsic limitations and the creation of 3D structures is difficult and time consuming. Thus the possibility of exploiting self-organizing nanostructures for practical fabrication is receiving increased attention. The order in such structures comes from their internal dynamics, meaning that they can exist at almost any length scale. Before any self-organizing structure can be reliably used, however, the process of its creation must be thoroughly understood.

The ripples spontaneously produced by ion sputtering may be a useful class of self-organizing structures. That tiny ripples form on a variety of materials under uniform ion irradiation has long been known [1], however the more recent discoveries that ripple characteristics are a predictable function of irradiation parameters and may be templated by existing structures on the material surface [2] have increased interest in understanding the dynamics of their formation and those of sputtered silicon in general.

The classical theory of sputtering [3] assumes that the energy of each incoming ion is distributed throughout the material in a series of collisions. When energy from these 'collision cascades' reaches the material surface, one or more atoms may be ejected. The rate of this sputtering is determined by the surface shape and material properties. This relationship is well understood for flat and gradually

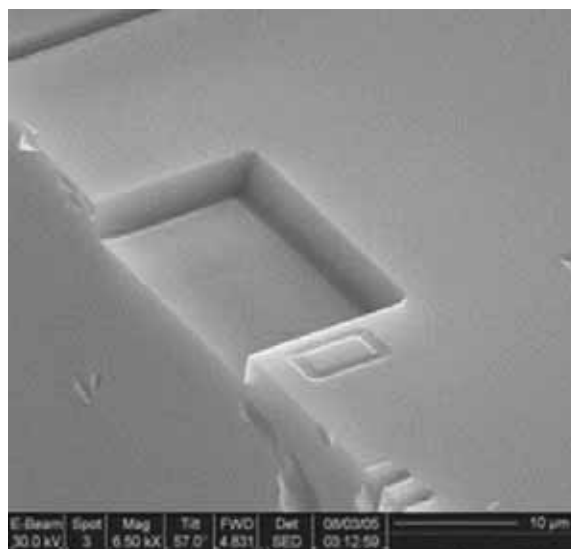


Figure 1: SEM of 80° slope cut into the side of the Si sample.

curved surfaces. Our group is developing a new theory [4] that is valid for the steep slopes present in ripples and other self-organizing structures.

Using a full nonlinear treatment of the sputtering problem, we identify several behavioral regimes in the evolution of sputtered slopes. Slopes below one critical value ( $\sim 68^\circ$ ) are expected to gradually dissipate. Above this angle, slopes are expected to sharpen to a dynamically selected angle ( $\sim 76^\circ$ ). The goal of these experiments was to ascertain the existence and precise values of these angles to check the theory with the simplest possible case: a steep, straight edge.

## FIB Machining and Bombardment:

A FEI dual-beam 235 FIB apparatus was used for all sample preparation and imaging steps. The samples were small ( $< 1 \text{ cm}^2$ ) chunks of Si <001> wafer. The pattern 'milling' feature of the instrument was used to prepare five identical pits per trial (see Figure 1), normally  $25 \mu\text{m}$  wide,  $12 \mu\text{m}$  long, and  $1.7 \mu\text{m}$  deep, along the cleaved sample edge. The ion beam current was 3nA, while the dwell time and overlap were 1 microsecond and 50%, respectively. The instrument stage was tilted before milling so that the experimental edge was cut at the desired angle. Each pit was then given a  $20 \times 20 \mu\text{m}$  high current raster at normal incidence, again using the FIB pattern feature, for either 128, 256, 384, or 512 seconds (see Figure 2).

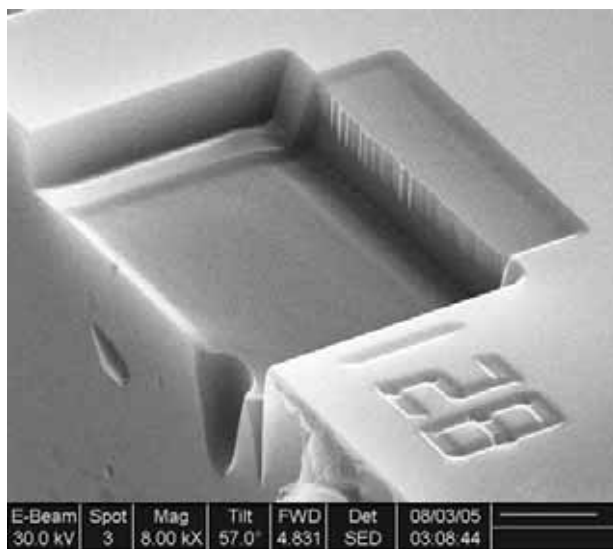


Figure 2: SEM of the 80° slope after 128 seconds of irradiation.

#### Optical Profilometry:

A hyphenated-systems OP-150 confocal optical profilometer with a 50X objective was used to quantitatively characterize the evolving edges. The maximum slope that the instrument can register in our application is about 45°, so a tilt stage built by H. Bola George was employed to allow complete profiles to be read from the steeper samples. All profiles were converted to averaged 2D line traces drawn perpendicularly to the experimental edge and rotated to the correct position in the plotting software.

#### Results:

The profilometer is an optical instrument and thus has difficulties analyzing features just two orders of magnitude larger than the wavelength of light; diffractions, reflections, and shadows can all confuse the profiling software. Thus, wholly satisfactory data has still not been obtained and the actual values for the critical angles have not yet been established. Indeed, there are gaps right in the most theoretically interesting regions of the edges. (See Figure 3). We postulate that these gaps occur because shadowing and/or multiple reflections from shock ripples on the evolving edge prevent the profiling software from discerning a clear maximum. Whatever the cause, it is clear that the optically generated profiles (Figure 3) do not yet agree well enough to the SEM images (Figures 1 and 2) for the profiling technique to be considered reliable. Nevertheless, 2D plots of the sequence of edges (Figure 4) do reveal the general evolution of the surface morphology.

Further refinements in the instrument and experimental technique are expected to allow more thorough confirmation of the theory.

#### Acknowledgements:

I would like to thank Dr. Aziz, Bola George, and all the other members of the Harvard 'matsci' group for

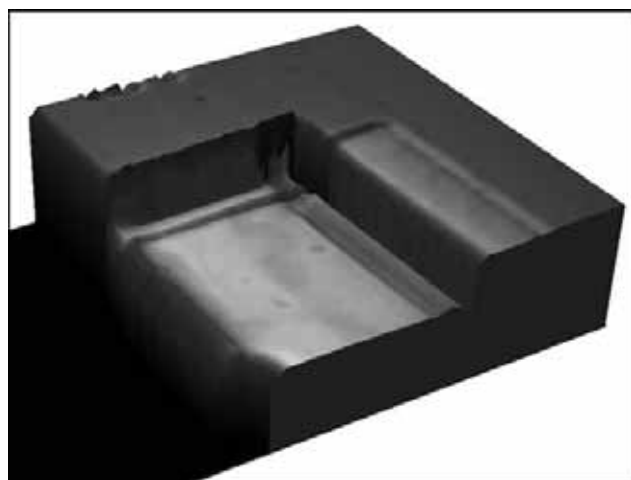


Figure 3: Optically generated profile of pit in Figure 2.

their support, guidance, and patience. I should also thank Dr. Richard Shaleck at the Harvard CNS and Dr. Eddy Robinson at Hyphenated Systems for technical guidance. My work was supported by the NNIN.

#### References:

- [1] M. Navez, D. Chaperot, and C. Sella, Comptes Rendus Hebdomadaires Des Seances De L'Academie Des Sciences 1962, 254, 240.
- [2] A. Cuenat, H. B. George, K.-C. Chang, J. Blakely, and M. J. Aziz, submitted to Advanced Materials, in press (2005).
- [3] Peter Sigmund, Journal of Materials Sci. 8, 1545 (1973).
- [4] H. H. Chen, Omar Urquidez, Stefan Ichim, L. Humberto Rodriguez, Michael P. Brenner, and Michael J. Aziz, Science, in preparation (2005).

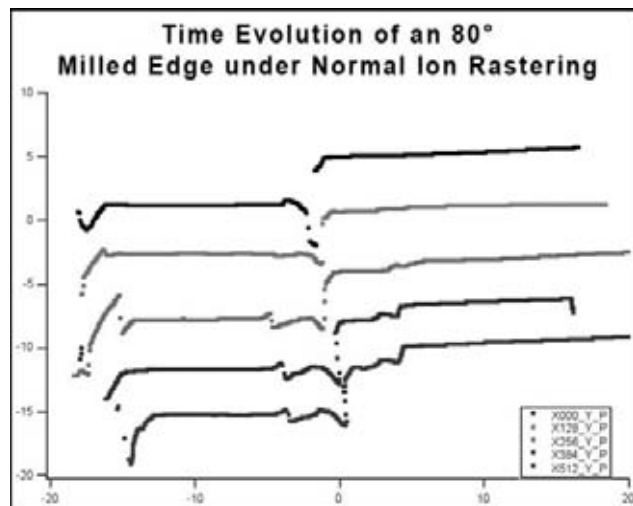


Figure 4: Time evolution of the 80° milled edge under normally incident ion radiation. The traces represent (from top to bottom) 0, 128, 256, 384, and 512 seconds of irradiation.

# Ferroelectric Nonvolatile Memory Materials: Fundamentals of Reliable Ferroelectric Switching

**David McIntosh, Electrical Engineering, Oregon State University**  
**NNIN REU Site: Stanford Nanofabrication Facility, Stanford University**

*NNIN REU Principal Investigator: Dr. Paul C. McIntyre, Materials Science & Engineering, Stanford University*

*NNIN REU Mentor: Mr. Mike Chen, Materials Science & Engineering, Stanford University*

*Contact: mcintoda@gmail.com, pcml@stanford.edu, yechen@stanford.edu*

## Abstract:

Fatigue, defined as loss of polarization under electrical field cycling, is a major obstacle in implementing ferroelectric films into Ferroelectric Random Access Memory (FeRAM/FRAM) non-volatile memories. Little is known about what causes polarization fatigue. It has been suggested that fatigue is related to trapping of carriers injected into  $\text{Pb}(\text{Zr,Ti})\text{O}_3$  (PZT) films from the PZT/electrode interface. It has been proposed that these traps can be optically excited, then measured electrically. This would ultimately lead to a spectroscopy methodology to characterize the trap concentration and energy of the traps. The success of this project depends on creating a thin top electrode such that it does not absorb most of the injected photons, yet still does not affect the electrical measurement.

In this study, various electrode configurations, electrode thicknesses and different electrode materials were examined, and process parameters for optically transparent electrodes were created.

## Introduction:

Ferroelectric films such as PZT, have attracted attention for their unique bistable nature, which makes them a candidate for non-volatile capacitor based memories. Polarization fatigue, however, impedes the commercial production of ferroelectric memories. Although the mechanism for fatigue is not known, some models suggest space charge defects accumulating from the ferroelectric/electrode interface as a primary cause.

To characterize the quantity and energy level of these trapped charge defects, optical methods have been suggested. A precise optical device setup will project monochromatic light, ranging from the infrared to the visible, through the top electrode onto the ferroelectric capacitor and excite the trapped charges to the conduction band of PZT. Then an applied voltage bias between the top and bottom electrode allows the charges to be collected thereby characterizing the quantity and energy levels of these charged defects.

In order to realize this characterization, an optically translucent yet continuous top electrode is required.

These must behave as good distributors of electric field but also allow light to pass through. The Beer-Lambert Law was used to approximate the absorption of monochromatic light ( $\lambda=1000$  nm) for Pt and Ir electrodes as a function of thickness. For greater than 75% absorption, a thickness of less than 20 nm is needed.

## Experimental Procedure and Results:

Translucent top electrodes were created using photolithography and shadow-mask methods. The bottom electrode was Ir. Two different types of top electrode structures were created: a circular structure (Figure 1) and a rib (Figure 2). The rib structure was a non-continuous electrode designed to allow light through yet still distribute a uniform electric field. This allows the rib electrode to be thicker than a continuous electrode. A conventional uniform round electrode was also investigated.

The rib electrode structure was fabricated using standard photolithography using single-layer metal lift-off, whereas the circular design was created using a shadow mask. The rib electrodes were created with Ir and Pt with thicknesses 70 nm and 50 nm, and 50 nm and 20 nm respectively. Circular Ir and Pt electrodes were deposited at thicknesses of 50 nm and 20 nm, and 20 nm and 10 nm, respectively. The thicknesses were measured with a quartz crystal deposition rate monitor.

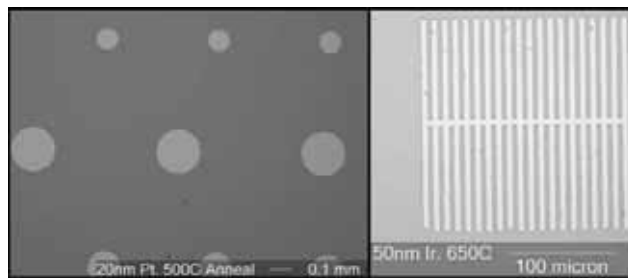


Figure 1, left: 20 nm thick Pt electrodes showing no signs of delamination or defects post-anneal.

Figure 2, right: 50 nm thick optically translucent Ir rib top electrode.



All Pt electrodes appeared uniform after deposition, whereas Ir electrodes showed varied results. Ir rib electrodes of thicknesses 20 nm and 50 nm appeared ragged at the edges, and of lower quality than Pt rib electrodes, but still were a functioning electrode. Ir circular electrodes with thicknesses greater than 20 nm appeared cracked, and peeled (Figure 3) following deposition, while 20 nm thick Ir electrodes appeared visually intact. Visually intact electrodes were annealed with flowing N<sub>2</sub> at 650°C. No delamination was found on the annealed electrodes.

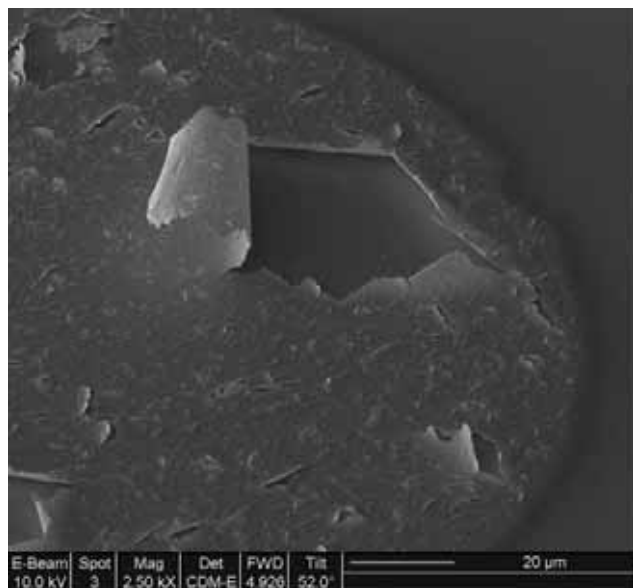


Figure 3: 50 nm thick Ir circular top electrode peeling pre-anneal.

Fatigue properties were characterized by comparing polarization vs. applied electric field (P-E) hysteresis loops at increasing levels of fatigue (0 to 10<sup>7</sup> cycles). Non-annealed Pt and Ir capacitors exhibited greater than 50% relative loss in switchable polarization after 10<sup>4</sup> cycles. Ir electrodes generally exhibited a very small relative change in switchable polarization after 10<sup>7</sup> cycles, whereas some Pt electrodes showed as much as 40% change. Films with Pt top electrodes exhibited higher negative coercive field, while the films with Ir top electrodes exhibited higher positive coercive field (Figure 4).

X-ray photoemission spectroscopy (XPS) was used to characterize the effects of the photolithography and cleaning processes on the chemistry of PZT. This was done at incident angles of 30° and 90°. Two samples were compared, a virgin 90 nm thick PZT

Pt	Type/Thick.	Visual Inspection		Hysteresis		
		Pre-Anneal	Post-Anneal	E <sub>c</sub> (V/cm)	-E <sub>c</sub> (V/cm)	Rel. Loss in P <sub>sw</sub>
	Circular					
	10nm	OK	OK	90.7	-101.3	42.5%
	20nm	OK	OK	77.3	-94.7	0.2%
	Rib					
	20nm	OK	OK	66.7	-82.7	59.0%
Ir	Type/Thick.	Visual Inspection		Hysteresis		
		Pre-Anneal	Post-Anneal	E <sub>c</sub>	-E <sub>c</sub>	Rel. Loss in P <sub>sw</sub>
	Circular					
	20nm	OK	OK	107.8	-93.3	2.0%
	50nm	Peeling	n/a	n/a	n/a	n/a
	Rib					
	20nm	OK	OK	64.0	-88.0	2.7%
	50nm	roughness	roughness	72.0	-82.7	2.6%

Figure 4: Physical characteristics of Pt and Ir electrodes of various thicknesses. Coercive field (Ec) and relative loss in switchable polarization after fatigue of 107 cycles.

film as well as a cleaned (acetone, isopropyl alcohol) and photolithography-processed film. The relative abundance of Pb, Zr, and Ti remained the same for both samples while the relative abundance at 30° of C decreased by 10% and 5% at 90°.

## Conclusions:

Translucent thin Ir and Pt electrodes (10-70 nm) were created on PZT film. Ir electrodes exhibited poor adhesion at thicknesses greater than 20 nm. Pt electrodes adhered well for 10-50 nm of thickness. Annealing at temperatures up to 650°C did not cause defects visible by optical microscope (pre/post anneal comparison). Polarization and leakage current (I-V) measurements were attained for these electrodes, demonstrating that thin non-conventional electrodes can be used for the purpose of the optical spectroscopy method of characterizing charge defects in ferroelectric films.

## Acknowledgements:

Thanks to my mentor Mike Chen, Joshua Symonds for SEM assistance, and Gloria Wong for photolithography guidance.

## References:

- [1] Auciello, Scott, and Ramesh, Phys. Today, "Physics of Ferroelectric Memories", Volume 51, Issue 7, July 1998, pp.22-27.
- [2] H. Takasu, Integr. Ferroelectr. 14, 1 (1997).
- [3] Tagantsev, Stolichnov, Colla, and N. Setter, J. of Appl. Phys., Vol. 90, Aug. 2001.

# Characterization of Beam Aberrations due to Magnetic Field Tilt in DIVA for Massively Parallel Electron Beam Lithography

Steve Meisburger, Physics, Carleton College

NNIN REU Site: Stanford Nanofabrication Facility, Stanford University

NNIN REU Principal Investigator: Fabian Pease, Electrical Engineering, Stanford University

NNIN REU Mentor: Dan Pickard, Electrical Engineering, Stanford University

Contact: meisburs@carleton.edu, pease@cis.stanford.edu

## Abstract:

Theoretically, electron beam systems can achieve sub-nanometer resolution, limited only by diffraction and spherical aberration. While this makes them attractive for meeting the future demands of nanolithography, single beam systems today are slow compared to optical methods because space charge effects limit the usable write current. Multibeam systems circumvent this limitation by distributing the total current over many spatially separate beams.

One such system, known as DIVA, takes advantage of the properties of the simplest electron lens, a uniform axial magnetic field, to image an array of apertures at unity magnification. We propose a theoretical model of electron motion due to a misaligned axial magnetic field in order to determine if astigmatism correctors will be necessary in the multibeam system. Pending experimental verification, magnetic field tilt does not seem to be a significant source of aberrations within modest mechanical tolerances (less than 10 mrad).

## Introduction:

Theoretically, electron beam systems can achieve sub-nanometer resolution, limited only by diffraction and spherical aberration. E-beam lithography systems currently available, such as the Leica VB6-UHR-EWF, have demonstrated features sizes of less than 10 nm [1], far exceeding the resolution of the best optical machines. While this makes them attractive for meeting the demands of nanolithography, single column systems today are slow compared to optical methods. This is due to the electron-electron interactions that blur the beam as current is increased, limiting the amount of current that can pass down a single column.

Multi-axis systems overcome this limit by distributing the total write current over many spatially separate beams writing simultaneously. DIVA (DIstributed axis, Variable Aperture), proposed by Groves et al. [2], uses a uniform axial magnetic field to form an image of an array of apertures at unity magnification and can accommodate as many as 10,000 beams. Advantages of this configuration include

extreme simplicity of the optics, scalability, and low aberrations. Previous work with uniform field systems has successfully demonstrated unity magnification SEM operation for a single beam, with resolution determined only by the size of the beam-limiting aperture [3].

In order to extend the current system to multiple beams, it is necessary to know what tolerances need to be met so that all beams perform equally well. Of particular concern is the possibility that astigmatism correctors will be needed for each beam, which could compromise the simplicity and scalability of the system. One likely source of astigmatism in the current system is magnetic field tilt with respect to the mechanically defined optic axis (Figure 1).

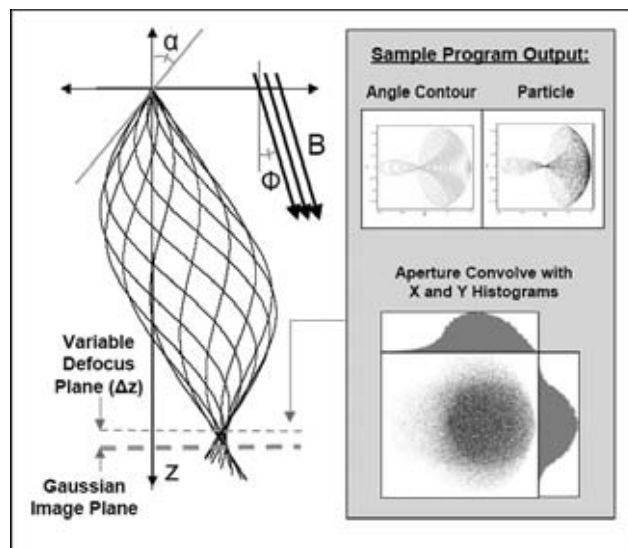


Figure 1: Schematic of particle motion in a uniform B-field tilted  $\phi$  with respect to the z-axis for a beam with half-angle  $\alpha$ . A computer program calculates particle positions in any plane perpendicular to the z-axis, producing the three types of output shown.

## Theoretical Model:

A non-relativistic particle moving in the presence of electric and magnetic fields feels a force given by the Lorentz Force Law,  $F = q(E + v \times B)$ . For a particle moving in a uniform magnetic field tilted at an angle  $\phi$

$$\begin{aligned}
\text{(a)} \quad & v_x'(t) = -\omega v_y(t) \cos \phi \\
& v_y'(t) = -\omega (v_x(t) \sin \phi - v_z(t) \cos \phi) \\
& v_z'(t) = \omega v_y(t) \sin \phi \\
\\
& x(t) = \frac{1}{\omega} (v_{0x} \omega t \sin^2 \phi + \cos \phi (v_{0y} (\cos(\omega t) - 1) + \\
& \quad v_{0z} \sin \phi (\omega t - \sin(\omega t))) + v_{0x} \cos^2 \phi \sin(\omega t)) \\
\text{(b)} \quad & y(t) = \frac{1}{\omega} (v_{0z} \sin \phi (\cos(\omega t) - 1) + v_{0y} \sin(\omega t) + \\
& \quad v_{0x} \cos \phi (\cos(\omega t) - 1)) \\
& z(t) = \frac{1}{\omega} (v_{0z} \omega t \cos^2 \phi + v_{0x} \cos \phi \sin \phi (\omega t - \sin(\omega t)) + \\
& \quad \sin \phi (v_{0y} (1 - \cos(\omega t)) + v_{0z} \sin \phi \sin(\omega t))) \\
\text{(c)} \quad & t = \frac{1}{v_{0z}} \left( wd + df + \frac{2n\pi}{\omega} \sin \phi (v_{0x} \cos \phi + v_{0z} \sin \phi) \right)
\end{aligned}$$

Figure 2: (a) Nonrelativistic equations of motion for an electron in a B-field tilted by  $\phi$  where  $\omega$  is the cyclotron frequency  $eB/m$ . (b) Second integral solution. (c) Time of flight approximation.

with respect to the z-axis, the equations of motion are given by Figures 2a and 2b.

Mathematica® programs were used to calculate particle positions given a set of initial velocities. The programs produced particle plots and contours of equal launch angle, varying magnetic field tilt and defocus distance. Blur in x and y of the aperture image was found by convolving the particle plot data with the aperture shape, generating x and y histograms, and finding the full width at half maximum for each (Fig1).

## Results:

The tri-lobed shapes of the angular contour plots (Figure 1) suggest that the dominant aberration type is elliptical coma [4], and not simple astigmatism as was expected. We ran the aperture image program for a 10 keV monoenergetic beam with a 10 mrad half-angle at a 10 mm working distance, using a 25 nm aperture with 0, 10, and 20 mrad tilt at 0.5  $\mu\text{m}$  steps through focus. The depth of focus, or trough width for a given image size, is comparable in the 0 and 10 mrad cases, but significantly worse in the 20 mrad case. (Figure 3). Additionally, the 20 mrad case showed significant astigmatism while the 10 mrad case did not (Figure 4).

## Conclusions and Future Work:

According to the proposed model, magnetic field tilt will not be a major source of astigmatism in DIVA, provided that modest mechanical tolerances are met. The system resolution is unaffected for tilt angles as large as 10 mrad, which should be easy to achieve in the multibeam system. The system chamber has been fabricated to within 0.002" over the 12" reference surface, which corresponds to a maximum tilt of 0.2 mrad. A micrometer stage has been constructed to

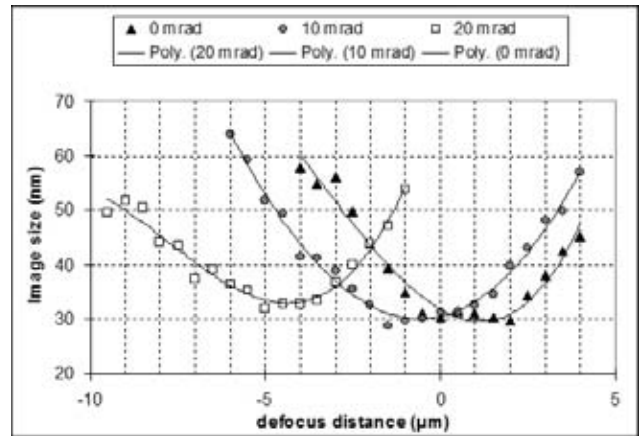


Figure 3: Size of aberrated image from a 25 nm aperture:  $\sqrt{x_{FWHM}^2 + y_{FWHM}^2}$ , through focus. At 20 mrad of tilt, depth of focus is impacted.

tilt the chamber of the single-beam DIVA within the magnetic field in order to measure tilt-induced aberrations. Pending experimental verification, astigmatism correctors should not be necessary in the multibeam system.

## Acknowledgements:

Dan Pickard, Prof. Fabian Pease, and Dan Meisburger for their input and guidance. NSF, NNIN, SNF, CIS, SRC, and DARPA for making this project possible.

## References:

- [1] T.R. Groves and R.A. Kendall, J. Vac. Sci. Technol. B 16, 3168 (1998).
- [2] D.S. Pickard, et al. J. Vac. Sci. Technol. B 20, 2662 (2002).
- [3] D.S. Pickard, et al. J. Vac. Sci. Technol. B 21, 2834 (2003).
- [4] J.C. Burfoot. Proc. Phys. Soc. B 67, 523-528 (1954).

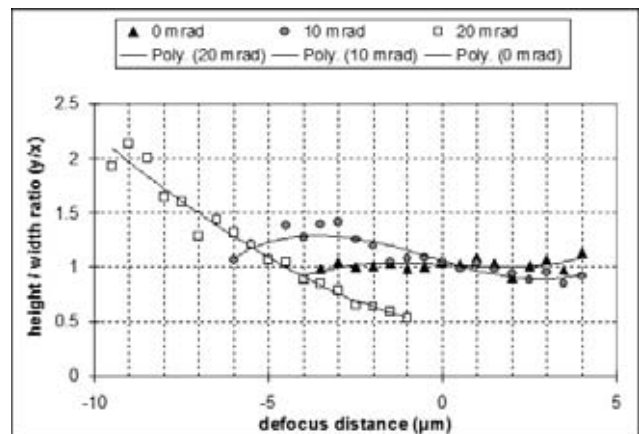


Figure 4: Ratio between FWHM measurements from x and y histograms through focus. Stigmators would be helpful for correcting aberrations in the 20 mrad case, but probably not in the 10 mrad case.



# In Situ Fabrication of Oxide Apertures in Vertical-Cavity Surface-Emitting Lasers

**Andrew Melton, Electrical Engineering, University of Portland**  
**NNIN REU Site: Stanford Nanofabrication Facility, Stanford University**

*NNIN REU Principal Investigator: Prof. James Harris, Electrical Engineering, Stanford University*

*NNIN REU Mentor: Zhilong Rao, Physics, Stanford University*

*Contact: amelton@up.edu, harris@snowmass.stanford.edu, zlrhao@stanford.edu*

## Abstract:

One way to define the spatial mode of a vertical-cavity surface-emitting laser (VCSEL) is by incorporating an oxide aperture above its active region. The oxide aperture can be grown in a conventional oxidation furnace, but this can take hours of preparation time and often yields inconsistent results. An alternative is to grow the oxide aperture *in situ*, allowing for precise definition of the size of the aperture.

The goal of this project was to configure an existing furnace designed for *in situ* oxidation monitoring to produce consistent and even oxidation on arrays of VCSELs.

## Introduction:

The spatial mode of a VCSEL is often defined by the size and shape of its air-post mesa. However this results in photon scattering losses at the edges of the mesa. By defining the mode with an oxide aperture instead, these losses can be greatly reduced, thereby increasing the efficiency and beam quality of the laser. In addition, this technique allows the mesa to be made larger, which makes fabrication of the VCSEL easier.

One way to create the oxide aperture is to grow it laterally in an oxidation furnace. However, standard oxidation furnaces do not allow monitoring of the reaction, and therefore require long setup times and often produce unpredictable results. A more promising alternative is *in situ* oxidation in a furnace that allows real-time monitoring. By watching the oxidation progress, the reaction can be stopped precisely when the correct aperture size has been achieved.

## Experimental Setup:

In this project, we created apertures in VCSELs by oxidizing AlGaAs layers just above the active region, as seen in Figure 1. Each sample consisted of an array of such structures with varying sizes on a GaAs substrate.

We used an oxidation furnace configured for optical monitoring. Nitrogen gas was available from a wall source and was pumped in through two separate

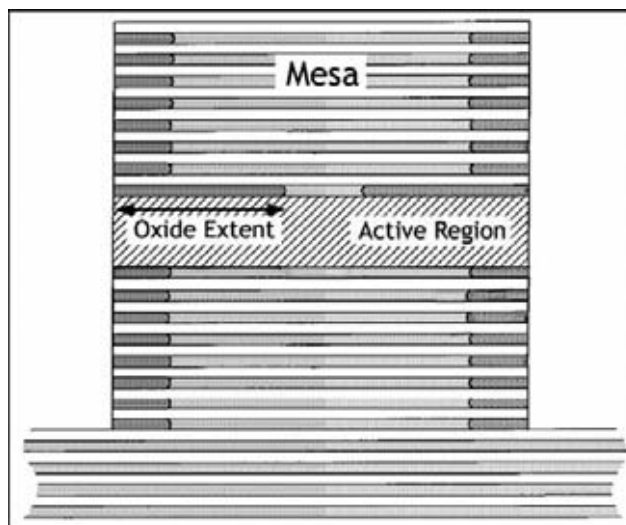


Figure 1: VCSEL with oxide aperture.

flowmeters equipped with valves. One flowmeter led directly into the furnace chamber, while the other led to a heated bubbler, then into the furnace chamber.

The furnace was equipped with a quartz viewport through which the oxidation could be monitored. The chamber was kept under a slight vacuum, which kept this viewport in place. Samples could be placed in the furnace by disconnecting the vacuum and removing the viewport.

The monitoring was achieved using a near-infrared sensitive silicon CCD camera with a high magnification lens system, which was mounted over the viewport. The camera connected to a video capture card on a computer, which allowed real-time viewing of the oxidation progress.

## Experimental Procedure:

The wet oxidation of AlGaAs requires a moist, heated environment devoid of oxygen gas. To provide this environment, samples being oxidized were heated on a graphite hot plate with a steady stream of water-vapor-saturated nitrogen gas flowing into the furnace chamber. Samples were typically oxidized at



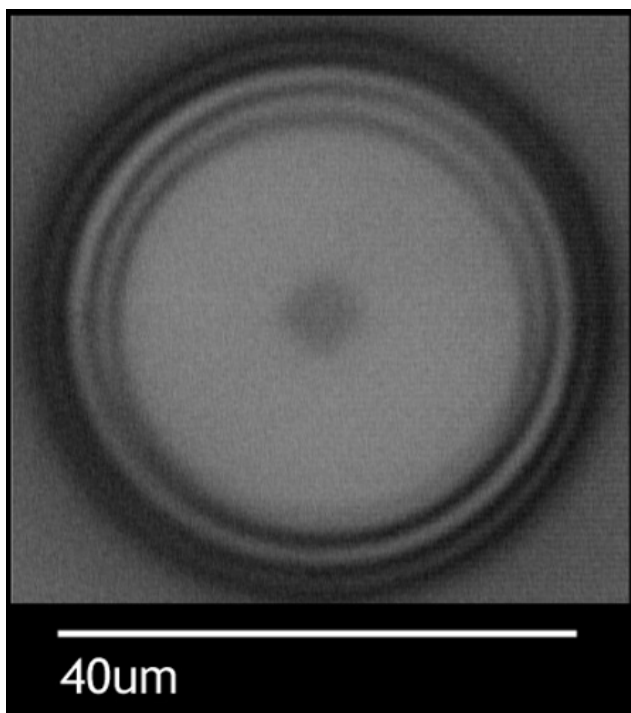


Figure 2: Top view of an oxide aperture.

a temperature of 430°C, with saturated nitrogen gas flowing in at a rate of 2 SCFH.

### Results and Conclusions:

Many samples were oxidized over the course of the project. This helped uncover several problems with the furnace setup that needed to be solved for it to be functional. These problems included vibration, poor image contrast, and non-uniform oxidation rates.

The first problem addressed was vibration. Vibrations from the floor of the lab were traveling up the legs of the furnace table and causing poor image quality. This was alleviated by adding air-filled supports under each table leg, though due to the long lens structure, it was impossible to remove all vibration.

Once we achieved a stable image, the next task was to maximize the contrast in the image between the oxidized and unoxidized regions. Computer simulations showed that maximum contrast would occur between 850 and 950 nm. For this reason an 850 nm long-pass filter was used. Figure 2 shows a top view image of a VCSEL oxidized in our furnace; in it, the dark dot in the middle is the unoxidized region and the light ring is the oxidized region.

The final problem addressed was non-uniform oxidation rates in different structures on a single sample. The oxidation rates on structures only 200  $\mu\text{m}$  away from each other varied by approximately 0.1  $\mu\text{m}/\text{min}$ . The oxidation rate of AlGaAs in similar systems has been shown to be highly dependant on both temperature and flow rate of water vapor. Therefore the two possible explanations for this non-uniformity were uneven temperature on the hot plate or uneven water vapor dispersion in the chamber.

### Future Work:

Unfortunately there was insufficient time for the final problem of non-uniform oxidation rates to be solved. One possible solution currently being pursued is to try an alternate material for the hot plate. The current hot plate is composed of graphite, which is a planar material. It typically has very good in-plane thermal conductivity, but very poor out-of-plane thermal conductivity. A material with a higher omnidirectional thermal conductivity (such as copper) could alleviate thermal non-uniformity.

### Acknowledgements:

I would like to thank Prof. Harris for allowing me to work in his group, Zhilong Rao for being a great mentor, and all the members of the Harris Group, especially Luigi Scaccabarozzi, Seth Bank, Hopil Bae, Rafael Aldaz, Tom Lee, and Ofer Levi for lending me their time and advice.

Many thanks also go to the SNF staff for their support, Mike Deal for his efforts organizing the NNIN REU at Stanford, and to CIS, NNIN, and NSF for funding this great program.

### References:

- [1] Choquette, K. D., et al. "Advances in Selective Wet Oxidation of AlGaAs Alloys". IEEE Journal of Selected Topics in Quantum Electronics, Vol. 3, No. 3, June 1997.
- [2] Feld, S. A., et al. "In Situ Optical Monitoring of AlAs Wet Oxidation Using a Novel Low-Temperature Low-Pressure Steam Furnace Design". IEEE Photonics Technology Letters, Vol. 10, No. 2, Feb. 1998.

# Focused Ion Beam Fabrication of Pt Electrodes with an Interelectrode Spacing Less Than 10 nm

Joshua Montague, Physics, Colby College

NNIN REU Site: Cornell NanoScale Science and Technology Facility, Cornell University

NNIN REU Principal Investigator: Dr. Michael Guillorn,  
Cornell Nanoscale Science and Technology Facility, Cornell University  
Contact: jrmontag@colby.edu, guillorn@cnf.cornell.edu

## Abstract:

Characterizing the electrical properties of materials with features less than 10 nm requires the fabrication of electrode pairs with similarly sized interelectrode gaps. Several techniques for fabricating these types of electrodes have been reported, varying in complexity and reproducibility. In this work we present a simple technique for fabricating these structures involving focused ion beam (FIB) induced deposition of Pt. This technique can reproducibly create electrode pairs with interelectrode gaps in the range of 5 to 10 nm. Electrical measurements on completed electrode structures show good electrical isolation at room temperature with leakage currents of less than 1 nA at biases up to 1 V.

## Introduction:

The fabrication of electrode pairs with interelectrode gaps ranging from 1 to 10 nm have been realized by several techniques including high resolution lithography [1], electrochemistry [2], physical vapor deposition [3], mechanical deformation [4], and electromigration [5]. However, the results obtained from these techniques are often irreproducible and the methods involved are frequently labor intensive. Numerous fabrication tools and a considerable amount of time are often required to complete a single testable structure.

In this work we report on a simple focused ion beam (FIB)-based nanofabrication technique for defining electrode pairs with sub 10 nm interelectrode spacing. This technique also uses a Si-supported low stress  $\text{Si}_3\text{N}_4$  membrane as the substrate to facilitate both fabrication and inspection using high resolution scanning electron and scanning transmission electron microscopy techniques. Using these methods, a testable device structure can be completed in less than 1 hour.

## Experimental Procedure:

An outline of the fabrication process is shown in Figure 1. 60-nm-thick low stress  $\text{Si}_3\text{N}_4$  membranes were created on <100> Si wafers using KOH etching

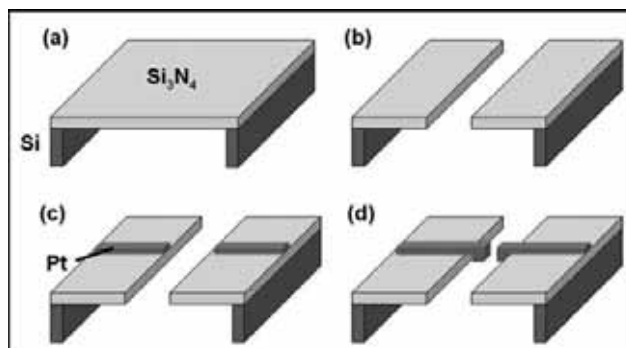


Figure 1: Overview of the fabrication process. (a)  $\text{Si}_3\text{N}_4$  membranes are suspended by a Si substrate. (b) 500 nm wide slits are milled in the membrane. (c) Pt electrodes are deposited perpendicular to the slit. (d) Deposition is halted at the appropriate interelectrode spacing.

(Figure 1a). Completed membranes were placed into an FEI 611 FIB workstation. This tool uses a 25 keV  $\text{Ga}^+$  ion beam for imaging and patterning. A 60 pA beam current was used to mill a 15  $\mu\text{m}$  long, 500 nm wide slit through the membrane (Figure 1b). FIB induced deposition of Pt from a methylcyclopentadienyl-trimethyl-platinum precursor was used for writing the electrode structure, contact pads, and interconnects. A writing current of 40 pA was used to perform these depositions. 100 nm thick interconnects and 200  $\mu\text{m}$  x 200  $\mu\text{m}$  square probing pads were deposited first to avoid modifying the interelectrode gap. Next, the electrodes were deposited by writing perpendicular to the slit (Figure 1c). This resulted in a narrowing of the slit in the region of deposition, forming a nanoscale interelectrode gap (Figure 1d). The imaging resolution of the FIB used in this work was insufficient to obtain a direct measurement of the interelectrode gap. However, by characterizing the lateral deposition rate of the Pt across the slit and acquiring periodic images during deposition, the patterning was arrested when the desired interelectrode spacing was achieved.

## Results and Discussion:

Post-fabrication analysis of the process was performed using a high resolution SEM (Carl Zeiss

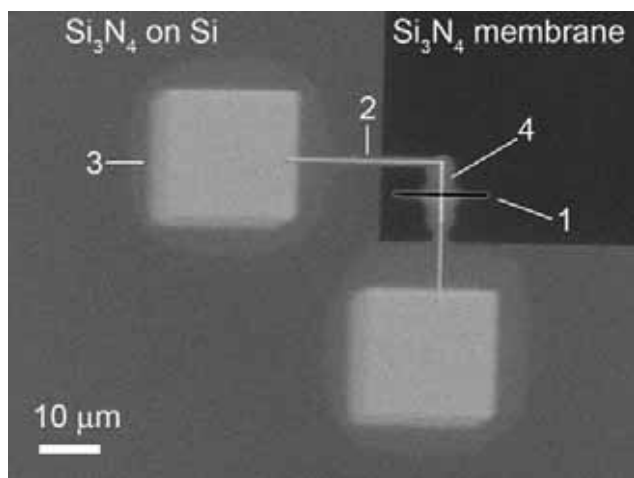


Figure 2: Micrograph of a completed structure. The patterning order is indicated: (1) slit (2) interconnects (3) probing pads (4) electrodes. The bright area surrounding the electrodes is excess Pt from the deposition process, and is less than 5 nm thick.

SMT Ultra 55). A low magnification SEM image of a completed structure is shown in Figure 2. High magnification images of two completed electrode pairs are shown in Figure 3. Measurements of the interelectrode gaps were obtained from the image's intensity profile in the interelectrode region. An example of a  $\sim 5$  nm electrode pairs is shown in Fig. 3.

Electrical characterization of the electrode structures was performed using a probe station and Keithley Instruments 236 source measurement unit. Current-voltage (I-V) data was obtained over a bias range of -1 to 1 V in 40 mV steps. The I-V characteristics of two completed electrode pairs are shown in Figure 4a. The maximum current observed in this bias range was less than 1 nA for both structures. This result was in stark contrast to data obtained from structures where the Pt deposition formed a point contact between the two

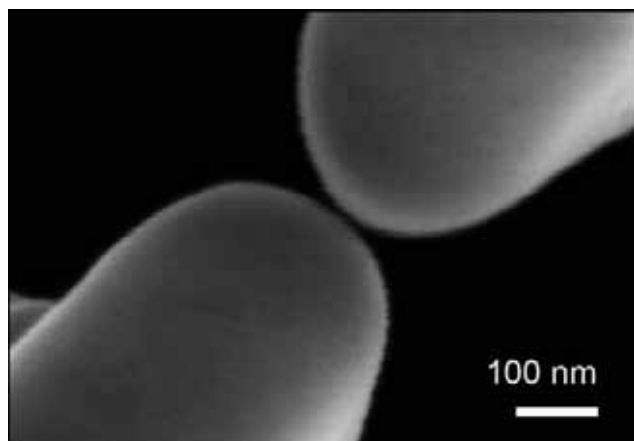


Figure 3: Micrograph of a completed nanoelectrode pairs showing a 5 nm interelectrode gap.

electrodes. In these structures, currents of  $\sim 0.1$  mA were routinely observed at biases of 1 V (Figure 4b).

### Conclusion:

This work presented a simple FIB-based technique for fabricating electrode pairs with interelectrode gaps of 5 to 10 nm. The observed I-V behavior indicates that the electrodes are electrically isolated from each other. This technique can produce a testable device in less than 1 hr using the instrumentation described by the authors. This fabrication technique provides a means to realize a useable set of nanoelectrodes in a rapid and reproducible manner.

### Acknowledgements:

This work was supported by the Intel Foundation and the National Nanotechnology Infrastructure Network Research Experience for Undergraduates Program.

### References:

- [1] M. A. Guillorn, D. W. Carr, and R. C. Tiberio, J. Vac. Sci. Technol. B 18, 1177 (2000).
- [2] A. F. Morpurgo and C. M. Marcus, Appl. Phys. Lett. 74, 2084 (1999).
- [3] A. Bezryadin, C. Dekker, and G. Schmid, Appl. Phys. Lett. 56, 481 (1990).
- [4] M. A. Reed, C. Zhou, C. J. Muller, T. P. Burgin, and J. M. Tour, Science 278 252 (1997).
- [5] H. Park, A. K. L. Lim, A. P. Alivisatos, J. Park, P. L. McEuen, Appl. Phys. Lett. 75, 301 (1999).

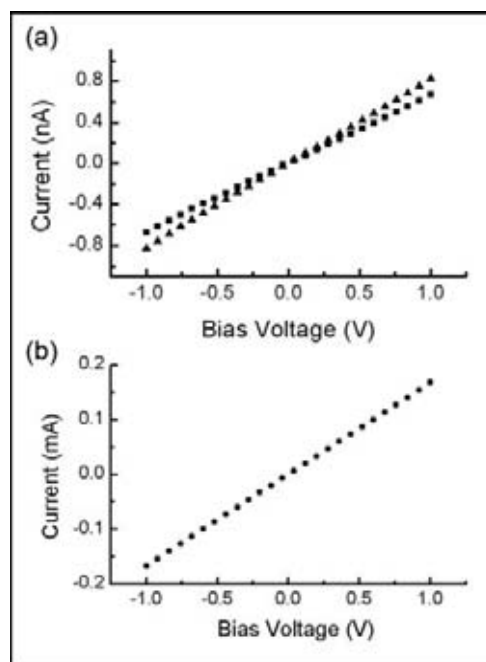


Figure 4: I-V measurements of (a) two electrically isolated electrode pairs, and (b) electrodes with a point contact.

# Fabrication of Two-Dimensional Arrays of Inorganic-Binding Polypeptides for the Template-Directed Self-Assembly of Nanoparticles

**Victoria Mooney, Chemistry, Viterbo University**  
**NNIN REU Site: NanoTech User Facility, University of Washington**

*NNIN REU Principal Investigator: Alex Jen, Material Science and Engineering, University of Washington*

*NNIN REU Mentor: Melvin Zin, Material Science and Engineering, University of Washington*

*Contact: vlmooney@viterbo.edu, ajen@u.washington.edu*

## Abstract:

Due to the unique properties exhibited by nanoparticles, there has been a surge of interest in nanotechnology for developing techniques to organize nanoparticles in a spatially resolved manner. It has been found that by combining inorganic nanoparticles with biological molecules, a high degree of organization and binding specificity can be acquired.

A septapeptide which binds to platinum was modified to form three repeat and one repeat, constrained genetically engineered polypeptides for inorganics (GEPIs). These GEPIs were patterned on two types of substrates: bare gold (Au) and a self-assembled monolayer (SAM) of (4-mercaptophenyl)-anthrylacetylene (MPAA). A high degree of binding specificity occurred on the MPAA due to Schiff base formation, particularly for the protein with three repeats of the platinum-binding sequence. On the Au substrate, the GEPI constrained with the sulfur-containing amino acids bound to the substrate better than the three repeat GEPI. This was because the two sulfurs were able to absorb onto the Au surface.

## Introduction:

Nanoparticles exhibit unique optical, catalytic, magnetic, and electronic properties which could find use in a variety of nanotechnological applications [1,2]. The problems encountered regarding organizing and assembling of these nanoparticles can be resolved by using biological molecules. One of the most promising types of biological molecules to be used in conjunction with nanotechnology is proteins. Proteins are able to recognize materials based on their chemical and physical characteristics and organize these materials into miniscule structures [2]. Recently, phage display and cell-surface display were used to sort through a vast library of random amino acid sequences to identify polypeptide sequences that recognize various inorganic materials such as metals, metal oxides, and semiconductors [2,3].

Through microcontact printing, GEPIs can be physically and chemically patterned onto a surface.

When physically patterned, these polypeptides are transferred directly onto a substrate; often, no covalent bonds are formed. When GEPIs are chemically patterned, the substrate has a SAM that can bond covalently with the proteins [3]. Previously, carboxylic acid terminated SAMs were used; however, additional reagents were required for reaction, thus introducing contaminants to the substrate [3]. Aldehyde terminated SAMs have been used recently because they can form Schiff base linkages ( $R-CHO + R'-NH_2 \rightarrow R-C=N-R' + H_2O$ ) with amine groups and only produce water as a byproduct. If a GEPI has many amine groups, then one would expect chemical patterning to be more advantageous than physical patterning.

## Methods:

**Substrates:** Bare Au substrate and Au substrate with a SAM of MPAA were used. The Au substrate was prepared by rinsing with water and ethanol, drying with  $N_2$ , and then heating 4 min at 53°C to remove any water remaining on the surface. The SAM was formed by submerging an Au substrate in 5 mL of 0.05 mM MPAA and 25  $\mu$ L  $NH_4OH$  (28-30%  $NH_3$ ) under a nitrogen atmosphere for approximately 48 hr. The SAMs were sonicated in ethanol for 10 min to remove excess MPAA, rinsed with ethanol and dried with  $N_2$  gas.

**Platinum-Binding Proteins:** Two GEPIs with strong peptide-substrate binding energies 4 were used: 10  $\mu$ g/mL 3R SD60 ([QSVTSTK]<sub>3</sub>), and 10  $\mu$ g/mL 1RC SD60 ([C-QSVTSTK-C]).

**Patterning of GEPIs:** A poly(dimethylsiloxane) (PDMS) stamp was inked 1.5 hr with protein. To remove excess protein, the PDMS stamp was allowed to float upside down in water for 3 min, rinsed with water (x3), and rinsed with phosphate buffered saline (x3). The stamp was then placed in contact with the Au substrate for 1 min or the MPAA substrate for 2.5 hr.

## Results:

After physically patterning 3R SD60 onto the Au substrate, it was found that the packing density of the proteins was approximately 220 proteins/ $\mu m^2$  (Figure



1). The physically patterned 1RC SD60 had a packing density of approximately 250 proteins/ $\mu\text{m}^2$  (Figure 2). The 3R SD60 chemically patterned onto the MPAA had a packing density of approximately 315 proteins/ $\mu\text{m}^2$  (Figure 3), and the 1RC SD60 on MPAA had a packing density of approximately 120 proteins/ $\mu\text{m}^2$  (Figure 4). All density values were obtained by doing a direct count of proteins in a patterned area.

### Discussion:

3R SD60's greater density on the MPAA substrate can be explained by examining the amino acids' side chains. In addition to the amine group at the N terminus, 3R SD60 also has three amine groups from the lysine residues. These amine groups provide binding sites for MPAA's aldehyde group, enabling Schiff base formation. On the bare Au substrate, the 3R SD60 is only able to bind non-specifically.

Conversely, 1RC SD60's packing density is higher on the bare Au substrate due to the sulfurs in the two cysteine groups which are able to absorb directly onto the Au surface. Also, 1RC SD60 has only one lysine group, greatly decreasing the protein's ability to bind to the MPAA via Schiff base formation.

In the future, patterning of 3R SD60 and 1RC SD60 on Au (111) should be done and the spatial conformation of the proteins examined. To determine how the two patterning methods affect the proteins' platinum-binding ability, platinum nanoparticles should be assembled onto the patterned substrate and the resulting platinum nanoparticle density examined.

### Acknowledgements:

Many thanks to NNIN, NSF, and the University of Washington for this research opportunity, and to Ethan Allen and Alex Jen for making this summer run smoothly. Also, thanks to Mehmet Sarikaya for providing the platinum-binding proteins and to my mentor, Melvin Zin, for his support and encouragement.

### References:

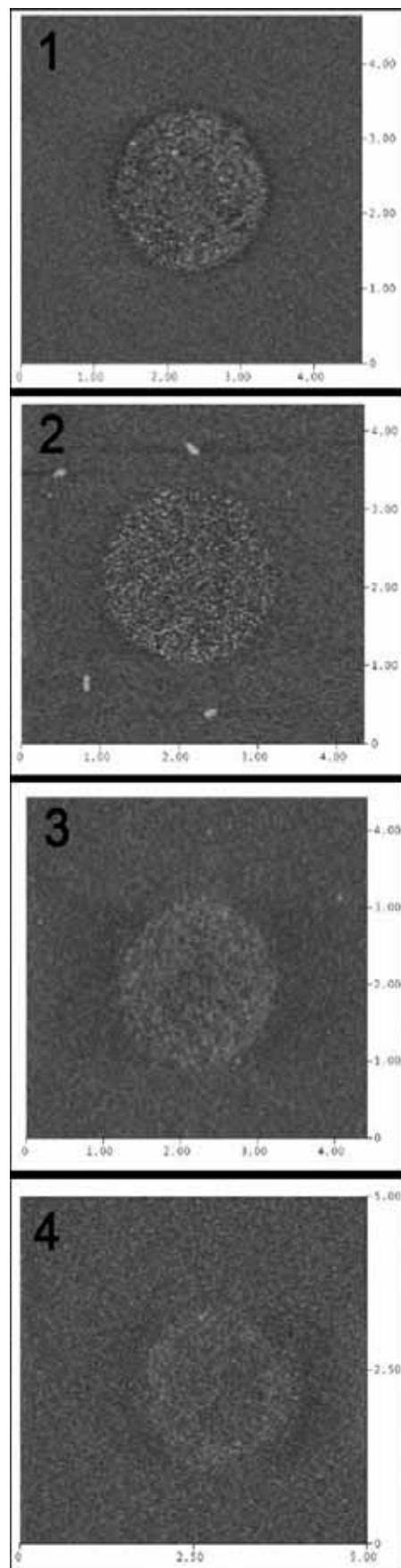
- [1] Niemeyer, C. M. *Angew. Chem. Int. Edn. Engl.* 2001, 40, 4128-4158.
- [2] Sarikaya, M., C. Tamerler, A. K.-Y. Jen, K. Schulten, F. Baneyx, *Nat. Mater.* 2003, 2, 577-585.
- [3] Zin, M. T., M. Hong, M. Sarikaya, A. K. -Y. Jen. *Small.* 2005, 7, 698-702.
- [4] Oren, E. E., C. Tamerler, M. Sarikaya. *Nano Letters.* 2005, 5, 415-419.

*Figure 1: AFM image of 3R SD60 patterned on polycrystalline Au.*

*Figure 2: AFM image of 1RC SD60 patterned on polycrystalline Au.*

*Figure 3: AFM image of 3R SD60 patterned on a SAM of MPAA.*

*Figure 4: AFM image of 1RC SD60 patterned on a SAM of MPAA.*



# Compositional Analysis of W and Ti Bilayer Electrodes at the Metal-Dielectric Interface and Its Effects on Work Function

Que Anh Nguyen, Engineering (Materials Science & Applied Chemistry),  
Franklin W. Olin College of Engineering

NNIN REU Site: Stanford Nanofabrication Facility, Stanford University

NNIN REU Principal Investigator: Professor Bruce Clemens, Materials Science & Engr, Stanford University

NNIN REU Mentor: Gloria Wong, Materials Science & Engineering, Stanford University

Contact: queanh.nguyen@students.olin.edu, bmc@stanford.edu

## Abstract:

In this work, we characterized the metal-dielectric interface of a W/Ti bilayer electrode capacitor to determine how varying the thickness of the Ti layer between 0.5 Å and 12 Å affects the device work function. Characterization using x-ray reflectivity and x-ray photoelectron spectroscopy (XPS) indicates that thin layers of Ti form islands on the dielectric and thus are insufficient in altering the work function of the device to that of Ti. Ti layers of greater than 3 monolayers in thickness are required for continuous coverage and work function control.

## Introduction:

As nanoscale transistors decrease in size, a new material is needed to replace the polycrystalline silicon gates currently used in these metal oxide semiconductor (MOS) devices. Metals are being investigated as the proposed replacement gate material because they would eliminate the problems of dopant penetration and poly-depletion currently seen in poly-Si gates, due to their high carrier density [1]. According to theory, only a few nanometers of material in contact with the dielectric interface controls the work function of a device [2]. Previous work has demonstrated that the work function of a metal gate can thus be tuned by using a bilayer metal system and varying the thickness of the bottom metal layer [3]. Yet, the mechanism for how this works is not well understood. In order to better understand the mechanism for work function tuning, we studied a W/Ti bilayer metal gate system, with the bottom Ti layer being monolayers in thickness. This paper focuses on the materials characterization part of the project.

## Device Fabrication:

MOS capacitors were fabricated using <100> p-type Si substrates, with a SiO<sub>2</sub> dielectric that was thermally grown at 900°C. The metal bilayers were deposited using sputter deposition for one set of samples, and e-beam evaporation for a second set. The thickness of the Ti layer ranged from 0.5 Å to 12 Å, while the W cap layer was consistently 500 Å. After patterning, all

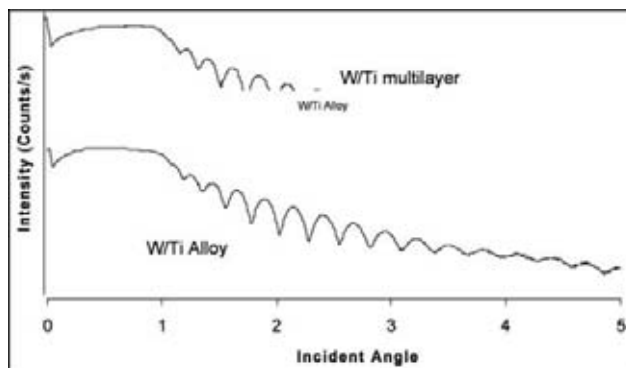


Figure 1: X-ray reflectivity scans of W/Ti multilayer and W/Ti alloy samples.

samples were subsequently annealed using forming gas (H<sub>2</sub> + N<sub>2</sub>) at 400°C for 30 minutes.

## Characterization Results and Discussions:

Figure 1 shows the low angle x-ray reflectivity scans of a W/Ti multilayer sample, and a W/Ti alloy with the same overall composition and thickness. The multilayer sample was made by sputter depositing two monolayers of Ti (4.68 Å) followed by 15 Å of W, and repeating this bilayer period 15 times. It shows a peak at the higher incident angle that is not characteristic of an alloy system. Complete intermixing between the W and Ti metals would have yielded a result that was more similar to the alloy data. Instead, we see an interruption in the W layers with a material that has a very different electron density. We are thus confident that there is minimal W/Ti intermixing in our capacitors during sputter deposition.

Type of Deposition	Expected Thickness (Å)	Calculated Thickness (Å)	Surface Percent Coverage
Sputtering	4.68	4	40%
Evaporation	4.00	10	48%
Sputtering	8.00	9	56%
Evaporation	8.00	16	60%

Figure 2: Layer thickness and Ti surface coverage of dielectric as calculated from XPS data.

Figure 2 gives the Ti percent coverage of dielectric surface as well as the measured average thickness of the thin Ti layer as calculated from XPS angle resolved measurements at 30° and 90°. The partial coverage of the surface indicates that instead of a continuous layer, there are islands of Ti metal on the dielectric. This is significant because the island morphology and surface coverage of the dielectric affects the work function of the device [4]. With the 4.68 Å sputtered Ti sample, approximately 40% of the interface is covered by Ti, resulting in the remaining 60% of the dielectric being covered by W. Such a sample should have a work function close to W, which we do indeed see with our MOS capacitors. Island growth was also studied using atomic force microscopy (AFM), and preliminary results are shown in Figure 3.

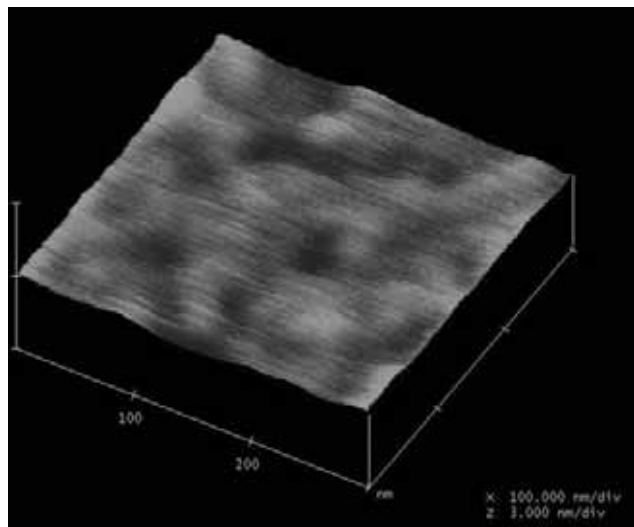


Figure 3: AFM showing metal islands on  $\text{SiO}_2$ , with 30 Å z-scale.

The discrepancy between expected and calculated thickness values (Figure 2) for the evaporation samples also illuminated the poor monitoring and control of layer thickness at such a small range using e-beam evaporation. Sputtering, on the contrary, showed a good agreement between the expected and measured thickness.

## Conclusions:

Although x-ray reflectivity data shows that we can achieve distinct W/Ti interfaces, we conclude that current sputtering and e-beam evaporation techniques do not allow for the deposition of a continuous layer of such a thin Ti film on  $\text{SiO}_2$ . Furthermore, it is unclear if any deposition technique could produce non-island growth of metal monolayers. Therefore, despite theory that only a monolayer worth of material is enough to control the work function of a device, due to islanding of Ti metal, a layer thickness greater than 3 monolayers is required to form a continuous film, and control the work function of a W/Ti MOS capacitor.

## Acknowledgements:

I would like to thank Gloria Wong, Professor Bruce Clemens, Heidi Wheelwright, Ching-Huang Lu, Dr. Michael Deal, Dr. Chih-Sheng Chang, and Professor Yoshio Nishi, as well as NNIN, CIS, and NSF, for making this work possible.

## References:

- [1] Y.-C. Yeo. Thin Solid Films, vol 462-63, pp. 34-41, Sept. 2004.
- [2] S. Park, L. Colombo, K. Cho, and Y. Nishi. Applied Physics Letters, vol 86, no. 7, pp. 073118, February 2005.
- [3] C.-H. Lu, G.M.T. Wong, M.D. Deal, W. Tsai, P.Majhi, C.O. Chui, M.R. Visokay, J.J. Chambers, L. Colombo, B.M. Clemens, and Y. Nishi. IEEE Electron Device Letter, vol 26, pp. 445-448, July 2005.
- [4] I.S. Jeon, J. Lee, P. Zhao, P. Sivasubramani, T. Oh, H.J. Kim, D. Cha, J. Huang, M.J. Kim, B.E. Gnade, J. Kim, R. M. Wallace. IEDM 04, pp. 303-306, 2004.

## **Electronic & Thermoelectric Properties of Semiconductor Nanostructures**

**Luke Niewiadomski, Electrical Engineering, Michigan State University**  
**NNIN REU Site: Michigan Nanofabrication Facility, The University of Michigan**

*NNIN REU Principal Investigator: Rachel S. Goldman, Materials Science & Engineering, University of Michigan*

*NNIN REU Mentors: Weifeng Ye and Matt Reason, Materials Science & Engineering; Abishek Yadav and*

*Kevin P. Pipe, Mechanical Engineering; Kimberley Appel, Michigan Nanofabrication Facility;*

*Xiaogang Bai, Yu-Jin, and Cagliyan Kurdak, Physics; University of Michigan*

*Contact: rsgold@umich.edu*

### **Abstract:**

Due to the unique properties of low-dimensional systems in comparison with those of bulk or thin film materials, nanostructures enable the tailoring of materials for new device applications. In this project, we explored the effects of dilute concentrations of impurities and highly ordered arrangements of quantum dots on the properties of GaAs-based heterostructures for electronics and thermoelectrics, respectively.

In the case of GaAs with dilute nitrogen concentrations, we used gated Hall measurements to explore the electronic states associated with pairs and clusters of nitrogen. In the case of highly ordered quantum dot arrays, we used Seebeck coefficient measurements, to determine the effects of quantum dot alignment on thermoelectric properties.

We focused on the design and implementation of test structures to facilitate these electronic and thermoelectric measurements.





# DNA Pyrosequencing Using Microfluidic Chips

**William Noderer, Chemical Engr, and Integrated Business & Engineering, Lehigh University**  
**NNIN REU Site: Stanford Nanofabrication Facility, Stanford University**

*NNIN REU Principal Investigator: Peter Griffin, Electrical Engineering, Stanford University*

*NNIN REU Mentor: Ali Agah, Electrical Engineering, Stanford University*

*Contact: wln2@lehigh.edu, griffin@stanford.edu*

## Abstract:

Pyrosequencing is a new method of DNA sequencing that shows promise in reducing costs by several orders of magnitude while increasing the throughput. In this project, we applied the pyrosequencing technique to a microfluidic device. The enzymes required for sequencing flowed through the channel while DNA was attached to superparamagnetic beads inside the channel. A novel bead trap was designed and tested in order to prevent the loss of DNA during the sequencing process. An oligonucleotide was used for preliminary sequencing experiments. Three base pairs were successfully sequenced. The results show potential for a revolutionary DNA sequencing technique.

## Introduction:

Genome sequencing has transformed the biological sciences. For the progress to continue, cheaper and faster sequencing techniques must be developed [1]. Current sequencing techniques employ dideoxy sequencing, commonly referred to as Sanger sequencing. This process was developed over 25 years ago and has gone through major improvements over the years but has some inherent limitations to its

effectiveness [2]. Using the Sanger method, the Human Genome Project took 13 years and 13 billion dollars to complete [3]. The enormous costs and time of DNA sequencing hinders a lot of genomic research.

Pyrosequencing is one possible technique that has potential to replace Sanger sequencing [2]. As shown in Figure 1, pyrosequencing works by detecting the pyrophosphate (PPi) released when a nucleotide is correctly incorporated into DNA by polymerase. ATP sulfurylase converts the released PPi into ATP. An enzyme from fireflies, called luciferase, converts the ATP into light, which can be detected by a camera. Therefore, by exposing the DNA to only one type of nucleotide at a time, one can detect whether or not the nucleotide corresponds to the next nucleotide in the sequence.

## Procedure:

In this project we created a microfluidic prototype for pyrosequencing, shown in Figure 2. The superparamagnetic beads with DNA attached were held in a bead trap with a magnet while the enzymes for pyrosequencing flowed over the beads. The microfluidic chip design consisted of a main channel with a recess to trap the beads. We at first used one 500  $\mu\text{m}$  long and 14  $\mu\text{m}$  deep recess as a bead trap, but testing showed that a series of 20  $\mu\text{m}$  long bead traps would be more effective. The channels and bead traps were patterned on a silicon wafer using standard

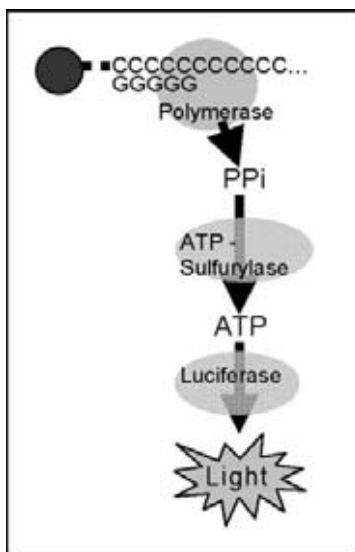


Figure 1: Pyrosequencing chain reaction.

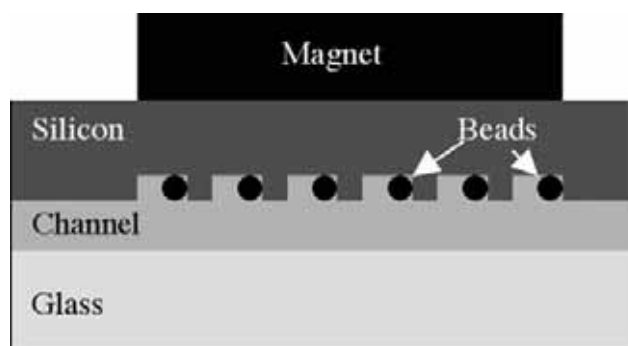


Figure 2: Diagram of bead trap design.

photolithographic techniques and etched using plasma etching. The channels were 54  $\mu\text{m}$  deep and 100  $\mu\text{m}$  wide. The inlet and outlet ports were created with a drill press and a 1.1 mm diamond tip drill bit. A glass wafer was anodically bonded to the silicon wafer to enclose the fluidic channel.

Four cylindrical neodymium rare earth magnets with a residual flux density between 13,400 to 13,700 Gauss [4] were stacked on the opposite side of the silicon wafer and used to pull the superparamagnetic beads into the bead traps. Superparamagnetic beads with a diameter of 2.8  $\mu\text{m}$  were flowed into the channels and examined on an inverse microscope to determine the successfulness of the bead trap. Once it was shown that the bead trap design successfully retained the beads, the beads were washed out to prepare for preliminary sequencing experiments.

The glass side of the chip was placed on a CCD camera to monitor light and the magnets were returned. A single stranded oligonucleotide with a primer was biotinylated to the superparamagnetic beads and flowed into the channel. A mixture of enzymes (polymerase, ATP sulfurylase, and luciferase) along with the nucleotide corresponding with the next nucleotide in the oligonucleotide sequence were flowed into the fluidic channel. The enzymatic fluid was flowed until the light signal degraded, at which point, the next nucleotide was flowed into the channel.

## Results and Discussion:

The bead traps successfully held the beads while fluid flowed through the channel. If a bubble entered the fluidic channel, it tended to remove some beads from a bead trap, but there was a high probability that the beads would be caught in another bead trap farther down the channel. This greatly increased the effectiveness of the bead trap design, because if long sequencing reads are to be successful, almost no beads can be lost. This bead trap design can be applied to many other fluidic devices and applications. It would be ideal for an electrowetting transport chip because of its ability to withstand the surface tension of bubbles.

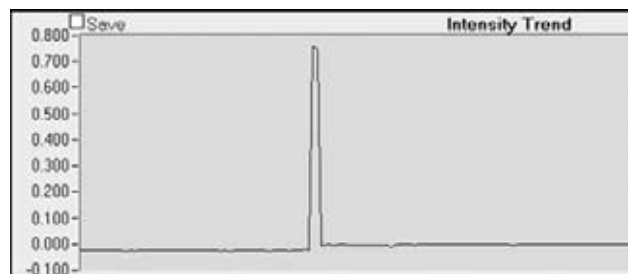


Figure 3: The peak in the light intensity corresponds to the incorporation of a nucleotide.

In our preliminary sequencing experiments, we successfully sequenced three nucleotides of an oligonucleotide. The camera detected distinct peaks in light intensity, which faded with time and then peaked with the addition of the next nucleotide. Figure 3 shows an ideal peak in light intensity we received.

One major problem was the time it took to sequence a nucleotide. The large dead volume in our inlet connectors and our extremely low flow rate of only 1  $\mu\text{L}$  per minute caused a large lag in time from when the next nucleotide was introduced to when a light signal was detected. Additionally, the time it took for the light signal to degrade was unacceptably long. The pyrosequencing reaction relies on diffusion for mixing of enzymes. Either better mixing techniques must be found, or the number of beads must be reduced.

Even though only three nucleotides were sequenced, the results prove that the chip design works. Much work needs to be done to optimize the chip design and sequencing process, but this technique may revolutionize DNA sequencing.

## References:

- [1] Kartalov, E., and Quake, S., Microfluidic device reads up to four consecutive base pairs in DNA sequencing-by-synthesis. *Nucleic Acid Research*, 2004, 2873-2879.
- [2] Ronaghi, M., Pyrosequencing sheds light on DNA sequencing. *Genome Research*, 2001, 11, 3-11.
- [3] National Human Genome Research Institute, <http://www.genome.gov>.
- [4] KJ Magnets, <http://www.kjmagnetics.com/specs.asp>.

## Growth of Cubic Silicon Carbide on Silicon Nano-Mesas

**Brian Noel, Electrical Engr and Biomedical Engr, Virginia Commonwealth University**  
**NNIN REU Site: Cornell NanoScale Science and Technology Facility, Cornell University**

*NNIN REU Principal Investigator: Michael Spencer, Electrical and Computer Engineering, Cornell University*  
*NNIN REU Mentors: M.V.S. Chandrashekar, Chris Thomas, Electrical and Computer Engr, Cornell University*  
*Contact: EdmondsonB@vcu.edu, spencer@ece.cornell.edu*

### Abstract:

Silicon pillars and tips were fabricated with 2, 3, 4, and 5  $\mu\text{m}$  spacings. The bases were 1  $\mu\text{m}$  with the pillars having an aspect ratio of 7:1 and the tips 1:1. A growth mask was applied to the tips only, and CVD was used to grow SiC on the structures. 2, 4, 6, 8, 12, 15, 30, and 60 minute growths were performed and characterized.

The 2  $\mu\text{m}$  spaced tips and pillars have exhibited the best terrain on which silicon carbide can grow, as the film seems to have coalesced to a further degree than on other spacings. Characterization is done using SEM and XRD to see the growth and determine the crystal structure.

### Introduction:

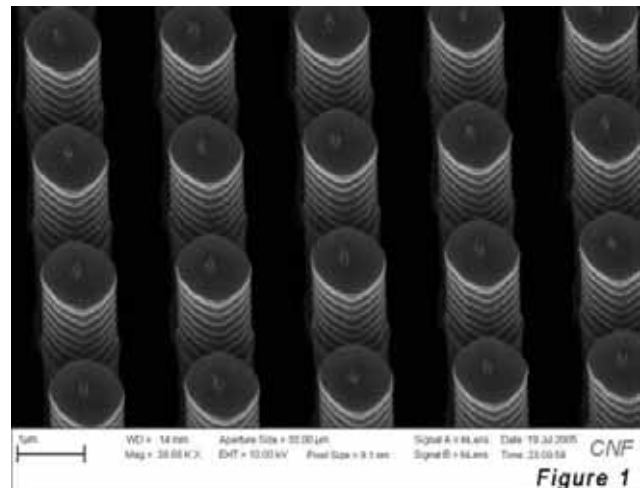
Silicon carbide is one of the strongest materials known, with a Young's modulus of 420 GPa ( $\text{Si}_3\text{N}_4$  - 320 GPa), and a rating of 9.5 on the Mohs hardness scale. It is already used as an abrasive in industry (carborundum), and is beginning to replace cubic zirconium as a cheaper alternative to diamond (moissanite). Silicon carbide is corrosion resistant and has a very high melting point (2700°C), making it suitable for MEMS or piezoresistive applications in harsh and extreme environments. With its bandgap ranging from 2.36 to 3.2 eV, it has obvious applications in high temperature, high power electronics. It also has a high refractive index, and so, along with exhibiting other novel electro-optic properties, silicon carbide has many theoretical applications in optics and photonic engineering. No other semiconductor material can boast this resiliency and robustness, making the growth of high quality silicon carbide films a very promising endeavor.

The cost of manufacturing it at present, however, is quite prohibitive. 2 inch wafers of silicon carbide can cost as much as \$2000, whereas a 4 inch wafer of silicon can be obtained for as little as \$8. This makes finding a way of growing silicon carbide on silicon a very attractive alternative to the current processing technology. Hence, the reason for attempting to grow on silicon pillars and tips.

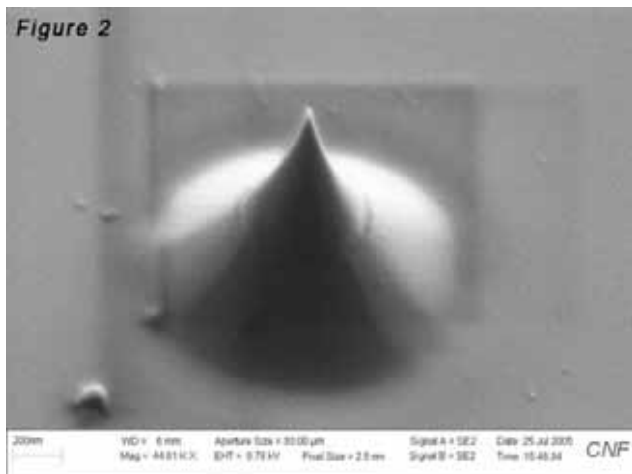
There are two main reasons for growing silicon carbide on silicon pillars and tips: the large lattice mismatch (~20%) and the mismatch in the thermal expansion coefficients (~8%). The lattice mismatch should have a reduced effect on the grown crystal as a small nucleation area is provided by the pillars (1  $\mu\text{m}$ ) and tips (~10 nm). This should help reduce defect density and provide a higher quality crystal than what is grown on planar silicon. The pillars also serve another purpose; as the two materials are cooled after growth, they will contract at different rates. Rather than introduce dislocations in the silicon carbide film, the pillars should buckle to relieve much of the strain that will inherently be caused by the mismatch in the thermal expansion coefficients.

### Procedure:

Silicon wafers were oxidized in a wet ambient until 900 nm of oxide was grown. Photolithography was then performed using a 10X i-line stepper to step the pillar/tip pattern into 140 die. The pattern was transferred into the oxide using a RIE plasma system. After stripping off the photoresist, the wafers were either subjected to a chlorine plasma ICP RIE, or the Bosch process. The Bosch process was used to fabricate pillars with flat tops and high aspect ratios, whereas the chlorine







plasma etch was used to fabricate tip precursors 1  $\mu\text{m}$  in diameter. (See Figures 1 and 2.)

After fabricating the tip precursors, the wafers were re-oxidized for 90 minutes in a wet ambient, creating tips. An etch-back process was then used to apply a growth mask and strip the oxide from a suitable area of the tips. Growth was performed by CVD at a temperature of 1350°C and a pressure of 200 torr. The carbon to silicon ratio was 3:1 using the gases propane ( $\text{C}_3\text{H}_8$ ) and silane ( $\text{SiH}_4$ ). 2, 4, 6, 8, 12, 15, 30, and 60 minute growths were performed on both tips and pillars. The resulting film was characterized using SEM and XRD.

### Results and Conclusions:

It was originally hoped to characterize the growth process, which is why so many short growths were performed. However, the longer growths seemed to yield more promising data, and thus much of the

attention was focused on these longer growths. It was determined that the 2  $\mu\text{m}$  spaced tips were most suitable for growth, as there was clear coalescence of the film after 1 hour of growth. (See Figure 3.) However, scanning electron micrographs that were taken on other spacings do suggest that coalescence is but a matter of time.

The pillars proved to be the more successful endeavor, as all spacings look to be able to experience coalescence. The 2  $\mu\text{m}$  spacings exhibited coalescence, but it is only a matter of time before the other spacings will follow suit. (See Figure 4.)

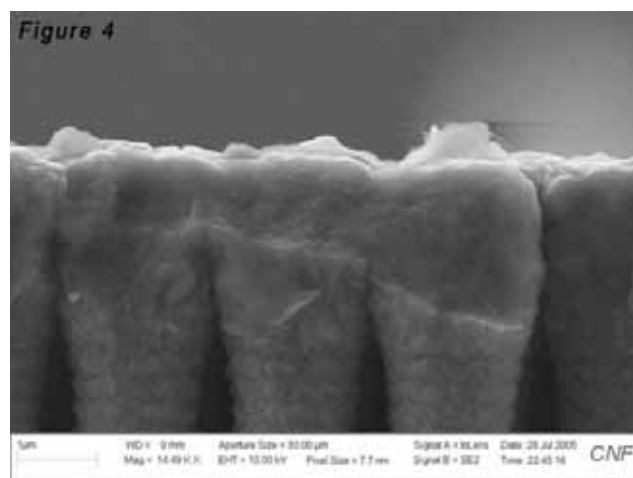
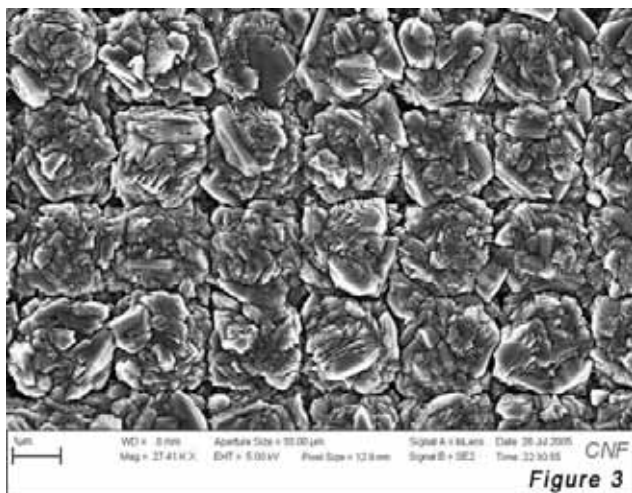
X-ray diffraction was performed on tip growth, post growth, and growth on planar silicon. Rocking curves were performed around the  $\langle 100 \rangle$  crystal direction on tip growth and planar growth. The FWHM value for planar growth was around 2.7 degrees, while that of the tip growth was around 1.7 degrees, proving that this technique yields a better oriented crystal.

### Future Work:

More work can certainly be done to optimize each growth process. With processes optimized for both tip and pillar scenarios, perhaps higher quality films can be grown in less time. The periodic spacing of the pillars may also lend itself to growth of a silicon carbide photonic crystal, although much more research is needed to pursue this idea.

### Acknowledgments:

NNIN, CNF, M.V.S. Chandrashekhar, Chris Thomas, Michael Spencer.



# Electrical and Structural Characterization of GaN for Optoelectronic Applications

**Christopher Olson, Materials Science & Engineering, University of Florida**  
**NNIN REU Site: Nanotech, University of California at Santa Barbara**

*NNIN REU Principal Investigator: Umesh K. Mishra, Electrical & Computer Engr, UC Santa Barbara*  
*NNIN REU Mentor: Michael Grundmann, Electrical & Computer Engr, University of California, Santa Barbara*  
*Contact: olsoncr@ufl.edu, mishra@ece.ucsb.edu*

## Abstract:

Many possible applications for Gallium Nitride (GaN) are currently being researched in the field of optoelectronics. GaN has a wide, direct band gap, which is useful for making LEDs that emit light in both the visible and ultraviolet spectrums.

This project focuses on the growth of N-face GaN films, specifically InGaN/GaN and p-type films. X-ray diffraction (XRD) is used to analyze the crystallographic structure and composition of GaN films. XRD analysis of InGaN/GaN multiple quantum well structures shows that at a given growth temperature, more Indium is incorporated into N-face films than into Ga-face films. Additionally, p-type GaN:Mg films were grown and analyzed using Hall effect measurements.

Practical uses of N-face GaN derive from the fact that it has the opposite polarization from Ga-face GaN with respect to the growth axis; it is thus useful for polarization engineering in optoelectronic devices.

## Introduction:

There is enormous potential for the use of LEDs in the world today due in part to the inefficiency of conventional fluorescent and incandescent. On average, an incandescent bulb requires fifty times the power an LED needs to generate the same amount of light, and has less than 1% the lifetime. LEDs have the capability of achieving power efficiencies near 100%. GaN is an

excellent material for the growth of LEDs because it has a wide, tunable direct band gap.

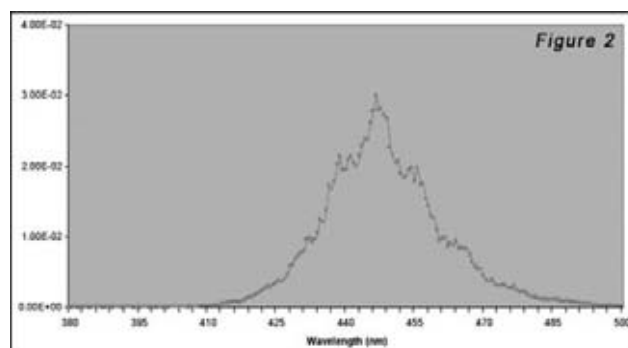
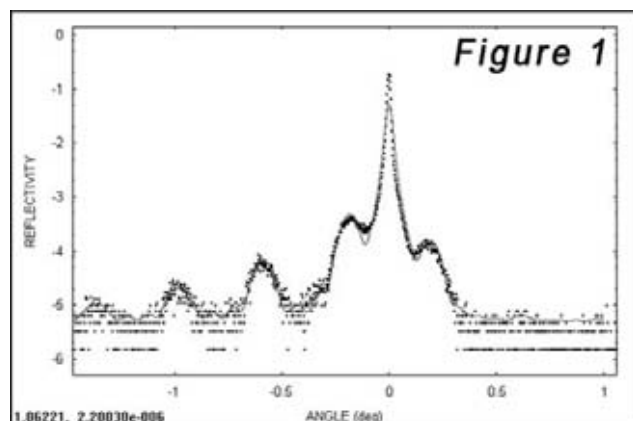
## Procedure:

GaN films were grown via Molecular Beam Epitaxy, typically in the form of multiple quantum well structures containing alternating layers of GaN and InGaN. X-ray diffraction, atomic force microscopy, photoluminescence, Hall effect, capacitance-voltage measurements, and deep level transient spectroscopy were used to characterize the films.

Triple axis XRD was performed using a Sharp MRD Pro II diffractometer to determine the exact thickness and composition of GaN and InGaN films. Digital Instruments D3000 and D3100 Atomic Force Microscopes were used to confirm uniformity of film surfaces as well as to measure their rms roughness.

Photoluminescence is used to optically characterize films after growth. The PL system shines a helium-cadmium laser at the sample. The energy from the laser excites electrons into the conduction band of the GaN. These electrons then fall back into their normal states in the valence band, releasing light with energy equal to the band gap. The emission of light from the sample is measured by a spectrometer and plotted as a function of varying wavelength. This information can be used to determine the wavelength of light being emitted and to approximate its intensity.

Electrical measurements performed include Hall effect, CV measurements, and DLTS. Micro-Hall effect samples were processed in a clean room using



GaN films grown in the MBE system. These samples had square contacts 50  $\mu\text{m}$  to a side. The Hall Effect measures the change in resistance through the material when a magnetic field is applied. From this change in resistance, the concentration and mobility of charge carriers can be calculated.

CV measurements were used to develop profiles of the concentration of donors or acceptors with respect to depth in the sample. Preliminary work was done to correct errors associated with the measurement of CV data. The impedance analyzer assumes a diode to be a resistor in parallel with a capacitor; however, this model does not account for the Schottky resistance of the metal contacts on the LED. By taking capacitance measurements at various frequencies, this Schottky resistance can be approximated, allowing for accurate CV data.

Often times in a material, impurities are present which create what are called trap levels. These levels are located in the band gap and momentarily “trap” carriers which could be in the conduction or valence bands. Even if the carriers are only held at the trap level for a small fraction of a second, performance can be degraded. High frequency devices, operating in the megahertz regime, will lose a significant amount of power just from momentary trapping of electrons.

## Results and Conclusions:

Physical characterization of films grown yielded positive results. When films were analyzed using XRD, they were typically found to be of the thickness and composition desired. Typical GaN/InGaN MQW structures had alternating layers of about 10 nm of GaN and 4 nm of InGaN. Additionally, rms roughness values obtained from AFM scans were on the order of one to two nanometers. Photoluminescence spectra for these structures yielded wavelengths of 445 nm, in the blue light regime.

Another research aspect for this project was the attempt to grow a p-type N-face GaN film. An Mg-doped GaN film was grown in an attempt to achieve p-type doping and was characterized via the Hall effect. Hall effect measurements showed a hole concentration of  $1 \times 10^{17}$  holes/cm<sup>3</sup> and a hole mobility of 9.6 cm<sup>2</sup>/V·s, the first recorded p-type N-face GaN film.

Preliminary results were obtained from performing DLTS on a film with a series of diodes processed onto it. This film was an N-type GaN film with a SiN cap to reduce leakage currents in the film. An electron trap was found in the material with an activation energy of approximately 75 to 90 meV, thereby indicating that the impurity present creates a trap level 75 meV below the conduction band.

## Future Work:

Continued research must be conducted in order to more completely understand the trap levels present in our films. The concentration, carrier type, and activation energy of these traps can be characterized in a variety of our MBE-grown films in order to try to determine their source and perhaps eventually determine how to eliminate them. Furthermore, the study of the growth of N-face GaN films is still in its infancy. N-face growth of GaN/InGaN will be optimized until luminescence is achieved, and then LEDs will be fabricated from these films. Finally, GaN LEDs need to be optimized for output and power efficiency in order to make it useful to the industrial community and to society as a whole.

## Acknowledgements:

Prof. Umesh Mishra, Mike Grundmann, the UCSB REU staff, the NNIN and NSF.

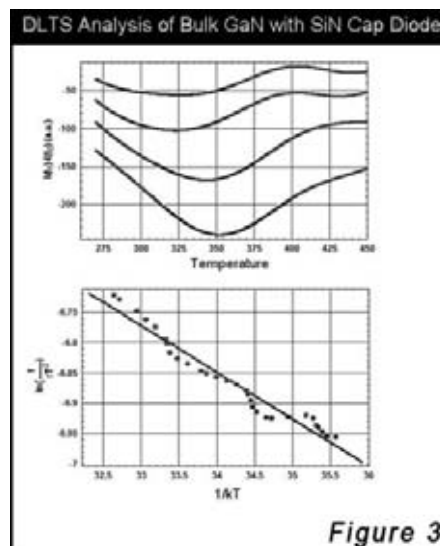


Figure 3

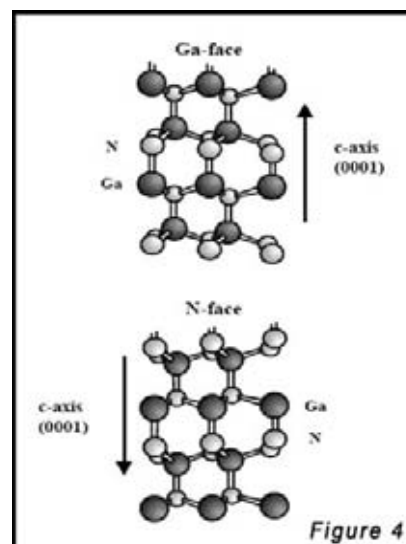


Figure 4

## **Social and Ethical Dimensions of Nanofabrication**

**Priscilla Paul, General Engineering, Concentration in Biomedical Engineering,  
The Cooper Union for The Advancement of Science and Art**

**NNIN REU Site: Cornell NanoScale Science and Technology Facility, Cornell University**

*NNIN REU Principal Investigator: Prof. Bruce Lewenstein, Departments of Communication,  
and Science & Technology Studies, Cornell University*

*NNIN REU Mentor: Ana Viseu, Ph.D, Department of Science & Technology Studies,  
and Cornell NanoScale Facility, Cornell University*

*Contact: paul@cooper.edu, b.lewenstein@cornell.edu, viseu@cnf.cornell.edu*

### **Introduction:**

This project focuses on the social and ethical dimensions of nano research and development. During this project at the Cornell NanoScale Facility, ethnographic work and interviews were conducted with a diverse group of researchers ranging from undergraduate students, to staff members and industry users, and a video was produced that reflects some of the themes which emerged from these conversations and investigations. Research participants discussed the social dimensions of making science by interacting with others and sharing the lab with them, how safety an overriding concern, research's toll on the environment, and expressed their opinions on public communication and how it relates to hype and funding. Looking at all these factors, some were then able to speak about the future and the difficulties of navigating the world of Nano. Put together, these findings allude to the centrality of social and ethical issues, often considered extra-scientific, in the practices of nano-researchers. The resulting video is just the beginning of the studies to come on the social and ethical dimensions of nanofabrication.

### **Procedure:**

To begin, background reading was done of articles and reports on the subject of nanotechnology such as *The Big Down: From Genomes to Atoms* [1] by the Erosion Technology and Concentration Group (ETC), and *Societal Implications of Nanoscience and Nanotechnology* [2] by the National Science Foundation (NSF). Organizing these readings helped build a database of such materials. Next, the lab was visited and ethnographic work was performed, studying the users and their interactions with one another and the machines, and engaging in conversation and informal interviews with undergraduate students, staff members, and industry users. We asked about which issues involved in doing nanotechnology research were most important to them. Several questions were asked such as what project they were working on, how the

products of their research would benefit the world, what their greatest worries were working in a clean room, and various other issues related to nano research such as toxicity, privacy and surveillance, environmental issues, hype and expectations, equity, and necessity of public communication, among other topics.

### **Results:**

The interviews gave a greater understanding of the large number of issues that compose the world of nanofabrication—economics, politics, definitions, safety, and uncertainty, among others. Their diverse character offers a glimpse into the difficulties of navigating the world of nano-related-research. CNF, being a lab shared by students, users, and staff, brought to light some of the social dimensions of making science, “communal lab living rules” that users had to follow to coexist in the lab and avoid obstacles. Failure to follow these guidelines would result in inefficient utilization of resources and hinder the research process. Some of these lab rules extended to negotiating and outlining the rules of doing research in shared conditions. For instance, how staff members’ contributions of to a user’s research should be acknowledged or how staff can juggle their professional identities as staff, lab technicians and researchers.

One of the most recurrent concerns was safety. In order to ensure the safety of the facility and of all users, all NNIN sites follow strictly enforced work procedures and regulations. These require that all operations be undertaken with the safety of both the individual user and other users as the primary consideration.

The need for strict regulations regarding the process of nanofabrication points to the larger interactions of science, with society and the environment, and proves that the social dimensions of Nano go beyond the confines of the lab and involve the community at large. In doing so, we come to realize the importance and necessity of communicating with the public. Consultation and communication have proved to be the



best ways to build trust and maintain a balance between public and scientific interests. They are also a way of informing the public of the some of the differences between the reality portrayed in the media and science fiction, and realities of nanofabrication and research. For many people, the media is their only entry point into laboratory life. Having no other comparison, it becomes difficult to differentiate between facts and fiction. In recent years, nanotechnology has been introduced to the general public most noticeably through works of science fiction.

Most of the researchers interviewed agreed that the kind of hype promoted in the media and sci-fi has always led to high unrealistic expectations of science and technology, and has also led to fomenting fear of the fictitious devices designed in these science thrillers. Yet, at the same time, they also agreed that playing on hype may lead to a funding advantage. By using certain eye-catching words that funding agencies consider cutting edge, they may be nudging their proposals to the top of the pile. It should not come as a surprise that the interaction between what sponsors and benefactors want to hear and are willing to fund, and what researchers feel compelled to specify in their applications, shape the kinds of projects that make it into the lab. This means that hype should not be dismissed as a mere media game. It plays an important role in framing the present and future of nano-research.

### **Future:**

The results of this study are not meant as definite answers. Instead, they are starting points—part of a larger NNIN research effort that aims to increase knowledge of the perspectives on Social and Ethical Dimensions of Nano. To this effect, a number of other researchers are conducting surveys and other empirical research. The main point is that all these social and ethical issues, that are seemingly extra-scientific or everyday concerns, are actually central to the process of doing nanotechnology; they are what people in the lab deal with in their everyday work. They complement each other and make Nano what we know it to be.

### **Acknowledgements:**

I would like to thank Ana Viseu and Bruce Lewenstein for their continued support and writing and editing assistance, and Brant Penman for video production. I would also like to thank all the CNF users that participated in the interviews, especially those that appear on the video, Mike Skvarla, Robert Stundtner, and Meredith Metzler.

### **References:**

- [1] ETC Group. 2003. The Big Down: Atomtech - Technologies Converging at the Nano-scale. Winnipeg, Canada.
- [2] Roco M.C. & Bainbridge, W.S. (eds.). Societal Implications of Nanoscience and Nanotechnology, Dordrecht: Kluwer, 2001.
- [3] Paul, Priscilla, Exploring the social and ethical dimensions of nanofabrication, video, <http://www.sei.nnin.org/archive.html>.

# The Effects of SiO<sub>2</sub> Shell Coatings on High Temperature Annealing Behavior of FePt Nanocrystals

**Jose Pelaez, Chemical Engineering, Columbia University**  
**NNIN REU Site: Microelectronics Research Center, University of Texas at Austin**

*NNIN REU Principal Investigator: Dr. Brian Korgel, Chemical Engineering, University of Texas at Austin*

*NNIN REU Mentor: Doh C. Lee, Chemical Engineering, University of Texas at Austin*

*Contact: jmp2115@columbia.edu, korgel@mail.che.utexas.edu*

## Introduction:

Iron Platinum (FePt) nanoparticles (NP's) have been a subject of intense study for many years due to their ease of synthesis, chemical stability, and potential applications in high density data storage [1]. However, as-synthesized NP's exhibit a low Curie temperature, low saturation magnetization, and low coercivity. In order to correct the aforementioned variables, the particles must undergo a high-temperature annealing, after which, through solid state diffusion, the Fe and Pt atoms rearrange from the chemically disoriented face-centered cubic (fcc) phase to the highly ordered face-centered tetragonal (fct) phase, in which Fe and Pt atoms are arranged in alternating layers. In the face centered tetragonal phase, the crystals exhibit a high Curie temperature, high saturation magnetization, and high coercivity, making them ideal candidates for data storage applications, with recording density attainments as high as 1 Tbit/in<sup>2</sup> estimated. However, exposure to extremely high annealing temperatures required for phase transition (650°C and up) decomposes the organic capping layer, and leads to particle sintering; the particles lose their quantum properties and assume the physical characteristics of a bulk FePt alloy.

By performing a post-synthesis coating of the FePt NP's with SiO<sub>2</sub>, it was hoped that the particles could be subjected to high-temperature annealing conditions and rearrange into the fct phase successfully, and due to their isolation within the SiO<sub>2</sub> core-shell structure, avoid the problem of inter-particle sintering.

## Experimental Procedure:

FePt nanoparticles were prepared following methods reported by Sun and coworkers [1,2]. A platinum precursor (Pt(acac)<sub>3</sub>) in an ether solvent, was reduced either thermally or by addition of the reducing agent 1,2-hexadecanediol, then heated to 100°C and combined with the iron precursor Fe(CO)<sub>5</sub> and organic capping ligands (oleic acid, oleyl amine). This was then allowed to reflux, with an interim incubation temperature and time dependant on desired particle size. The resulting black solution was collected using chloroform, then combined with ethanol (EtOH) as an anti-solvent and centrifuged. The resulting nanoparticle precipitate was dispersed in cyclohexane for silica coating via the inverse micelle method reported by Yi, et al. [3]; the particles were combined with the surfactant Igepal CO-520, a catalytic amount of ammonium hydroxide (30%), and the silica source tetraethylorthosilane (TEOS), and vigorously

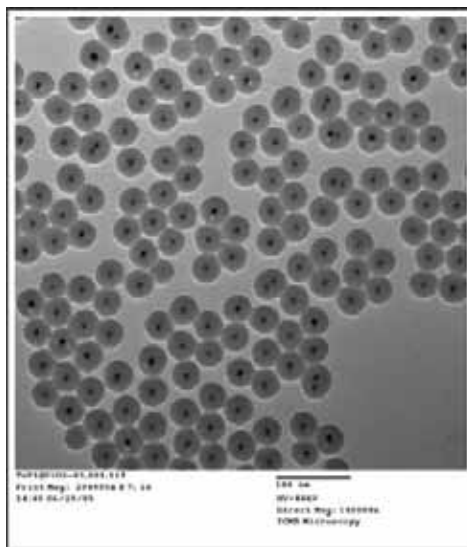


*Figure 1:  
TEM image of  
as-synthesized  
silica coated  
FePt nano-  
particles.*

stirred for 72 hours. The brown mixture was then separated using methanol in a separatory funnel. The FePt@SiO<sub>2</sub>/MeOH mixture was collected and centrifuged. (“@” denotes a shell material around another core nanocrystal.) The glass-like precipitate was then washed multiple times using various solvents before being re-dispersed into ethanol, forming a colloidal suspension of silica coated particles (Figure 1).

## Surface Functionalization:

The as-synthesized silica coated particles were found to exhibit strong interparticle forces, aggregating into large clusters undesirable for data storage applications (Figure 2). Various methods were tried in order to achieve formation of an ordered monolayer. The first two attempts—spin casting and vertical evaporation—proved unsuccessful. The third, a surface functionalization reported by Wei, et al. [4], brought success. In this method, the suspension of FePt@SiO<sub>2</sub> in EtOH was mixed with a small amount of NH<sub>4</sub>OH (30%) and a 10% by volume solution of the reactant orthotridecylmethoxysilane (OTMOS) in chloroform, and allowed to react for 24 hours in a vigorously stirred vessel. The result was the grafting of long alkane chains onto the silica surface, making the previously hydrophilic silica particles hydrophobic. By dispersing the hydrophobic particles into an organic solvent then depositing it into a water-filled trough, an ordered monolayer was obtained at the air-water interface.

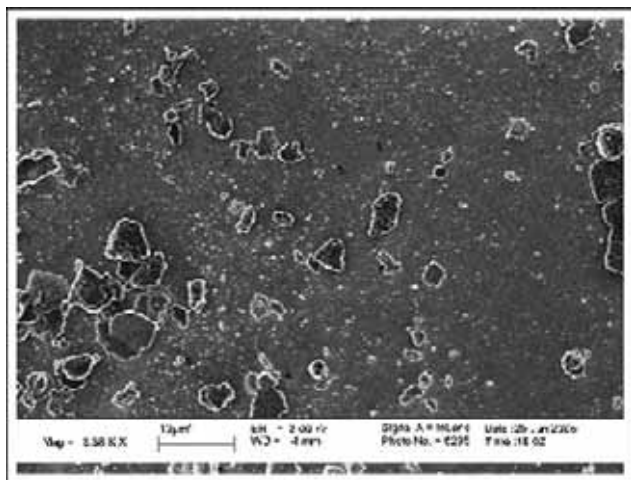


Figure 2: SEM image of agglomerated FePt@SiO<sub>2</sub> nanoparticles.

### Annealing:

Two glass substrates were prepared by drop-casting a large amount of FePt@SiO<sub>2</sub> colloidal suspension. The samples were then placed into an x-ray diffractometer (XRD) and annealed *in situ* under air at various temperatures, ranging as high as 800°C.

### Results:

From both SEM and XRD studies, it appears that as-synthesized FePt nanoparticles experienced significant inter-particle sintering (Figure 3). However, SiO<sub>2</sub> coated particles exhibited no such sintering (Figure 4). XRD shows that the SiO<sub>2</sub> shells prevented sintering as expected, however, it also appears that they may be inhibiting the fcc to fct phase transition.

### Future Work:

Further study of the FePt@SiO<sub>2</sub> nanoparticles is required under different annealing conditions to determine if the

occurrence of a phase transition on the FePt core is possible. Magnetic characterization of the particles using SQUID or MFM both before and after annealing is required to determine the relevance of FePt@SiO<sub>2</sub> core-shell particles in the field of high-density data storage.

### Conclusion:

FePt nanoparticles were prepared using a one-pot synthesis, and then coated with SiO<sub>2</sub> via an inverse micelle method. The particle surfaces were functionalized with OTMOS in order to form a monolayer at the air-water interface. Two substrates were prepared: one using the as-synthesized FePt nanoparticles and one using the SiO<sub>2</sub> coated FePt. The substrates were then placed in an XRD and annealed *in situ*, with as-synthesized nanoparticles exhibiting significant inter-particle sintering, and the SiO<sub>2</sub> coated nanoparticles exhibiting no inter-particle sintering. However, the SiO<sub>2</sub> coating also appears to inhibit the fcc to fct phase transition. The extent of this inhibition is unknown.

### Acknowledgements:

Dr. Brian Korgel, Chemical Engineering, University of Texas at Austin; Doh C. Lee, Chemical Engineering, University of Texas at Austin; the Korgel Research Group; NNIN and NSF for funding.

### References:

- [1] Chen, Min, Liu, J.P., and Sun, Shouheng. "One-Step Synthesis of FePt Nanoparticles with Tunable Size." JACS Communications, submitted (2004).
- [2] Sun, Shouheng, et. al. "Monodisperse FePt Nanoparticles and Ferromagnetic FePt Superlattices." Science: Vol. 287.
- [3] Yi, Dong Kee, et. al. "Silica-Coated Nanocomposites of Magnetic Nanoparticles and Quantum Dots." J. Am. Chem. Soc. 127, 4990-4991 (2005).
- [4] Wang, Wei. et. al. "Fabrication of Two- and Three-Dimensional Silica Nanocolloidal Particle Arrays." J. Phys. Chem. B 107, 3400-3404 (2003).

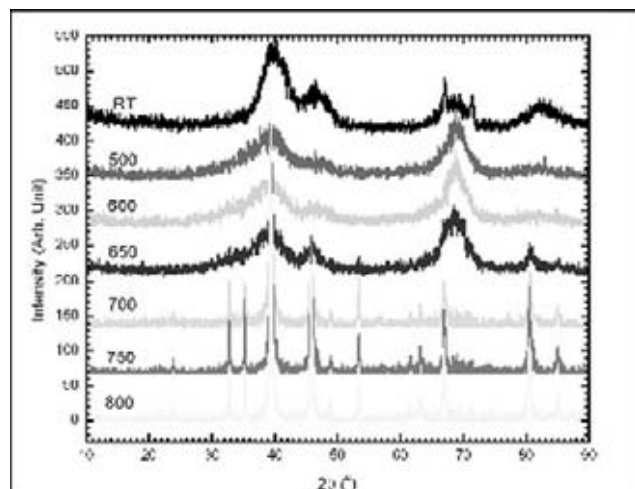


Figure 3: XRD of high-temperature annealing of uncoated 2 nm FePt nanoparticles. Peak sharpening indicates particle sintering.

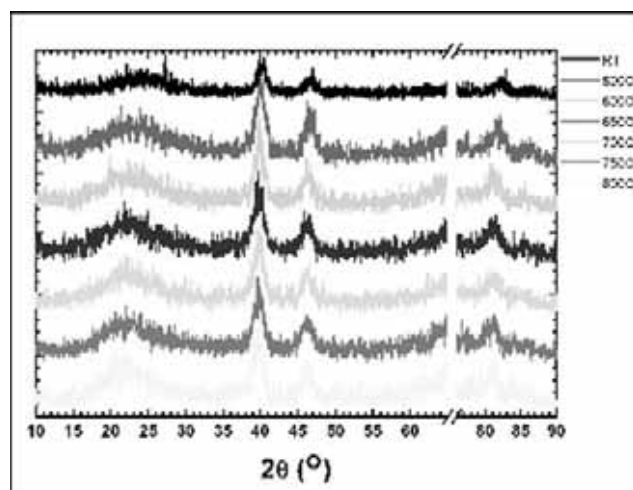


Figure 4: XRD of annealed FePt@SiO<sub>2</sub> nanoparticles at various temperatures. No peak sharpening was observed.

## Hexabenzocoronene as a 1-D Organic Semiconductor in FETs

**Calvin Peng, Materials Science and Engineering, University of Pennsylvania**

**NNIN REU Site: Nanotech, University of California at Santa Barbara**

*NNIN REU Principal Investigator: Thuc-Quyen Nguyen, Chemistry and Biochemistry, UC Santa Barbara*

*NNIN REU Mentors: Mark Dante and Joshua Garretson, Chemistry and Biochemistry, UC Santa Barbara*

*Contact: quyen@chem.ucsb.edu*

### **Abstract:**

Organic field effect transistors (FETs) have potential applications in low voltage, low cost, and mechanically flexible devices, including displays. However, organic FETs face problems of low mobility and high degradation relative to conventional inorganic FETs. Hexabenzocoronene (HBC) derivatives are organic semiconducting materials due to their strong interactions, and may self-assemble into 1-dimensional nanostructures in their liquid crystalline phase.

In this work, we studied the molecular packing of an HBC derivative, tetradodecyloxyhexabenzacoronene (THBC), by atomic force microscopy (AFM). In spin-cast films at room temperature, the molecules do not form perfect 1-D columns but are slipped, due to strong electron repulsion between large aromatic cores.

To align the THBC molecules, a thin layer of PTFE (Teflon®) fibers was deposited on Si/SiO<sub>2</sub> using a friction transfer method, forming grooves that may have guided the self-assembly of THBC.

The performance of FETs fabricated from films with and without the alignment was then compared.





# Growth and Characterization of Vertically Aligned High-Density Gallium Nitride Nanowires

**Edgar A. Peralta, Applied & Engineering Physics, Cornell University**  
**NNIN REU Site: Howard Nanoscale Science & Engineering Facility, Howard University**

NNIN REU Principal Investigator: Dr. Gary Harris, Howard Nanoscale Science & Engr Facility, Howard University

NNIN REU Mentor: Dr. Maoqi He, Howard Nanoscale Science & Engineering Facility, Howard University

Contact: eap39@cornell.edu, gharris@msrce.howard.edu

## Abstract:

Synthesis of vertically aligned, single crystal Gallium Nitride nanowires (GaN NWs) was achieved through a catalyst-assisted vapor-liquid-solid (VLS) process by the reaction of Ga with  $\text{NH}_3$  in the presence of a nickel (Ni) catalyst. Such products are important in the fabrication of optoelectronic nanodevices. The experiments were carried out inside a tube furnace at  $1000^\circ\text{C}$ , a pressure of 5 Torr, and an anhydrous ammonia flow rate of 20 sccm. Metal Ga and Ni-patterned substrates were placed on separated boron nitride (BN) boats in a quartz liner inside the furnace.

The optimal growth parameters were determined on silicon substrates, which generated a high density of nanowires with diameters between 30-70 nm, several micrometers in length, growing in random directions. MgO  $\langle 111 \rangle$  substrates were then used for controlled growth orientation, which produced vertically aligned GaN nanowires.

## Introduction:

Single-crystalline one-dimensional semiconducting nanostructures are considered to be one of the critical building blocks of nanoscale optoelectronic devices [1]. GaN's large band gap ( $\sim 3.4$  eV at room temperature), its short wavelength (UV to blue) light-emission, its large dielectric breakdown field, and its high melting point, make this material ideal for high-power/high-temperature optoelectronic applications.

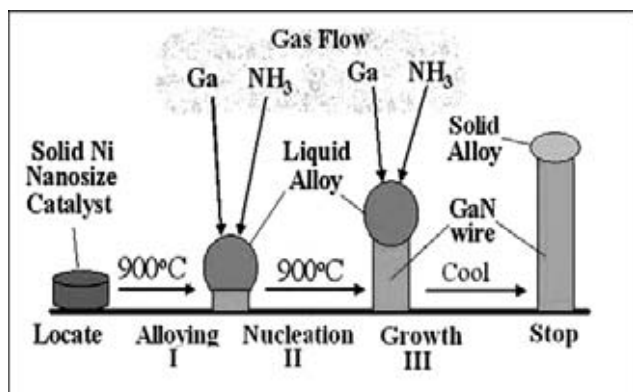


Figure 1: The vapor-liquid-solid (VLS) growth mechanism.

The most common growth techniques used in the synthesis of GaN NWs include: laser-ablation [2], carbon-nanotube confined reaction [3] and catalytic reaction [4]. We achieved synthesis through a catalytic reaction;  $\text{Ga} + \text{NH}_3 \rightarrow \text{GaN} + \text{H}_2\uparrow$ , based on a vapor-liquid-solid (VLS) growth mechanism [5], illustrated in Figure 1.

Unfortunately, not many studies have been done on controlling the orientation of catalytic NW growth without the use of MOCVD [6] or templates [7]. Control of the crystallographic growth direction of the nanowires is desired since anisotropic parameters such as thermal/electrical conductivity, index of refraction, piezoelectric polarization, and band structure among other optical/electrical properties often depend on this orientation. Our approach to achieve this growth orientation control was based on the results obtained by T. Kuykendall et al. [6], where they determined that matching the symmetry and lattice constant between the substrate—which must be single crystal—and GaN strongly influences the NW growth direction.

Essentially, any desired growth orientation could be obtained as long as that match was made. Our particular interest, GaN NWs perpendicular to the surface, required substrates which match the threefold symmetry of the  $\langle 001 \rangle$  plane of GaN and lattice constant  $a = 3.19$  Å. We used  $\langle 111 \rangle$  MgO, having threefold symmetry and an interatomic separation of 2.98 Å for atoms in the  $\langle 111 \rangle$  plane.

## Experimental Procedure:

We first experimented with silicon substrates to determine the optimal conditions to use for the  $\langle 111 \rangle$  MgO. The silicon substrates were prepared for metal deposition by a photolithography process using a thinned down Shipley S1818 photo resist spun at 4000 RPM for 9 seconds, and then developed to leave  $3\text{ }\mu\text{m}$  diameter holes with  $2\text{ }\mu\text{m}$  separation between holes. Nickel films were then evaporated at 7, 10, 15 and  $30\text{ }\text{\AA}$  thicknesses and liftoff was performed. Thicknesses were confirmed by ellipsometry and AFM.

The substrates were then cut into  $10 \times 5\text{ mm}^2$  rectangular samples and evenly distributed on top of a boron nitride (BN) boat ( $1 \times 4\text{ cm}^2 \times 5\text{ mm}$ ) inside a quartz liner about 1 cm from the gallium boat. The quartz liner was then placed inside a tube furnace (see Figure 2), and evacuated to pressures of 4-5 Torr. The furnace was ramped to  $1000^\circ\text{C}$  in 25 min, and remained at this temperature for 5-15 min and then cooled down. Anhydrous  $\text{NH}_3$  flowed in the furnace at 20-30 sccm during the heating process; once cooled below

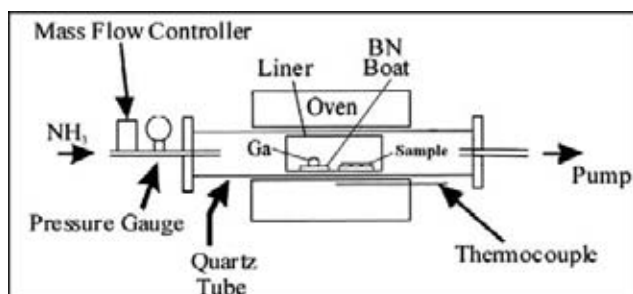


Figure 2: Illustration of tube furnace setup.

700°C, we switched to  $N_2$  at 50 sccm. The resulting samples were then observed under the optical microscope and SEM to determine the characteristics of the grown NWs, and thus determine the optimal conditions for growth on  $\langle 111 \rangle$  MgO.

### Results and Conclusions:

First, we determined the appropriate reaction time: 5 min at 1000°C produced NWs with the smallest tips, while 10 min yielded slightly thicker, longer NWs. The 15 min reaction produced a “mesh” of nanowires, which was completely undesirable. We wanted small tips and dimensions that would be suitable for vertical growth so we chose a time of 8 minutes.

Second, we determined the appropriate Ni deposition thickness to use. Although all resulting samples had NWs ranging from 30 to 70 nm in diameter, those corresponding to the 10 Å depositions had the least amount of big crystalline structures and not so curved and entangled NWs. This suggests that the VLS process favors thin layers of Ni which are nearer the substrate surface than thick ones. This is a very important result because when using the  $\langle 111 \rangle$  MgO, the substrate plays a key role on the growth direction, so the thinnest Ni deposition would yield better results. However, when we attempted to grow on the 7 Å Ni samples, there were no resulting NWs, mainly because such thin layers would evaporate before the GaN deposition. For this reason, we chose the 10 Å Ni deposition.

Third, we determined the best location along the BN boats that would yield vertical growth NWs once the  $\langle 111 \rangle$  MgO

was used. When we had three samples on a BN boat, only at the right of the second, and left of the third, we obtained a large number of NWs without the presence of large crystalline structures. For our sample holder BN boat having 4 cm along which to place samples, the best location was the region between the 2 and 3 cm mark.

After a few tries using the  $\langle 111 \rangle$  MgO and getting the same results as with Si, with no vertical growth yet present, we experimented with a smaller amount of Ga (0.33g rather than 0.5g) because during one run such an amount produced straighter NWs on the Si (see Figure 3). Finally, at a pressure of 5 Torr, a  $NH_3$  flow rate of 25 sccm, at 1000°C for 8 min, and with 0.33g of Ga, samples with 10 Å thick Ni films produced good results—namely, vertically aligned GaN nanowires with diameters ranging from 80 to 140 nm (see Figure 4). It is evident from comparing Figure 3 and Figure 4 that the  $\langle 111 \rangle$  MgO substrate served its key function of favoring perpendicular growth of the nanowires. This can be seen not only by looking at a big area of the sample but also by looking at the insert on the top right corner of Figure 4 which shows the hexagonal cross section of one of these NWs. Since only the top of the NWs is visible, they therefore must be oriented perpendicular to the substrate.

### Acknowledgements:

I'd like to thank the following people for their support and guidance: Dr. Harris, Dr. He, Mr. Griffin, Dr. Zhou, Mr. Taylor, and the rest staff at HNF. I'd also like to thank Ms. Melanie-Claire Mallison for giving me the opportunity to participate in the program, and NSF for providing the funding for it.

### References:

- [1] Xia, Y. et al. Adv.Mater. 2003, 15, 353.
- [2] Duan, X. F.; Lieber, C. M. J. Am. Chem. Soc. 2000, 122, 188.
- [3] Han, W.; Fan, S.; Li, Q.; Hu, Y. Science 1997, 277, 1287.
- [4] Chen, C.C.; Yeh, C.C. Adv. Mater. 2000, 12, 738.
- [5] Wu, Y.; Yang, P.; J. Am. Chem. Soc. 2001, 123, 3165.
- [6] Kuykendall, T et al., Nature Materials, 2004, 3, 524.
- [7] Cheng G. et al. Mat. Sci. & Eng. 2000, 165-168.

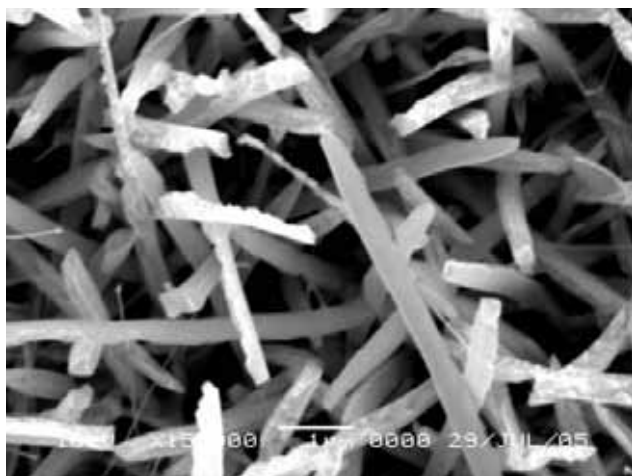


Figure 3: SEM of GaN NWs grown on silicon.

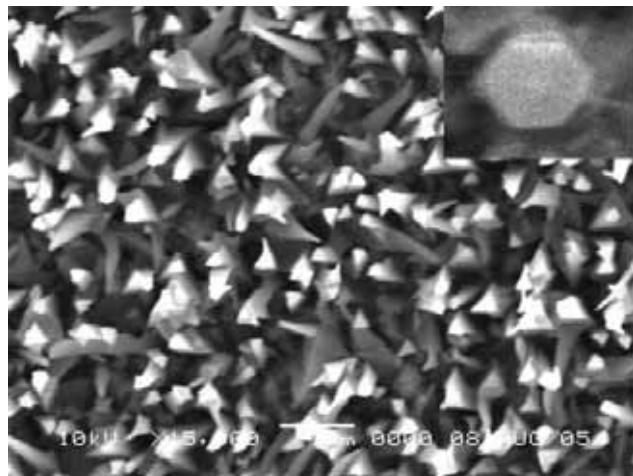


Figure 4: SEM of GaN NWs grown on  $\langle 111 \rangle$  MgO.

## **Molecular Packing of Charged Conjugated Polymer Studied by Atomic Force Microscopy**

**Alexandra Polosukhina, Physics, University of San Francisco**  
**NNIN REU Site: Nanotech, University of California at Santa Barbara**

*NNIN REU Principal Investigator: Thuc-Quyen Nguyen, Chemistry, University of California at Santa Barbara*

*NNIN REU Mentor: Andres Garcia, Chemistry, University of California at Santa Barbara*

*Contact: quyen@chem.ucsb.edu*

### **Abstract:**

Conjugated polymers are polyunsaturated compounds which consist of at least one backbone chain of alternating double and single bonds. These organic semiconductors are used in various applications such as light-emitting diodes, photovoltaic devices, field-effect transistors, and flexible displays. Emission color (band gap) can be tuned by molecular structures. The conformation of polymer chains and the subsequent packing of these chains in film influence the electronic properties. By introducing charged side-groups, the polymers are soluble in water or methanol, and therefore, can find application in biosensors. Also, the polymer conformation can be controlled by changing solution pH or adding salt.

We studied two charged conjugated polymers (conjugated polyelectrolytes), trimethylammonium polyfluorenes, that contain either an electron transporting unit (ETP) or hole transporting unit (HTP) under different processing conditions. The HTP contains a 1,4-phenylene unit whereas the ETP has a 2,1,3-benzothiadiazole unit.

Specifically, we examined changing the polymer concentration, solvent (water versus methanol), and salt (type of salt, NaBIm<sub>4</sub> or NaBr, and salt concentration). Change in polymer conformation in solution and molecular packing in film were monitored by spectroscopy and atomic force microscopy.





# Engineering Protein Scaffolds for Interactions with Nanoparticles

Laralynne Przybyla, Biochemistry and Molecular Biology, Purdue University  
NNIN REU Site: NanoTech User Facility, University of Washington

NNIN REU Principal Investigator: Dr. Beth Traxler, Microbiology, University of Washington

NNIN REU Mentor: Eliora Gachelet, Microbiology, University of Washington

Contact: lprzybyl@purdue.edu, btraxler@u.washington.edu

## Abstract:

The focus of this project is to exploit the self-assembly properties of proteins to arrange inorganic compounds in predictable patterns. Part of this effort has involved the genetic manipulation of the *E. coli* TraI protein, a DNA helicase involved in F plasmid conjugation. TraI has a high affinity for DNA, and we are using TraI-derivatives with specific metal binding capacities to make DNA-protein-nanoparticle assemblies. Polypeptide sequences that mediate binding to gold were incorporated into previously identified TraI-permissive sites, without altering the *in vivo* function of the TraI protein.

Two of these TraI proteins, TraI-GBP7Q and TraI-GBP5Q, have been purified and subsequently imaged using an atomic force microscope (AFM). The proteins have been observed binding to both single-stranded DNA and gold nanoparticles, thus producing a linear ordered array of nanoAu. These conjugates of DNA-TraI-nanoAu, which demonstrate a binding, and ordering of gold nanoparticles along a DNA strand may be used in nanowire applications, or as a proof-of-concept for making devices.

## Introduction:

TraI, also known as *E. Coli* DNA helicase I, has the function of nicking, then unwinding, DNA during F plasmid conjugation—the transfer of DNA between bacteria, as seen in Figure 1 [4].

Derivatives of the TraI protein have been created which are capable of binding metal ions. We have used TraI derivatives with gold-binding polypeptide sequences inserted into the previously identified permissive sites Q369 and L1753 (Traxler et al, in

preparation). These gold-binding sequences (GBP) were of either 5 or 7 repeats of a gold-binding domain identified by Brown [1].

AFM imaging was then performed on the TraI derivatives TraI-GBP7Q and TraI-GBP5Q. The proteins were examined bound to both single-stranded DNA and gold nanoparticles in order to analyze the structure of the proteins in this configuration and to see if the AFM is a useful tool to directly image these proteins. The idea was to create a linear ordered array of nanoparticles using a DNA substrate, which could have many applications, including creating nanowires or semiconductors.

## Procedures:

TraI-GBP derivatives were purified from the soluble fraction of cell extracts. TraI-GBP was separated from other soluble proteins first on a DEAE column using the following buffer at increasing NaCl concentrations: 20 mM TrisCl pH 7.6, 0.1 mM EDTA, and 10% glycerol. The 0.15 M NaCl fractions were pooled and dialyzed. The TraI then was further purified using a heparin column with the above buffer, and the 0.40 M NaCl fractions were collected and stored at -80°C.

The *in vivo* function of the TraI-GBP derivatives was measured in a conjugation assay where donors (XK1502 F'lac ΔTraI with various plasmids) and recipients (BT8) were each diluted 1:10 into LB and incubated at 37°C for 45 min. Dilutions were plated onto lactose minimal with streptomycin plates, and colonies were counted after incubation at 37°C.

To prepare the samples for use in the AFM, ssDNA, protein, and/or gold colloid were incubated together at 4°C for 1 hour, in 20 mM TRIS, pH-7.5, 5 mM KCl, 5 mM gCl<sub>2</sub>, 1 mM DTT (Sattin). 20 μl of this solution was then deposited on 1 cm x 1 cm freshly cleaved mica and allowed to bind to the mica substrate at room temperature for 20 minutes. Next, the mica chip was rinsed drop-wise with dH<sub>2</sub>O and dried under an Ar stream.

The AFM was operated on tapping mode, at which the probe oscillates at its resonant frequency. The AFM

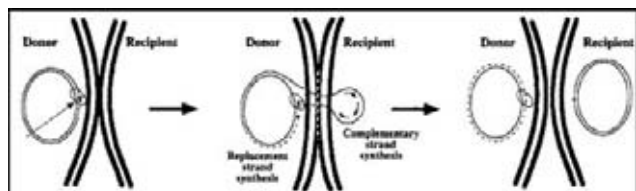


Figure 1: F plasmid conjugation (Firth et al 1996). Left arrow indicates the TraI protein.

used was the Nanoscope IIIa/MMAFM system (Veeco, Inc). ssDNA was prepared by boiling  $\lambda$  dsDNA (NEB) cut with BstEII for 10 minutes, then immediately cooling in liquid nitrogen. 15 nm Au particles were purchased in colloid form from Ted Pella, Inc.

## Results and Conclusions:

TraI-GBP proteins were purified, and assays were done on the TraI derivative proteins to ensure their functionality. The quantitative mating assay checked the efficiency of F plasmid conjugation with the TraI-GBP and demonstrated that they functioned properly *in vivo*. The results of this assay are shown in Figure 2.

Donor Strain	Avg. Mating Efficiency	% of Wild Type
pTrec99A (vector control)	0	0
pTrec99traI+ (positive control)	$3.588 \times 10^{-5}$	100
p99I::i31Q (5Q/7Q parent)	$4.806 \times 10^{-3}$	13393
p99I::GBP5Q	$2.668 \times 10^{-3}$	7437
p99I::GBP7Q	$2.180 \times 10^{-3}$	6076
p99I::GBP5L	$3.925 \times 10^{-5}$	109
p99I::GBP7L	$1.201 \times 10^{-3}$	3348

Figure 2: Quantitative mating assay.

We next demonstrated that the TraI-GBP derivatives could be manipulated *in vitro*. We imaged these proteins bound to DNA and simultaneously to DNA and gold nanoparticles, as shown in the AFM images (Figures 3 and 4). Figure 4 shows a quantitation, in which the percentage of gold particles bound to DNA and thus presumably to the TraI protein was found to be  $68 \pm 18\%$ .

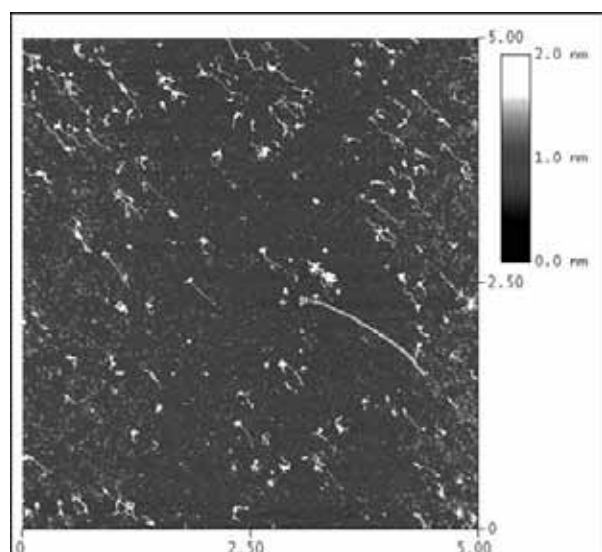


Figure 3: ssDNA and TraI: 30  $\mu$ g/ml DNA, 3  $\mu$ g/ml TraI-GBP7Q.

## Future Work:

In the future, TraI could be imaged with different metal binding sites, including platinum, chromium, and cuprous oxide. We could also use TraI with more than one type of metal binding site, for example, TraI with a gold binding site at Q369 and a cuprous oxide binding site at L1753, to create composite nanowires.

Using conjugates of DNA, TraI, and nanoAu, we could create a hydrophilic/hydrophobic pattern by contact printing, then deposit the conjugate onto the pattern. We expect that the conjugates will have affinity for hydrophilic surface and therefore will only deposit on the hydrophilic part of the pattern. This process could be used as a proof-of-concept for making devices.

## Acknowledgments:

The NNIN REU program, lab members Rembrandt Haft and Jessica Smith, Dr. Sarikaya's lab, and Hanson Fong for assistance with the AFM.

## References:

- [1] Nat. Biotech. 1997 15:269-272 Metal-recognition by repeating polypeptides Brown S.
- [2] Ann. Rev. Mat. Sci. 1997 27: 175-222 Characterization of Polymer Surfaces with Atomic Force Microscopy Magonov SN, Reneker DH.
- [3] Biophysical J. 2004 87(5):3430-6 Direct observation of the assembly of RecA/DNA complexes by atomic force microscopy Sattin BD, Goh MC.
- [4] "Escherichia coli and Salmonella: cellular and molecular biology" 1996, pp. 2377-2401. Firth NK, Ippen-Ihler K, Skurray R. Structure and function of the F factor and mechanism of conjugation (ASM Press).

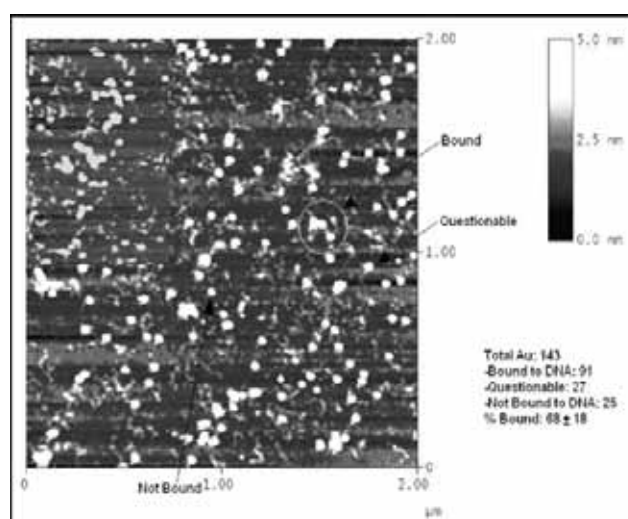


Figure 4: DNA, TraI, nanoAu: 25  $\mu$ g/ml DNA, 10  $\mu$ g/ml TraI-GBP7Q.

# Modeling of Anisotropic Surface Energies for Quantum Dot Formation and Morphological Evolution

**Marc Punkay, Mathematics, Pomona College**

**NNIN REU Site: Michigan Nanofabrication Facility, The University of Michigan**

*NNIN REU Principal Investigator: Katsuyo Thornton, Materials Science and Engineering, University of Michigan*

*Contact: marc.punkay@pomona.edu, kthorn@umich.edu*

## Abstract:

Quantum dots are nanoscale structures that can be formed during heteroepitaxy of a thin film onto a substrate. These dots form as a result of the lattice misfit (the difference between the lattice parameters of the film and the substrate materials), which results in strain. Quantum dots exhibit distinctive properties, such as electrical properties, which have proven useful in recent advances in nanotechnology, resulting for example in quantum dot lasers, and could enable further advancements in electronics and computing. The purpose of this project is to build a mathematical framework for describing the anisotropic surface energies to be implemented in the simulations of growth of quantum dots and other relevant materials.

In the first part of the project, the commercial program, Mathematica®, was used to find mathematical descriptions of anisotropic surface energies with various symmetries that are expected from the underlying crystallographic structure of materials. Two-dimensional descriptions of the surface energies were created first, which were then extended to three-dimensional descriptions. After the mathematical formulas of the descriptions were obtained, the equilibrium shapes, or Wulff shapes, associated with these surface energies were calculated and visualized, again using Mathematica®.

## Introduction:

Quantum dots can be formed through a variety of different processes. This project focused on modeling the energy anisotropy for the quantum dots formed through a process known as heteroepitaxy, a process in which a thin film of one material, such as germanium, is deposited on a substrate of another material, such as silicon. There is a lattice misfit between the film and the substrate due to the difference in the lattice parameters of the two materials, which results in strain. The formation of quantum dots is the result of the system attempting to minimize the total energy—the interfacial energy and the strain energy.

Surface energy anisotropy contributes to the manner in which quantum dots self-assemble. It has been found

that the kind of surface energy anisotropy that the system has, greatly influences the way that quantum dots grow and configure themselves [1].

Information obtained in experiments can be used to model the interfacial energy anisotropy for actual crystal systems. For example, for a metal alloy AlSn, Napolitano and Liu grew crystals experimentally, then measured the equilibrium shapes for the liquid droplets entrained in the crystalline phase [2]. Given these equilibrium shapes, they extracted the interfacial free energy anisotropy as a mathematical function and parameters to fit the experimental result. The equilibrium shapes of crystals grown in semiconductor systems can also be measured and used to model the surface energy anisotropy using similar means.

## Methods:

Mathematical models of various anisotropic surface energies were first obtained. Two-dimensional descriptions of surface energies as functions of the direction of the surface normal were created to have various symmetries. These two-dimensional surface energy descriptions were expressed in polar coordinates and plotted using Mathematica®. Then, trigonometric identities and other mathematical methods were used to extend these two-dimensional descriptions into equivalent three-dimensional descriptions (as functions of three normal components) to model the anisotropic surface energies of three-dimensional crystals. The surface energies with various degrees of anisotropy were visualized by writing the normal components in spherical coordinates and plotting them using Mathematica®.

These three-dimensional surface energy descriptions can then provide the corresponding equilibrium shapes of the crystals using a process called Wulff construction. Geometrical, Wulff construction involves drawing a plane perpendicular to each normal unit vector on the energy graph; the inner envelope formed by these planes is the equilibrium shape. We instead used the plot  $\xi = \gamma n + \gamma_\theta \theta + \gamma_\phi \phi$  [3] to visualize the equilibrium shapes in spherical coordinates.



## Results:

Using Mathematica® for plotting, equilibrium shapes were modeled with different degrees of anisotropy for energies with four-fold, eight-fold, and twelve-fold symmetries in the three principle planes. Results are shown in Figures 1-4. “Ears” and “flaps” are present on equilibrium shapes associated with high degrees of anisotropy. These ears and flaps are also called missing angles. These equilibrium shapes approach shapes such as an octahedral in the case of four-fold symmetry; the equilibrium shapes of actual systems will not display these missing angles seen in the ears and flaps. Nonetheless, it is still important to examine such models because these anisotropic interfacial energies with missing angles model the facets of crystals.

## Conclusion:

In this project, a mathematical framework was developed for modeling the anisotropic surface energies with various symmetries expected in the structures of various material systems. Two-dimensional energy descriptions were obtained, which were then extended to three-dimensional models. The equilibrium shapes associated with these three-dimensional surface energy models were obtained for different degrees of anisotropy. The descriptions obtained in this project will be used in simulations of the growth and the morphological evolution of quantum dots and their arrangements during heteroepitaxy.

## Acknowledgements:

I would like to thank Professor Katsuyo Thornton for her help with this project and for the time she sacrificed for it. I would like to thank Sandrine Martin and Deb Swartz for all that they did for the interns at the University of Michigan. Finally, I am grateful to the NNIN for giving me the opportunity to pursue this project.

## References:

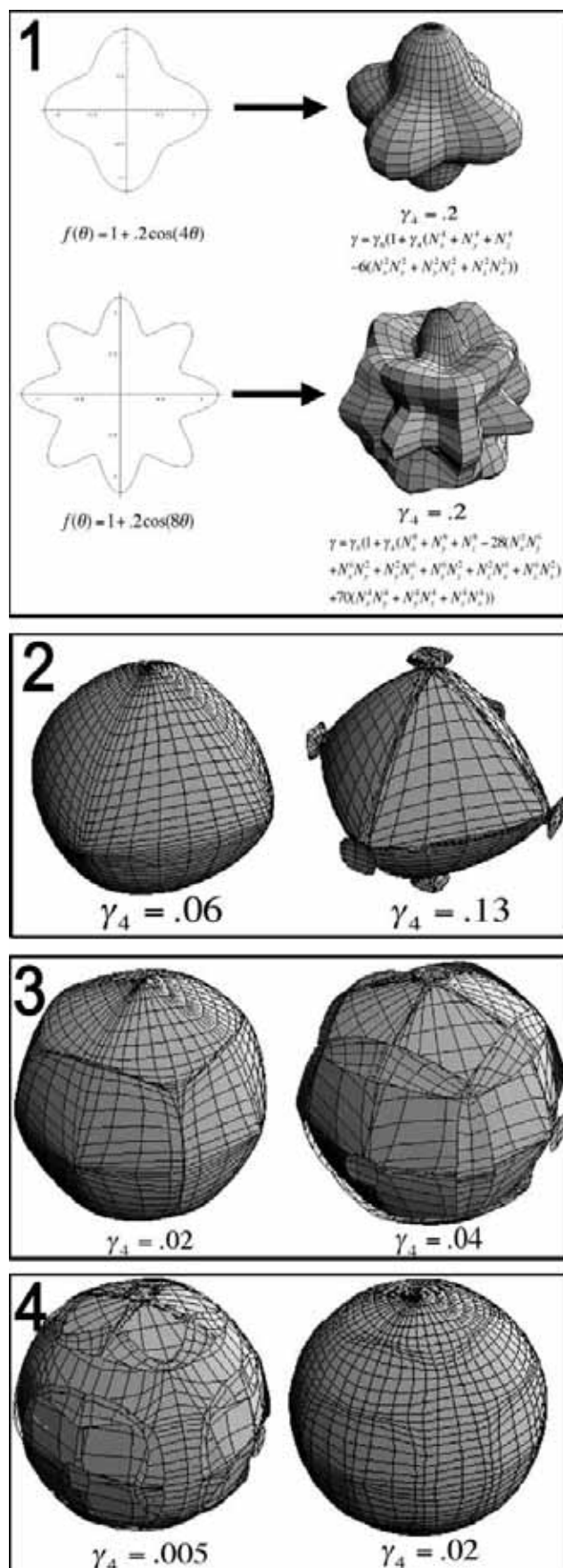
- [1] S.M. Wise, J.S. Lowengrub, J.S. Kim, K. Thornton, P.W. Voorhees, and W.C. Johnson, Appl. Phys. Letters, in press (2005).
- [2] R.E. Napolitano and S. Liu, Three-dimensional crystal-melt Wulff-shape and interfacial stiffness in the Al-Sn binary system, Physical Review B 70, 214103 (2004).
- [3] R.F. Sekerka, Analytical criteria for missing orientations on three-dimensional equilibrium shapes, Journal of Crystal Growth 275 77-82 (2005).

Figure 1: Anisotropic surface energy models in 2D and 3D with four-fold and eight-fold symmetry.

Figure 2: Equilibrium shapes for four-fold symmetry.

Figure 3: Equilibrium shapes for eight-fold symmetry.

Figure 4: Equilibrium shapes for 12-fold symmetry.



# Electromechanical Characterization of One-Dimensional Solids

**Nakul Reddy, Electrical Engineering, Georgia Institute of Technology**

**NNIN REU Site: The Penn State Nanofabrication Facility, The Pennsylvania State University**

*NNIN REU Principal Investigator: Prof. Amanul Haque, Mechanical & Nuclear Engr, Pennsylvania State University*

*NNIN REU Mentor: Amit Desai, Mechanical & Nuclear Engineering, The Pennsylvania State University*

*Contact: gtg621q@mail.gatech.edu, mah37@psu.edu, avd112@psu.edu*

## Abstract:

Materials exhibit unique electrical and mechanical properties at the nanoscale such as quantized conductance and high elastic modulus, which make them ideal for next-generation sensors, actuators and nano-electronics. To study these properties, we have developed MEMS-based nano-Newton force and nanometer displacement resolution sensors. The design philosophy exploits the amplification of displacement and attenuation of structural stiffness in the post-buckling deformation of slender columns. The research experience aims to: (a) explore reliable methods for placing a nanowire or nanotube on the device or co-fabrication, and (b) study the electromechanical coupling in ZnO nanowires. The devices have been patterned on silicon-on-insulator (SOI) wafers using UV photolithography and DRIE. The movable silicon beams were made freestanding using vapor-phase HF etching. Dispersion for ZnO nanowires has been characterized and a focused ion beam (FIB) with a tungsten probe (capable of nanometer level positioning) was used to place the nanowires on the device. An upper bound of 5 GPa for the Young's modulus of ZnO nanowires has been observed. Stress-strain curves for these nanowires have been computed. The experimental

setup has also been extended to include electromechanical characterization, and experiments are being conducted to determine strain-conductance relations.

## Introduction:

Nanotubes and nanowires are expected to have superior thermal, electrical, and mechanical properties that promise breakthroughs in the development of super-strong composite materials and ultra-high resolution sensors. There has been extensive research on the mechanical, electrical and thermal properties but very little effort is evident on determining these properties under coupled (and not individual) domains. This is mainly due to the high measurement resolution requirements and challenges in experimentation at the nanoscale. Existing technologies for obtaining nanostructure stress-strain and strain-conductance data, such as nanoindentation and mechanically-controllable break junction (MCBJ) do not provide for *in situ* experimentation and do not work for nanowires and nanotubes with large variations in structure and chemistry.

We therefore have designed and fabricated a MEMS-based tensiometer based on post-buckling deformation of thin silicon cantilevers, for studying the mechanical and electro-mechanical coupling of nanowires and nanostructures.

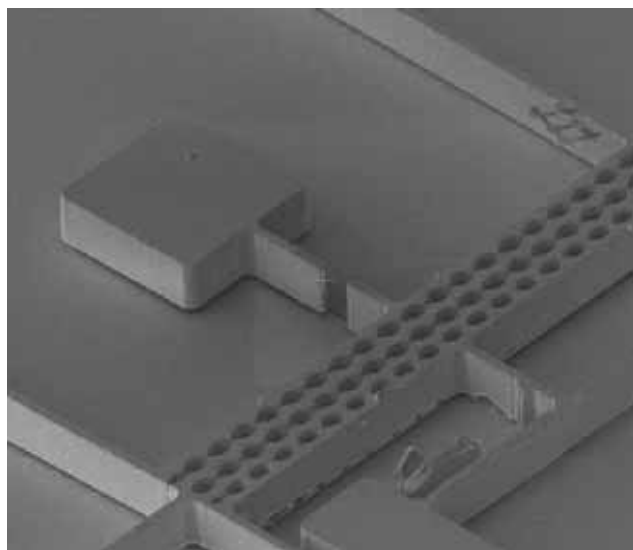


Figure 1: SEM image of the buckling beam device.

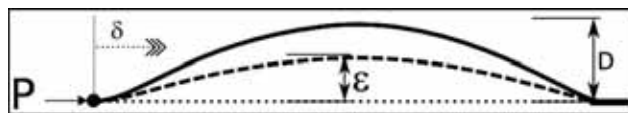


Figure 2. Buckling beam with labeled axial load ( $P$ ), axial displacement ( $\delta$ ), lateral displacement ( $D$ ), and initial imperfection ( $\epsilon$ ).

## Buckling Beam Theory:

Buckling of a beam can be used to amplify the axial displacement ( $\delta$  in Figure 2) into lateral displacement ( $D$  in Figure 2), by as much as a factor of 250. The

axial force ( $P$  in Figure 2) can also be computed as a function of lateral displacement. The post-buckling deformation mechanics results in reduction of stiffness with increasing lateral displacement and hence the force resolution increases.

The device design consists of two pairs of beams (as shown in Figure 3). One end of the specimen is fixed and the other end is attached to the movable middle rib, as shown in Figure 3. On loading the device, the middle rib moves to the right and applies very small forces and displacements on the specimen. The tensiometer can achieve much higher resolution than a single set of buckling beams by exploiting the small difference in axial displacement and load for each set of beams ( $\delta_1 - \delta_2$  and  $P_2 - P_1$ ). The average lateral displacements,  $D_1$  and  $D_2$  are on the order of microns, and can be measured using a high-power optical microscope.

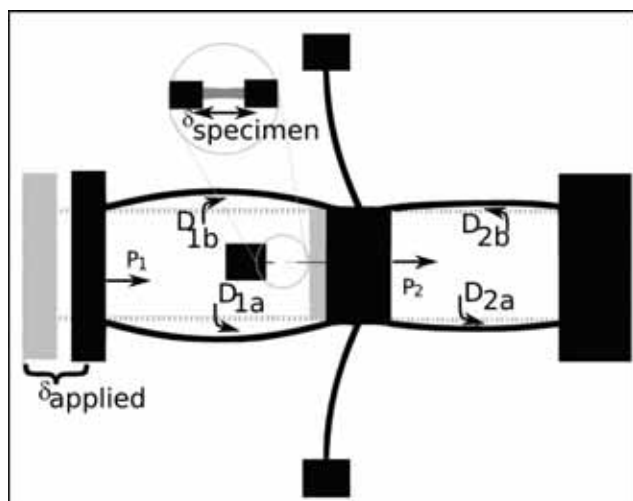


Figure 3: Buckling beam device schematic with labeled displacements.

### Fabrication and Preparation:

The devices were fabricated on a silicon-on-insulator wafer with a  $20\ \mu\text{m}$  Si layer on a  $1\ \mu\text{m}$  oxide layer. The device was patterned using Shipley 3012 resist, and the Si layer was etched using deep reactive ion etching with  $\text{SF}_6$ . The oxide layer was then etched with a  $3\ \mu\text{m}$  undercut using a vapor-phased HF tool. The photoresist was then stripped and the devices were sputtered with 100 nm of gold for improved conductivity and imaging.

Nanowires were dispersed on a thin but stiff oxide grid with a 75 nm gold layer for conductivity. The focused ion beam (FIB) was used to deposit an

adhesive Pt compound on the ends of the nanowire. A grid with a freestanding nanowire was then cut using the FIB, and picked up using the OmniProbe<sup>®</sup> nanomanipulator. The FIB was then used to etch posts onto the jaws of the device, and the nanomanipulator was used to place the grid onto the posts (see Figure 3). The ends of the grid were cut so that the sample was the only conductive path between the two jaws.

### Results and Progress-to-Date:

The characterization of dispersion of ZnO nanowires made it possible to successfully prepare samples. Preliminary results for the Young's modulus for ZnO nanowires were estimated to 5 MPa using the aforementioned method. Electrical measurements were not possible due to the lack of a reliable conductive path between the device and the specimen, possibly due to the low conductivity of FIB deposited Pt. Chemical vapor deposited growth of nanotubes directly onto the jaws of the device is also being explored for nanotube measurements.

### Acknowledgements:

The research was made possible by Amit Desai, Benedict Samuel, and Prof. Aman Haque at the Nanomechanical Systems Lab in Penn State University, and the NNIN. Special thanks to Dr. Basgall and Mr. McIntosh of the Penn State Nanofab.

### References:

- [1] "Microscale application of column theory for high resolution force and displacement sensing." Samuel, B.A.; Desai, A.V.; Haque, M.A. Applied Physics Letters, v 87, n 2, 11 July 2005.

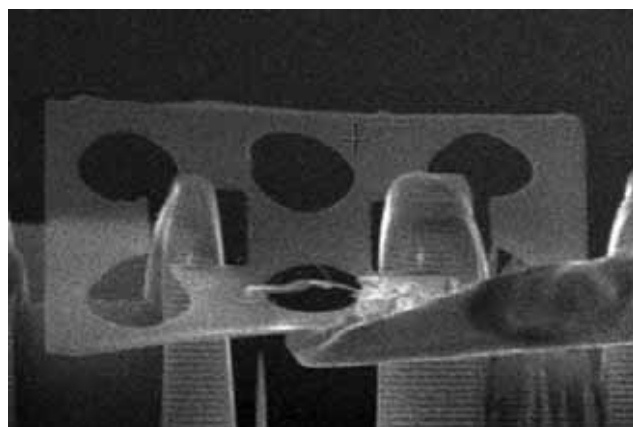


Figure 4: Oxide grid being placed on device jaws using a nanomanipulator.

# Adhesion in Nanoimprint Lithography & Embossing Related Thin-Films

**Emily Rice, Physics and Economics, University of Florida**  
**NNIN REU Site: Stanford Nanofabrication Facility, Stanford University**

*NNIN REU Principal Investigator: Reinhold H. Dauskardt, Materials Science Engineering, Stanford University*

*NNIN REU Mentor: Eric P. Guyer, Materials Science Engineering, Stanford University*

*Contact: ricem84@ufl.edu, dauskardt@stanford.edu*

## Abstract:

One of the critical issues during nanoimprint lithography (NIL) and the embossing process is the generation of defects in the mold due to the repeated removal of the mold/stamp from the polymer film. The goal of this project was to characterize the adhesion of the salient polymer-mold interfaces. The effects of interface chemistry and the geometry of patterned structures were investigated. Model polyacrylates were cured on silica surfaces with and without a fluorine-based release layer and were separated using a common fracture mechanics technique to examine the effects of interface chemistry on adhesion. The release layer reduced adhesion compared to the samples containing no release and ensured that the fracture path remained at the polymer-silica interface. Lithographically patterned arrays of Si lines coated with Teflon® were fabricated to examine the effects of mold pattern geometry on adhesion energies. Increasing aspect ratios of patterned arrays will be demonstrated to yield higher fracture energies, while crack growth orientation will be revealed to have little effect on adhesion.

## Introduction:

Embossing and NIL are promising new ways to create micro- and nano-scale features, respectively. Both processes involve pressing a mold or stamp into a polymer film, curing the film while the two are in contact, and then removing the mold. As molds are used many thousands of times, repeatedly overcoming the adhesion between the mold and polymer film often damages the mold. The first step to overcoming this problem and reducing damage to the mold is to characterize the adhesion of salient interfaces. In this study, the effects of interface chemistry on adhesion between NIL-related thin-films (with and without a release layer) as well as the effects of geometry on adhesion using embossing-related patterned molds and a relevant thin-film are investigated.

## Procedure:

Double cantilever beam (DCB) fracture specimens were fabricated for testing with cross-sections as shown in Figure 1. Two sets of the interface chemistry samples were prepared: one set with a release layer (Cytonix 4500) and one without. The polyacrylate was made up of: 92% lauryl acrylate, 5% 1,3 butanediol diacrylate,

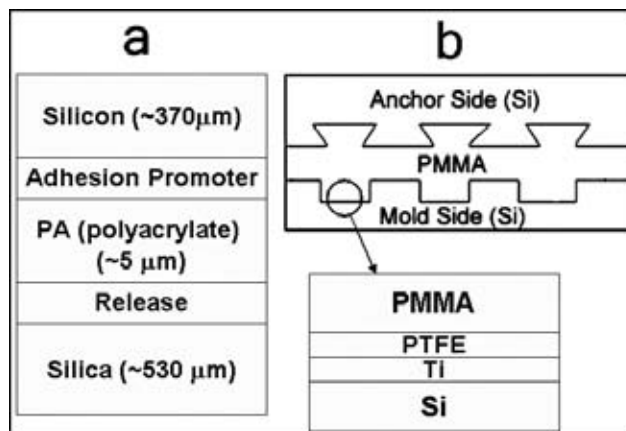


Figure 1: a) Cross-section of interface chemistry samples (release optional). b) Cross-section of geometry samples.

and 3% Ciba Darocur 4265. Half of the embossing samples with patterned structures were cut parallel to the features, and half were cut perpendicular. Testing was conducted using a micromechanical test system, which concurrently measures the load (the force applied) and the displacement (the distance between two cantilever beams). The samples were loaded and unloaded multiple times, and the slopes of the linear regions where the sample was unloaded were used to calculate the crack length, while the critical load (the beginning of the non-linear region) along with the crack length was used to calculate  $G$ , the interface fracture energy, in  $\text{J/m}^2$ . Then  $G$  vs. the crack length was graphed. X-ray photoemission spectroscopy was used to determine along which interfaces the samples debonded.

## Results and Conclusions

### Interface Chemistry:

The desired result was for the samples to debond at the polyacrylate-silica interface, which would indicate that the release layer was not functional and there was no added benefit to the release layer. The samples examined in this study debonded for the most part at the desired polyacrylate-silica interface (Figure 2),



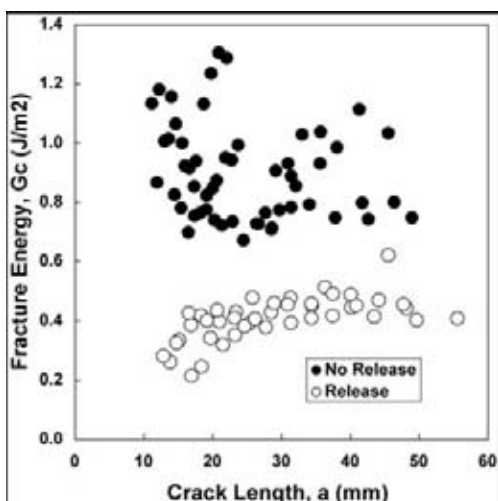


Figure 2: Release layer samples had lower adhesion than no release samples.

and the  $G$  values of the samples with the release layer were significantly less than those with no release layer (roughly in the range of  $0.7\text{--}1.2\text{ J/m}^2$  compared to  $0.3\text{--}0.5\text{ J/m}^2$ ).

### Geometry:

Figure 3 compares the fracture energies measured for the  $6.5\text{ }\mu\text{m}$ ,  $13\text{ }\mu\text{m}$ , and  $18\text{ }\mu\text{m}$  tall structures where crack growth was propagated parallel to the lines. The adhesion for the  $6.5\text{ }\mu\text{m}$  samples was less than those for the  $13\text{ }\mu\text{m}$ , which were less than those for the  $18\text{ }\mu\text{m}$  samples. This was expected because the samples with greater structure depths have more surface area in contact with the PMMA. This means that removing molds with deep structures from PMMA will cause more wear and tear than molds with shallow structures.

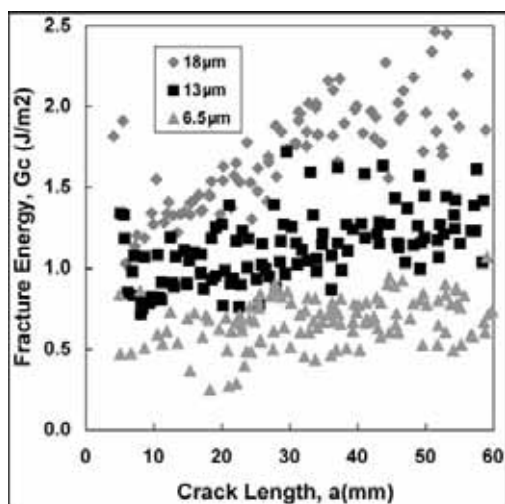


Figure 3: Fracture energy increases with aspect ratio.

Figure 4 compares how the orientation of crack growth affects the fracture energies of the  $18\text{ }\mu\text{m}$  lines where cracks were propagated parallel as well as perpendicular to the lines. The majority of the  $G$  values of both types of samples are approximately within the same range ( $1.25\text{--}2.25\text{ J/m}^2$ ). The  $13\text{ }\mu\text{m}$  perpendicular samples'  $G$  values were much more erratic than the  $G$  values for the  $13\text{ }\mu\text{m}$  parallel, and the  $6.5\text{ }\mu\text{m}$  perpendicular samples had  $G$  values significantly lower than its parallel counterparts. In conclusion, the direction at which the mold is separated from the PMMA is trivial at this length scale, although the data is not entirely conclusive.

### Acknowledgements:

Thanks to Professor Reinhold H. Dauskardt and Dr. Eric P. Guyer, WonHyoung Ryu and Dr. Rainer Fasching for the embossing samples, Dr. Frances Houle at IBM for the NIL samples, Dr. Michael Deal and Stanford University, the National Nanotechnology Infrastructure Network Research Experience for Undergraduates Program, and the National Science Foundation for funding.

### References:

- [1] E.P. Guyer, "Effects of Aqueous Solution Chemistry on the Fracture of Nanoporous Thin-Films", Ph.D. Dissertation, Stanford University, 2004.
- [2] Guo, L.J. "Recent progress in nanoimprint technology and its applications." Journal of Physics D: Applied Physics 37 (2004): R123-R141.

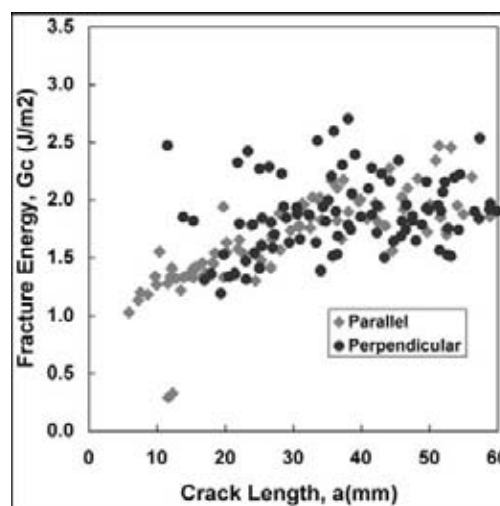


Figure 4: Fracture energies for the parallel and perpendicular samples are commensurate.

## Universal File Translator for First Principles Codes

**Nathan Ridling, Physics, North Georgia College and State University**  
**NNIN REU Site: Cornell NanoScale Science and Technology Facility, Cornell University**

*NNIN REU Principal Investigator: Dr. Derek Stewart, Cornell Nanoscale Facility, Cornell University*  
*Contact: pogalog@gmail.com, stewart@cnf.cornell.edu*

### Abstract:

Currently, over twenty density functional (DFT) codes exist for calculating properties of crystal structures and molecules using first principle approaches. While each has its own strengths and weaknesses when describing a particular system, the ability to migrate from one approach to another easily is essential for comprehensive research.

In this work, we create a program that can convert between multiple formats of DFT codes. As a test case, we examine a magnetic nanowire system, converting between two popular DFT codes, LMTO and Abinit. LMTO uses a compact basis set derived from atomic-like orbitals to calculate system properties quickly. While LMTO is very efficient for closed pack systems, special care is required for structures with large amounts of open space. Abinit, by contrast, is based on a plane wave basis and can handle a wide range of systems at the expense of greater computation time. Since the plane wave basis set is not localized, Abinit treats empty space more effectively than LMTO. The system properties calculated using both techniques are compared and situations where format conversion would be ideal are also discussed.

### Introduction:

While each of the DFT codes uses its own approach for determining the total energy of a system, they all rely on the underlying tenets of density functional theory. Density functional theory basically takes an  $n$ -body problem for all electrons and neutrons and reduces it to a function (the charge density,  $\rho(x,y,z)$ ) of three variables. The assumption made (originally by the Hartree-Fock method) is that the electrons do not interact, which allows the problem to be viewed by using a Schrödinger equation that deals with only a single electron.

One of the major goals of density functional theory is to calculate the equilibrium crystal structure for a molecule. This can be done by adjusting the system volume for DFT calculations. If this data is plotted as energy versus volume (as seen in Figure 1) it will appear to be parabolic in shape. We say that the

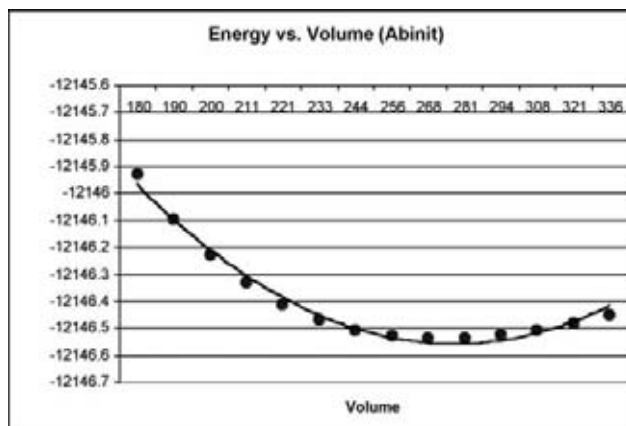


Figure 1: Abinit energy plot with a quadratic curve fit.

equilibrium structure for the given system occurs at the minimum of that curve. The reason this distribution appears parabolic is due to electron-electron repulsion that raises the energy as the system becomes too closely packed or too spread apart.

### Procedure:

The majority of the project consisted of programming a file format translator. After work on the file translator program was completed, the next step was to test the quality of the program's ability to translate between file formats. To do this, we inserted a LMTO input file into the translation program to obtain a converted Abinit input file describing the same system. We would then analyze the results of parallel computations of the two codes to determine how well the computed equilibrium lattice constants and magnetic moment per atom agree.

While converting between Abinit and LMTO was the main concern of the project, another function intended for the translation utility was to make it able to convert to a simple file format for use in the program called "RasMol." RasMol takes Z-numbers and atomic positions and plots atoms in a three-dimensional graph. This is a feature that we felt would be important to a user of the translation utility as it allows a simple way to view the system with which the user is working.

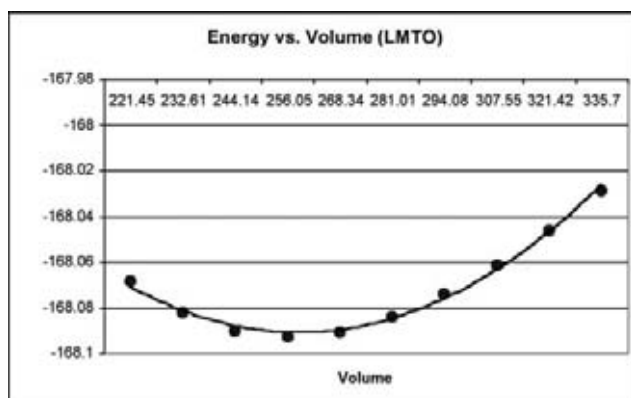


Figure 2: LMTO energy plot with a quadratic curve fit.

### Results and Conclusions:

The results that we analyzed were those of calculations run by Abinit and LMTO using information about the same structure. To run tests, we ran calculations on a single atom Nickel-Face Centered Cubic (Ni-FCC) system; first with Abinit, and again with a converted input file for LMTO. The data obtained by the calculations was for a small range of lattice constants centered about the experimentally accepted value for nickel. The data that we wanted was the value that each of the calculations claimed to be the energy minimum for the system. For the Abinit calculation, the equilibrium lattice constant was calculated to be 6.35 Bohr (approximately 3.36Å). LMTO found the lattice constant to be 6.45 Bohr or 3.41Å (percent difference of 1.48%). The magnetic moment calculated by Abinit was 0.603 Bohr-Magnetons with a percent difference of 2.01% from the LMTO value of 0.591 Bohr-Magnetons.

### Future Work:

The current status of the project is functional, but largely incomplete. The translation program presently converts between LMTO and Abinit input file formats as well as from Abinit and LMTO to RasMol. Since there are more than twenty density functional theory codes available, more coding can be done to add translation capabilities for additional codes. In the future a universal file format is planned that can be read by multiple DFT codes. The success of this future project will depend on its ease of use and readability as well as the potential acceptance and implementation by DFT code authors. Since the translator program is coded in Java, a web-based interface for use on the Cornell NanoScale Facility web site will be created for remote users who wish to convert between available file formats.

### Acknowledgements:

Dr. Derek Stewart, PI; CNF Staff; National Science Foundation.

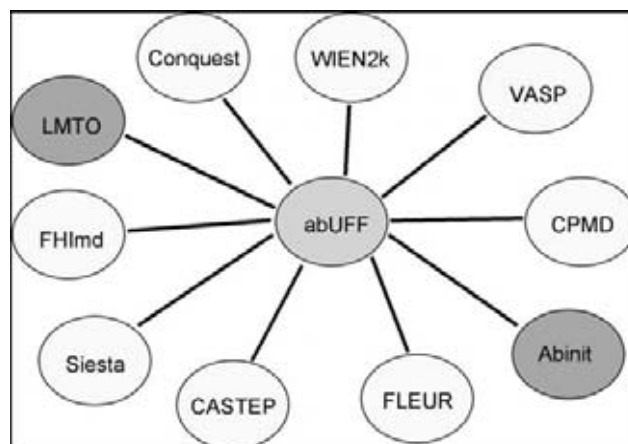


Figure 3: Some of the available DFT codes with the file translator in the center.

## Integrated UHF Magnetic Transducers

**Sarah Ruch, Mechanical Engineering, University of Texas at Austin**  
**NNIN REU Site: Cornell NanoScale Science and Technology Facility, Cornell University**

*NNIN REU Principal Investigator: R. Bruce van Dover, Materials Science and Engineering, Cornell University*

*NNIN REU Mentor: Noble Woo, Chemistry and Chemical Biology, Cornell University*

*Contact: sarandipity237@mail.utexas.edu, rbv2@cornell.edu*

### Abstract:

Creating a surface acoustic wave (SAW) device on a silicon substrate would allow for integration leading new on-chip low-cost functionality (e.g., high-Q analog filters). Instead of using standard piezoelectric materials, our device creates SAWs using magnetostriction. In this approach, a copper wire is embedded in a magnetostrictive material,  $\text{Co}_{46}\text{Fe}_{46}\text{Ta}_3\text{Zr}_5$ . Current passed through the wire creates a magnetic field around the wire. The magnetic moment of the  $\text{Co}_{46}\text{Fe}_{46}\text{Ta}_3\text{Zr}_5$  rotates in the presence of the magnetic field, and the material elongates along that direction. As alternating current passes through the wire, the elongation and relaxation of the magnetic material creates compression waves in the silica substrate. The compression waves traveling along the surface of the substrate are surface acoustic waves (SAWs). We detect the SAWs some distance away on the silica substrate using another SAW device.

We have fabricated two designs for the device. The first design included magnetic material only on the top and bottom of the copper wire. The insertion loss for this design has been on the order of 70 dB. The new design seen in Figure 1 has magnetic material on the sides of the wire as well as the top and bottom in order to improve magnetic response and reduce insertion loss.

### Introduction:

Current passing through a wire creates a magnetic field around the wire according to the right hand rule. We take advantage of this magnetic field by filling the area closest to the wire, the area of highest magnetic field strength, with a ferromagnetic, magnetostrictive

material. In a magnetostrictive material, when in a magnetic field, the magnetic moments of the material align and the atomic orbitals shift according to spin-orbit coupling, changing the shape of the material. As the magnetic field is raised and lowered, the substrate undergoes compression and relaxation, which moves across the substrate as ripples move across water. The speed that the compression wave moves across the substrate is determined by the substrate material. In our case, we have used silica and intend eventually to utilize silicon. This speed, the speed of sound in the material, is around 4000 meters per second for our substrate. By making rows of wires, we can select what frequencies we want to filter out. The compression waves created by our devices will have a natural wavelength proportional to the frequency supported by constructive interference. That frequency is equal to the velocity of the compression waves across the substrate divided by the pitch of the wires. We have made devices with pitches ranging from 20  $\mu\text{m}$  to 60  $\mu\text{m}$  which should operate as filters at frequencies ranging from 66 MHz to 200 MHz.

### Experimental Procedure:

We created alignment marks on the fused silica substrate using the Oxford 100 to etch the silica and using 1818 resist as a mask. We sputtered 350 nm of the  $\text{Co}_{46}\text{Fe}_{46}\text{Ta}_3\text{Zr}_5$  material followed by 300 nm of copper. All sputtering was done without heating the substrate.

We used standard photolithographic procedures to create the inner pattern of our device. We ion-milled the exposed area leaving copper wires on a thin film of magnetic material. While ion milling, the bombardment of argon ions was limited to take place in 15 second intervals with 45 second cooling periods so that the resist would not burn. This allowed us to remove the resist by soaking in acetone. We then sputtered another 350 nm of magnetic material on top of the wires. Repeating the photolithographic procedure we exposed an outer pattern which encompasses the inner pattern, creating a copper wire embedded in magnetic

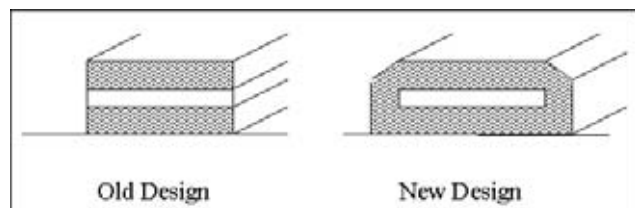


Figure 1: Cross-sectional diagram of old and new design.



material. We used the ion mill to remove the magnetic material in between the wires because no feasible chemical reaction could have removed the material in a reactive ion etcher. The removal rate for our ion mill was approximately 33 nm per minute for the magnetic material and about 65 nm per minute for the copper.

Several parameters helped us to determine the quality of the device. We initiated measurements of the scattering parameters using a network analyzer. Scattering parameters indicate the proportion of the transmitted signal that is detected or reflected.

### Results and Conclusions:

The magnetically transduced surface acoustic wave device should be easily integrated in Si-based ICs. No new materials need be introduced to the processing facility as the MTSAW devices may be added in a separate facility, eliminating possibilities of contamination from bringing new substances into the front-end process area. The deposition and removal of material are both room temperature operations. There are a few concerns about how the transistors may be affected by plasma, which is used in deposition and removal of the material. The alternative lift-off method has worked for removal of material in these devices in the past [1].

### Future Work:

Future work on this project includes finishing the electrical measurements stated here along with further characterization of the ferromagnetic magnetostrictive material used. We would like to understand why ion milling created CFTZ sidewalls of the shape that we observe in Figure 2. In addition, we would like to characterize the behavior of the magnetic fields in the CFTZ material over a step. Also, we plan to investigate the use of low-magnetostriction materials in similar devices for use as inductors [2].

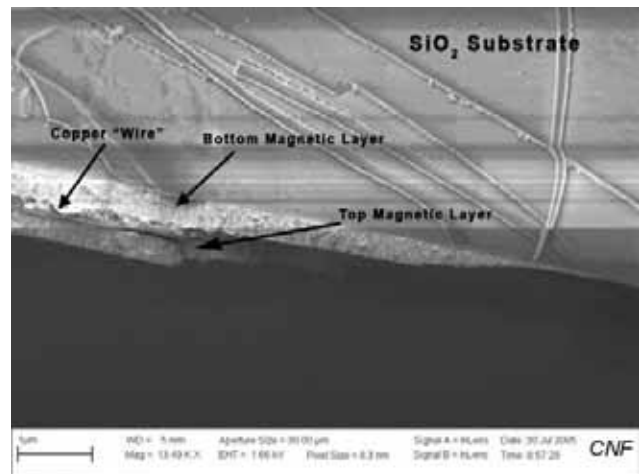


Figure 2: SEM image of cross-section of copper wire surrounded by magnetic material.

### Acknowledgments:

I would like to acknowledge my Principal Investigator, Dr. R. Bruce van Dover, for his knowledge, patience, and teaching expertise. I would also like to thank my mentor, Noble Woo, for guiding me through the program, and the CNF staff for their countless hours of training and technical expertise.

### References:

- [1] K. A. Ellis, R. B. van Dover, T. J. Klemmer, and G. B. Alers, J. Appl. Phys. 87, 6304 (2000).
- [2] A. Gromov, V. Korenivski, K. V. Rao, R. B. van Dover, and P. M. Mankiewich, "A model for impedance of planar RF inductors based on magnetic films," IEEE Transactions on Magnetics, vol. 34, pp. 1246-8, (1998).

# Nanoscale Gold Deformation and Characterization

**Yaniv Scherson, Mechanical Engineering and Materials Science, UC Berkeley**

**NNIN REU Site: Nanotech, University of California at Santa Barbara**

*NNIN REU Principal Investigator: Professor David Clarke, Department of Materials, UC Santa Barbara*

*NNIN REU Mentor: Jesse Williams & Giuliano Gregori, Department of Materials, UC Santa Barbara*

*Contact: yanivds@berkeley.edu, clarke@engineering.ucsb.edu*

## Abstract:

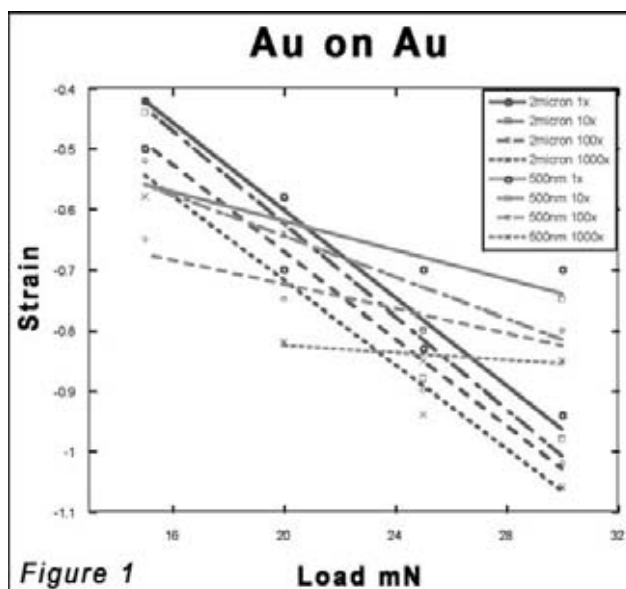
As a soft metal, gold undergoes significant deformation at the contact points in a MEMS switch causing failure after repeated cycles. An adhesion force is created as the indentation into the gold increases, causing the switch to stick in the closed position. Additionally, the gold curiously retains some grain roughness even after repeated cycles of indentation. By replicating the effects of roughness of the gold at a larger scale with the placement of gold columns on a gold substrate and nanoindenting, a better understanding of the deformation is obtained. Greater insight into the mechanics and behavior of the nanoscale gold deformation is achieved through varying the cycles, force, gold feature substrate, and the feature aspect ratio of the nanoindentation.

## Experimental Procedure:

The approach of the experiment was to replicate the effects of nanoscale roughness on gold. Therefore, the main idea of the experiment was to recreate the effects of “gold roughness” at a larger scale by placing small vertically oriented square columns on a thin gold film. The thin film of approximately  $15\text{ }\mu\text{m}$  Au was sputtered onto either a hard silicon substrate or a soft gold substrate. Gold square columns are then placed onto the gold film, extending upward. The columns are given three sizes. The largest columns were  $2\text{ }\mu\text{m}$  wide and  $500\text{ nm}$  in height. The next two sets of columns were  $1\text{ }\mu\text{m}$  and a half micron in width, while both had two different heights,  $200$  and  $100\text{ nm}$ .

The samples were then subjected to indentations of varying force and cycle number. Using a  $50\text{ }\mu\text{m}$  radius tip indenter, sixteen indentations are made on each sample. Forces of  $15$ ,  $20$ ,  $25$ , and  $30$  microNewtons are applied for  $1$ ,  $10$ ,  $100$ , and  $1000$  cycles each, thus producing sixteen different indentations. As an example, Figure 4 depicts  $1\text{ }\mu\text{m}$  pillars indented under a  $25$  milliNewton load. As one can see, the spherical indenter creates a depression into the gold pillars where the change in height of the center pillar can be used to calculate strain.

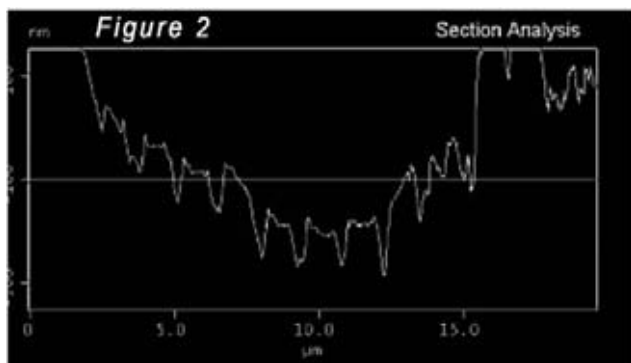
From the indentations, insight into the strain and



effects of the hard or soft substrate can be gathered. Most insightful was the change in height of the column features at the center of the indentation. This height change measures the strain which that particular feature undergoes calculated by  $(\text{height final} - \text{height initial}) / \text{height initial}$ . Additionally, the final displacement of the substrate helps determine how much of the strain in the indentation was due to feature height displacement versus substrate displacement.

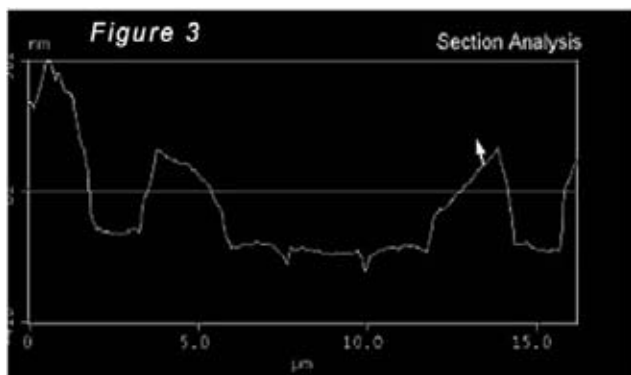
## Results:

Of particular interest in the experiment are the effects in strain of the different sized columns and the effects of the silicon vs. gold substrate. Figure 1 depicts the variance in behavior of  $0.5\text{ }\mu\text{m}$  columns vs.  $2\text{ }\mu\text{m}$  columns by creating linear fits for the load vs. strain data points. The red lines represent the  $2\text{ }\mu\text{m}$  columns while the blue lines represent the  $0.5\text{ }\mu\text{m}$  columns. Additionally, the more dashed lines underwent a greater number of cycles. Therefore, as seen in the figure, increasing the load as well as the number of cycles of an indentation increases the strain in the columns, as one would expect. However, more interesting was the



varying behavior of the larger and smaller columns. The slopes of the  $2\ \mu\text{m}$  columns are steeper than the  $0.5\ \mu\text{m}$  columns. This suggests that as the applied load to the columns was increased, the increase in strain was smaller. A smaller change in strain to a higher load implies that the smaller  $0.5\ \mu\text{m}$  columns appear to have a higher yield stress, or in other words, appear to be effectively harder possibly due to the distribution of the applied load or constraint to column expansion when compressed by closely lying neighbors. Under the same 30 milliNewton load, the height of the  $2\ \mu\text{m}$  column in Figure 3 was displaced all the way down to the substrate while the height of the  $0.5\ \mu\text{m}$  columns in Figure 2 didn't displace fully to the substrate. The fact that the  $0.5\ \mu\text{m}$  columns maintained a larger height value further demonstrates the smaller columns' greater resistance to height displacement, or in other words, increased strength.

Yet an additional interesting trend was the lack of difference in strain of the columns on different substrates. Columns of equal size and initial height undergoing the same loads and indentation cycle number have no significant difference in strain. This trend was contrary to the expected outcome of a higher strain in the columns that are placed on a harder substrate that would displace less and direct more strain to the columns themselves.



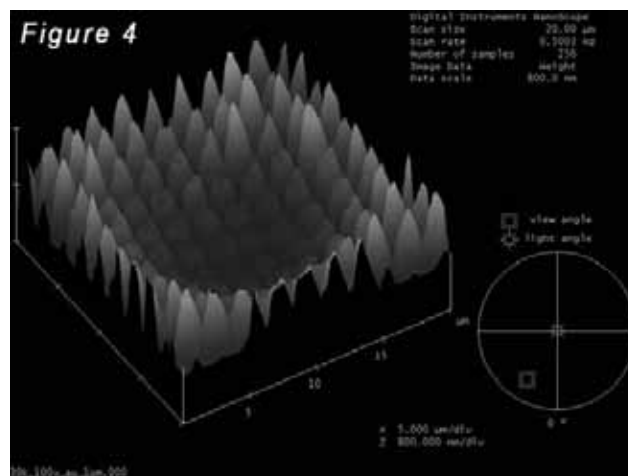
### Future Work:

In order to see if the effective higher yield stress observed in the smaller columns was due to an innate increase in yield stress or perhaps more simply constraint effects from neighboring features, the experiment should be run using  $0.5\ \mu\text{m}$  or smaller columns with a larger spacing between columns. It is unclear how much the neighboring columns affect one another, but it is obvious that as the smaller  $0.5\ \mu\text{m}$  features displace into the substrate neighboring columns smash into one another and impede lateral displacement of material. This constraint effect would give better insight into the reasons why a higher yield stress was observed in the smaller columns.

Additionally, more telling trends and data could be obtained by increasing the range of applied loads, indentation cycle number, and reducing column size, which is currently limited by the fabrication process.

### Acknowledgements:

This project would not have been possible without the great help and support of Professor David Clarke, Jesse Williams, Giuliano Gregori, Angela Berenstein, NNIN, NSF, and UCSB.



# Microfabrication of a Parallel-Array DNA Pyrosequencing Chip

Neel Shah, Engineering, Harvey Mudd College

NNIN REU Site: Stanford Nanofabrication Facility, Stanford University

NNIN REU Principal Investigator: Peter Griffin, Electrical Engineering, Stanford University

NNIN REU Mentor: Ali Agah, Electrical Engineering, Stanford University

Contact: nshah@hmc.edu, griffin@stanford.edu

## Abstract:

DNA sequencing is essential to genomics and must be performed efficiently. Pyrosequencing is a new innovation that confirms a correct nucleotide addition by emitting light through enzymatic reactions. The objective is to fabricate a parallel-array pyrosequencer on a chip. The obstacle is to bring a camera sufficiently close to the microwells where the sequencing takes place so it can capture emitted light while eliminating crosstalk errors between adjacent wells. We have tested several designs for achieving this objective. If one succeeds, we will have developed an enabling technology for a scaled down DNA sequencer.

## Introduction:

Developing a low-cost genomic DNA sequencer has become an urgent necessity in order for genomics to progress. The NHGRI has been issuing grant requests for developing such low-cost alternatives [1]. The current cost of sequencing a mammalian genome is \$10 million. Pyrosequencing shows promise to lower this to \$10,000.

Unlike Sanger sequencing, which utilizes gel electrophoresis, pyrosequencing uses enzymatic reactions to detect correct nucleotide additions. This procedure change reduces bulky DNA sequencing equipment to a silicon chip. As detailed in Figure 1, the first pyrosequencing step is the release of a

pyrophosphate (PPi) from correct nucleotide incorporation [2]. The PPi is converted to ATP using the enzyme ATP-sulfurylase, which then provides energy for the firefly enzyme luciferase to oxidize luciferin and emit light. This light is then recorded by a camera.

Current technology brings the camera to within 500  $\mu\text{m}$  of the reaction wells, by resting the camera on top of a glass wafer. This limits well size and pitch to no less than 500  $\mu\text{m}$ ; if the size or pitch was any smaller, crosstalk error would occur between the chip wells and camera pixels. The objective here is to bring the camera to 10-50  $\mu\text{m}$  of the wells. This will allow experimentation with smaller well sizes and pitches, and result in a large increase in well density and parallel processing.

## Experimentation and Results:

Four different channel patterns and four different well patterns were designed to test functionality of the parallel-array aspect of the chip. At the micrometer scale, fluid flow is purely laminar. Thus, it is necessary to fabricate something to spread a 1 mm flow of fluid coming from the inlet channel over the 6 mm wide atrium where the wells reside. A series of pillars (designs 1 and 4) and branches (designs 2 and 3)

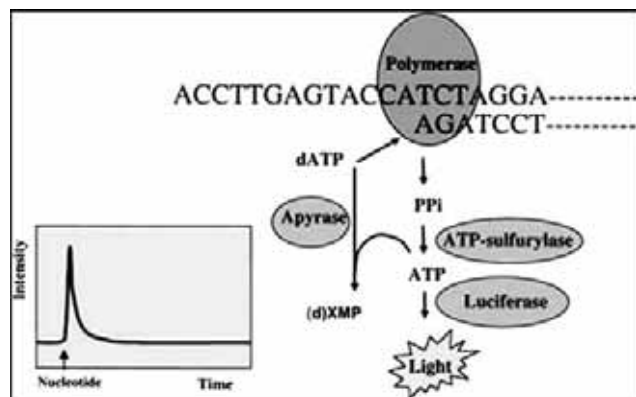


Figure 1: Pyrosequencing process. Light indicates correct nucleotide incorporation.

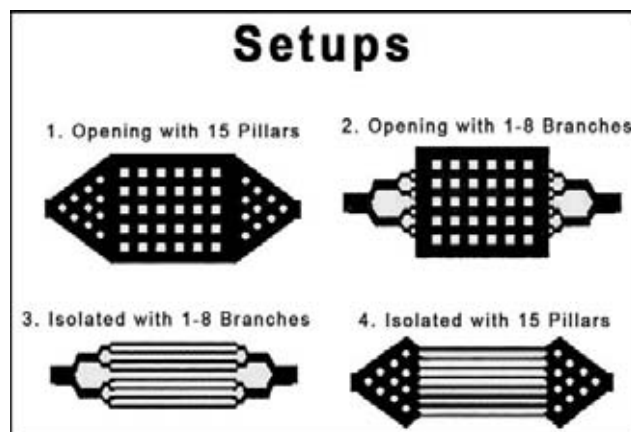


Figure 2: 4 channel/well designs. Pillars/wells exaggerated.





Figure 3: Cutaway depiction of initial experiment.

accomplish this (see Figure 2). Isolating rows of wells is another method, which was implemented in designs 3 and 4.

The first procedure attempted involved etching wells and channels, and drilling inlet/outlet holes into one silicon wafer. On a second sacrificial silicon wafer, 5000 Å layers of  $\text{SiO}_2$ ,  $\text{Si}_3\text{N}_4$ , and PSG were deposited in succession. This procedure is illustrated in Figure 3. The wafers were anodically bonded through the PSG, but the bonding failed. This prompted an investigation into the bonding process to determine why failure occurred. By deriving the electrical model in Figure 4, it was determined that bonding failed because the electric field across the PSG was too small, at 5 V/cm. The oxide and nitride layers were reduced to 500 Å and the PSG layer was increased to 10000 Å. In addition, the PSG layer was etched to reduce its area from 78.5 cm<sup>2</sup> (the area of the 4" Si wafer) to 8 cm<sup>2</sup> (the 500 μm surrounding each channel). This decreased the oxide and nitride resistances and increased the PSG resistance, since layer resistance is  $R = \rho t/A$ ,  $\rho$  being resistivity,  $t$  being thickness, and  $A$  being area. This increased the electric field over the PSG to 300 V/cm. However, anodic bonding still failed, leading to the conclusion that even a field of 300 V/cm was insufficient for anodic bonding.

The next method involved anodic bonding between silicon and Pyrex<sup>®</sup> 7740 wafers. This has been shown to succeed, and calculations show the electric field produced across the 500 μm glass wafer is 10000 V/cm, in contrast to the earlier 300 V/cm. This method required etching wells, channels, and drilling inlet/outlet holes into one silicon wafer. The next steps were to bond to glass and reduce glass thickness, which required HF etching. A 49% concentrated HF solution etches Pyrex<sup>®</sup> 7740 at 8.5 μm/min [3].

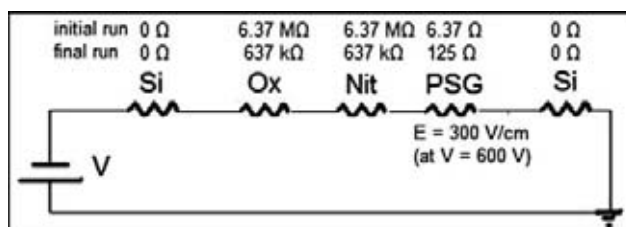


Figure 4: Electrical representation of bonding process, with initial/final resistances.

A 50 μm thinned Pyrex<sup>®</sup> wafer was bonded to the back of a double-polished silicon wafer, and a normal glass wafer was bonded to the front, before HF etching. This protected the drilled holes and the inside of the front glass wafer from HF, and served to mark when the stack should be removed from the HF solution. When the back Pyrex<sup>®</sup> wafer disappeared, it indicated the front Pyrex<sup>®</sup> wafer was 50 μm thick and the stack should be removed. This method succeeded in leaving a thin glass membrane of 15 μm.

#### Future Work:

The successfully fabricated chips need testing. The first test will be to run water at varying rates and observe if the glass membrane will withstand the pressure generated. These results will be compared with a standard glass wafer bonded to silicon. If these chips perform satisfactorily, then initial pyrosequencing data will be collected, and compared to the current standard as well. If these tests return satisfactory results, we will have accomplished our objective to create a more efficient DNA sequencer.

#### Acknowledgements:

I thank Peter Griffin and Ali Agah for guidance in executing this research. I also thank NSF for funding, and SNF staff for facilitating this research.

#### References:

- [1] <http://grants.nih.gov/grants/guide/rfa-files/RFA-HG-04-003.html>
- [2] Ronaghi, M. 2001. "Pyrosequencing Sheds Light on DNA Sequencing". Cold Spring Harbor Laboratory Press.
- [3] Diepold, T. and E. Obermeier. 1996. "Smoothing of Ultrasonically Drilled Holes in Borosilicate Glass by Wet Chemical Etching". IOP Publishing Ltd.

# Electrical Characterization of Semipolar Gallium Nitride Thin Films

**Yu-ping Shao, Electrical Engineering, Colorado State University**

**NNIN REU Site: Nanotech, University of California at Santa Barbara**

*NNIN REU Principal Investigator: Shuji Nakamura, Materials Department, UC Santa Barbara*

*NNIN REU Mentor: John Kaeding, Materials Department, University of California Santa Barbara*

*Contact: yshao@engr.colostate.edu, shuji@engineering.ucsb.edu*

## Abstract:

Considerable economic and environmental savings will be achieved through the successful development of high efficiency solid state lighting sources. Recent breakthroughs have been made in the development of GaN based blue, green, and white light emitting diodes (LEDs) and blue laser diodes (LDs). Typically, GaN optoelectronic devices are heteroepitaxially grown on C-axis oriented sapphire substrates using techniques such as metalorganic chemical vapor deposition (MOCVD). Such structures suffer from polarization-induced internal electric fields along the {0001} growth direction which limit the radiative efficiency of the device. Recent theory suggests that growth of semipolar GaN orientation will reduce these internal fields and improve device performance. However, the successful growth methods for semi-polar GaN thin films are still under development.

GaN crystals grown under different conditions call for characterization techniques such as measuring the Hall Effect using the Van de Pauw technique, a method of measuring the resistivity and Hall coefficient on lamellae of arbitrary shape. It is from these properties that the mobility and concentration of charge carriers are derived. The two variables allow for the comparison of the quality of different crystals, leading to the successful optimization of growth conditions for semi-polar GaN thin films.

## Introduction:

Solid materials are classified by the way the atoms are arranged. Materials with atoms placed in ordered structure are called crystalline as opposed to amorphous. GaN and its alloys are most stable in wurtzite crystal structure, which is based on the hexagonal form of zinc sulfide (ZnS), and is described by two or three basal axis on the same plane, each 120° apart respectively, and each normal to the same c-axis. GaN and its alloys grown along this c-axis possess spontaneous polarization parallel to the plane vector, and the wurtzite structure possesses piezoelectric polarization. Most of the current optoelectronic devices have c-plane quantum wells that suffer from the effect

of the strong internal electric field caused by the spontaneous and the piezoelectric polarizations. This reduces the recombination efficiency by causing spatial separation of holes and electrons.

A combination of techniques could reduce the internal electric field. First technique is to grow GaN devices on semipolar planes. These planes are referred by two non-zero values in the basal axis in the Miller indices  $h$ ,  $i$ , and  $k$ , and another non-zero value describes the  $c$ -axis ( $\{h\ i\ k\ c\}$ ). Common examples include  $\{1013\}$ , and  $\{1011\}$  planes. The plane vector in this case points at some degrees away from the  $c$ -axis. Due to this, the spontaneous polarization is reduced. Second technique is to grow heterostructure GaN that has thin layer of ternary and quaternary GaN compounds such as AlGaIn, InGaIn, and AlInGaIn. Due to difference in lattice constants, a layer of InGaIn on GaN produces compressive strain, while a layer of InGaIn produces tensile strain. These strains are the cause of piezoelectric polarization, and by alternating layers, the types of strain counteract each other reducing the piezoelectric polarization.

GaN crystals are grown epitaxially. In metalorganic chemical vapor deposition (MOCVD), substrates provide close lattice match to GaN. Common substrates are spinel ( $\text{MgAl}_2\text{O}_4$ ) and sapphire ( $\text{Al}_2\text{O}_3$ ). In a vacuumed space, the substrate sits upon a spinning hot plate. A mixture of carrier gases and metalorganic gases supplies the gallium or its compounds, while the gaseous ammonia supplies the nitrogen. GaN crystals are formed when the metalorganic mixture and the ammonia reacts and bonds to the surface of the substrate, creating layers of GaN materials having crystal orientation similar to the orientation of the

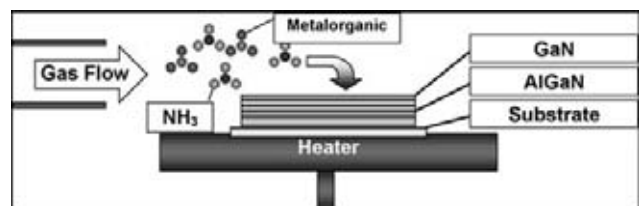


Figure 1: MOCVD.

substrate (Figure 1). This is known as a heteroepitaxial relationship.

### Procedure:

The Van de Pauw method offers an alternative and easier way to measure the resistivity and Hall coefficient on lamellae of arbitrary shape, rather than on the difficult Hall Effect sample bars. These two properties at different temperatures are essential part of the electrical characterization of semiconductor materials. It is from these values the mobility and charge carrier concentration are derived [1].

After a wafer of GaN crystal is grown, it is cleaved into sample squares. A sample should be a flat lamella completely free of holes. The metal contacts are placed as close to the corners of the squares as possible to reduce errors (Figure 2). Contacts are made with indium dots or gold deposition to provide electrical conduction for the Hall Effect measurement.

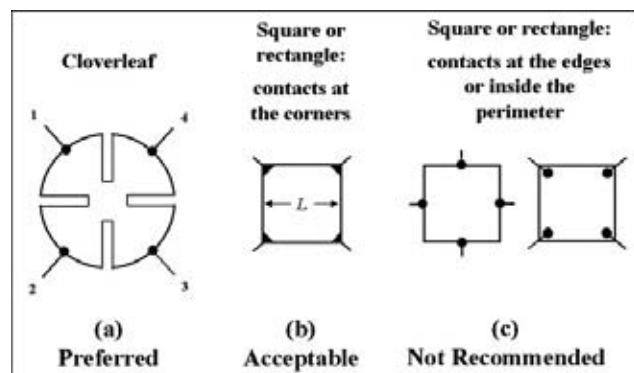


Figure 2: Sample shape and position of contacts.

### Results and Conclusion:

Semipolar GaN crystals were grown currently with a general outline of growth parameters in pressure between 400 to 1000 torrs, and temperature between 600°C to 1400°C. Suitable substrate can increase the stability of GaN growth and reduce the variation in temperature and pressure for specific semipolar planes.

Surprisingly, despite having the same temperature and pressure, samples grown using different carrier gases produced different surface morphology as shown by the optical microscope (Figure 3, 4). These samples are then characterized by the Hall Effect measurement. Using hydrogen gas carrier seems to produce higher mobility in crystal. However, more data is required to confirm this condition.

Future film optimization techniques include growth on nucleation layers (NL). NL employs the use of

polycrystalline nitride material deposited at a thickness of 100 Å to 2000 Å before the growth of GaN. While the physics of how NLs improve the surface morphology is not well understood, the advantage of NLs on improving surface morphology is broadly practiced on c-plane growth. However, use of NLs in GaN semipolar growth has not yet been previously achieved.

### Acknowledgements:

Thanks to my mentor John Kaeding, and to the rest of the Nakamura group. Hitoshi Sato, Troy Baker, Dr. Kim, Mike Iza, Ed Letts, for their willingness to work with me. Finally, thanks to NNIN, UCSB and Shuji Nakamura for providing this opportunity.

### References:

- [1] I. J. Van der Pauw. Philips Technical Review, vol. 26, 260, 1958.

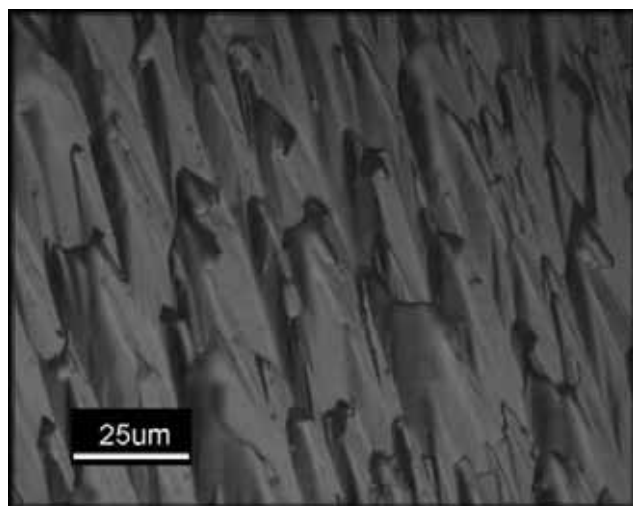
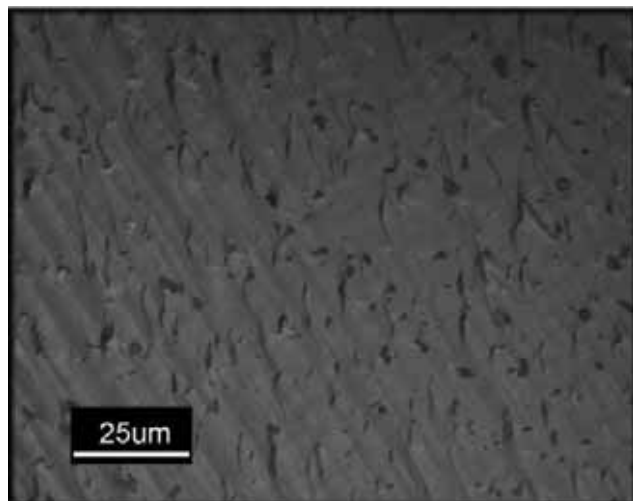


Figure 3, above: Hydrogen gas carrier.

Figure 4, below: Nitrogen gas carrier.



# Gallium Nitride Nanowire Growth, and FET Device and Biosensor Fabrication

**Kaylee Sill McElroy, Physics, Brigham Young University**

**NNIN REU Site: Cornell NanoScale Science and Technology Facility, Cornell University**

*NNIN REU Principal Investigator: Michael G. Spencer, Electrical & Computer Engineering, Cornell University*

*NNIN REU Mentor: Huaqiang Wu, School of Electrical & Computer Engineering, Cornell University*

*Contact: kaylees@gmail.com, spencer@ece.cornell.edu*

## Abstract:

Gallium nitride nanowires (GaN NWs) may be used to fabricate devices such as field effect transistors (FETs) and bio-/chemical sensors. This study focused on controlling the growth of the nanowires for fabrication of FETs. GaN NWs were grown using annealed Ni as catalyst. To control nanowire growth density, the anneal time and temperature were varied. The initial thickness of the Ni and the nanowire growth conditions were varied as well. Using standard lithography processes, several Ni patterns were created and nanowires were grown from the patterns. FETs were created by putting a source and drain over the patterned nanowires. Current/Voltage measurements of these transistors showed that nearly every device behaved as a transistor, however, pinch-off was not observed and there was little gate modulation.

## Introduction:

Nanowire research is important to the development of nanoscale electronics. One of the properties that makes GaN nanowires interesting is that GaN has a wide direct band gap of 3.4eV at room temperature. Since GaN can be doped to be either a p- or n-type semiconductor, electronic devices like diodes can be made from the nanowires. Other devices such as Field Effect Transistors (FETs) have also been made. Our research concentrated on forming a high-yield fabrication process for GaN NW FETs. To get the high yield we desired, it was important to learn to control the density of NW growth by varying several growth conditions. The geometry of the transistor design was also important. By shaping the transistor as in Figure 1, a NW growing in almost any direction will connect the source and drain.

## Materials and Methods

### Catalyst Preparation:

One to two nm of Ni was e-beam evaporated onto a Si substrate with 40 nm of thermally grown SiO<sub>2</sub>. These samples were then put in the rapid thermal

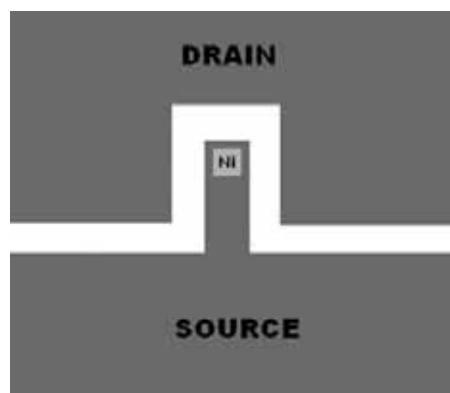


Figure 1

annealer (RTA) for temperatures ranging from 850-1050°C and times from 1-3 min. This process caused the Ni to form balls all over the surface. Some samples were re-annealed at the same temperature to see if this had any affect on Ni ball formation. Ni balls were then characterized using AFM as in Figure 2.

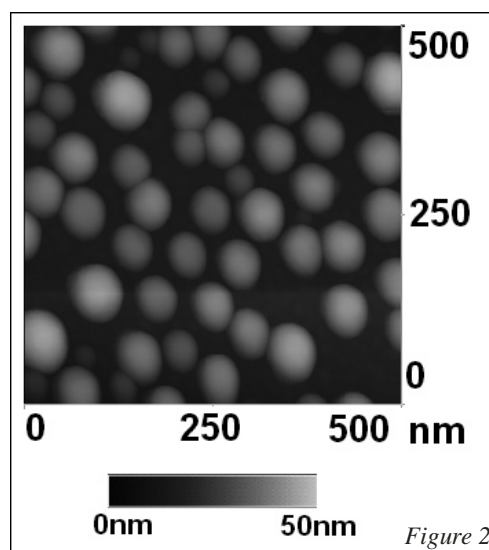


Figure 2

### Nanowire Growth:

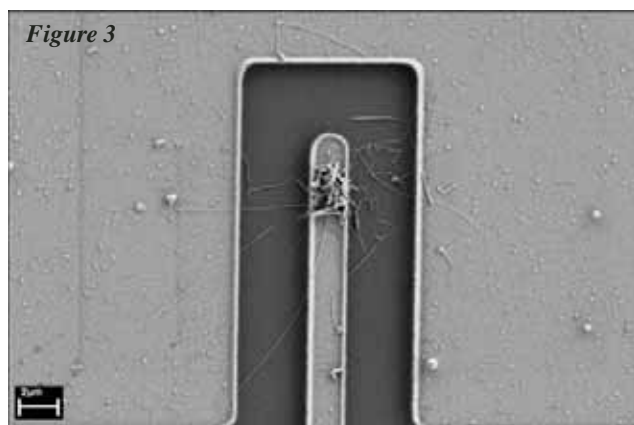
Nanowires were grown in a homemade furnace. A drop of Ga was placed upstream of the annealed substrate and the chamber was pumped down. Typical



growth conditions had 200 sccm of ammonia flowing through the chamber with another 200 sccm  $H_2$  as carrier gas. The reaction occurred at 1 atm. The furnace was heated to 900°C for the growth and the reaction time was 30 min.

### FET Fabrication:

Using standard lithography processes small dots of Ni (0.5-1  $\mu m$  squares) were patterned over a wafer. NWs were grown from the Ni pattern and 15nmTi/150nmAl/50nmTi/50nmAu source/drains were patterned on top of the NWs. The distance between the source and the drain was varied from 1-3  $\mu m$ . The natural oxide layer was etched off the back of the samples before current/voltage measurements were taken.



### Results and Conclusions:

All of the FET devices that we looked at with the SEM had more than 2 NWs connecting the source to the drain. The device with the fewest connecting NWs is shown in Figure 3. In the case where there was only 1  $\mu m$  between the source and the drain, the NWs are so crossed and tangled it was not possible to count how many NWs were connecting the source and drain. This study has shown that for a 1 NW connection, only one Ni dot is necessary for each FET and that the distance between the source and drain (for our geometrical configuration) should probably be between 4-6  $\mu m$ .

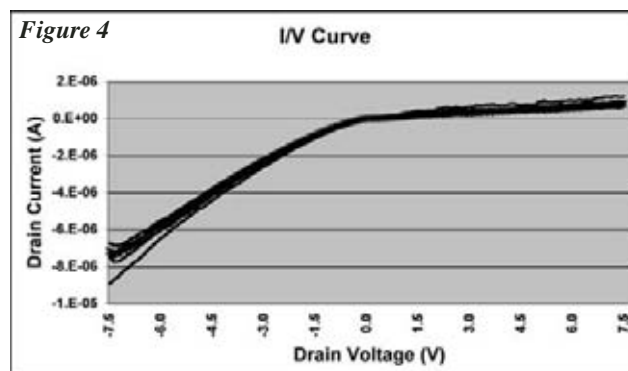
Current/voltage curves showed little modulation as the back gate voltage was changed. This may be because we had not put a metal contact on the back of the devices. Some of the devices were asymmetrical about the y-axis, which may be caused by poor contact with the GaN NW (see Figure 4). Despite these imperfections, almost every single device measured demonstrated FET electrical behavior: a linear relationship between source and drain current and voltage until high voltages were reached and current was close to constant.

### Further Studies:

Further studies of GaN FETs will include adding a metal back gate to see if that increases gate modulation and if the FETs will be pinched off. The metals used for the source and drain will also be optimized to ensure ohmic contact. Once these studies have been made, the use of GaN NWs as a biosensor will be able to be investigated.

### Acknowledgements:

The author wishes to thank Prof. Michael Spencer, Huaqiang Wu, the CNF, NNIN and NSF.



## Surface Preparation for 3C-SiC Growth on 3C- and 6H-SiC by In Situ Etching in HCl

**Janessa Smith, Mechanical Engineering, University of Delaware**  
**NNIN REU Site: Howard Nanoscale Science & Engineering Facility, Howard University**

*NNIN REU Principal Investigator: Dr. Gary Harris,  
Director, Howard Nanoscale Science & Engineering Facility, Howard University  
NNIN REU Mentor: Crawford Taylor, HNF, Howard University  
Contact: draupadi@udel.edu, gharris@msrce.howard.edu*

### Abstract:

Large-area, device-quality thin active layers of cubic silicon carbide (3C-SiC) are desirable for semiconductor applications but are difficult to manufacture. The only method of manufacture is chemical vapor deposition (CVD) upon a substrate, known as epitaxial growth. The surface quality of the substrate is critical to the growth of a high quality epilayer. In this project, we investigate hydrochloric (HCl) gas as an in situ etchant to improve the surface morphology before growth in a CVD reactor. We determined etch rates for HCl on hexagonal silicon carbide (6H-SiC), and found that the etching resulted in a terraced surface, as reported in literature. After the etching, growth of 3C-SiC was attempted on substrates of 3C- and 6H-SiC. The effect of the in situ HCl etching upon the quality of the SiC epilayer could not be determined from the results.

### Introduction:

SiC has many desirable characteristics that make it an excellent material for semiconductor applications. It can withstand high temperatures, high radiation and harsh environmental conditions and has excellent electronic qualities, such as high thermal conductivity, a wide band gap, large saturation drift velocity, and a large breakdown field. Unfortunately, because SiC sublimates, it is difficult to manufacture. It cannot be melted and then cooled into a crystal. In addition, SiC is susceptible to a high density of crystal defects by any manufacturing method. Due to these factors SiC technology, although promising, is still relatively immature.

Commercially available bulk 3C-SiC has been manufactured by heteroepitaxial growth using chemical vapor deposition. Though 4H- and 6H-SiC can be produced by more convenient methods, 3C-SiC has at least two advantages over the other polytypes. It lacks

micropipe crystal defects, which is the bane of the other polytypes, and it is better for CMOS applications because the hole mobility is almost equal to the electron mobility.

While many factors contribute to high quality growth of SiC, we will be considering the surface morphology of the substrate. Other literature has shown that an in situ HCl etch on 6H-SiC will create a smooth surface with periodic microsteps [4]. These microsteps have specific heights determined by the lattice size of the crystals and theoretically would encourage more orderly deposition with fewer crystal defects. An in situ HCl etch on 3C-SiC would theoretically result in a smoother surface. The goal of this project was to obtain an etch rate for HCl on 6H- and 3C-SiC and evaluate the etchant's effectiveness in producing smooth epilayers during subsequent growth on 6H- and 3C-SiC substrates.

### Procedure:

All etching and growth took place in a horizontal cold-wall CVD reactor. Because etch heights could only be measured using a removable mask that would

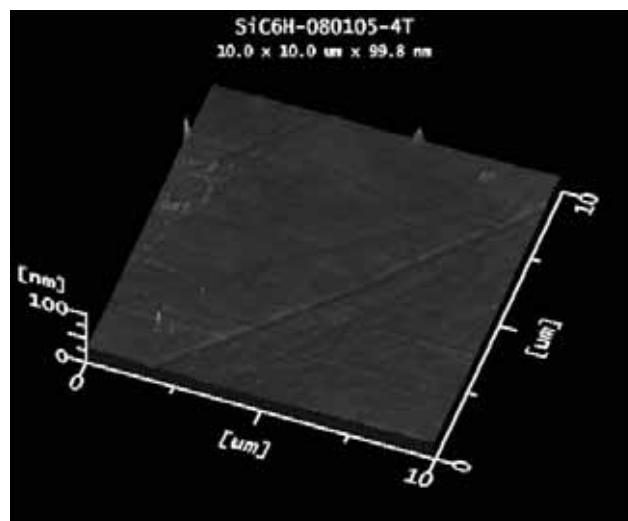


Figure 1: 6H-SiC surface before etching.

allow the “step” between the etched and unetched area to be measured, we used SiO<sub>2</sub> as a partial mask on 6H-SiC samples. Typically, 180 nm of SiO<sub>2</sub> was grown on <100> 6H-SiC. Using this mask necessitated limiting the temperature to less than 1250°C to prevent the complete degradation of the mask by the carrier gas. For all trials, the carrier gas of H<sub>2</sub> was 10 slpm, and the chamber pressure was 200 Torr. The HCl concentration varied between 30 and 120 sccm, the temperature varied between 1050-1200°C, and the time varied between 15-45 minutes.

Growth on 3C- and 6H-SiC occurred in the chamber after an HCl etch of 30 minutes at 120 sccm and 1200°C. After a short lag time to ramp up the temperature, the growth took place at 1300°C for 30 minutes. The silicon to carbon ratio in the gas phase was varied from 1 to 0.85.

### Results:

We only obtained measurable etching results at a temperature of 1200°C. Under varying HCl concentrations and times, we obtained a maximum etch depth of about 100Å. Etch depths for all samples were measured using a surface profilometer. There was no discernible difference between the etch depth using 60 or 120 sccm of HCl. The effect of the time on the etch depth was inconclusive. Qualitatively, the HCl-etched material had a terraced surface, with pits and scratches that were not removed but exaggerated by selective etching.

The growth of SiC on the SiC substrates tended to be polycrystalline. We failed to obtain an epilayer of 3C-SiC on the 6H substrate.

### Conclusions:

We found in our experiment that the minimum temperature for in situ etching that will yield etch rates of any significance is 1200°C. At this temperature, 60 sccm of HCl produced the maximum etch rate, as doubling this amount did not result in an increase in etch rate. The effectiveness of using in situ HCl etching before epitaxial growth of SiC is still unknown, and further testing is needed to determine its merit.

### Acknowledgements:

I would like to thank Mr. Crawford Taylor, Dr. Gary Harris, Mr. James Griffin, Dr. Peizhen Zhou, and all of the staff, graduate students and interns at the HNF.

### References:

- [1] P. G. Neudeck, J. A. Powell, A. J. Trunek, X. R. Huang, M. Dudley, Mat. Sci. Forum, 389-393 (2002) p. 311.
- [2] K. Teker, J. of Crystal Growth, 287 (2003) p. 245.
- [3] J. A. Powell, P. G. Neudeck, A. J. Trunek, G. M. Beheim, L. G. Matus, R. W. Hoffman, L. J. Keys, App. Phys. Lett., 77 (2000) p. 1449.
- [4] J. Zhang, O. Kordina, A. Ellison, E. Janzen, Mat. Sci. Forum, 389-393 (2002), p. 239.
- [5] Z. Y. Xie, C. H. Wei, L. Y. Li, J. H. Edgar, J. Chaudhuri, C. Ignatiev, MRS Internet J. Nitride Semicond. Res. 4S1, G3.39 (1999).
- [6] A. A. Burk, L. B. Rowland, J. of Crystal Growth, 167 (1996) p. 586.
- [7] C. Hallin, F. Owman, P. Martensson, A. Ellison, A. Konstantinov, O. Kordina, E. Janzen, J. of Crystal Growth, 181 (1997), p. 241.

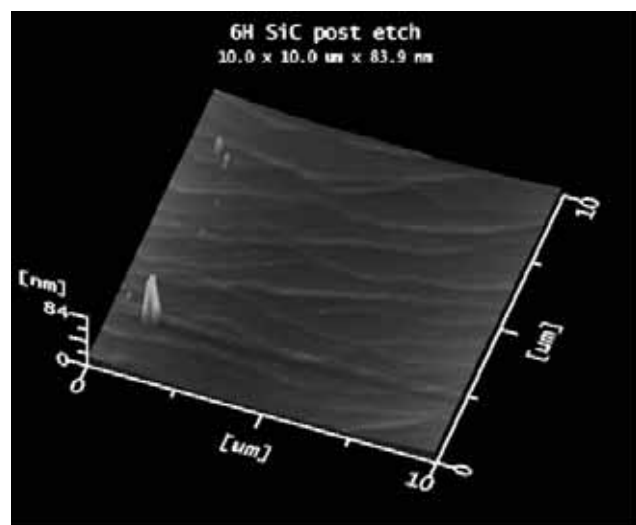


Figure 2: 6H-SiC surface after etching.

# Nanometer-Thick Dielectric Films Deposited by Electron Cyclotron Resonance PECVD System

**Matthew J. Smith, Material Science and Engineering, Johns Hopkins University**  
**NNIN REU Site: Center for Nanoscale Systems, Harvard University**

*NNIN REU Principal Investigator: Dr. Erli Chen, Center for Nanoscale Systems, Harvard University*

*NNIN REU Mentor: Dr. Ling Xie, CNS, Harvard University*

*Contact: MJSmith@jhu.edu, erlichen@cns.fas.harvard.edu, lxie@deas.harvard.edu*

## Abstract:

Depositing ultra-thin high quality dielectric films to be compatible with nanoscale devices is a challenge. The aims of this study are: (i) to investigate the deposition of nanometer thick silicon nitride films using electron cyclotron resonance plasma-enhanced chemical vapor deposition (ECR-PECVD); and (ii) to characterize these films. X-ray photoelectron spectroscopy (XPS) was used for film composition analysis, and spectroscopic ellipsometry for thickness and refractive index measurements. The results show a strong relationship between the refraction index and compositions for the films with a thickness of 50 nm. Important trends are also identified concerning index of refraction and deposition time for ultra-thin films. Mathematical formulae that use XPS peak intensity ratios to estimate the thickness of ultra-thin films are modified for ultra-thin silicon nitride films. The preliminary results show that the thickness of these silicon nitride films can be estimated using XPS peak intensity ratios.

## Introduction:

The purpose of this project was to further our understanding of silicon nitride films fabricated using ECR-PECVD. We were interested in depositing ultra-thin (less than 10 nm) silicon nitride films using ECR-PECVD because this process allows for very low deposition temperatures, below 150°C. In this project, we studied the effects of SiH<sub>4</sub> flow rates on the composition of films with a thickness of 50 nm; the variation of index of refraction with deposition time; and the estimation of the thickness of ultra-thin silicon nitride films using XPS.

## Experiment:

The composition of nitride films formed by ECR-PECVD was controlled by several factors, primarily the gas flow rate into the chamber. For silicon nitride deposition, SiH<sub>4</sub> and N<sub>2</sub> react and produce silicon nitride (Si<sub>3</sub>N<sub>4</sub>) and hydrogen gas. The nitrogen to silicon concentration ratio was measured using x-ray photoelectron spectroscopy, and then analyzed. For a

stoichiometric nitride film, the concentration ratio of N/Si should be 1.33 (4 nitrogen for every 3 silicon) and the refractive index should be about 2.0, which can be measured using the spectroscopic ellipsometer (SE). The index of refraction was also analyzed vs. deposition time for thick and ultra-thin films. The Si substrates used for ultra-thin depositions were etched in HF solution to minimize native silicon oxide. The data collected using the ellipsometer was fitted to a 2-layer model to account for the native oxide present at the interface between substrates and films. Several oxide thicknesses were tested with the model, and the model with the lowest MSE was chosen for each series of films.

The ultra-thin films, ranging from 3-8 nm in thickness, were thin enough that photon electrons from the silicon substrate could escape through the thin film and appear as a Si-Si signal on the XPS measurements. The thinner the film, the larger the number of photon electrons that escape from the substrate, and thus a larger Si-Si peak appears at 98.9 eV, separate from the Si-N peak at 102.0 eV. We explored using the area ratio of these peaks to calculate the thickness of the film. This was done previously for silicon oxide thin films [3], but has not been applied to silicon nitride films.

## Results and Discussion:

The XPS and SE measurements of the films deposited with different flow rates showed that the films deposited at higher silane flow rates (above 55-60 sccm) were silicon rich and had an index above 2.0, while those deposited at lower flow rates were indeed nitrogen rich and had an index below 2.0. Our data agreed with the accepted index-composition ratio correlation (Figure 1); a film with a N/Si ratio of 1.33 should have an index of 2.0.

When evaluating the index of refraction change with deposition time, we found that the thicker films had a constant index of refraction when the deposition time was varied from 400 to 600 seconds. However, the index of refraction of ultra-thin films, with variable deposition time from 10 to 60s, did not remain



constant with deposition time, as shown in Figure 2. This implied that a unique combination of deposition time and flow rate was required to obtain a particular thickness and index of refraction when depositing ultra-thin Si<sub>3</sub>N<sub>4</sub> films with ECR-PECVD.

When using XPS data to estimate ultra-thin film thickness, the inelastic-mean-free-path and the silicon concentration ratio of the film to the silicon substrate per unit volume, had to be approximated. We found that our best approximations for these constants could not get reasonable values for estimated film thickness. A scaling constant was introduced into the equation and this technique was able to return thicknesses that paralleled those determined by our best spectroscopic ellipsometry models. Figure 3 shows the simulation as well as the ellipsometer results.

### Future Work:

In the future, we hope to refine the process of using XPS to measure silicon nitride film thicknesses of less than 10 nm. An alternate method of knowing film thickness is necessary, so that we have more accurate data to model our formulae after.

### Acknowledgements:

I would like to thank Dr. Ling Xie, Dr. Erli Chen, David Lange, and the CNS Staff at Harvard University, the National Nanotechnology Infrastructure Network and the NSF.

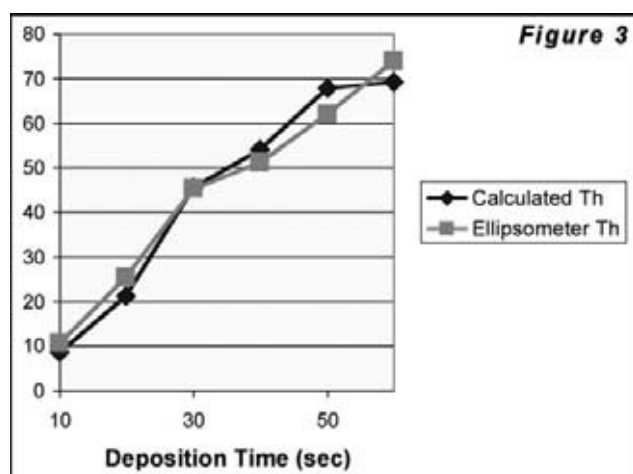
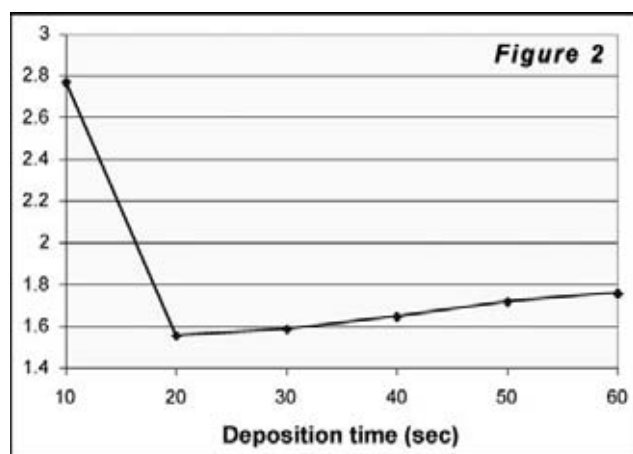
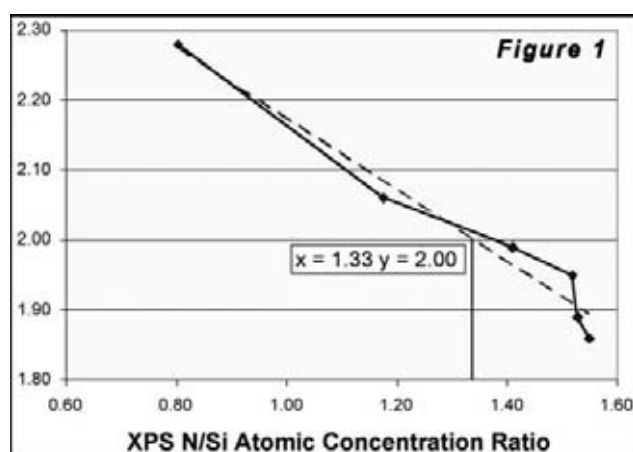
### References:

- [1] Xie L, Deng J, Shepard S, Tsakirgis J, Chen E, "Low-Temperature Deposition of High-Quality, Nanometer-Thick Silicon Nitride Film in Electron Cyclotron Resonance (ECR) Plasma-Enhanced CVD System", presented at Nanotech 2005, Anaheim CA, May 2005.
- [2] Flewitt A.J., Dyson A.P., Robertson J, Milne W.I., "Low Temperature growth of silicon nitride by electron cyclotron resonance plasma enhanced chemical vapour deposition", Thin Solid Films 383 (2001) 172-177.
- [3] Xie L., Zhao Y., White M.H., "Interfacial oxide determination and chemical/electrical structures of HfO<sub>2</sub>/SiO<sub>x</sub>/Si gate dielectrics", Solid-State Electronics 48 (2004) 2071-2077.

*Figure 1, top: A stoichiometric silicon nitride film has an index of refraction of 2.*

*Figure 2, middle: Unlike in thicker films, ultra thin silicon nitride films have an index of refraction that varies with thickness.*

*Figure 3, bottom: After introducing a scaling constant, the XPS data can be used to predict thicknesses that parallel the thicknesses measured using ellipsometry.*



# Nanoscale Surface Acoustic Wave Sensors for Early Cancer Detection

Wafa Soofi, Bioengineering, Rice University

NNIN REU Site: Microelectronics Research Center, Georgia Institute of Technology

NNIN REU Principal Investigator: Dr. William D. Hunt, Electrical Engineering, Georgia Institute of Technology

NNIN REU Mentor: Christopher Corso, Biomedical Engineering, Georgia Institute of Technology

Contact: wsoofi@rice.edu, bill.hunt@ece.gatech.edu

## Abstract:

The variety of research areas involving applications of surface acoustic wave (SAW) devices has recently been extended to include the field of biosensing technology. The velocity of the surface acoustic waves, and thus the operating frequency, is dependent upon the mass density of a biolayer on the surface of the device. This biolayer contains antibodies directed against cancer cell proteins; if the target proteins are present in the environment, they will bind to the antibody layer. This causes a change in the mass of the biolayer, which in turn results in a change in the operating frequency of the device. This change can then be detected by interrogating the device with a radio frequency (RF) signal, which is reflected back via an input/output interdigital transducer (IDT) so that the signal can then be analyzed for perturbations caused by binding effects within the biolayer. Presently, the SAW device understructure has been fabricated using electron beam lithography and tested for response to electrical probing. Ultimate goals include addition and testing of the biolayer and antenna for RF interrogation.

## Introduction:

In the field of biosensing technology, SAW sensors can be used to determine the presence of specific molecules in the surrounding environment. SAWs are generated by interrogating piezoelectric substrates with an electrical signal; the extreme sensitivity of SAW devices to small surface mass changes makes them

ideal for detecting nanoscale particles. Our specific SAW sensor is comprised of a single input/output IDT with an array of reflector strips on either side. An electrical signal is sent to the I/O IDT, causing SAWs to propagate outward towards both reflector arrays, one of which was coated with a biolayer composed of a protein cross-linker and antibodies specific to the target protein. If the target proteins are present in the environment, they adhere to the antibodies, causing a change in the mass of the device. By the principle of mass loading, a frequency shift occurs in the SAW propagating back towards the I/O IDT from the reflector array coated with the biolayer [1]. This shift can then be detected using radio frequency identification (RFID) technology by adding an I/O antenna to the IDT.

The novelty of our project arises from the application of SAW biosensors to cancer detection and the addition of RFID technology (see Figure 1). To this end, modifications to the general SAW device blueprint include use of antibodies whose target proteins are specific to cancer cells, addition of an RFID antenna, and the fabrication of nanoscale IDTs to produce an operating frequency in the GHz range.

Since SAW devices operate on a principle very similar to that of thickness shear wave devices, in which, by the Sauerbrey equation, the central operating frequency is inversely proportional to the amount of observable mass change, such a high operating frequency allows mass changes posed by minute targets such as cancer cell proteins to be detected [2].

## Fabrication:

The complexity of the RFID SAW device design made it necessary for us to focus solely on fabrication of the metal understructure of the device and achieving a response to electrical signal probing. The metallization design was created using graphic design software, and electron-beam lithography was used for exposure of the resist. An ST-quartz wafer was coated with ZEP520A photoresist and a thin layer of gold to dissipate charge buildup during electron-beam

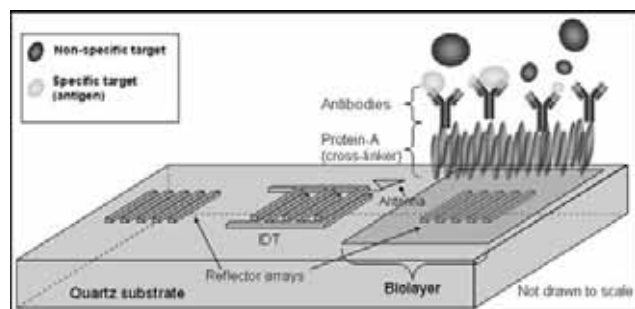


Figure 1: Schematic layout of a completed RFID SAW device.

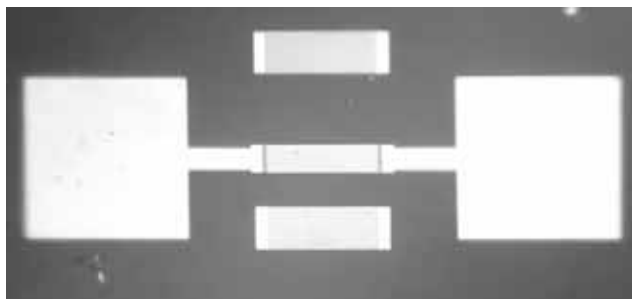


Figure 2: Metallization (Au) of a SAW device.

lithography. The wafer was then exposed, developed, and metallized with chromium (for adhesion) and gold (see Figure 2).

### Experimental Procedure:

For our preliminary runs, several variations of the basic device design were fabricated in parallel to test the effect of individual geometrical parameters on the strength of the return signal. Some variables tested included the number of IDT finger pairs and reflector strips, shorted versus unshorted reflector strips, and resonating versus nonresonating devices. In subsequent runs, it became necessary to increase the size of the device pads to facilitate probing with our equipment. Metallization thickness was also varied in order to determine an ideal resist-to-metallization thickness ratio.

### Results and Discussion:

After fine-tuning the fabrication procedure and achieving a satisfactory yield, a network analyzer was used to test the devices for resonance. A distinct return loss was detected in several of the devices (see Figure 3). It was found that the distinctness of the response (Q) varied approximately directly with the number of

reflector strips in each array. Though the Q of the S11 return loss was high, the magnitude was only about 0.18 dB. It was also found in nearly all of the devices tested, resonance occurred at a significantly lower frequency than the expected 2.440 GHz (as in Figure 3). This anomaly was found to be part of an unexpected trend wherein the resonant frequency of the device decreased as the metallization mass increased (see Figure 4).

Future work on the RFID SAW devices should involve the addition of the biolayer and RF antenna. Experiments should be undertaken with specific and non-specific antigens to verify that the target proteins are binding properly to the antibodies and a detectable mass change results from immobilization. The inverse relationship of the metallization mass of the device to its resonant frequency should also be more fully investigated.

### Acknowledgements:

I would like to thank Dr. Hunt and Dr. Edmonson for overseeing the project, Dr. Raghunath Murali and Devin Brown for their aid in the electron beam lithography process, and the members of the Microelectronic Acoustics Group for their invaluable help with researching, modifying, and testing the devices.

### References:

- [1] Handbook of Biosensors and Electronic Noses. Kress-Rogers, Erica, ed. Boca Raton: CRC Press, 1997.
- [2] Dr. Peter J. Edmonson, private communication.

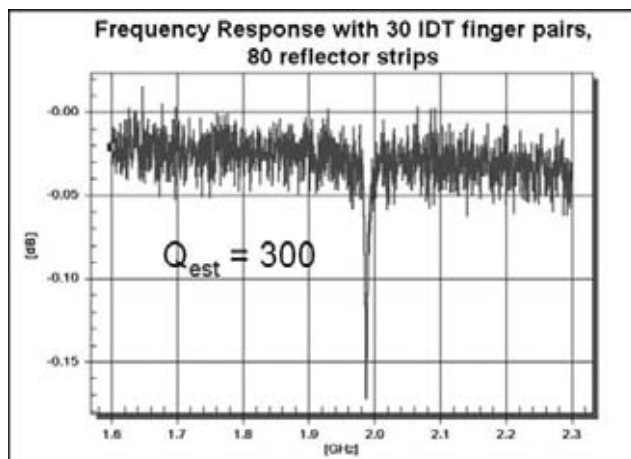


Figure 3: Frequency response of a fabricated SAW device.

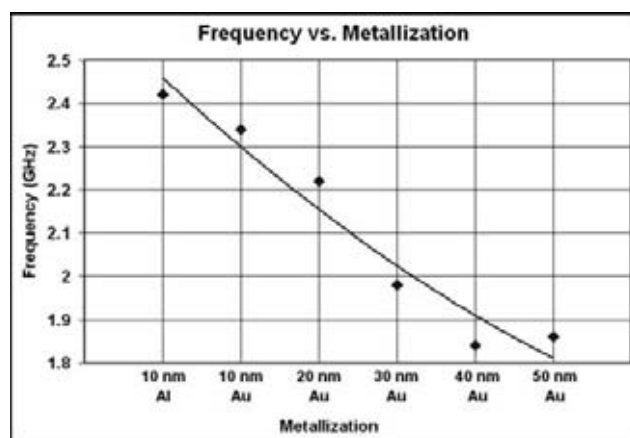


Figure 4: Frequency vs. metallization curve.

# Nanoscale Magnetic Characterization of FIB Patterned Bits on Perpendicular Magnetic Recording Media

**Joshua Symonds, Physics and Applied Mathematics, University of Rochester**  
**NNIN REU Site: Stanford Nanofabrication Facility, Stanford University**

*NNIN REU Principal Investigator: Robert Sinclair, Materials Science and Engineering, Stanford University*

*NNIN REU Mentor: Unoh Kwon, Materials Science and Engineering, Stanford University*

*Contact: jsymonds@gmail.com. bobsinc@stanford.edu*

## Abstract:

Patterning perpendicular magnetic recording media is one of the methods being investigated currently in order to increase magnetic storage capacity, and allow the next generation of recording devices to attain storage densities above 300 Gb/in<sup>2</sup>. Work has been done with patterning CoCrPt perpendicular media, but so far there has been no work done patterning CoCrPt-oxide media. This type of film is considered to be a strong candidate for perpendicular recording media due to its magnetically decoupled grain structure.

In this project we examine two sizes of patterned magnetic bits with sizes ~225 nm and ~115 nm, created by patterning conventional CoCrPt-oxide thin-film perpendicular recording media using focused ion beam (FIB) milling. FIB-patterned structures are characterized by using atomic force microscopy (AFM). Using magnetic force microscopy (MFM) we determine the magnetic characteristics of the patterned bits. These results give us insight into how useful it will be to pattern CoCrPt-oxide perpendicular magnetic films for use in the next generation of hard disks.

## Introduction:

Magnetic storage devices are used in almost every modern computer, and increasing demands require improvements in this technology. In most conventional magnetic storage devices, the magnetization direction of magnetic grains used to store data is in the plane of the magnetic film. The grains in these films have a hexagonal close-packed (hcp) structure and develop magnetizations with the c-axis orientation [1], so perpendicular media employ grains with c-axes and magnetizations oriented out of the plane.

By physically isolating magnetic bits in the film using an easily controlled process like lithography, a scanning head encounters much less noise, and higher storage densities become practical. This project investigates the properties of magnetic bits patterned into a perpendicular magnetic film, employing both of these solutions to achieve the higher storage densities.

## Procedure:

CoCrPt-oxide film was used for our magnetic media. We investigated the magnetic domain structure of patterned bits with different dimensions, since domain behavior is dominated by size for isolated pieces of a given ferromagnetic material. Patterning was accomplished using focused ion beam (FIB) milling at 1pA beam current, using different mill times to see when the milled trenches began decoupling bits. Patterns of squares with 300 nm and 160 nm bit-periods were examined. The film we used was composed of a 20 nm magnetic layer with a 5 nm-thick protective surface layer of carbon. We cut FIB-milled trenches 4 nm deep into this layer, but, as observed by Rettner et al. [2], the Ga<sup>+</sup> ions used in the FIB process penetrated the film and decoupled the film, creating bits. After patterning the film, the physical and magnetic characteristics of the bits were determined using atomic force microscopy (AFM) and magnetic force microscopy (MFM), respectively. The sample was ac-demagnetized before the AFM and MFM analysis.

## Results:

The trenches cut into the film were observed to be ~ 4 nm deep after patterning for 60 seconds at 1pA beam current. In the SEM images, grids patterned for 10 to 20 seconds seemed to be the cleanest with the most well-defined bits, but MFM data showed there was not sufficient decoupling of the magnetic domains.

In the patterned grids with bit periods of 300 nm, the actual bits we measured were ~ 220 nm across, with trench line widths of ~ 80 nm. Figure 1 shows the cross section profile one 220 nm square grid, and Figure 2 shows the AFM image of the same grid. In these bits, multi-domain behavior was observed in the MFM image, as shown in Figure 3. In many of these bits, as Figure 3 shows, the majority of a bit is magnetized in one direction (into or out of the film plane) and a separate domain becomes magnetized in the opposite direction near the center of the bit. This is expected to be the case in multi-domain bits since two uncoupled



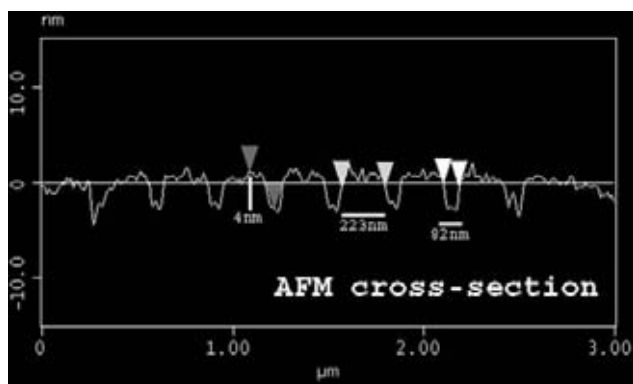
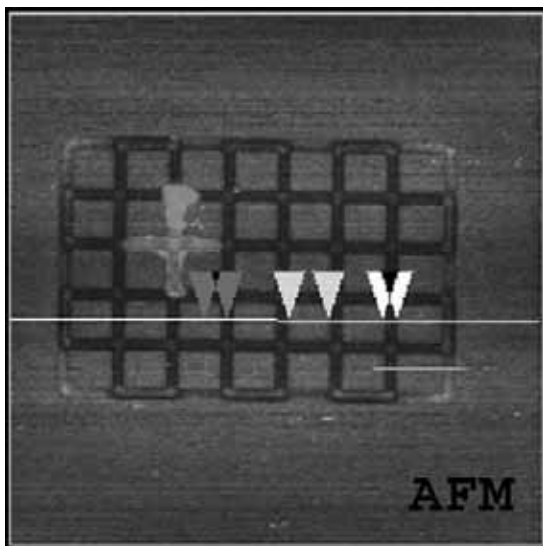


Figure 1, above: Cross section of 300 nm bit period pattern showing topography of bits.

Figure 2, below: AFM image of 300 nm pattern, indicating line which Figure 1 details.



domains would tend to become magnetized in opposite directions to reduce the magnetostatic energy. This behavior is often seen in the center of a bit since the flipping force on a domain would be strongest at the center of an oppositely magnetized domain.

In the grids with a 160 nm bit period, the squares measured 110 nm, with trench widths of 50 nm. The MFM data in Figure 4 shows that these bits are in single domain states, and two of the bits in the pattern are magnetized in the opposite direction. The MFM data shows that the domain boundaries lie neatly along the trenches we cut.

## Discussion and Conclusions:

Since only two sizes of bits were investigated, it is impossible to say exactly where the single-domain threshold lies for CoCrPt-oxide perpendicular recording media. We do know that single-domain bits were observed for 110 nm squares, and this may be larger than we initially expected. The patterning process has room for improvement, and with more time it should be possible to mill narrower trenches and further increase bit density in the sample. Finally, after investigating a wider range of bit sizes, it should be possible to determine where bits make the transition from multi-domain to single domain, which is necessary for any application in future storage devices.

## Acknowledgements:

Unoh Kwon, Robert Sinclair & the Sinclair Group, Liangliang Li, NSF, NNIN.

## References:

- [1] CA Ross Annu. Rev. Mat. Res, 31:203-35, 2001.
- [2] Rettner et al. IEEE Trans. Mag. Vol. 38, No. 4, July 2002.

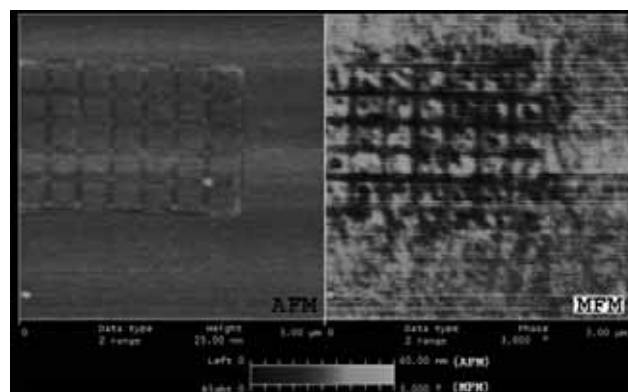
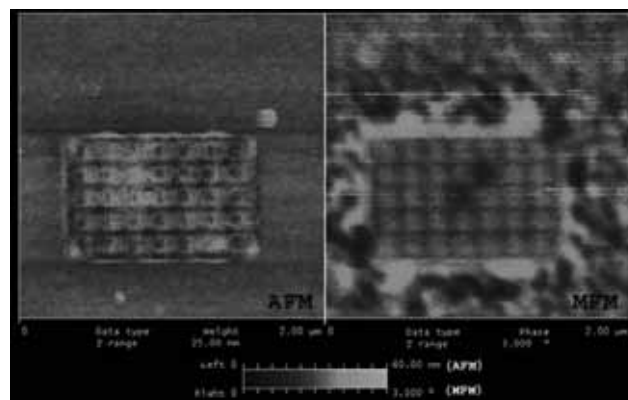


Figure 3, above: AFM/MFM image of 300 nm pattern. Images show the same area.

Figure 4, below: AFM/MFM image of 160 nm pattern.



# Nanofiber Catalyst Production Using Anaerobic Bacteria

Rachel Thompson, Chemistry, Rockford College

NNIN REU Site: The Penn State Nanofabrication Facility, The Pennsylvania State University

NNIN REU Principal Investigators: Dr. Wayne Curtis & Dr. Jong-In Hahn,  
Chemical Engineering, The Pennsylvania State University

NNIN REU Mentor: Michael Lee, Biology, The Pennsylvania State University

Contact: rthompson@rockford.edu, wrc2@psu.edu

## Abstract:

The goal of this research was to carry out comparative studies on nanowires fabricated using nanoparticle (NP) catalysts from several different strains of bacteria. We identified and selected four NP-producing candidates: magnetotactic bacteria strains MS-1, MV-1, and MC-1, which produce magnetite ( $\text{Fe}_3\text{O}_4$ ) NPs; and a strain of sulfate-reducing bacteria (SRB), *Desulfovibrio gigas*, which may produce ZnS NPs. The size and shape of these catalysts affect the diameter and cross section of the nanowires, which are important in potential nanoelectronic applications. We also plan to test zinc oxide nanowires in a nano-biosensor for detection of molecules tagged with green fluorescent protein.

Since formation of ZnS NPs has only been documented for mixed natural cultures of SRB, an initial study examined media that might stimulate ZnS NP growth in *D. gigas*. Scanning electron microscopy (SEM) and energy dispersive spectrometry (EDS) were not yet able to detect the presence of ZnS particles.

## Introduction:

Miniaturization goals in electronics will require new, cost-efficient, highly-reproducible methods for producing nano-scale devices, of which nanowires

(NW) and carbon nanotubes (CNTs) are integral components. Controlling diameter, shape, orientation, and alignment of NW/CNTs is important to researchers. One approach is production of NP catalysts via self-regulating biological systems. Four anaerobic strains of bacteria, requiring complex culturing techniques, were selected to produce NPs of unique size and shape because these variables should directly influence the attributes of subsequently grown nanofibers. The three magnetotactic strains also have potential to aid in lateral alignment of the NPs (and thus the nanofibers).

*D. gigas* was selected because it was readily available and was one of the species included in the natural, mixed SRB culture study in which ZnS NPs were successfully produced [1]. Our group previously produced NPs using MS-1, the easiest of the four strains to culture, for ZnO nanowires growth.

## Materials and Methods:

The MV-1 and MC-1 bacteria were obtained from Dr. Dennis A. Bazylinski (Department of Microbiology, Iowa State University). Samples from the concentrated liquid cultures of MV-1 were refrigerated in epitubes for use in initiating new cultures and CNT growth. MC-1 cannot be refrigerated, thus samples were isolated for immediate CNT growth. The remainder of both bacterial solutions was cryopreserved at  $-80^\circ\text{C}$  in an 80% glycerol solution.

Growth media for a live liquid culture of MV-1 was prepared using an as of yet unpublished recipe received from Dr. Bazylinski's lab. Preparation required sparging with  $\text{N}_2$  gas, use of an anaerobic chamber for addition of several ingredients, and replacing the headspace with  $\text{N}_2\text{O}$  gas. Media and components were autoclaved (liquid cycle, 20 minutes). Remaining components were added anaerobically and aseptically, then the media was refrigerated until inoculation.

*D. gigas* was obtained from Dr. Christopher House (Department of Earth and Geological Sciences, Pennsylvania State University). Growth Media 149 and Media 63 (<http://DSMZ.de>) were used. Both

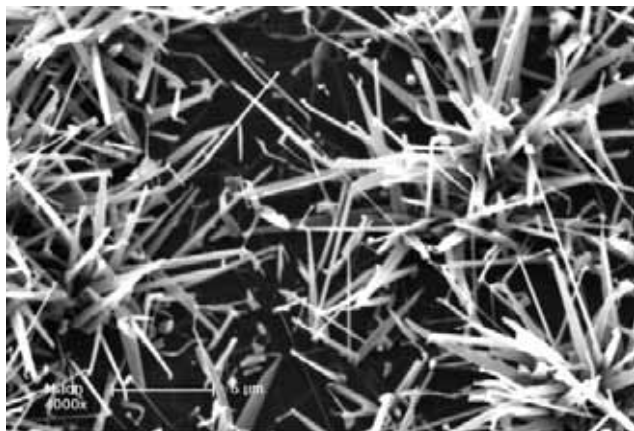


Figure 1: MS-1 NP-catalyzed ZnO nanowires (SEM, 4000x magnification).

formulations were altered to create an environment promoting ZnS formation by the addition of  $\text{ZnSO}_4$ . Basicity of the media (pH  $\sim 7.5$ ) caused  $\text{Zn(OH)}_2$  precipitation. Media 63 pH was decreased to  $\sim 6.3$  to solubilize the precipitate, but the pH of Media 149 was retained at 7.8. A 20% $\text{N}_2$ /80% $\text{CO}_2$  mix (0.5 bar) comprised the headspace gas for both media. Five samples of each media, with Zn concentrations ranging from 0 to 0.01 g/mL, were inoculated with *D. gigas* and allowed to incubate unshaken at 30°C for 4 days.

### Results and Conclusions:

MV-1 and MC-1 cultures were printed onto silicon wafers and ignited (800°C, 1 hour) in preparation for CNT growth. Atomic force microscopy revealed successful CNT formation on the MC-1 sample wafer. However, the MV-1 bacteria cells did not lyse and disintegrate as expected, and nanofiber catalysis was unsuccessful. Although we cannot explain this unexpected behavior, salt build-up on the surface of the cells was suspected to have contributed to this phenomenon.

Presence of *D. gigas* growth and particle formation could not be visually assessed for 4 out of 5 Media 149 samples and high-zinc Media 63 samples due to precipitation of  $\text{Zn(OH)}_2$ . Growth was visually confirmed in both samples containing no Zn. Media 63 samples containing 0.01 g/mL  $\text{ZnSO}_4$  and no Zn were placed on silicon wafers and ignited for SEM/EDS analysis. No particles were observed on either wafer using SEM. This could have resulted from limitations in the resolution of this technique. Significant presence of zinc and sulfur could not be confirmed in either sample by EDS. We suspect that this failure to obtain ZnS NPs using *D. gigas* can be reversed by using a lower Zn concentration. Exposing NPs to conditions for nanowire growth could also aid in detection.

### Future Work:

Further study requires availability of these bacteria cultures. Thus, an immediate goal is to sustain a living culture of each strain, starting from the cryopreserved stock cultures. In the future, we want to use a magnetic field to laterally align magnetotactic cultures prior to printing. Also, CNTs catalyzed from each particle

type need to be characterized (i.e. number of walls, diameter). The ZnS NPs represent a potential for much smaller wire formation. Experiments will focus on identifying culture conditions that could facilitate formation of these particles from *D. gigas*. Alteration of Zn concentration and pH is a starting point. More sophisticated strategies of feeding Zn to avoid toxicity yet facilitate NP formation could be tested. Finally, since the utility of these ZnS NPs is still exploratory, attempting to isolate these NPs from mixed culture conditions where they have been reported [1] may prove worthwhile in establishing their utility, thus warranting the effort of developing a production strategy.

### Acknowledgements:

Funding: NNIN-REU, NSF, Weyerhaeuser. Student Mentors: Mike Lee, Nitin Kumar. Other contributors: Dr. House, Dr. Bazylnski, Penn State Nanofab staff.

### References:

- [1] Labrenz, et al., Formation of Sphalerite (ZnS) Deposits in Natural Biofilms of Sulfate-Reducing Bacteria. Science, 290, 1744-1747 (2000).

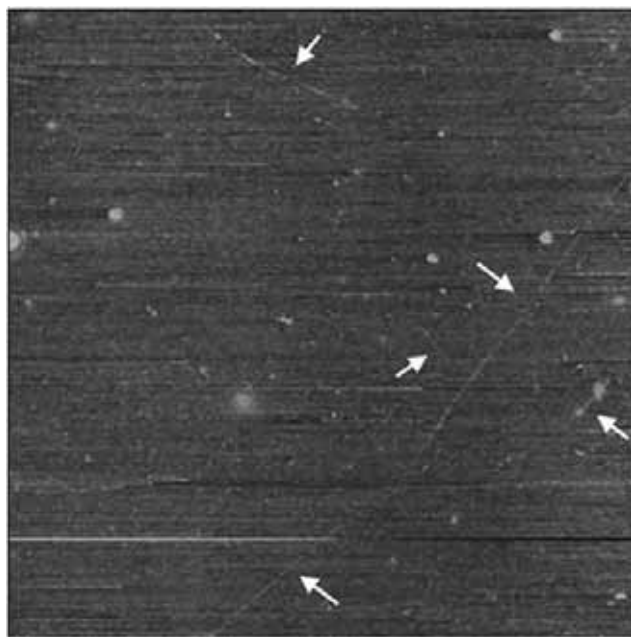


Figure 2: 7-by-7  $\mu\text{m}$  AFM image of CNTs on MC-1 NPs, indicated by white arrows.

# Whispering-Gallery-Mode Microdisk Optical Biosensor: Fabrication and Characterization

**Abbie Tippie, Electrical Engineering, Colorado State University**  
**NNIN REU Site: Center for Nanoscale Systems, Harvard University**

*NNIN REU Principal Investigator: Erli Chen, Center for Nanoscale Science, Harvard University*

*NNIN REU Mentor: Jiangdong Deng, Center for Nanoscale Science, Harvard University*

*Contact: abbie@tippietoes.com, erlichen@cims.harvard.edu, jdeng@cims.harvard.edu*

## Abstract:

The need for sensitive yet miniaturized instruments for bio-detecting has accelerated the development of micrometer-scale optical biosensors. Microsphere biosensors based on the resonant shifting of whispering-gallery mode (WGM) have been demonstrated previously. Despite its high sensitivity (high Q-factor), microspheres face challenges such as large mode volume (size is uncontrollable during fabrication) and difficulty in integration with other optical components. In this work, the fabrication of microdisk WGM resonators using photolithography and wet etching is studied. SiO<sub>2</sub> microdisks with diameters ranged from 400-1200  $\mu\text{m}$  and thicknesses of 1 and 15  $\mu\text{m}$  were fabricated on Si substrates. Preliminary spectroscopic tests showed that the as-fabricated disks have a Q-factor better than 10<sup>4</sup>, indicating that microdisks are viable alternatives to microsphere sensors. Since the fabrication process used in the study is compatible with that in standard microfabrication, the sensors can be easily integrated with other electronic and optical components on a semiconductor chip. Further improvement in sensor fabrication and performance is also investigated.

## Introduction:

Developing biosensor technology is a major development being pursued for medical, food or environmental testing. The detection of particles of proteins or DNA is key to successful biosensor advances. The biosensor developed in this paper uses whispering-gallery-mode optical resonances with high-Q factors to implement a high sensitive, robust system.

Whispering-gallery-modes (WGM) are generated when light is confined near the surface of a disk or spherical object by total internal reflection and is returned in phase after revolution about the perimeter [1]. If an eroded optical fiber is placed in close proximity to a resonant disk, the evanescent wave from the light in the fiber will excite the WGM modes of the disk. Resonant disks with high Q values will result in high sensitivity, as displayed by sharp dips transmission as observed at the output of the optical fiber.

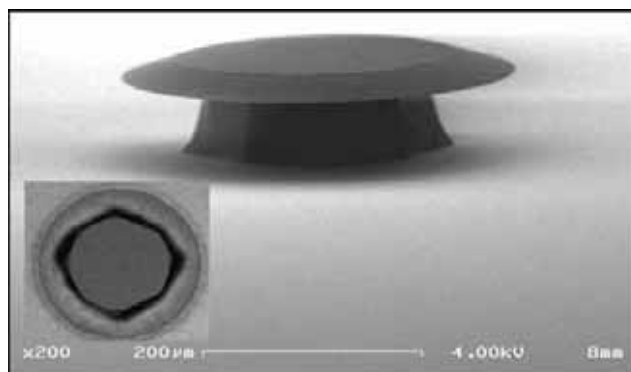


Figure 1: SEM image of 400  $\mu\text{m}$  disk; inset: top down view taken with optical microscope.

Previous biosensor work has already been developed by Vollmer et al [2] to identify DNA using microsphere resonant cavities. The drawback to the current microsphere approach is the lack of control over the fabrication process and exact size of the microsphere. In this paper, we show how the controlled fabrication of disk-shaped WGM resonators offers a new form of optical biosensors.

## Experimental Procedure:

The fabrication of the microdisks involved three steps: Mask generation, HF wet etching and KOH wet etching. The initial substrate consisted of a 15  $\mu\text{m}$  layer of SiO<sub>2</sub> thermally grown on a 1 mm thick Si <100> wafer. Disks of photoresist were created following the photolithography process. To reduce the roughness of the disks' sidewall, the samples were then postbaked at 200°C for 10 min. The photoresist acted as a mask for the SiO<sub>2</sub> during the HF wet etching process. The silicon surface was then etched in KOH solution at a temperature of 100°C until the silicon base was  $\sim 30 \mu\text{m}$  narrower than the undercut edge of the SiO<sub>2</sub> disk. Figure 1 shows the final microdisk structure, composed of a 15  $\mu\text{m}$  thick undercut disk of SiO<sub>2</sub> sitting upon a Si support base.



Evanescent coupling was used to excite the whispering modes of the microdisk structure. To expose the evanescent field, the outer polymer of a 125  $\mu\text{m}$  diameter optical fiber was first dissolved using dichloromethane. A butane/nitrous oxide flame was then used to melt and stretch the fiber to a diameter of  $\sim 5 \mu\text{m}$ . The fiber was then positioned into a loop for easier alignment with the microdisk. A 1310 nm wavelength laser was coupled into the fiber. The eroded portion of the fiber was aligned under an optical microscope to contact the edge of the microdisk and thereby introduce coupling between the two objects. The transmission intensity was then measured using a photodiode interfaced with LABview.

To observe sensing properties, the microdisk was placed on a temperature-controlled surface. The surface of the plate was varied in temperature from 18°C to 25°C. A specific dip in transmission was then used to observe changes in the wavelength as the temperature varied with time.

### Results:

As a means of determining the sensitivity and feasibility of the microdisk structure as a sensing device, Q-factor was calculated and sensing performance was observed. The optical resonances of the WGM modes in the disks were evidenced by dips in the intensity, as shown in Figure 2. For a 15  $\mu\text{m}$   $\text{SiO}_2$  microdisk, a Q-factor of  $4.5 \times 10^4$  was obtained. In Figure 3, we see how an increase in the temperature resulted in longer resonant wavelengths. Our data shows this effect is reversible; a decrease in temperature results in shorter resonant wavelengths.

### Conclusions:

In conclusion, the microdisk structure is a viable alternative to the microsphere for sensing capabilities. The controlled fabrication and ease of integration provided by the microdisk are more advantageous to further development of WGM optical biosensors. These new microdisk optical biosensors will be easier to integrate on a semiconductor chip, thus resulting in a more robust design.

### Future Work:

Further improvements to the fabrication and sensing will be implemented upon future experimentation. In order to achieve a higher Q-factor, some edge treatment techniques, such as  $\text{CO}_2$  laser melting [2] and focused ion beam drilling are proposed. Other variations of substrate materials may also be explored. We hope to design and integrate a waveguide with the microdisk on the same surface in order to develop a fully integrated

chip, sensitive and robust enough for the applications of biosensing.

### Acknowledgments:

Erli Chen; Jiangdong Deng; Frank Vollmer; Dr. Kathryn Hollar; Chris Stokes; Jim Reynolds; James Houlahan; Rowland Institute at Harvard; Harvard University; NNIN; NSF.

### References:

- [1] Quan, H. and Z. Guo, "Simulation of whispering-gallery-mode resonance shifts for optical miniature biosensors," *Journal of Quantitative Spectroscopy and Radiative Transfer* 93, 231-243 (2005).
- [2] Vollmer, F., D. Braun, A. Libchaber, M. Khoshima, I. Teraoka, S. Arnold, 'Protein detection by optical shift of a resonant microcavity'. *Appl. Phys. Lett.* 80, 4057-4059 (2002).
- [3] Armani, D.K., T.J. Kippenberg, S.M. Spillane, and K.J. Vahala, 'Ultra-high-Q toroid microcavity on a chip'. *Nature (London)* 422, 925 (2003).

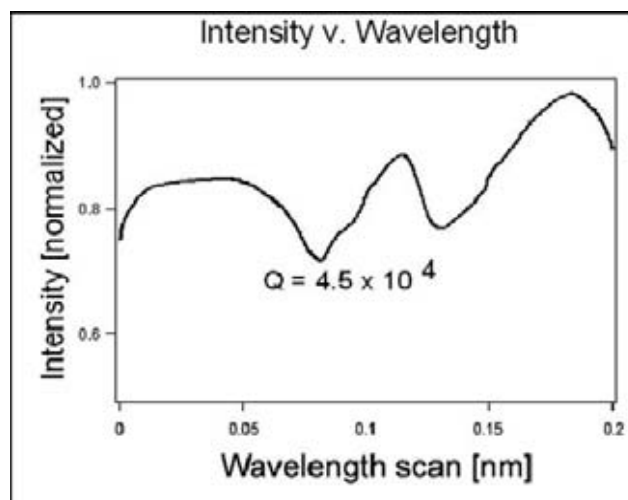
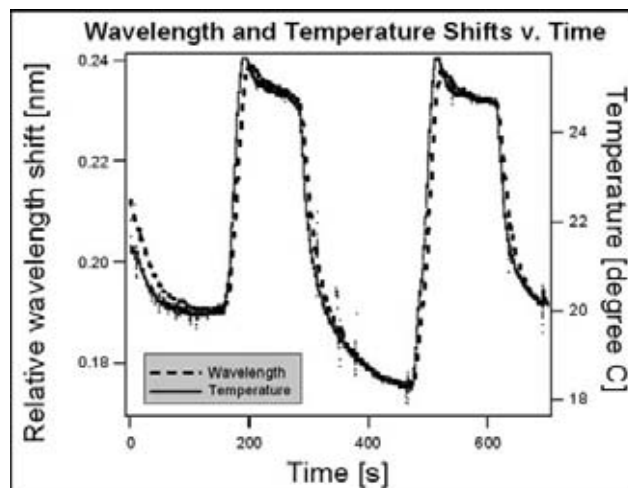


Figure 2, above: Microdisk/tapered fiber coupling.

Figure 3, below: Changes in wavelength and temperature v. time.



# Synaptic Ultrastructural Reconstruction Using Serial Electron Microscopy

**Winnie J. Tsang, Biomedical Engineering, Johns Hopkins University**  
**NNIN REU Site: Center for Nanoscale Systems, Harvard University**

*NNIN REU Principal Investigator: Professor Jeff Lichtman, Molecular and Cellular Biology, Harvard University*

*NNIN REU Mentor: Dr. Richard Schalek, Center for Nanoscale Systems, Harvard University*

*Contact: wtsang2@jhu.edu, jlichtman@mcb.harvard.edu, rschalek@deas.harvard.edu*

## Abstract:

The goal of this project was to create a three-dimensional representation of the neuromuscular junction (NMJ), taken from a five-day and seven-day-old mouse, using serial transmission electron microscopy and the image-manipulation software Reconstruct. A reconstruction of the week-old NMJ helps us to understand the neuroanatomy of the target region prior to synapse elimination, an important process that occurs in the second week of post-natal nerve development [1, 2]. Practical use of thin section electron microscopy also gives us insight into a process we hope to automate.

## Introduction:

The first few weeks of post-natal nervous development are marked by a process known as synapse elimination. This phenomenon, during which two or more existing axonal branches compete for control of one post-synaptic cell, ends the polyneuronal innervation established in pre-natal life [1]. At any given target cell, one axon becomes the sole input; all other axon branches retreat by releasing axonal materials into nearby glial cells or by other forms of degeneration [3]. Though individual postsynaptic cells are losing innervating axons, it is important to note that the winning axons create enough new contacts to offset any net loss in synapses [1]. On a broader level, there is evidence that synaptic elimination plays a role in learning and memory formation.

In this study of the NMJ, we use serial transmission electron microscopy (TEM), because it offers a level of resolution and detail of cellular structures not afforded by light-microscopy methods. Though synaptic competition occurs in many areas throughout the nervous system, researchers frequently use samples of the NMJ for its easy accessibility [3]. This project uses NMJ samples extracted at post-natal five (P5) and seven (P7) days. The reconstructions will show the neuroanatomy in the vicinity of a NMJ prior to axon removal, when some or most muscle fibers are still innervated by more than one motor axon.

## Methods and Procedures:

Imaging of the NMJ using serial TEM requires a series of time- and labor-intensive steps which cover sample preparation, the acquisition of images with TEM and CCD

cameras, and image reconstruction.

A sample epoxy block embedded with muscle tissue was cut into ultra-thin sections of 50 nm using a Leica UCT ultramicrotome and diamond knife. Meticulous technique was essential for collecting the thin sections and preserving continuity in their sequence. The delicacy of both the sections and grids made it difficult to bring both components through the preparation process intact.

Section-staining with uranyl acetate and lead citrate is a well-known technique used to improve the TEM imaging of skeletal muscle fibers. The dense electron clouds of the heavy metal atoms interact with the TEM electron beam to produce a detailed, high-contrast image [4]. Stain-prepared grids were viewed under the TEM, where target structures were pinpointed, captured with a CCD camera, and imported into Reconstruct.

The computer algorithms of Reconstruct allowed us to crop, montage, scale, and realign images from serial electron microscopy [4]. In addition to adjusting for spatiotemporal differences in images, Reconstruct also fixed problems associated with specimen and optical distortions [4]. Completed 2D sections, cross-sectional profiles of the specimen, were stacked on top of each other to mimic the original orientation of the sample in three dimensions.

## Results and Conclusions:

While sectioning through the P7 sample, we troubleshooted problems associated with the preparation of ultra-thin sections for electron microscopy. In the first few weeks, we improved the quality and readability of our sections by introducing heavy metal dyes and semi-thin survey sections. The semi-thin sections, which were 750 nm thick and easier to prepare, afforded us a quick survey image of our tissue cross-section under the high magnification of an optical microscope. We were then able to find a promising region around which we fine-trimmed the specimen block face. Because the specimen was so information-dense, we could not properly identify a NMJ under the TEM. To solve this problem, we used the focused ion beam (FIB) to etch fiduciary marks on the surface of our specimen block. This allowed us to orient ourselves in the section geography around a reference point, which was especially useful under the high magnification of the TEM and in Reconstruct. Trimming the block face into an unsymmetrical trapezoid

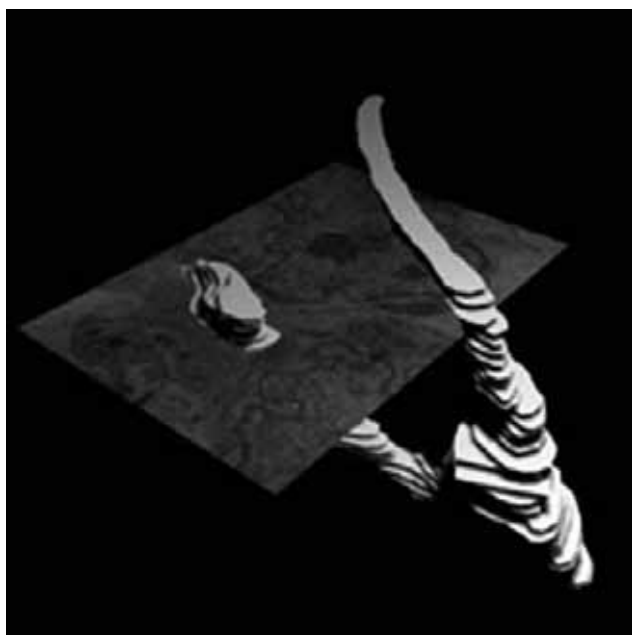


*Figure 1: 3D reconstruction of axonal branch, superimposed onto corresponding electron micrograph.*

also aided in the identification of section orientation.

An axon from 45 sections—previously prepared, imaged, and montaged—was reconstructed for proof-of-concept. Figure 1 shows the 3D axon reconstruction superimposed onto one of the 2D electron micrographs from which it originated. Additional reconstruction is possible and intended with the other structures found within this stack of data.

We also began work on the P5 sample. After prominent axon bundles were found on survey sections, we prepared ultra-thin sections from the P5 block and viewed them under the TEM. At present, at least one NMJ and many axon profiles have been found in both the optical and TEM images. The myelin sheath, which encapsulates the axon cross-section, makes a distinct boundary around the axon cross-section, which allows for easy identification. The presence of the sheath around most of the observed axons also indicates that we are imaging parts of the branch away from the NMJ. As we cut and image deeper into the sample, we should be able to witness some axons making synaptic contacts on muscular fibers. Figure 2 locates these notable regions on the P5 TEM image. Using these leads to specify our search, collection, and eventual 3D reconstruction will be the next endeavor.

#### **Future Work:**

In the immediate future we plan to fully reconstruct NMJs found in the P5 sample. Ultimately, the full 3D reconstruction of the NMJ ultrastructure will yield a great

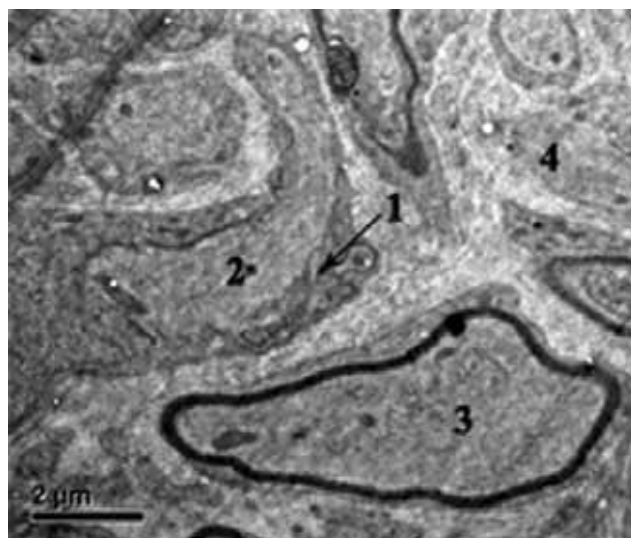


*Figure 2: 1. NMJ site at interface of light-gray axonal profile and distinctive pattern of muscular tissue; 2. cross-section of axon contacting muscle fiber; 3. profile of proximal axon, which is not yet contacting muscle fiber; 4. surrounding cellular and sub-cellular material, including the organelles of Schwann cells and capillaries.*

deal of anatomical information about this region prior to synaptic elimination. While we expect to see polyneuronal innervation at so early a post-natal stage, the detail of 3D reconstructions using electron micrographs will give us confirmation. In addition to improving the quality of collected data, the procedural solutions and experience with ultra-thin sections for serial TEM will eventually allow us to automate this useful, but labor-intensive process.

#### **Acknowledgments:**

Thank you to Prof. Jeff Lichtman and Dr. Richard Schalek for their expert guidance and enthusiasm throughout this summer. Thank you also to the Lichtman lab—particularly Kate Mahoney, Bobby Kasthuri, and Ju Lu—for their time, information, and help. This program would not have been possible without the Harvard CNS, NNIN, and NSF.

#### **References:**

- [1] Brown, M.C., Jansen, J.K., and Van Essen, D. (1976). Polyneuronal innervation of skeletal muscle in newborn rats and its elimination during maturation. *J. Physiol.* 261: 387-422.
- [2] Colman, H., Nabekura, J., and Lichtman, J.W. (1997). Alterations in synaptic strength preceding axon withdrawal. *Science* 275: 356-361.
- [3] Bishop, D.L., Misgeld, T., Walsh, M.K., Gan, W.-B., and Lichtman, J.W. (2004). Axon Branch Removal at Developing Synapses by Axosome Shedding. *Neuron* 44: 651-661.
- [4] Fiala, J.C. (2005). Reconstruct: a free editor for serial section microscopy. *J. Microscopy* 218: 52-61.

# Patterning Proteins on Glass and Silicon Substrates

**Brandon Walker, Department of Chemistry, Grambling State University**  
**NNIN REU Site: Cornell NanoScale Science and Technology Facility, Cornell University**

*NNIN REU Principal Investigator: Mandy Esch, Ph.D., Cornell NanoScale Facility, Cornell University*

*NNIN REU Mentor: Ebenezer Amponsah, Electrical & Computer Engineering, Cornell University*

*Contact: brandonwalker318@yahoo.com, esch@cnf.cornell.edu*

## Abstract:

We have developed two bio-assays in which molecular analytes (streptavidin and anti rabbit IgG) are detected upon binding to patterns of BSA-biotin and rabbit IgG on a glass substrate. The protein pattern was created by microcontact printing with PDMS stamps. We further aimed to develop a microcontact printing process that would enable us to pattern both BSA-biotin and rabbit IgG in an aligned fashion. The success of the aligned microcontact printing process was examined by performing the binding assays with quantum dot conjugates of streptavidin and anti rabbit IgG. Qualitative data analysis was performed by means of optical and fluorescence microscopy.

The experiments showed that both proteins could be patterned and that both binding assays were successful when performed on separate substrates. However, when trying to create bi-arrays on a single substrate, the protein printed first was lifted off in the second printing step.

## Introduction:

Microcontact printing has been used by researchers to pattern proteins on silicon and glass substrates. Printed protein patterns are utilized in applications such as biosensors and guided cell growth [1]. In this study we worked towards developing a protocol that would enable us to pattern multiple proteins in an aligned fashion. Multiple aligned protein patterns on the micrometer scale would enhance biosensors by allowing them to test for multiple analytes in one test. Projects that aim at guided growth of cells would also benefit from patterning multiple extracellular matrix proteins on the same substrate.

To achieve alignment of biotin and rabbit IgG we used alignment marks on the substrate as well as on the two PDMS stamps. During microcontact printing we aligned the first stamp with alignment marks on the substrate. The same marks were used to align the second stamp, which was designed with pattern geometries different from the first stamp. The success

of the aligned microcontact printing was tested by conducting two binding assays with FITC or quantum dot conjugates of streptavidin and anti rabbit IgG. The use of quantum dot conjugates together with appropriate filters allowed us to visualize both types of bound molecules at the same time [2].

## Experimental Procedure

### PDMS Stamps:

We first fabricated the desired patterns on two silicon wafers using contact photolithography and deep reactive ion etching. The two components of PDMS (Sylgard 184, Dow Corning Inc.) were mixed in a ratio of 10:1 by volume and were then cast on the surface of the two wafers. After heating to 60°C for one hour, the PDMS was removed from the wafers. The substrates were prepared via a lift off process with two alignment marks in gold.

### Microcontact Printing of Proteins:

We coated the PDMS stamps with solutions of BSA-biotin or purified rabbit IgG (1 mg/mL in phosphate buffer, pH 7.0) and let them sit to dry at room

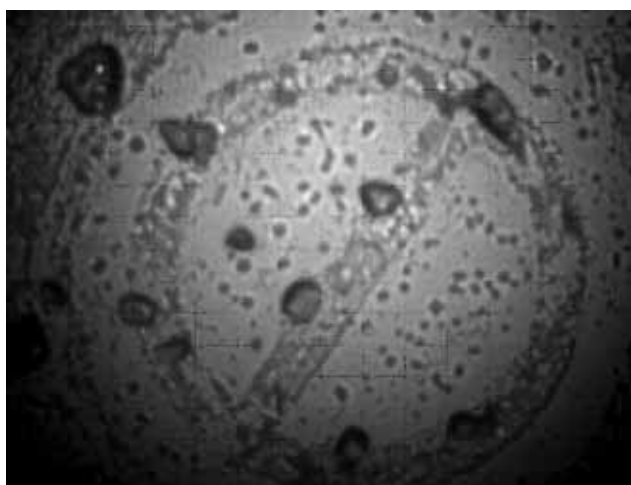


Figure 1: Biotin BSA/ Streptavidin quantum dots patterned on a silicon wafer.



temperature. The stamps were aligned to the marks on the substrate and pressed against the surface. After printing BSA-biotin, rabbit IgG was printed as well on the same substrate.

### Bio-Assay:

The surface of the wafer was blocked with a 6% (w/v) BSA solution for 15 minutes. It was washed with phosphate buffer (pH 7.0) and subsequently anti rabbit quantum dot conjugates (maple red, Antibodies Inc.) were incubated on the surface for 15 minutes. The surface was then washed with phosphate buffer containing 0.40% tween for 5 minutes followed by a final rinse with PBS buffer. The same procedure was followed using streptavidin quantum dot conjugates (lake placid blue, Antibodies Inc.). The wafers were the examined with a fluorescence microscope.

### Results and Discussion:

On silicon or quartz wafers, the biotin/streptavidin assay produced a distinct fluorescent pattern according to the pattern printed by microcontact printing (see Figure 1). We obtained the same result for the second assay with rabbit IgG/anti rabbit IgG (see Figure 2). These results confirm that the microcontact printing does not affect, in a significant way, the binding capabilities of the proteins printed. For both assays the conditions were sufficiently stringent to produce little unspecific binding of the analyte to the substrate. However, when we performed aligned microcontact printing and the two assays combined, we did not achieve a product of two-colored patterns. One reason for this result may be that the first protein was lifted off from the substrate when the second protein was printed.

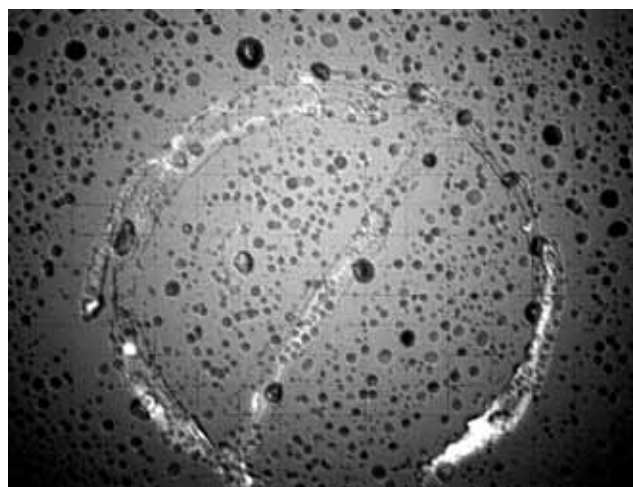


*Figure 2: Rabbit IgG / goat anti-rabbit IgG quantum dots patterned on a silicon wafer.*

When combining the two assays we also observed an increase in non-specific binding. This may be due to residues left on the wafer from the PDMS stamp.

### Conclusion:

In conclusion we found that both microcontact printing procedures and assay protocols worked when performed separate from each other. Though able to produce a single array the method was ineffective in producing a bi-array. Future work needs to be done to examine whether protein is lifted off from the substrate during the second printing process.

### Acknowledgements:

NSF, NNIN, and Cornell NanoScale Facility and staff. Special thanks to the Intel Foundation for funding this project.

### References:

- [1] R.S. Kane, S. Takayama, E. Ostuni, D.E. Ingber, and G.M. Whiteside. Patterning proteins and cells using Soft-lithography. *Biomaterials* 20 (1999) 2363-2376.
- [2] G. McDonald, J. Naydeau, K. Nealson, M. Storrie-Lombardi, and R. Bhartia. Fluorescent Quantum dots for Biological Labeling. *NASA Tech Briefs*. October 2003. Vol. 27, No. 10.

# Fabrication and Electrical Analysis of Metal Bilayer Electrodes for Nanodevices

**Heidi Wheelwright, Physics, Utah Valley State College**  
**NNIN REU Site: Stanford Nanofabrication Facility, Stanford University**

*NNIN REU Principal Investigator: Yoshio Nishi, Electrical Engineering, Stanford University*  
*NNIN REU Mentor: Ching-Huang Lu, Materials Science and Engineering, Stanford University*  
*Contact: hjw@cc.usu.edu, nishiy@stanford.edu*

## Abstract:

In this study we investigated how the work function of a W/Ti bilayer metal gate depends on the Ti thickness. The work function for each metal gate was determined by measuring the capacitance-voltage (C-V) characteristics of our metal oxide semiconductor (MOS) capacitors. We compared the work function behavior of the as-deposited and annealed samples. For the as-deposited samples, with 4.7Å (2 monolayers) of Ti and thinner, the Ti is electrically transparent. After the 400°C FGA, up to 8Å of Ti is electrically transparent and doesn't affect the work function. Islanding and diffusion have been proposed to explain this behavior.

## Introduction:

In order to continue the scaling of integrated circuits (ICs), new materials need to be introduced. Metal gates are needed in complementary metal oxide semiconductor (CMOS) technology to reduce the resistivity, depletion effects, and dopant penetration of polysilicon gates. Metal bilayer gates have been proposed to provide adjustable work functions [1]. The ability to control the work function will help optimize device performance. Previous work demonstrated how changing the bottom metal thickness could modify the work function [1,2]. However, the mechanism for this is not clear. In this paper we report on the work function behavior of a W/Ti bilayer metal gate for 12Å of Ti and thinner.

## Experimental Procedure:

We prepared bilayer metal gates of W/Ti on a SiO<sub>2</sub> dielectric. The thickness of Ti was varied from 0.25-3.5 monolayers, and the Ti was capped with 500Å of W. On some of the samples, the metal was deposited using e-beam evaporation, and on other samples by the sputtering method. The MOS capacitors were then fabricated using standard processing techniques. Characterization and electrical analysis were performed on these MOS capacitors. This paper will focus on the electrical analysis.

To investigate the electrical properties of these

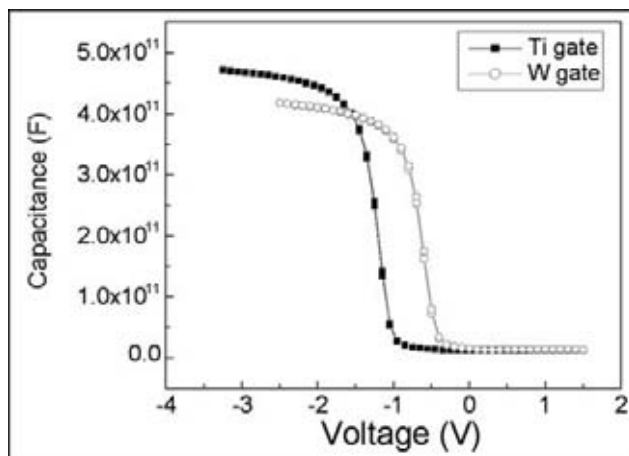


Figure 1: C-V curves of Ti and W showing a shift for different work functions.

capacitors, capacitance-voltage (C-V) measurements were performed. The C-V curves for Ti and W are shown in Figure 1. Because of the difference in the work functions, the two curves are shifted with respect to each other and thus have different flat band voltages ( $V_{fb}$ ). There is a linear relationship between the  $V_{fb}$  and the thickness of the oxide that allows for the work function of each metal gate to be calculated. For this

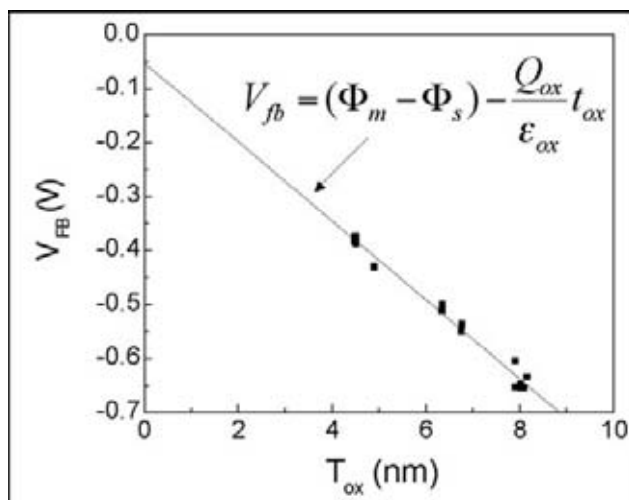


Figure 2:  $V_{fb}$  vs.  $T_{ox}$ , showing a linear relationship.

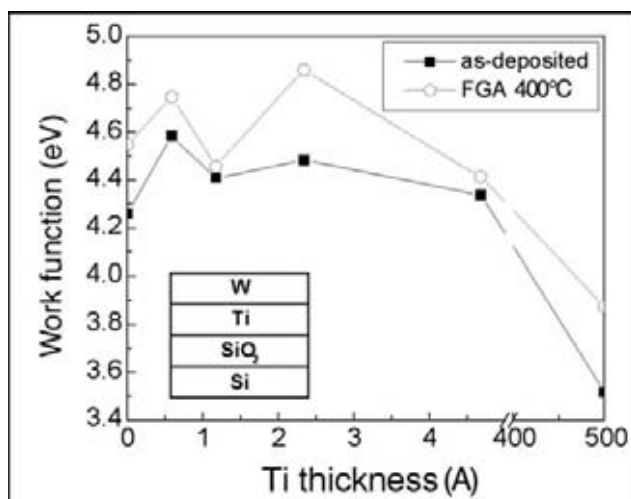


Figure 3: Work function vs. Ti thickness results from sputtered deposition samples.

reason we used four different thicknesses of oxide, 4-10 nm, for each thickness of Ti. The  $V_{fb}$  for each oxide thickness was determined using the NCSU C-V program [3]. Figure 2 shows this linear relationship and the equation that allows for the work function ( $\Phi_m$ ) to be extracted from these characteristics. Using this procedure, the work function of each metal gate was determined. A 400°C forming gas anneal (FGA) was further performed on these samples for 30 min.

### Results and Discussion:

Figure 3 presents the results for the sputtered method of metal deposition for the W/Ti/SiO<sub>2</sub> bilayer metal gate showing the relationship between the work function and the Ti thickness. The as-deposited results are compared with the results after the FGA. Before the FGA, the work functions of the thin layers of Ti are close to the work functions of W. Metal islanding has been proposed by Hung et. Al. [1] to explain this behavior. The Ti could be forming islands on the surface, in which case, some of the W is touching down onto the SiO<sub>2</sub> interface. For Ti thicknesses of 4.7Å or less, the Ti doesn't cover enough surface area to cause any change in the work function. The results after the FGA are similar.

The results for the evaporated method of metal deposition are shown in Figure 4. Ti thicknesses of 12Å and below show the dependence of the work function on the Ti thickness. Again, the as-deposited and FGA samples are compared. Notice the results from the Ti thickness of 8Å. For the as-deposited sample, the work function is in between Ti and W. After the FGA, the work function is close to W. One possible theory to explain this behavior is that the W could be diffusing

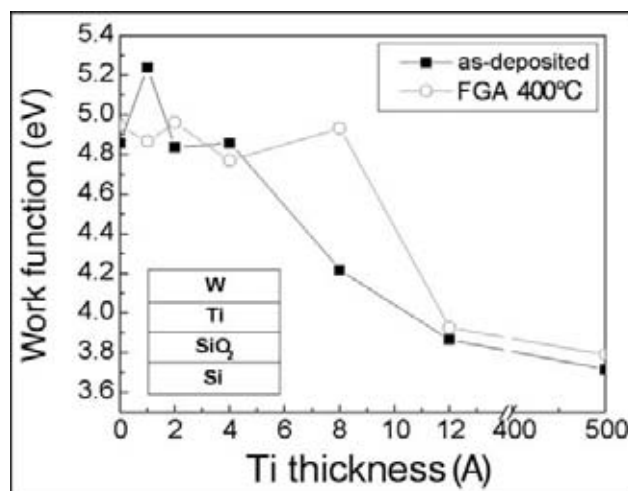


Figure 4: Work function vs. Ti thickness results from evaporated deposition samples.

down through the Ti toward the SiO<sub>2</sub> interface during the annealing process, changing the work function to W.

### Conclusions and Future Work:

Theoretically, 1 or 2 monolayers of bottom metal thickness is enough to completely determine the work function based on *ab initio* simulations [4]. In this experiment we found that 3 or 4 monolayers are needed to change the work function from one metal to the other. Metal islanding could be the cause of this observation for the as-deposited samples, and diffusion for the annealed evaporated samples. To continue researching the work function behavior of bilayer metal gates, different metal combinations will be investigated to provide more information to what determines the work function. From this, we expect to learn how to control and tune the work function of the gate.

### Acknowledgements:

I would like to thank Prof. Yoshio Nishi, Ching-Huang Lu, Dr. Michael Deal, Gloria Wong, Que-Anh Nguyen, Prof. Bruce Clemens, and Dr. Chih-Sheng Chang for their help and assistance with this research project. I would also like to thank the NNIN, CIS, and NSF for their support.

### References:

- [1] S. C.H. Hung, J. Hoyt, J. Gibbons, C.-H. Lu, M. Deal, and Y. Nishi, 2003 Semiconductor Interface Specialists Conference.
- [2] CH Lu, GMT Wong, MD Deal, W Tsai, P Majhi, CO Chui, MR Visokay, JJ Chambers, L Colombo, BM Clemens, and Y Nishi, IEEE Electron Device Lett., vol 26, pp. 445-448, July 2005.
- [3] J.R. Hauser and K. Ahmed, Proc. AIP Conf., pp. 235-239, 1998.
- [4] S. Park, L. Colombo, K. Cho, and Y. Nishi, Appl. Phys. Lett., vol. 86, no. 7, p. 073118, Feb. 2005.

# Production and Analysis of Conjugate Polymer/ZnO Solar Cells

**Michael White, Chemistry Major, Saint Michael's College**  
**NNIN REU Site: NanoTech User Facility, University of Washington**

*NNIN REU Principal Investigator: Daniel Gamelin, Department of Chemistry, University of Washington*  
*NNIN REU Mentor: William Liu, Department of Chemistry, University of Washington*  
*Contact: mwhite3@smcvt.edu, gamelin@chem.washington.edu*

## Abstract:

The goal of this research is to fabricate a low cost and efficient solid state solar cell by coupling zinc oxide (ZnO) nanorods with a conjugated polymer of regio-regular poly(3-hexylthiophene) (P3HT). ZnO structures were grown onto FTO/*nc*-ZnO substrates through either hydrothermal solution phase or by electrodeposition and resulted in different morphologies depending on the growth parameters.

## Introduction:

Conventional solar cells provide cheap and clean energy that can help reduce the world's dependence on oil. Currently, silicon solar cells have the highest solar energy conversion efficiency of around 24%, however, the efficiency is offset by the high cost of production [1]. Dye-sensitized solar cells have been explored as possible substitutions for conventional silicon cells [2], but they suffer from possible dye agglomeration [3] or electrolyte leakage. To overcome the limitations of dye-sensitized solar cells, conjugate polymers coupled to semiconductors to form 'solid state' cells are actively being explored [4].

In these solid-state heterojunction conjugated polymer/inorganic semiconductor solar cells, photoexcitation of the conjugated polymers leads to generation of a bound electron-hole pair or exciton. The exciton can be separated into free charge carriers by transferring the electron to the inorganic semiconductor. One semiconductor often used is ZnO because it is environmentally friendly, stable indefinitely, and can be synthesized easily and inexpensively into different shapes and sizes using various methods [5]. The use of ZnO nanorods anchored to the transparent conducting substrate will not only provide a direct path for electrical transport to the back contact, but also increase the polymer/ZnO interfacial area, both parameters that should improve overall cell performance.

## Fabrication:

A layer of colloidal nanocrystalline ZnO (*nc*-ZnO) was spin-coated onto a cleaned fluorine doped tin oxide

(FTO)-covered glass substrate and annealed at 400°C for 30 minutes. ZnO nanorods were grown on the FTO/*nc*-ZnO layer using two different adapted methods.

The first method was by a solution phase hydrothermal process [5]. The FTO/*nc*-ZnO substrate was submerged in an equimolar 25 mM aqueous solution of  $\text{Zn}(\text{NO}_3)_2$  and hexamethylene tetraamine and heated at 90°C for several hours.

The second method was by electrodeposition under galvanostatic control [6] in an  $\text{O}_2$  saturated 25 mM  $\text{ZnCl}_2$  and 25 mM KCl aqueous solution at 65°C using a current range of 0.4-0.8 mA.

After either synthesis method, the FTO/*nc*-ZnO/ZnO(nanorods) substrates were thoroughly rinsed with distilled water and annealed at 400°C for 30 minutes. P3HT was spin-coated onto the FTO/*nc*-ZnO/ZnO(nanorods) and heated for 1 hour at 100°C. Subsequently, PEDOT:PSS was spin-coated on top of the P3HT layer.

Finally, a gold layer was deposited onto the PEDOT:PSS by thermal evaporation in vacuum to form an ohmic contact. Illumination of the cell was performed using a (200 W) mercury xenon lamp coupled to a monochromator. Film morphology was examined by scanning electron microscopy (SEM) (FEI Sirion XL30). Electronic absorption spectra were collected using a Cary 5E spectrophotometer (Varian).

## Results:

The absorption spectrum, Figure 1, of the ZnO grown by the solution phase hydrothermal method shows the

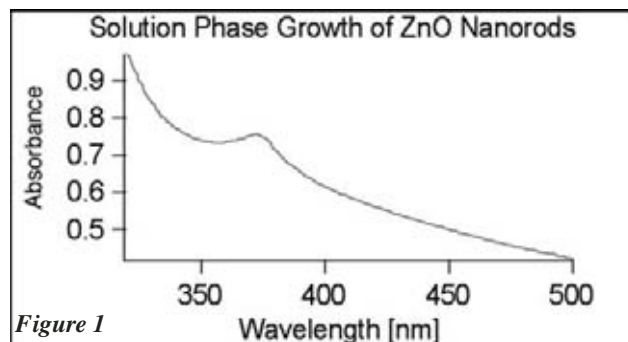
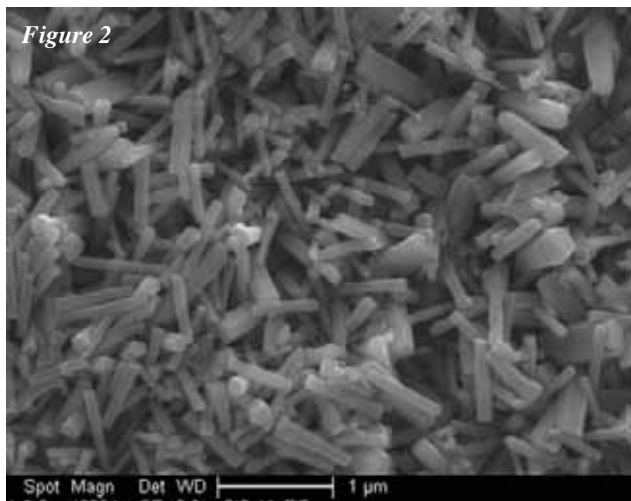


Figure 1

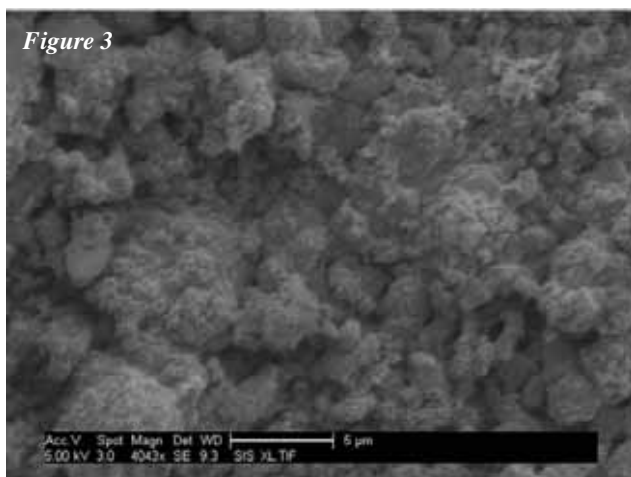


Figure 2



ZnO band gap transition at 375 nm (3.3 eV), which is in agreement with bulk ZnO [7]. The absorption spectrum shows a broad tail due to light scattering from the opaque ZnO film. The SEM, Figure 2, of the same film shows that the ZnO grown are in the shape of rods; however, the rods do not show well-oriented growth or attachment to the FTO/*nc*-ZnO substrate and therefore may not provide a good electrical pathway for the photogenerated electron to travel to the FTO back contact. The SEM of the electrodeposited ZnO layer, Figure 3, does not show any rod structures but rather a porous film network. Although ZnO rods are absent, this type of morphology does provide a greater surface-area-to-volume than a flat solid film and may offer the same advantages as the rods. Unfortunately, under illumination all the solar cells that were built exhibited a short-circuit behavior and so no cell efficiency data could be collected.

Figure 3



### Summary and Future Work:

ZnO was grown onto FTO/*nc*-ZnO substrates through either hydrothermal solution phase or by electrodeposition, resulting in different morphologies. Preliminary results for the fully assembled solar cell indicated a possible short in the cell. A possible source of this short could be the P3HT penetrating the ZnO layer and contacting the FTO. Further investigation is needed to identify and correct the short circuit. Once properly functioning cells have been fabricated, the influence on cell efficiency from different film morphology can be determined.

### Acknowledgements:

I would like to thank the University of Washington and NNIN for making this summer possible. I would also like to extend a sincere thank you to the Gamelin Lab for all of their help and encouragement.

### References:

- [1] Photoelectrochemical Cells. M. Grätzel. *Nature* 2001, 414, 338.
- [2] Photosensitization of Nanocrystalline ZnO Films by Bis(2,2'-bipyridine)(2,2'-bipyridyl-4,4'-dicarboxylic acid)ruthenium(II). I. Bedja, P.V. Kamat, X. Hua, A.G. Lappin, and S. Hotchandani. *Langmuir* 1997, 13, 2398-2403.
- [3] Studies of the Absorption Process of Ru Complexes in Nanoporous ZnO Electrodes. K. Keis, J. Lindgren, S.-E. Lindquist, and A. Hagfeldt. *Langmuir* 2000, 16, 4688-4694.
- [4] Hybrid Zinc Oxide Conjugated Polymer Bulk Heterojunction Solar Cells. W.J.E. Beek, M.M. Wienk, M. Kemerink, X. Yang, and R.A.J. Janssen. *J. Phys. Chem. B* 2005, 109, 9505-9516.
- [5] Growth of Arrayed Nanorods & Nanowires of ZnO from Aqueous Solutions. L. Vassieres. *Adv. Mater.* 2003, 15, 464-466.
- [6] Optical properties of nanocolumnar ZnO crystals. B. Mari, M. Mollar, A. Mechakour, B. Hartiti, M. Perales, and J. Cembrero. *Microelectron J.* 2004, 35, 79-82.
- [7] On the optical band gap of zinc oxide. V. Srikant and D.R. Clarke. *J. Appl. Phys.* 1998, 83, 5447-5451.

# Characterization of Semipolar, and N-Face Group III Nitrides

**Jason Winders, Electrical Engineering, Penn State University**  
**NNIN REU Site: Nanotech, University of California at Santa Barbara**

*NNIN REU Principal Investigator: Umesh K. Mishra, Electrical & Computer Engineering, UC Santa Barbara*

*NNIN REU Mentor: Arpan Chakraborty, Electrical & Computer Engineering, UC Santa Barbara*

*Contact: jcw215@psu.edu, mishra@ece.ucsb.edu*

## Abstract:

Gallium nitride (GaN) is a wide, direct band gap material used for optoelectronic and electronic devices. Conventional GaN-based structures used in these devices are grown along the Ga-face or polar c-axis. This results in the presence of piezoelectric and spontaneous polarization in the quantum wells. This polarization and subsequent separation of electron and hole wave-functions in the quantum wells reduces the overall performance of conventional optoelectronic devices such as light emitting diodes (LEDs) and lasers. Performance can potentially be improved by growing GaN-based quantum wells along the semi-polar direction. These quantum wells are almost free from the polarization effects, and thereby promise increased efficiency and performance of these devices. In addition to growing along the semipolar direction, devices are also grown with a nitrogen-face or N-face GaN. These devices still are polarized, but the polarization is the opposite that of c-plane GaN. When fabricating these devices, it is extremely important to have high quality films. Defects in the crystalline structure limit device performance.

There are two main methods used for characterizing these films; x-ray diffraction and atomic force microscopy (AFM). X-ray diffraction is used to analyze the crystallographic structure and the composition of the films. AFM takes nanoscale topographical images of the films. This can be used to find sub-micron defects and surface roughness in the film. Once the film quality and composition are characterized, devices are fabricated, and electrically and optically characterized. These characterizations help optimize the properties of the semipolar and N-face GaN-based films, which provides better fabrication of devices. Currently the film quality has a large amount of defects. There is a high surface roughness, which inhibits device fabrication.

## Introduction:

There is a growing demand for higher power LEDs. When compared to conventional lights, LEDs use less power, are compact, generate less heat, and have long lifetimes. LEDs in the blue to deep UV range have many applications. These have a potential to increase

the storage density of optical storage devices, aid in water purification, detect and decontaminate biological agents, and provide efficient sources of light. Semipolar devices show great promise to fill the demand for devices for these applications. In order to fabricate devices, the growth of the film must be optimized to achieve a quality comparable to c-plane GaN based films.

## Procedure:

The nitride films in this work are grown by metal-organic chemical vapor deposition (MOCVD). Multiple quantum well structures are formed by growing alternating layers of indium gallium nitride (InGaN) and GaN to form the active region of the LEDs. After

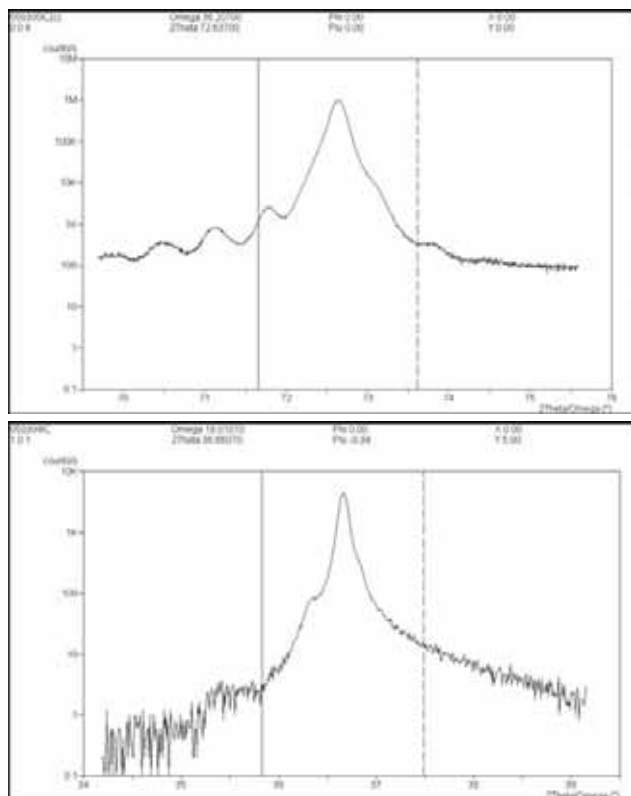


Figure 1, above: XRD of polar c-plane InGaN.

Figure 2, below: XRD of semipolar InGaN.

the growth of these films, they are characterized using x-ray diffraction (XRD) and atomic force microscopy (AFM). XRD is used to analyze the crystallographic structure of the film including composition, and stress. AFM takes a topographical image of the surface that can be used to find surface roughness and defects such as pits. If a surface is rougher than the thickness of the quantum structures that are grown, it is a good sign that the structures are not formed into coalescent layers.

### Results And Conclusion:

The XRD data (Figure 1, 2) shows differences between polar c-plane InGaN-based quantum structures and semipolar InGaN-based quantum structures respectively. In the polar c-plane sample, the central peak is the GaN peak. The additional peaks located to the left of this GaN peak are the superlattice peaks due to the interference between the GaN and InGaN layers.

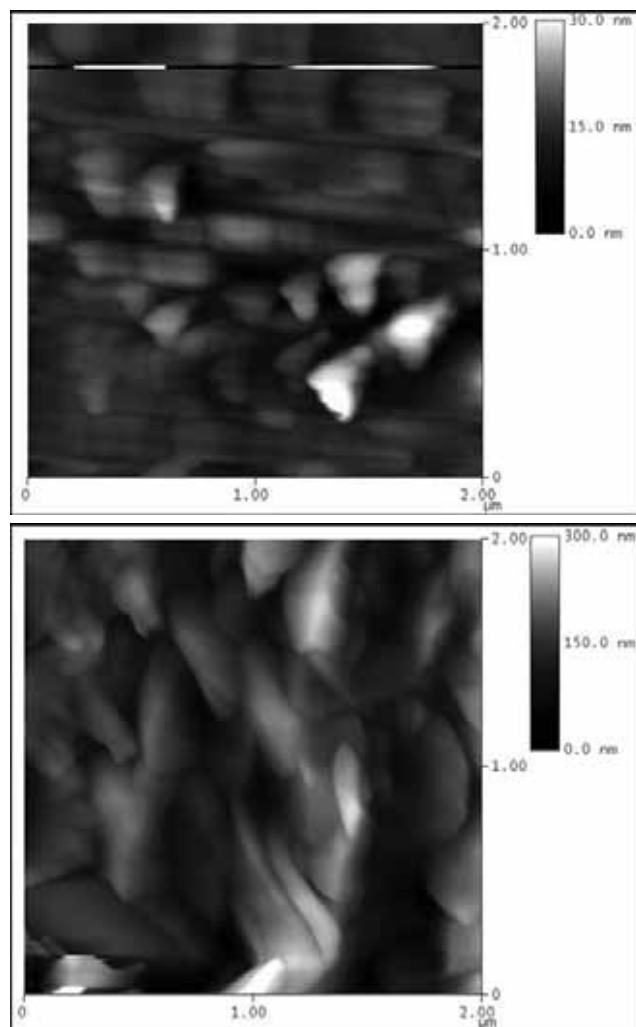


Figure 3, above: 2  $\mu$ m AFM image of semipolar GaN.

Figure 4, below: 2  $\mu$ m AFM image of n-face GaN.

These represent the presence of multiple coherent InGaN layers in the film. Taking the peak locations on the  $2\theta$  axis, with the growth time for the barrier and well, the indium concentration and barrier and well thicknesses can be computed. The semipolar sample has the main GaN peak, but it is lacking the InGaN superlattice peaks. The only sign of the indium in the film is the small shoulder on the left side of the GaN peak. This shows that there is indium in the film, but due to defects in the film, such as disorder, the quantum structures are not coherently formed. They should be in quantum layers.

The AFM images (Figures 3, 4) show the surface morphology of semipolar GaN and N-face GaN respectively. The semipolar GaN has a rough surface with a RMS roughness of about 10 nm. The N-face GaN has a surface roughness of about 45 nm. Also when larger scans were completed of the surface, large hexagonal features were found. These were compared to conventional c-plane GaN which have an RMS roughness of less than 0.2 nm. This level of roughness was unacceptable. The quantum wells, which were the foundation of the operation of these devices, were in the range of 2 nm thick.

When comparing these films, it is apparent that MOCVD growth of semipolar and N-face GaN-based films is still in its infancy. The semipolar XRD shows a lack of superlattice peaks. The AFM data shows a rough surface, which proves that the film is not growing uniformly. This agrees with the XRD data, which shows the lack of quantum structures. There is some disorder that is affecting the quantum wells. They are not completely forming, and only forming in places. These defects in the film need to be resolved. The growth of GaN based films needs to be optimized before functional devices can be fabricated.

### Future Work:

Future work includes the optimization and characterization of the MOCVD growth of semipolar and N-face GaN based films. The film quality needs to be improved to achieve a comparable quality to polar c-plane GaN. Once the film quality is optimized, Hall effect devices and LEDs will be fabricated and characterized. This research is continuing to develop quality films.

### Acknowledgements:

The author wishes to thank Prof. Umesh K. Mishra, Arpan Chakraborty, SSLDC, UCSB, NNIN and NSF.

# Gray-Scale Electron-Beam Lithography

**Yin Ian Yang, Electrical Engineering, University of Virginia**

**NNIN REU Site: Microelectronics Research Center, Georgia Institute of Technology**

*NNIN REU Principal Investigator: Dr. Kevin Martin,*

*Microelectronics Research Center, Georgia Institute of Technology*

*NNIN REU Mentor: Dr. Raghunath Murali, Microelectronics Research Center, Georgia Tech*

*Contact: kevin.martin@mirc.gatech.edu, yy2c@virginia.edu*

## Abstract:

Gray-scale lithography is the patterning of 3-D surface topographies. Its relevance is a result of a demand for applications in optics and micro/nano-electromechanical systems (M/NEMS). In optics, various geometries for gratings or lenses require a gradient or sloped profile. In M/NEMS, 3-D structures allow for flexibility in mechanical motion.

Our goal, through the JEOL JBX-9300FS e-beam lithography (EBL) system, is to produce a blazed grating. The characteristic of such a grating is high sensitivity to a peak wavelength of light upon incident polychromatic light. Our specifications require a blazed angle of  $1.1^\circ$ , groove period of  $11\text{ }\mu\text{m}$ , and a depth of  $220\text{ nm}$ . With these specifications, the device will be used in a spectrometer in the very-near infrared (VNIR) range [1].

## Introduction:

The key notion behind gray-scale lithography is having control over the incident energy. Varying this energy across the resist produces differential solubility rates and, therefore, differences in resist depth. In EBL, incident energy is indicated by dose (charge per unit area). The EBL system features a serial, direct-write beam that pixilates the pattern; the entire pattern is exposed one pixel at a time. This allows for direct control over the dose applied to each pixel, a concept known as *shot modulation*.

Limitations of EBL arise out of electron scattering within the resist (forward scattering) and substrate (backscattering) layers. The deposited energy profile is approximated by the point spread function [2]:

$$f(r) = \frac{1}{1+\eta} \left( \frac{1}{\pi\alpha^2} \exp\left(-\frac{r^2}{\alpha^2}\right) + \frac{\eta}{\pi\beta^2} \exp\left(-\frac{r^2}{\beta^2}\right) \right)$$

Equation 1: Beam energy profile, termed proximity function in context of EBL.

Here,  $r$  is the radial distance from the point of beam incidence,  $\alpha$  is the forward scattering parameter (typically small),  $\beta$  is the backscattering parameter (typically large), and  $\eta$  is the ratio of total backscattered

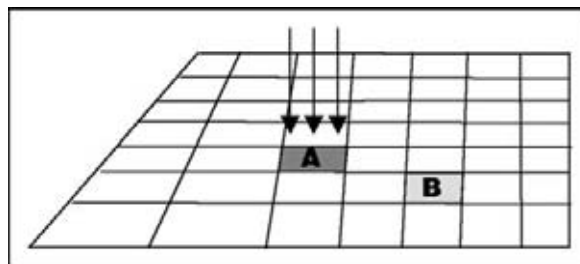


Figure 1: Exposure at pixel A affects pixel B, illustrating proximity effect.

to forward scattered electron energies. This energy spread leads to *proximity effects*: the incident pixel is underexposed while the remaining energy is distributed to surrounding pixels (Figure 1). Proximity effect correction is utilized to counteract these effects.

## Experimental Procedure:

To design the gratings, we took a single groove and divided its entire area into many, very thin rectangles. Along individual rectangles, dose was kept constant, while from rectangle to rectangle dose was varied (Figure 2). Essentially, we approximated each slope by a staircase pattern. The distance between pixels was denoted the shot pitch.

PMMA was the preferred resist because it exhibits low contrast. We obtained the contrast curve for  $220\text{ nm}$

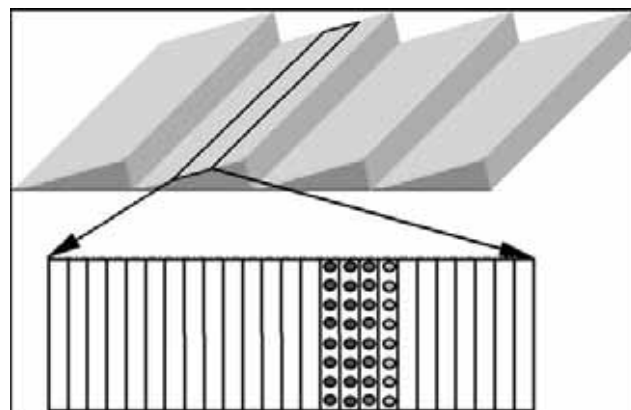


Figure 2: CAD file preparation.



thick PMMA resist on silicon, and map doses to our grating profile. The proximity correction algorithm determined the resultant physical profile from this dose profile. To achieve the desired profile, the algorithm adjusted doses accordingly. Optimization of the algorithm was accomplished by fine-tuning the three proximity function parameters. We held  $\alpha$  and  $\beta$  constant and varied  $\eta$ . After exposure, PMMA was developed by a 1:1 solution of MIBK:IPA; characterization was performed using an atomic force microscope (AFM).

Initially, each groove was fabricated by a 100-step staircase pattern without proximity correction. This caused a groove at the edge to be underexposed in comparison to a groove in the middle. This was consistent with the proximity model because proximity effects are lower for a groove at the edge. This non-uniformity ultimately required us to utilize proximity correction.

### Results and Conclusions:

The first few iterations with proximity correction produced overexposed grooves. We achieved the desired profile by settling on a negative  $\eta$ , but this was unphysical and led to even greater uniformity problems. We identified the fault as an oversight in our method for obtaining data for our contrast curve. This curve assumes an ideal energy distribution. If pixel A were to receive a dose of X, the measured depth corresponding to a dose of X should be measured at a location where exactly that amount of dose is applied. We cannot obtain this ideality but reproduce the situation by exposing a sufficiently large region (box) to include the full effects of backscattered electrons. Now, depth is measured at the center of the box rather than at the edge.

With a new contrast curve, we settled on a positive  $\eta$ . However, we also discovered that beam fluctuations affect exposure: a larger beam current leads to underexposure (all proximity effect parameters

constant). The beam diameter and, as a result,  $\alpha$ , is directly linked to beam current. Thus proximity correction is sensitive to beam fluctuations. The final iteration (Figure 3) used a 40 nm shot pitch, 1.3 nA current, and an  $\eta$  of 0.2. The grooves had a depth of 210 nm.

Preliminary roughness measurements were taken. Roughness was found to increase with increasing groove depth and increasing shot pitch. The best and worst case numbers were about 3 nm and 9 nm, respectively. As for pattern uniformity, there was a 15% difference between the middle and edge grooves when proximity correction was used; this is a drastic improvement over the 60% error in the uncorrected design. These characterizations reveal the importance of proximity correction.

### Future Work:

For a given beam condition, there was good control over the design and the final profile could be predicted well by the proximity correction models. Once the beam fluctuated, proximity effect parameters had to be extracted for the new beam conditions. Therefore, finding the optimal proximity effect parameters for different beam settings would be a valuable addition to the project.

### Acknowledgements:

I would like to thank my mentor Dr. Raghunath Murali for his support and guidance, my PI, Dr. Kevin Martin, our site coordinator Jennifer Tatham, Dr. James Meindl, NNIN and NSF for funding the research, the GSI group, and the clean room and administrative staff at MiRC.

### References:

- [1] J. Fisher, J. Antoniadis, "A Hyperspectral Imaging Sensor for the Coastal Environment", Naval Research Laboratory.
- [2] A. van de Kraats, N. Kikuchi, "Electron Scattering Effect in Electron Beam Lithography".

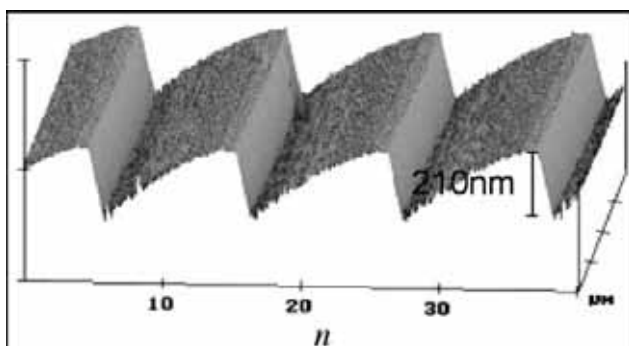


Figure 3: AFM image of final patter.

## Partially Self-Assembled Planar Photonic Structures

**Shelley Zieren, Chemical Engineering, University of Texas-Austin**

**NNIN REU Site: Cornell NanoScale Science and Technology Facility, Cornell University**

*NNIN REU Principal Investigator: Prof. Michal Lipson, Electrical and Computer Engineering, Cornell University*

*NNIN REU Mentor: Bradley Schmidt, Electrical and Computer Engineering, Cornell University*

*Contact: shelleyz@gmail.com, ml292@cornell.edu*

### Abstract:

Waveguides, which are planar photonic structures, use the principles of refractive index contrast to propagate light in a desired path. One of the major problems with current waveguides is optimizing the efficiency. Various sources for loss in waveguides exist, including sidewall roughness which results in scattering. The motivation behind this project is to improve the efficiency of waveguides by eliminating surface roughness, without implementing a complex process.

We fabricated new smooth waveguides by exploiting the surface tunability of a silicon wafer using patterned hydrophobic and hydrophilic regions. The hydrophilic region was a film of  $5.6\ \mu\text{m}$  of oxide, while the monolayer FOTS was used to make the hydrophobic area. Norland Optical Adhesive 71 ( $n = 1.56$ ) was used as the waveguide material. The adhesive, when applied in a very thin, uniform layer, selectively forms on the hydrophilic lines and dewets from the hydrophobic surroundings. The waveguides were found to have a lens-shaped cross-section with a ratio of 10:1 width to height by SEM. Observations using SEM and AFM showed these waveguides were indeed smoother than current technology. They were also coupled with an optical fiber and successfully guided light with a measurable output. Waveguides of various lengths were measured to calculate the loss vs. length. Loss results are still in progress.

### Introduction:

Nanophotonics research is becoming more significant in today's society of smaller and faster systems. Waveguides use index of refraction contrast to direct light down a desired path. Through direction of this light, information can also be transferred. These waveguides can be used in areas such as telecommunications, data transfer on silicon using chip-to-chip interconnects, and even in biology—using them to direct light on a micro-scale.

A problem with the current fabrication of these waveguides is scattering due to sidewall roughness. The current fabrication process involves lithography and etching, both of which add to sidewall roughness.

In order to alleviate this problem, an entirely new process was developed and tested. Our process involved patterning hydrophilic and hydrophobic regions on silicon in order to self-assemble ultra smooth waveguides.

### Experimental Procedure

#### Wafer Fabrication:

Oxide was deposited on a  $\langle 100 \rangle$  N-type silicon wafer using plasma enhanced chemical vapor deposition (PECVD) at a rate of  $457\ \text{nm/min}$  for 15 minutes. Oxide was used because we required a material that was less hydrophobic than FOTS and had a lower index of refraction than our waveguide material. PECVD was chosen over thermal oxide because thermally growing over  $5\ \mu\text{m}$  of oxide would have taken more than 12 hours in the furnace. Using an optical measurement system, thickness measurements were found to be  $6.5\ \mu\text{m} \pm 0.1\ \mu\text{m}$ . Shipley Photoresist 220-3 was then spun at 4000 rpm, ramp 1800 rpm/s for 60 seconds. The wafer was baked for 90 seconds at  $130^\circ\text{C}$ . A 5 inch square photomask was used that produced  $8.5\ \mu\text{m}$  lines with  $200\ \mu\text{m}$  spaces in between when exposed using a 5X i-line autostepper. An exposure time of 0.4 seconds with a focus offset of -7 was used and a step size of 2 cm. The postexposure bake was for 3 minutes also at  $130^\circ\text{C}$ .

The wafer was developed in MIF300 developer 60 seconds using an automated wafer developing tool. After development the wafer consisted of oxide where the exposed resist was developed away and  $8.5\ \mu\text{m}$  unexposed photoresist lines. Using a molecular vapor deposition tool (1, 1, 2, 2-Perfluorooctyl) trichlorosilane, FOTS (a hydrophobic monolayer) was deposited on the entire wafer.

To lift off the resist, the wafer was placed in acetone for 1-2 minutes followed by IPA for another minute, and then water to rinse the wafer. Dissolving the resist in acetone also released the FOTS on top of the resist, and therefore the resulting wafer had hydrophilic oxide lines with hydrophobic FOTS monolayer surrounding

them. The FOTS monolayer is not affected by the acetone, IPA, or water.

### Waveguide Fabrication:

10 microliters of Norland Optical Adhesive 71 (NOA71) ( $n=1.56$  cured) were dropped in the hydrophobic square surrounding the waveguides. The adhesive begins as a viscous liquid. This volume was then squished by a Teflon<sup>®</sup> piece to give an even, thin layer which allowed the adhesive to selectively stay on the hydrophilic waveguides and dewet from the hydrophilic surroundings back onto the larger hydrophilic region where it was dropped. This was repeated until it was verified under microscope that the lines were uniformly covered. The wafers were then cured for 10 minutes under UV lamp. After curing, the NOA 71 hardens into a solid.

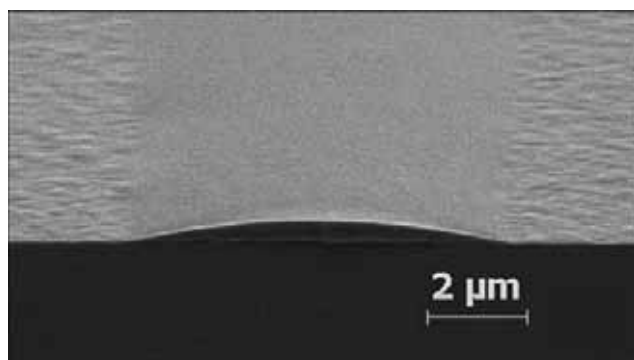


Figure 1: SEM image of profile 8.5  $\mu\text{m}$  waveguide.

### Results and Conclusions:

This new fabrication process did in fact produce ultra smooth waveguides using a self-assembled method. The waveguides produced displayed a 10:1 width to height ratio as shown by the scanning electron microscope in Figure 1. These waveguides were also smoother than current technology waveguides as

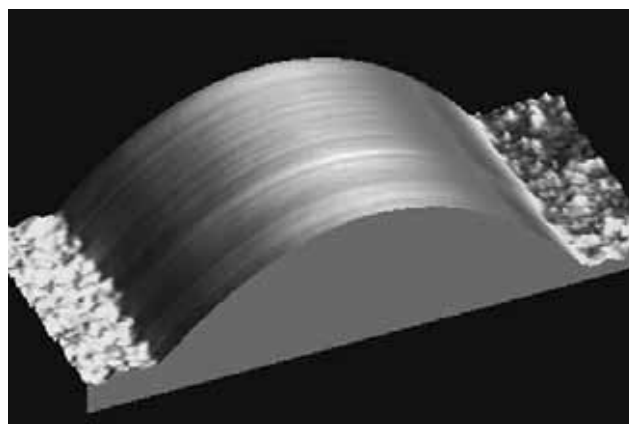


Figure 2: AFM image of smooth surface of 8.5  $\mu\text{m}$  waveguide.

shown by the AFM in Figure 2. Using the calculation software, the roughness of these structures was reported to be less than 1 nm, while current technology stands around 5-6 nm. Actual losses are being measured and we expect them to be less than current technology waveguide losses.

This project illustrated a way to decrease losses in waveguides using an entirely new approach to the problem. This new, simple fabrication process showed that there are other methods to making usable waveguides that could prove to be better than just optimizing the current fabrication method. Future work on this project will include applications to flexible substrates, greater control of the waveguide profile, and investigation of new materials.

### Acknowledgements:

I would like to thank Michal Lipson, Brad Schmidt, Sam Shrauth, CNF staff, NSF, NNIN, and the Cornell Nanophotonics Group.

### References:

- [1] Moench, W. and Zappe, H. Feb 2004. Journal of Optics: Pure and Applied Optics. Institute of Physics Publishing. 6 330-337.

**The 2005 National Nanotechnology Infrastructure Network  
Research Experience for Undergraduates Program  
Research Accomplishments**

## Index

### REU Reports by NNIN Site

Cornell University .....	6, 8, 16, 34, 46, 48, ..... 60, 64, 70, 88, 98, 104, 122, 126, 134, 150, 162
Georgia Tech .....	10, 30, 38, 56, 140, 160
Harvard University .....	80, 138, 146, 148
Howard University .....	12, 14, 100, 110, 124, 136
Pennsylvania State University .....	28, 44, 50, 54, ..... 58, 118, 144, 152
Stanford University .....	26, 52, 76, 82, ..... 84, 86, 92, 96, 120, 130, 142, 154
UC Santa Barbara .....	20, 22, 24, 72, ..... 78, 102, 108, 112, 128, 132, 158
University of Michigan .....	4, 18, 66, 94, 116
University of Minnesota .....	36, 42, 68
University of New Mexico .....	32, 74
University of Texas Austin .....	40, 62, 106
University of Washington .....	2, 90, 114, 156

• • •

### REU Reports by Last Name

(The NNIN REU Interns are in **Bold**)

#### A

Adyam, Venimadhav .....	44
Agah, Ali .....	96, 130
Amponsah, Ebenezer.....	150
Appel, Kimberley .....	94
Awadelkarim, Osama O. ....	28
Aziz, Michael J.....	80

#### B

Badaire, Stephane.....	6
Bai, Xiaogang.....	94
Bakir, Muhannad.....	38
Banerjee, Sanjay.....	62
Bansal, Tushar .....	18
Bleier, Alan.....	60
Bond, Judith .....	152
<b>Bovington, Jock .....</b>	<b>2</b>
<b>Brannan, Amber .....</b>	<b>4</b>
<b>Brettmann, Blair.....</b>	<b>6</b>
Brueck, Steve .....	74
<b>Burger, Caitlin .....</b>	<b>8</b>

#### C

Campbell, Steven .....	68
Cannon, Fred .....	50
<b>Carson, Ashley .....</b>	<b>10</b>
<b>Castillo, Richard A. ....</b>	<b>12</b>
Cha, Ho-Young.....	16
Chakraborty, Arpan .....	158
Chandrashekhar, M.V.S.....	98
Chen, Erli .....	138, 146
Chen, Mike .....	82
Cheng, Li-Jing (Larry) .....	66
<b>Chestnut II, Michael Donnell.....</b>	<b>14</b>
Chin, Richard .....	52
<b>Cho, Clara Ji-Hyun .....</b>	<b>16</b>
<b>Chu, Eric .....</b>	<b>18</b>
Clarke, David .....	128
<b>Cleary, Frank.....</b>	<b>20</b>



Cleland, Andrew .....	20
Clemens, Bruce .....	92
Corso, Christopher .....	140
<b>Cruz, Samantha C.</b> .....	<b>22</b>
<b>Cullinan, Michael</b> .....	<b>24</b>
Curtis, Wayne .....	144

## D

Dai, Hongjie .....	26
Dante, Mark .....	108
<b>Dao, Minh Phuc Nguyen</b> .....	<b>26</b>
Dauskardt, Reinhold H. ....	120
Demirel, Melik C. ....	152
Deng, Jiangdong .....	146
Desai, Amit .....	118
De Silva, Anuja .....	34
<b>Dinin, Aileen</b> .....	<b>28</b>
Dong, Jianchun .....	2
<b>Doyle, Laura</b> .....	<b>30</b>

## E

El-Sayed, Mostafa A. ....	56
Esch, Mandy .....	150
<b>Escudé, Nicole</b> .....	<b>32</b>
Eustis, Susie .....	56
<b>Ezeife, Nkemdilim</b> .....	<b>34</b>

## F

Felix, Nelson .....	34
Fidaleo, M. ....	36
<b>Figuroa, Johangel M.</b> .....	<b>36</b>
Flickinger, Michael C. ....	36

## G

Gachelet, Eliora .....	114
Gamelin, Daniel .....	156
<b>Gan, Wand</b> .....	<b>38</b>
Garcia, Andres .....	112
Garretson, Joshua .....	108

George, H. Bola .....	80
Goldman, Rachel S. ....	94
Gregori, Giuliano .....	128
Griffin, James .....	12, 124
Griffin, Peter .....	96, 130
Grundmann, Michael .....	102
Guillorn, Michael .....	46, 88
Guo, Lingjie (Jay) .....	66
<b>Gutierrez, Niusha E.</b> .....	<b>40</b>
Guyer, Eric P. ....	120

## H

Hahm, Jong-In .....	144
Hai-Ting, Andy .....	100
Haque, Amanul .....	118
<b>Harrington, Matthew</b> .....	<b>42</b>
Harris, Gary L. ....	12, 110, 124, 136
Harris, James .....	86
<b>Harris, Paul</b> .....	<b>44</b>
He, Ate .....	30
He, Maoqi .....	110
<b>Helton, James Thorpe</b> .....	<b>46</b>
<b>Heremans, Joseph</b> .....	<b>48</b>
Holmes, Jr., Archie L. ....	40
<b>Honsowetz, Nathan</b> .....	<b>50</b>
Horn, Mark .....	152
<b>Hsu, Derek Hsen Dai</b> .....	<b>52</b>
<b>Huda, Sabil</b> .....	<b>54</b>
<b>Hughey, Jacob</b> .....	<b>56</b>
Hunt, William D. ....	140
Hurst, Jeff .....	40

## I

Ilic, Rob .....	8
<b>Iwata, Jodi M.</b> .....	<b>58</b>

**J**

<b>Jackson, Jamie</b> .....	<b>60</b>
Jain, Puja .....	54
<b>James, Miktosha</b> .....	<b>62</b>
Jen, Alex .....	90
<b>Johnson, Joy</b> .....	<b>64</b>
Jones, Kimberly.....	14

**K**

Kaeding, John.....	132
Kelly, David .....	62
Kim, Seong Chan .....	42
Kleiman-Shwarscstein, Alan.....	22
Kline, Tim .....	58
<b>Koehn, Thaddeus</b> .....	<b>66</b>
Kohl, Paul.....	30
Korgel, Brian.....	106
Kramer, Edward J. ....	72
Krishna, Sanjay .....	32
<b>Kuehl, Arthur K.</b> .....	<b>68</b>
Kurdak, Cagliyan .....	94
Kwon, Unoh .....	142

**L**

Lal, Amit .....	48
<b>Lee, Amy</b> .....	<b>70</b>
<b>Lee, Cheng-Yuk</b> .....	<b>72</b>
Lee, Doh C. ....	106
Lee, Michael.....	144
Lee, Stephanie .....	70
Lewenstein, Bruce.....	104
Li, Qi .....	44
Lichtman, Jeff.....	148
Liddell, Chekesha.....	70
<b>Light, David</b> .....	<b>74</b>
Lipson, Michal .....	162
Liu, William .....	156
Lloyd, Matthew .....	60
Lu, Ching-Huang.....	154

Lueking, Angela .....	54
<b>Luhman, Wade</b> .....	<b>76</b>

**M**

MacDonald, Noel C.....	24
Maharbiz, Michel Martin .....	18
Martin, David .....	4
Martin, Kevin .....	10, 38, 160
Matthews, Jermey.....	14
<b>McDaniel, Aaron</b> .....	<b>78</b>
McFarland, Eric W. ....	22
<b>McGrath, Matthew R.</b> .....	<b>80</b>
<b>McIntosh, David</b> .....	<b>82</b>
McIntyre, Paul C. ....	82
<b>Meisburger, Steve</b> .....	<b>84</b>
<b>Melton, Andrew</b> .....	<b>86</b>
Mishra, Umesh K. ....	102, 158
Mitchell, James.....	100
<b>Montague, Joshua</b> .....	<b>88</b>
<b>Mooney, Victoria</b> .....	<b>90</b>
Murali, Raghunath.....	160

**N**

Nakamura, Shuji.....	132
Narayanan, Deepa .....	54
<b>Nguyen, Que Anh</b> .....	<b>92</b>
Nguyen, Thuc-Quyen.....	108, 112
<b>Niewiadomski, Luke</b> .....	<b>94</b>
Nishi, Yoshio .....	154
<b>Noderer, William</b> .....	<b>96</b>
<b>Noel, Brian</b> .....	<b>98</b>
<b>Noxon, Virginia</b> .....	<b>100</b>

**O**

Ober, Christopher .....	34
<b>Olson, Christopher</b> .....	<b>102</b>
Osterfeld, Sebastian.....	76

---

**P**

Parviz, Babak .....	2
<b>Paul, Priscilla .....</b>	<b>104</b>
Pease, Fabian .....	84
<b>Pelaez, Jose.....</b>	<b>106</b>
<b>Peng, Calvin .....</b>	<b>108</b>
<b>Peralta, Edgar A. ....</b>	<b>110</b>
Pickard, Dan .....	84
Pinelis, Mikhail .....	18
Pipe, Kevin P. ....	94
Plis, Elena.....	32
<b>Polosukhina, Alexandra .....</b>	<b>112</b>
Pourmand, Nader.....	76
<b>Przybyla, Laralynne.....</b>	<b>114</b>
Pui, David Y. H.....	42
<b>PunKay, Marc.....</b>	<b>116</b>
Pursel, Sean .....	152

**R**

Radhakrishnan, Shankar.....	48
Rao, Zhilong.....	86
Raub, Alex.....	74
Reason, Matt.....	94
Redding, Adam.....	50
<b>Reddy, Nakul .....</b>	<b>118</b>
<b>Rice, Emily .....</b>	<b>120</b>
Richardson-Burns, Sarah.....	4
<b>Ridling, Nathan .....</b>	<b>122</b>
<b>Rodríguez Dátil, Idaliz.....</b>	<b>124</b>
Rodriguez Gutierrez, Humberto .....	54
Rodwell, Mark.....	78
<b>Ruch, Sarah .....</b>	<b>126</b>

**S**

Schaefer, Kathleen E. ....	72
Schaff, William J. ....	16
Schalek, Richard.....	148
<b>Scherson, Yaniv.....</b>	<b>128</b>
Schmidt, Bradley .....	162

Sen, Ayusman .....	58
<b>Shah, Neel.....</b>	<b>130</b>
<b>Shao, Yu-ping.....</b>	<b>132</b>
<b>Sill McElroy, Kaylee.....</b>	<b>134</b>
Sinclair, Robert.....	52, 142
<b>Smith, Janessa .....</b>	<b>136</b>
<b>Smith, Matthew J. ....</b>	<b>138</b>
So, Eric .....	152
<b>Soofi, Wafa .....</b>	<b>140</b>
Spencer, Michael G. ....	98, 134
Stewart, Derek.....	122
Stroock, Abraham.....	6
<b>Symonds, Joshua .....</b>	<b>142</b>

**T**

Taylor, Crawford .....	136
Thacker, Hiren.....	10
Thibeault, Brian.....	78
Thomas, Chris .....	98
<b>Thompson, Rachel.....</b>	<b>144</b>
Thornton, Katsuyo.....	116
<b>Tippie, Abbie.....</b>	<b>146</b>
Tiwari, Sandip .....	64
Traxler, Beth.....	114
<b>Tsang, Winnie J. ....</b>	<b>148</b>

**V**

Van Delden, Jay S.....	64
van Dover, R. Bruce .....	126
Viseu, Ana .....	104

**W**

<b>Walker, Brandon .....</b>	<b>150</b>
Wang, Qian .....	26
Wang, Shan X. ....	76
Ward, Marcus S. ....	24
<b>Welch, David .....</b>	<b>152</b>
<b>Wheelwright, Heidi .....</b>	<b>154</b>
<b>White, Michael.....</b>	<b>156</b>
Wiedmann, Isaac .....	62
Williams, Jesse .....	128
<b>Winders, Jason .....</b>	<b>158</b>
Wong, Gloria .....	92
Woo, Noble.....	126
Wood, David.....	20
Woody, Joseph.....	6
Wu, Huaqiang.....	134

**X**

Xie, Ling.....	138
Xu, Jian.....	28

**Y**

Yadav, Abishek .....	94
<b>Yang, Yin Ian .....</b>	<b>160</b>
Ye, Weifeng .....	94
Yoshimizu, Norimasa .....	48
Yu-Jin .....	94

**Z**

<b>Zieren, Shelley .....</b>	<b>162</b>
Zin, Melvin.....	90

• • •

**Find the 2005 NNIN REU Research Accomplishments  
on the web, in PDF, at: <http://www.nnin.org>**

• • •

*This publication was formatted by Ms. Melanie-Claire Mallison, NNIN REU Program Assistant.  
She welcomes your comments at: [mallison@cnf.cornell.edu](mailto:mallison@cnf.cornell.edu)*